THE UNIVERSITY *of* EDINBURGH

Developing an Object-Based Colocalisation Analysis Method to Measure Synaptic Diversity

Vlad Anton

Ph.D.

University of Edinburgh

Centre for Clinical Brain Sciences

2019

Declaration

I declare that this thesis has been composed solely by myself and that it has not been submitted, in whole or in part, in any previous application for a degree. Except where stated otherwise by reference or acknowledgment, the work presented is entirely my own.

Vlad Anton April 2019

Acknowledgements

I thank the Grant lab for making this work possible, with special thanks to Dr Babis Koniaris and Dr Zhen Qiu for their assistance.

I would like to express my deepest gratitude to Nathanael O'Neill, Maximilian Kratschke and George Kanatouris for their friendship through the hardest time of my life so far.

I would like to thank Prof Alfred William Rutherford for being an inspiration and a true mentor. I further thank Prof Erik Fransén for his friendship and mentorship.

I would also like to thank Prof Rory Duncan and Dr Steven Lee for their valuable scientific advice.

Finally, I would like to thank all past and present members of the research teams and staff in the Chancellor's Building and the neighbouring canteen for all the times we shared a smile or a nice conversation.

Abstract

Protein colocalisation is of particular importance in the study of protein function. To address the inadequacies of previous colocalisation analysis methods, the novel Vicinity-based Localisation Adjacency Determination (VLAD) object-based colocalisation analysis method was developed. VLAD provides three main colocalisation measurements: the proportion of colocalising objects in a dataset, the probability of true colocalisation for individual objects, and the spatial relationship (distance) between colocalising objects. VLAD, validated by extensive testing in simulated data in a wide range of conditions (localisation densities, levels of colocalisation and colocalisation distances), was shown to outperform the state-of-the-art colocalisation analysis method SODA (Statistical Object Distance Analysis).

VLAD was used to study the distribution and colocalisation of three key synaptic proteins: GluN1 (obligatory subunit of NMDA receptors), PSD95 and SAP102 (scaffolding proteins at excitatory synapses). In total, over 62.5 million puncta or puncta assemblies of these proteins were analysed in the mouse hippocampus during early development, making this the largest triple colocalisation brain mapping study of this sort.

GluN1, PSD95 and SAP102 associate in a combinatorial fashion, giving rise to 7 synaptic protein punctum subtypes. The subtype compositions of the hippocampal subregions diverge in development and the differences in subtype compositions in the adult hippocampus may underlie the distinct functions performed by each component of the hippocampal circuit. It was found that a high proportion of the puncta of each protein were non-colocalising in the adult mouse – 67% of GluN1, 48% of PSD95 and 27% of SAP102. Interestingly, NMDA receptors (GluN1) appear to colocalise with PSD95 only in the presence of SAP102, hinting at a possible co-dependence between these proteins.

This study demonstrated the potential of VLAD in the field of brain mapping.

Lay Summary

Each of the many neurons in the human brain (~85 billion) has, on average, 10,000 connections to other neurons. These connections, called synapses, are made up of complex mixtures of component proteins and not all of them are identical. It is believed that synaptic diversity is providing humans with the ability to exert many complex behaviours, prompting us to study it in detail, using mice as a model organism. Through genetic manipulation, synaptic proteins can be labelled with light-emitting (fluorescent) molecules, allowing us to image them with a light microscope.

Different fluorescent synaptic proteins appear as different colour puncta (spots) in microscope images, and it is of interest to identify when these puncta are together (colocalised) and when they are separated. To this end, I developed a new method that measures such colocalisation more accurately than all other pre-existing methods.

I applied this new method to study three important synaptic proteins, all of which are crucial to brain development, learning and memory. I produced a detailed characterisation of synaptic diversity resulting from different combinations of these three proteins in the mouse hippocampus, a brain structure essential to memory formation and spatial navigation.

Table of Contents

List of Figures

List of Tables

Abbreviations

2D (3D) – 2 (3) Dimensions

Adj-R^2 – Adjusted R-squared (R^2 – Coefficient of Determination)

AMPA – α-amino-3-hydroxy-5-methyl-4-isoxazolepropionic acid

AMPAR – AMPA Receptor

ANOVA – Analysis of Variance

AU – Arbitrary Unit

CA (CA1, CA2, CA3) – Cornu Ammonis (1, 2, 3)

CA1ori – CA1 Stratum Oriens (also 2, 3)

CA1rad – CA1 Stratum Radiatum (also 2, 3)

CA1slm – CA1 Stratum Lacunosum Moleculare (also 2, 3)

CA3slu – CA3 Stratum Lucidum

CaMKII – Calcium/Calmodulin-Dependent Protein Kinase II

CBC – Coordinate-Based Colocalisation

CFEM – Correlative Fluorescence and Electron Microscopy

CI – Confidence Interval

CSU – Confocal Scanning Unit

CTD – C-terminal Domain (of NMDA receptor subunits)

CTX – Cortex (here: part of Layer 6 adjacent to the hippocampus)

DABCO – 1,4-diazabicyclo[2.2.2]octane (anti-fading agent)

D-AP5 – R-2-amino-5-phosphonopentanoate

DAPI – 4′,6-diamidino-2-phenylindole

DG – Dentate Gyrus

DGmo – Dentate Gyrus Molecular Layer

DGpo – Dentate Gyrus Polymorphic Layer

DLG – Disks Large Homolog

DNA – Deoxyribonucleic Acid

DoG – Difference of Gaussians

EC – Entorhinal Cortex

eGFP – Enhanced Green Fluorescent Protein

EMCCD – Electron Multiplying Charged Coupled Device

EPSP – Excitatory Postsynaptic Potential

ex – Excitation Wavelength

FN – False Negative

FOV – Field of View

FP – False Positive

FWHM – Full Width at Half Maximum

GluN1 – Glutamate NMDA Receptor Subunit 1 (also GRIN1, NR1, NMDAR1)

H_0 – Null Hypothesis (Randomly Distributed Puncta in Colocalisation Analysis)

IF – Interaction Factor (Colocalisation Analysis Method)

KS – Kolmogorov-Smirnov (test for comparing distributions or testing for normality)

LTD – Long-Term Depression

LTP – Long-Term Potentiation

M – Million(s)

MAGUK – Membrane-Associated Guanylate Kinase

mKO2 – Monomeric Kusabira Orange 2

MOC – Manders Overlap Coefficient

N/A – Not Applicable

NA – Numerical Aperture

NMDA – N-Methyl-D-Aspartate

NMDAR – NMDA Receptor

NN – Nearest Neighbour

OOF – Out-Of-Focus

PCC – Pearson's Correlation Coefficient

PCD – Peak Colocalisation Distance

pdf – Probability Density Function

PDL – Poly-D-lysine hydrobromide

PDZ – PSD95, DLG1 and Zona Occludens-1 protein

PFA – Paraformaldehyde

PSD – Postsynaptic Density

PSD93 – Postsynaptic Density 93 (also DLG2)

PSD95 – Postsynaptic Density 95 (also DLG4)

PSF – Point Spread Function

RI – Refractive Index

RNAi – Ribonucleic Acid Interference

ROI – Region of Interest

RT – Room Temperature

SAP102 – Synapse-Associated Protein 102 (also DLG3)

SAP97 – Synapse-Associated Protein 97 (also DLG1)

SBR –Signal-to-background Ratio

SD – Standard Deviation

SDM – Spinning Disk Confocal Microscope

SIM – Structured Illumination Microscopy

SMLM – Single Molecule Localisation Microscopy

SODA – Statistical Object Distance Analysis

STORM – Stochastic Optical Reconstruction Microscopy

SUB – Subiculum

SV2A – Synaptic Vesicle Protein 2 A

S-W – Shapiro-Wilk (statistical test for normality)

TAP-tag – Tandem Affinity Purification tag

TARP – Transmembrane AMPAR Regulating Protein

TH – Thalamus (here: part of dorsal thalamus adjacent to the hippocampus)

TP – True Positive

TRIPLE – Assembly of Colocalised GluN1, PSD95 and SAP102 puncta

VGluT1 – Vesicular Glutamate Transporter 1

VGSC – Voltage-Gated Sodium Channel

VLAD – Vicinity-based Localisation Adjacency Determination

1 Introduction

1.1 Mapping the brain

The brain is one of the most complex objects known to man. Its complexity is, in part, determined by the vast numbers of neurons and even greater numbers of connections – synapses – between them. The average human brain contains 86 billion neurons (Azevedo *et al.*, 2009) and an estimated 150,000 billion synapses, an average of over 1,700 synapses per individual neuron. Mice (*Mus musculus*) have long been used as model organisms for studying the brain. Yet, even an adult mouse brain contains 71 million neurons (Herculano-Houzel, Mota and Lent, 2010) and approximately 500 billion synapses (Schüz and Palm, 1989), a staggering average of 7,000 synapses per neuron.

Fundamental studies of neuronal function, ion channel or neurotransmitter receptor dynamics and protein-protein interactions, to name a few, have made vital contributions to neuroscience but their often narrow focus makes them insufficient for a complete understanding of the brain (Frackowiak and Markram, 2015). To address this, ambitious initiatives to map the entire mouse brain have already produced the first maps of brain-wide gene expression (Lein *et al.*, 2007), inter-regional connectivity (Oh *et al.*, 2014) and individual excitatory synapses (Zhu *et al.*, 2018). The promise of these immense sets of data is that they will one day complete a unified working model of the mouse brain, perhaps of the like attempted by the Blue Brain Project (Markram, 2006) or its successor, the Human Brain Project (Frackowiak and Markram, 2015).

1.2 Excitatory neurotransmission in the brain

A resting (inactive) neuron maintains an electric potential of approximately -70 mV (a net negative charge on the intracellular side) across its cell membrane: the resting membrane potential. In this state, the membrane is said to be polarised and positive ion concentration gradients are present across the mostly impermeable membrane, with higher concentrations of sodium and calcium ions outside the cell and a higher concentration of potassium ions inside. A nerve impulse, or action potential, is triggered when a moderate membrane depolarisation (up to ~-55 mV) activates voltage-gated sodium channels (VGSCs). Activated VGSCs open, allowing

an influx of sodium ions into the cell and leading to rapid membrane depolarisation. Shortly after, voltage-gated potassium channels open and the outflow of potassium leads to the repolarisation of the membrane. Ion pumps are responsible for maintaining the ion concentration gradients across the membrane. When the membrane is depolarised at a specific location, nearby VGSCs are activated and the action potential is thus propagated through the neuron. This usually happens unidirectionally, through the neuron's dendrites, towards the cell body (soma) and then through the axons and away from the soma, all the way to the axon terminals (Miller and Yeh, 2016).

A neuron's axon terminals are located at synapses, where they are apposed to another neuron, separated by a narrow gap called the synaptic cleft. Action potentials cannot propagate from the presynaptic neuron to the postsynaptic neuron through the synaptic cleft. This communication is mediated by neurotransmitters – chemical substances stored in vesicles at the axon terminal and released into the synaptic cleft in response to an action potential. Once released, excitatory neurotransmitters can activate receptors on the postsynaptic neuron, depolarising it and originating an action potential (Miller and Yeh, 2016).

Glutamate is the primary excitatory neurotransmitter in the central nervous system, and it activates three main types of receptors: α-amino-3-hydroxy-5-methyl-4-isoxazolepropionic acid (AMPA) receptors (AMPARs), N-methyl-D-aspartate (NMDA) receptors (NMDARs) and kainate (kainic acid) receptors. There are 4 AMPAR subunit (monomer) genes in mice and in humans – GluA1-GluA4 (alternatively GluR1-GluR4 or Gria1-Gria4) – and they typically assemble into heterotetramers (Miller and Yeh, 2016). 7 NMDAR subunits have been identified to date – GluN1, GluN2A-GluN2D, GluN3A and GluN3B (alternatively NR1, NR2A-NR2D, NR3A and NR3B or GRIN1, GRIN2A-GRIN2D, GRIN3A and GRIN3B). NMDAR subunits assemble into heterotetramers always containing 2 GluN1 subunits (called obligatory subunits) and 2 other identical or different subunits (Paoletti, Bellone and Zhou, 2013). There are 5 kainate receptor subunits – GluK1-GluK5. GluK1-GluK3 can assemble as homotetramers and GluK4 and GluK5 must assemble as heterotetramers together with GluK1-GluK3 subunits (Miller and Yeh, 2016).

All excitatory receptors are neurotransmitter-gated sodium channels: upon glutamate binding, they open and allow sodium into the postsynaptic neuron,

leading to a small membrane depolarisation, called excitatory postsynaptic potential (EPSP). An EPSP resulting from the opening of a single receptor channel typically does not result in an action potential. It is the summation of EPSPs that brings the membrane potential of the postsynaptic neuron to the action potential threshold, at which point VGSCs open and initiate an action potential (Miller and Yeh, 2016).

Synaptic AMPARs are the main mediators of excitatory transmission in the mammalian brain. The number of AMPARs and their properties at individual synapses can be modulated through the process of synaptic plasticity (Miller and Yeh, 2016). The best-studied processes of synaptic plasticity are long-term potentiation (LTP) and long-term depression (LTD) in the postsynaptic neuron, although other types of plasticity can take place on either side of the synaptic cleft (Lisman, 2017). LTP enhances synaptic transmission (by increasing the response of the postsynaptic neuron to glutamate release) in a persistent fashion and LTD does the opposite (reduces the response of the postsynaptic neuron to glutamate release).

NMDARs play a smaller role in excitatory transmission but are central to synaptic plasticity. They open upon co-activation by glutamate and glycine but their pore is blocked by a magnesium ion while the membrane is close to its resting potential. Only if the membrane is sufficiently depolarised (e.g. due to sustained neuronal activity), the magnesium block is removed and they allow the influx of positive ions into the cell. Unlike other receptors, when open, NMDARs are permeable to calcium in addition to sodium (Miller and Yeh, 2016). Calcium acts as a signalling molecule. Upon entering a postsynaptic terminal, it binds to and activates calcium/calmodulin-dependent protein kinase II (CaMKII), one of the most abundant postsynaptic proteins, triggering a biochemical signalling cascade (Gold, 2012). Following CaMKII activation, AMPAR-dependent synaptic strength can be enhanced in two ways. First, CaMKII can phosphorylate AMPARs directly, increasing their sodium conductance (i.e. upon activation by glutamate, they allow sodium into the cell more quickly, leading to a faster membrane depolarisation and a larger EPSP). Second, CaMKII can activate other enzymes downstream in the signalling cascade, leading to the incorporation and stabilisation of more AMPARs at the synapse (Lisman, Yasuda and Raghavachari, 2012). Interestingly, NMDARs can also mediate the opposing process of LTD and the timing of sodium influx spikes in the postsynaptic neuron appears to be the deciding factor between LTP and LTD (Lisman, 2017).

1.3 The postsynaptic density

Synapses are not only highly abundant in the brain, but they also house complex networks of proteins. A proteomic study identified at least 240 different proteins in the proteome – entire possible set of expressed proteins – of the presynaptic active zone (Morciano *et al.*, 2009). A study of the postsynaptic proteome identified over 1,400 different proteins (Bayés *et al.*, 2010). Among these, a 'core' subset of 1,000 proteins appears to be conserved across humans, mice (Bayés *et al.*, 2012) and, interestingly, zebrafish (Bayés *et al.*, 2017). Much of this complexity is the result of two rounds of whole genome duplications that occurred about 550 million years ago in vertebrate evolution (Van De Peer, Maere and Meyer, 2009), allowing duplicated genes to diversify and specialise their functions. It is believed that this expansion facilitated the evolutionary enlargement and enhancement of the nervous system by increasing the diversity of possible synaptic protein complexes (Emes and Grant, 2012). The postsynaptic proteome also manifests regional diversity within the brain in mice (Roy, Sorokina, McLean, *et al.*, 2018) and in humans (Roy, Sorokina, Skene, *et al.*, 2018).

At most excitatory synapses in the brain, the postsynaptic neurons contain a postsynaptic density (PSD), an electron-dense area visible under an electron microscope (EM). The PSD is a concentrated network of protein complexes responsible for locating neurotransmitter receptors in front of the active zone of the presynaptic neuron and linking them to the cytoskeleton and a host of intracellular signalling proteins (Gold, 2012). An illustration of key PSD components is shown in Figure 1-1. While most of these influence innate and learned behaviours in mice (Komiyama *et al.*, 2018), this thesis will focus on PSD95, SAP102 (scaffolding proteins – introduced next), and GluN1 (or NR1, the obligatory subunit of all NMDARs). Most of the machinery involved in LTP and LTD – forms of synaptic plasticity believed to underlie learning and memory – resides in or is associated with the PSD (Lisman, 2017). The importance of the PSD to brain function is demonstrated by the involvement of PSD protein mutations in over 130 neuropsychiatric disorders such as schizophrenia and autism (Bayés *et al.*, 2010).

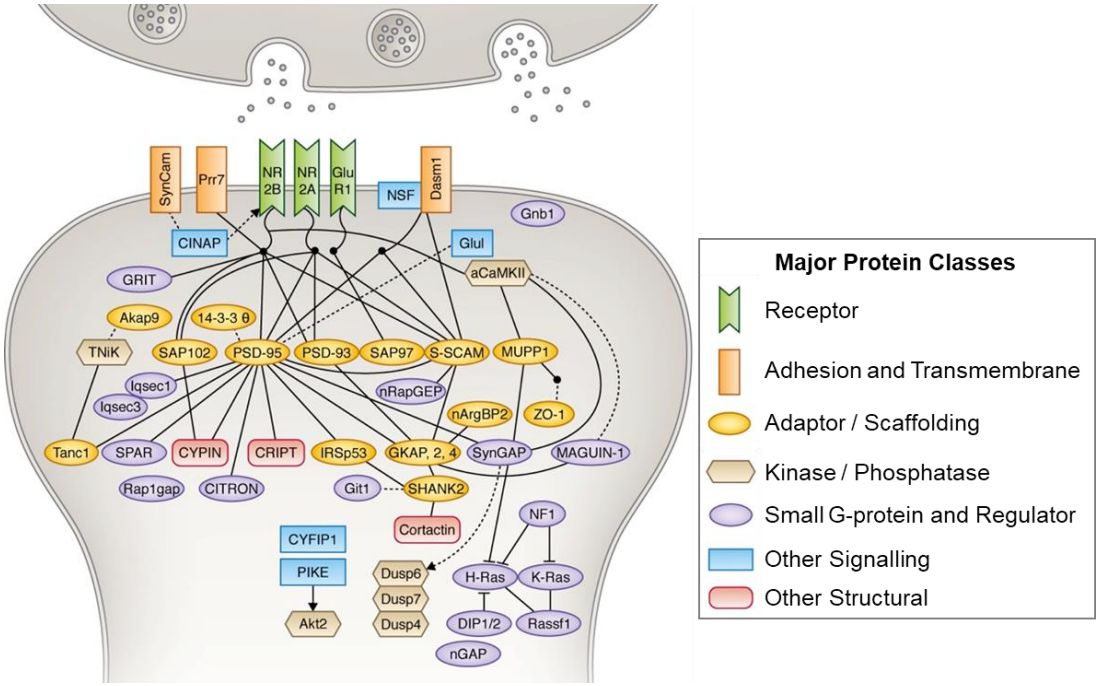

Figure 1-1. Key molecular components of the postsynaptic density. This diagram illustrates interactions between major PSD components and AMPAR and NMDAR subunits. PSD95 emerges as a highly inter-connected central node of the PSD protein network. Solid lines indicate confirmed protein-protein interactions and dotted lines indicate other functional interactions. Adapted from (Komiyama *et al.*, 2018).

Central to the PSD and present in high copy numbers are members of the Disks Large Homolog (DLG) family of scaffolding proteins, especially postsynaptic density 95 (PSD95 or DLG4), one of four paralogs. The four DLG paralogs (DLG1/SAP97, DLG2/PSD93, DLG3/SAP102 and DLG4/PSD95) are part of the Membrane-Associated Guanylate Kinase (MAGUK) family of scaffolding proteins (Kim and Sheng, 2004). The DLG proteins have a common structure made up of PDZ (PSD95, DLG1 and zona occludens-1 protein) domains, an SH3 (Src homology 3) domain and a catalytically inactive GK (guanylate kinase-like) domain from N- to C-terminus. All of these domains, but predominantly the PDZ domains, enable DLG family members to form vast protein interaction networks at the PSD, reviewed in (Zhu, Shang and Zhang, 2016; Won *et al.*, 2017).

1.4 PSD95, SAP102 and GluN1

PSD95 is the archetypal PSD scaffolding protein. It is highly abundant at excitatory synapses (Sheng and Hoogenraad, 2007), where it is clustered and retained at the postsynaptic membrane mainly by its palmitoylated N-terminus (Craven, El-Husseini and Bredt, 1999). Here, PSD95 can interact directly with the cytoplasmic C-terminal

tails of GluN2A-D subunits of NMDARs via its PDZ domain (Husi and Grant, 2001). NMDAR transmission is not impaired in PSD95 knockout mice (Elias *et al.*, 2006) and PSDs are formed in its absence as well (Migaud *et al.*, 1998). The structure of the PSD is only disrupted during acute ribonucleic acid interference (RNAi) knockdown of PSD95 (Chen *et al.*, 2011). PSD95 also interacts indirectly with AMPARs via Stargazin, a transmembrane AMPAR regulating protein (TARP) essential for the surface expression and synaptic clustering of AMPARs (Chen *et al.*, 2000). AMPAR transmission is reduced in PSD95 knockout mice (Carlisle *et al.*, 2008) and enhanced when PSD95 is overexpressed (El-Husseini, Schnell and Chetkovich, 2000). Super-resolution light microscopy has revealed that PSD95 forms nanoclusters – concentrations of PSD95 with diameters of approximately 80 nm – that, in turn, also concentrate AMPARs at the postsynaptic membrane (MacGillavry *et al.*, 2013; Nair *et al.*, 2013). The presence of these nanocluster has been confirmed in fixed mouse brain tissue as well (Broadhead *et al.*, 2016).

PSD95 knockout mice show spatial learning deficits despite enhanced LTP (Migaud *et al.*, 1998) and, in humans, PSD95 mutations have been associated with autism spectrum disorders and Williams' syndrome (Feyder *et al.*, 2010).

Unlike PSD95, SAP102 lacks an N-terminal palmitoylation motif, making it more mobile in dendritic spines (Zheng *et al.*, 2010). Studies of dendritic spine dynamics revealed that SAP102 is the first DLG protein to accumulate at newly formed spines, within a few hours from formation (Lambert *et al.*, 2017). PSD95 is incorporated into newly formed spines up to 20 hours later than SAP102 and is important for synapse maturation (Berry and Nedivi, 2017). This sequence of expression at individual spines is replicated in development: SAP102 is expressed earlier in development compared to PSD95 (Sans *et al.*, 2000). Altogether, these observations point to a developmental transition from SAP102 to PSD95 (though both proteins remain highly expressed in the adult brain) and place a larger emphasis on the role of SAP102 in development (Zheng *et al.*, 2011).

Despite the high structural similarity to PSD95, SAP102 is present in smaller molecular weight, biochemically distinct protein complexes at the PSD, implying that PSD95 and SAP102 may link NMDARs to distinct downstream signalling pathways within the PSD (Frank *et al.*, 2016).

GluN2B-containing NMDARs interact with SAP102 via a PDZ binding domain on the intracellular tail of the GluN2B subunit, just like with the other MAGUKs. GluN2B interactions with the other MAGUKS (SAP97, PSD93 and PSD95) stabilise NMDARs at synaptic sites, where the MAGUKS are retained due to their palmitoylated N-termini (Schluter, Xu and Malenka, 2006). A recent study found the basis of an observed coincidence between the higher mobility of SAP102 and GluN2B-containing NMDARs in dendritic spines. It was previously known that NMDARs deficient in binding to the PDZ domains of MAGUKs fail to accumulate at synaptic sites. This study found that disrupting a non-PDZ domain interaction between GluN2B and SAP102 restored synaptic expression of PDZ-deficient GluN2B subunits at synapses, implying that their binding to mobile SAP102 would otherwise contribute to their diffusion away from synaptic sites (Chen *et al.*, 2012).

SAP102 knockout mice display spatial learning deficits (Cuthbert *et al.*, 2007) and, in humans, SAP102 mutations are associated with mental retardation (Tarpey *et al.*, 2004).

The importance of PSD95 and SAP102 is partly owed to their interactions with NMDARs, linking these receptors to downstream signalling pathways. NMDARs have been studied extensively due to their involvement in synaptic plasticity (a proposed component of learning and memory) (Hunt and Castillo, 2012), brain and synaptic development (Sanz-Clemente, Nicoll and Roche, 2013) and clinical importance, both as disease substrates and therapeutic targets (Paoletti, Bellone and Zhou, 2013). NMDARs are not exclusively located at postsynaptic sites. They are mobile and can diffuse along the neuronal membrane into perisynaptic and extrasynaptic sites (Petralia, 2012). During early postnatal development, NMDARs can occur presynaptically, at axonal growth cones or nascent active zones (Gill *et al.*, 2015). Numerous non-neuronal cells can also express NMDARs. In the central nervous system, microglia, astrocytes and oligodendrocytes all express various NMDAR subunits (Hogan-Cann and Anderson, 2016).

NMDARs are heterotetrameric ion channels composed of two obligatory GluN1 (also NR1 or GRIN1) subunits and two GluN2 (of 4 types: A-D) and/or GluN3 (of 2 types: A/B) subunits. Most possible combinations of NMDAR subunits exist and they show distinct regional and developmental expression patterns (Paoletti, Bellone and Zhou, 2013). Their different functions are determined by different intracellular C-terminal domains (CTDs). The GluN2 subunits have 400-500 amino acid long CTDs

containing various protein binding motifs enabling them to interact with different partners, including scaffolding proteins, cytoskeletal proteins and signalling enzymes (Traynelis *et al.*, 2010). The most abundant NMDAR varieties are diheteromeric GluN1-GluN2A or GluN1-GluN2B receptors and triheteromeric GluN1-GluN2A-GluN2B receptors (each containing 2 GluN1 subunits) and a developmental switch from predominantly GluN2B-containing NMDARs to GluN2A-containing NMDARs occurs between birth and early adulthood (postnatal day 35) in rodents but GluN2B remains highly expressed in the adult brain (Sans *et al.*, 2000).

In adult mouse synaptosome preparations (isolated membrane-bound compartments containing synaptic terminals), GluN1 subunits are equally distributed amongst two populations of protein complexes: 0.8 MDa (megadalton) complexes lacking PSD scaffolding protiens and 1.5 MDa complexes that also include PSD95 and PSD93 (both necessary for the formation of 1.5 MDa-NMDAR complexes) (Frank *et al.*, 2016). Later work on the stoichiometry in these 1.5 MDa complexes showed that, on average, they contain one tetrameric NMDAR and a PSD95 dimer (Frank *et al.*, 2017).

The persistent nature of certain forms of synaptic plasticity, especially LTP, has led many to postulate that it is the substrate of memory. The discovery of R-2-amino-5-phosphonopentanoate (D-AP5), a selective NMDAR inhibitor, was pivotal in establishing the role of NMDARs in learning and memory. D-AP5 enabled Graham L. Collingridge and his colleagues to first show that LTP depended on NMDARs (Collingridge, Kehl and McLennan, 1983). Then, it was Richard Morris et al. who first performed spatial learning experiments on rats treated with D-AP5, showing that the inhibition of NMDARs prevented rats from learning the location of a hidden platform in a water maze that later became known as the Morris Water Maze (Morris *et al.*, 1986). Since then, an explosion of behavioural experiments in the presence of NMDAR inhibitors and, later, in mice with NMDAR subunit gene knock-outs, have shown that NMDARs are needed for memory encoding, but not memory retrieval, in a variety of processes, from spatial learning to episodic-like memory and contextual fear conditioning (Morris, 2013).

In humans, NMDAR mutations are associated with autism spectrum disorders (Lee, Choi and Kim, 2015). More importantly, NMDARs are important therapeutic targets. Ketamine, an NMDAR antagonist, had long been used as an anaesthetic and, more

recently, it has shown promise in the treatment of clinical depression (Lee *et al.*, 2015).

1.5 Synaptic diversity

Proteins perform their myriad functions as part of complexes, interacting with other proteins. It is important to note that the ability of two proteins to interact with each other does not always result in their co-occurrence. The more than one thousand known PSD proteins may associate in a combinatorial fashion, giving rise to a diverse population of synapses. It is reasonable to think that such diversity of molecular composition underlies functional diversity (Grant, 2007). This creates a need for tools that enable the quantification of synaptic diversity. Complementary approaches, such as proteomics, fluorescence light microscopy and electron microscopy will shed light onto this under-explored area of neuroscience (O'Rourke *et al.*, 2012).

Currently, much work is required to integrate results obtained with different techniques. For example, a recent study mapping PSD95- and SAP102-containing synaptic puncta across the mouse brain using fluorescence microscopy revealed a high degree of synaptic diversity within and between brain regions, and an overall high degree (over 50% in most cases) of colocalisation between the two proteins (Zhu *et al.*, 2018). At the same time, biochemical studies revealed that PSD95 and SAP102 are in distinct, separable protein complexes (Frank *et al.*, 2016). The same study also showed that SAP102 is present in lower molecular weight complexes, typically smaller than a tetrameric NMDAR. At the same time, predominantly outside synapses, SAP102 has been shown to interact with endocytosed NMDARs during trafficking towards synaptic sites (Washbourne, 2004) and SAP102 is also involved in the synaptic clearance of NMDARs (Chen *et al.*, 2012). This example is only meant to highlight the fact that different approaches are appropriate for characterising different aspects of synaptic protein function and that a complete understanding of synaptic diversity will require the successful integration of multiple techniques.

1.6 Analysing colocalisation

1.6.1 Pixel-based colocalisation analysis methods

Many insights into functional relationships between proteins have been obtained by analysing their colocalisation, typically from fluorescence microscopy data. The colocalisation of two proteins does not guarantee their physical interaction but non-colocalisation almost certainly implies non-interaction. Colocalisation could be viewed as a necessary but not sufficient condition for physical interaction.

Colocalisation is most commonly measured in fluorescence microscopy images because different proteins can readily be labelled with different fluorophores to allow their simultaneous identification in biological samples. An early colocalisation analysis method was the Pearson's correlation coefficient (PCC), measuring the correlation of fluorescent light intensity values between two images on a pixel-by-pixel basis (Manders *et al.*, 1992). PCC can provide an unbiased measure of image correlation but it is negatively affected by noise, background signal and unequal absolute intensities between channels. PCC may be useful for semi-quantitatively assessing the colocalisation of diffusely distributed fluorophores or signals with irregular shapes but it is less useful for measuring colocalisation between spot-like objects such as synaptic protein puncta, as it does not provide information on the proportions of colocalising puncta of each protein imaged. Furthermore, PCC cannot be computed for single molecule localisation microscopy (SMLM) data, where objects are represented as dimensionless points with xy (2D) or xyz (3D) coordinates.

Manders overlap coefficient (MOC) uses an intensity threshold to compute the intensity-weighted proportion of pixels in one channel overlapping with another channel (Manders, Verbeek and Aten, 1993). It is less sensitive to noise than the PCC but background and above-threshold signal still contribute to false positive measurements. Like the PCC, MOC is not suitable for measuring colocalisation between puncta, since it also lacks individual punctum information.

Multiple ways of assessing statistical significance of colocalisation were devised for PCC and MOC, reviewed in (Bolte and Cordelières, 2006). The Costes randomisation approach is perhaps the most commonly used one (Costes *et al.*, 2004). It involves dividing one of the two images analysed into pixel blocks roughly equal to the imaged object size (or the resolution of the microscope) and shuffling

the blocks multiple times, measuring either PCC or MOC for every randomised image. A p-value is then obtained by comparing the original PCC or MOC to those measured in randomised images. This p-value can help identify data sets that are indistinguishable from randomness but does little else to overcome the limitations inherent to pixel-based colocalisation analysis methods.

1.6.2 Object-based colocalisation analysis methods

The punctate appearance of many fluorescently labelled proteins (e.g. synaptic proteins accumulated at PSDs) required a different approach to image analysis. Object-based colocalisation analysis methods – reviewed in (Lagache *et al.*, 2015) – consist of two steps. First, objects (puncta or spots) are identified and represented as points in space (xy coordinates in 2D and xyz coordinates in 3D). A set of points is called a point process. When every point has additional features, such as the diameter or fluorescence intensity of its corresponding punctum, this set of points with associated data is called a marked point process. For simplicity, they will only be referred to as points or puncta. Second, spatial relationships between puncta of the same protein or of different proteins are measured based on the distances between them.

Object-based colocalisation analysis methods have two advantages. First, puncta detection is a separate step that can be optimised independently from colocalisation analysis. Second, unlike pixel-based methods, they can be used to measure colocalisation in SMLM data.

Many types of puncta detection algorithms exist (Chenouard *et al.*, 2014). In this thesis, the TrackMate ImageJ plugin (Tinevez *et al.*, 2017) was used. TrackMate detection is based on a difference of Gaussians (DoG) filter – a feature-enhancing operation. In DoG-based detection, two Gaussian filters of different radii are applied to the raw image. Then, by subtracting the image blurred with the larger-radius Gaussian filter from the one with the smaller-radius filter, edges and features (such as puncta) are enhanced in the resulting image. While no detection method is perfect, DoG-based detection has been shown to be reliable in detecting synaptic puncta (and any punctate signals) of varying intensities in the presence of diffuse and non-uniform background signals (noise) (Iwabuchi *et al.*, 2014) and was confidently applied to the data in this thesis following parameter threshold optimisation.

Detector parameter thresholds can be optimised by establishing a ground truth – often manually counted puncta – and plotting a precision-recall curve that allows choosing the combination of parameter thresholds that maximises both precision and recall (minimises both false positives and false negatives, respectively) (Fawcett, 2006). With optimal parameter thresholds, these detectors can readily detect puncta even in lower quality image data with poor signal to noise ratios or high levels of background fluorescence. Furthermore, as the precision-recall curve guides the objective choice of thresholds, detection data will be more robust and reliable than if thresholds were manually (and subjectively) chosen. More recently, machine learning has been applied to puncta detection to match the experimenter-defined ground truth ever more closely (Zhu *et al.*, 2018).

Once puncta (points) are detected, their colocalisation can be measured after analysing the spatial relationships between them. Two hypothetical sets of puncta, S1 and S2, will be used to illustrate the various spatial analysis methods. Each set of points is characterised by its point (punctum) density: number of points per surface area or volume. For example, the two sets of points could correspond to PSD95 and SAP102 puncta detected in a specific brain region. Spatial relationships between puncta can be characterised in three main ways: Ripley's K function (Ripley, 1976), its derivative, the pair correlation function (Wiegand and Moloney, 2004) and nearest neighbour (NN) distance (Clark and Evans, 1954).

Ripley's K function counts, for every point in S1, the number of S2 points located within a given radius r (circle or sphere). It is sometimes used to describe spatial patterns within a population of points (within S1 rather than between S1 and S2) but cannot be used directly for assessing colocalisation. The pair correlation function, is the derivative of Ripley's K function and consists of the difference between Ripley's K function for two different radii r_1 and r_2. It counts, for every point in S1, the number of S2 points in the ring between circles (or spheres) r_1 and r_2. The state-of-the-art colocalisation analysis method SODA (Statistical Object Distance Analysis) is based on the pair correlation function (Lagache *et al.*, 2018).

The NN distance is the Euclidean distance (straight line) between one point from S1 to the nearest point of S2. Using a NN distance threshold is an intuitive but flawed way of measuring colocalisation. It is intuitive because of the simple concept that, when the distance between two points is short, they colocalise, and when the

distance between them is long, the do not. It is flawed, however, because ‘short’ NN distances can occur between puncta even when they are randomly distributed.

Indeed, the null hypothesis (H_0) in colocalisation analysis is not the absence of points (that would be too easy), but their random distribution in space (at a matching punctum density). As a result, the main challenge in object-based colocalisation analysis becomes the separation of true colocalisation from false positive colocalisation that occurs by chance. Statistical tests have been included in multiple colocalisation analysis methods but their ability is limited to answering whether a measured colocalisation coefficient is different from what would be expected by chance. For example, the Distance Analysis (DiAna) method (Gilles *et al.*, 2017) compares the NN distance threshold-based colocalisation measured in experimental data with colocalisation measured in matching randomised data. It then assesses whether the cumulative NN distance distribution in experimental data falls outside the 95% confidence interval of randomised NN distance distributions to conclude whether colocalisation is statistically significant. Nevertheless, this method fails to recognise that measured colocalisation is, in turn, made up of true and false positives. In a hypothetical example, if 60% colocalisation is measured in a set of data, it remains unknown whether 3% or 30% of measurements are false positives (the result of crowding and not true colocalisation). The requirement for the experimenter to manually choose a distance threshold further undermines the robustness of these colocalisation measurements.

Malkusch et al. (2012) developed the coordinate-based colocalisation (CBC) analysis method, also based on NN distance measurements, removing the requirement for a NN distance threshold. CBC assigns, to each point, a colocalisation score from -1 (exclusion) to +1 (correlation), with 0 representing non-correlation or randomness. While this excludes long NN distances from measured colocalisation, it cannot discriminate short NN distances that arise due to chance and, as such, is also affected by undetermined amounts of false positives.

In an effort to better characterise the contribution of false positives to measured colocalisation, Eliscovich et al. (2017) proposed choosing a NN distance threshold that would limit the amount of false positives to a pre-determined amount. For example, a threshold may result in 10% colocalisation in matching randomised data and, by using the same threshold in experimental data, no more than 10% of the measured colocalisation could be due to chance. The contribution of false positives

still remains undefined but it is bound between zero and a pre-determined limit (an arbitrary 10%, as used in the original publication). Furthermore, there is no mention of false negatives, which are unknown but could be significant if a strict threshold is chosen to limit false positives.

Zhang et al. (2008) introduced the False Discovery Rate method, which measures the distances between all points of one set (S1) and all points of the other (S2) in experimental data and matching randomised controls. Then, it computes the ratio between inter-point (S1-S2) distances shorter than those in randomised data and all inter-point distances as a measure of colocalisation that excludes false positives. This approach is equivalent to subtracting the maximum possible colocalisation occurring in a H_0 control from the colocalisation measured in experimental data and is potentially exposed to significant false negatives. More importantly, this ratio is difficult to interpret, as it does not represent a proportion of colocalised points (an intuitive output). The Interaction Factor (IF) method of Bermudez-Hernandez et al. (2017) similarly subtracts the probability of overlap (colocalisation) in a H_0 control from measured colocalisation. IF was tested on some simulated data and showed modest performance, producing colocalisation measurements with low precision (widely spread values).

Helmuth et al. (2010) correctly highlighted the inadequacy of NN distance thresholds for measuring colocalisation and devised a novel analysis method that measures interaction strength. Their method appears statistically robust but it was not tested on simulated data, so its accuracy and reliability were not confirmed. Moreover, the interaction strength quantity is also removed from the more intuitive measure of colocalisation in the form of a proportion of objects in a group.

In colocalisation analysis methods that rely on Ripley's K function, it is typically normalised to the punctum density in the analysed data, such as in the Molecular Interactions in Super-Resolution (MIiSR) method (Caetano *et al.*, 2015). This step facilitates comparisons between datasets with different punctum densities and adjusts the baseline of measurements to levels of colocalisation (or clustering) expected in randomly distributed puncta. However, this does not determine the proportion of measured colocalisation in a given experimental setting caused by chance. As such, this approach also cannot separate true colocalisation from colocalisation occurring by chance (false positive colocalisation).

The Statistical Object Distance Analysis (SODA) method developed by Lagache et al. (2018) is an improvement on all previous colocalisation analysis methods and addresses most of their shortcomings successfully. SODA provides a coupling index (the proportion of colocalised objects in a group), a probability of true coupling for every detected object and a coupling distance – describing the distances between colocalised objects. It corrects for false positives via a punctum density-dependent threshold and adapts to different situations without requiring *a priori* knowledge or arbitrary thresholds. Finally, SODA is convincingly supported by its high performance (high accuracy and precision) in simulated data across a multitude of different conditions (punctum densities, colocalisation levels and colocalisation distances). For all these reasons, SODA is an excellent benchmark for colocalisation analysis methods.

1.7 Motivation and aims

When analysing the relationship between puncta of two proteins A and B, three simple questions are generally asked. First, what proportion of puncta of protein A colocalise with protein B? Second, does an individual punctum of A colocalise with B? Third, when they do colocalise, over what distance does this take place? Despite recent progress in the field of colocalisation analysis, existing object-based colocalisation analysis methods are still affected by significant limitations.

Some methods, as identified by Lagache et al. (2018) (the authors of SODA), lack a basic output that reflects the proportion of protein A colocalised with protein B, thus failing to answer the first question. Examples include the False Discovery Rate (Zhang *et al.*, 2008) and the Interaction Strength methods (Helmuth, Paul and Sbalzarini, 2010).

Answering the second question – does a punctum of protein A colocalise with B? – is not as straightforward as it would seem, and requires a shift away from thinking about colocalisation in binary yes-or-no terms and towards assessing it in a probabilistic fashion instead. The question requires an answer in form of a probability of true colocalisation. This is important because colocalisation can arise due to chance and most current methods fail to correctly account for false positives. Many methods either do nothing to quantify the proportion of false positives in a colocalisation measurement (Malkusch *et al.*, 2012; Caetano *et al.*, 2015; Gilles *et*

al., 2017) or impose arbitrary thresholds to limit false positives, thus exposing the measurements to potentially significant amounts of false negatives (Eliscovich, Shenoy and Singer, 2017).

Just because a colocalisation measurement is higher than what would be expected in a randomised control, this does not mean the measurement is free from false positives, and the comparison with a control cannot reveal the proportion of false positives. Conversely, subtracting control levels of colocalisation from a measurement is flawed because it is entirely possible for all measurements in a given setting to be true and not the result of chance.

The third question, on the spatial relationships between colocalising puncta, is usually answered well by Ripley's K function-based methods (Caetano *et al.*, 2015), though not by nearest neighbour distance-based methods that impose arbitrary distance thresholds for colocalisation (Eliscovich, Shenoy and Singer, 2017), and many other methods leave it wholly unanswered.

The recently developed Statistical Object Distance Analysis (SODA) method appears to be the only method to date that successfully answers all three questions (Lagache *et al.*, 2018). SODA provides a coupling index (what proportion of A colocalises with B?), a probability of true coupling for every punctum (does this punctum of A colocalise with B?) and a coupling distance (at what distance do A and B colocalise?). SODA entails a robust way of dealing with false positives and of assigning probabilities of true colocalisation. However, as will be shown next, SODA's approach to correct for false positives is over-conservative and results in significant false negatives in data with high levels of true colocalisation.

Even so, currently available methods may be sufficient for measuring colocalisation in experiments where two groups of data are compared. If their errors – whether including false positives or omitting false negatives – are systematic, they would not preclude comparisons between groups and statistically significant results. However, this standard cannot be applied to exploratory studies, such as brain mapping, where the goal is an accurate description of biology and not comparison to a control group. An imperfect analogy to genomics could be made: the Human Genome Project did not aim to sequence more human deoxyribonucleic acid (DNA) bases than bacterial ones – that would be absurd. Instead, it aimed to determine the true sequence of the human genome, a task where no amount of false positives or false negatives was acceptable (Lander *et al.*, 2001). By the same token, data analysis

methods employed in future brain mapping efforts should strive for the highest attainable accuracy.

This thesis presents the development and validation of the Vicinity-based Localisation Adjacency Determination (VLAD) method, based on a novel approach to measuring colocalisation. VLAD aims to answer the three basic colocalisation questions from before, and to do so with a level of accuracy that qualifies it for being used in brain mapping.

Once developed and validated, VLAD was applied to a vast dataset of GluN1, PSD95 and SAP102 puncta in the developing mouse hippocampus. This proof-of-concept experiment was the largest-scale triple colocalisation analysis of synaptic proteins in fixed brain tissue to date. This large-scale analysis aims to provide new insights into the organisation of these key synaptic proteins and the spatial relationships between them.

2 Materials and Methods

2.1 Mouse generation

The mice used for this work had three proteins genetically tagged, either with a fused fluorescent protein or a tandem affinity purification tag (TAP-tag). Postsynaptic Density 95 (PSD95 or DLG4) was fused to enhanced green fluorescent protein (eGFP) and Synapse-Associated Protein 102 (SAP102 or DLG3) was fused to monomeric Kusabira Orange 2 (mKO2) as described in (Zhu *et al.*, 2018). The extracellular N-terminus of the N-methyl-D-aspartate receptor (NMDAR) subunit 1 (GluN1 or NR1) was fused to a TAP-tag as described in (Frank *et al.*, 2016). These mice were reported to be phenotypically and electrophysiologically normal. They were crossed to obtain the triple-labelled mice (PSD95-eGFP, SAP102-mKO2 and GluN1-TAP-tag) used in this study.

Mouse line generation was previously described (Fernández *et al.*, 2009). Both PSD95 (Dlg4) and SAP102 (Dlg3) were tagged with their respective fluorescent proteins (eGFP or mKO2) at their C-termini. The fluorescent tag coding sequences were inserted downstream of the final exons of each gene, in vectors where the fluorescent tag sequences were flanked by upstream homologous sequences up to exon 9 for Dlg4 and up to exon 17 for Dlg3, and by downstream homologous sequences containing the 3' untranslated region of each gene. In the case of GluN1 (Glun1), the TAP-tag was added upstream of exon 1 (as an in-frame insertion) but downstream of the predicted signal peptidase cleavage site at Aspartate 22 (Asp22). Within the vector, the upstream homologous sequence extended 2249 base pairs into the Glun1 5' region and downstream to include exon 1 and the first 500 base pairs of intron 1. In all cases, the vectors also contained a neomycin resistance gene flanked by loxP sites, to allow selection and then excision using by Cre recombinase. The vectors were electroporated into mouse embryonic stem cells for homologous recombination to occur. Recombinant cells were selected based on their antibiotic resistance, and recombinant cells were injected into mouse blastocysts following polymerase chain reaction confirmation of recombination. The chimeric mice obtained were bred with wild type mice. Offspring expressing the genetic tags were then crossed with a Cre recombinase line to remove the neomycin resistance cassette. Multiple rounds of breeding were then performed to obtain mice with the desired genotypes.

2.2 Mouse brain section preparation

The sagittal hippocampal sections used in the developmental study were provided by Dr Melissa Cizeron. Adult mice (over postnatal day 31 – P31) were anaesthetised via an intraperitoneal injection of 0.1 ml of 200 mg/ml sodium pentobarbital (Pentoject, Animalcare Ltd.). Dosage was reduced for younger mice, from 0.03 ml for P1 pups to 0.05 ml for P30 mice. After complete anaesthesia was confirmed, the mice were transcardially perfused with 10 ml phosphate buffered saline (PBS; Sigma-Aldrich) followed by 10 ml 4% (volume/volume – v/v) paraformaldehyde (PFA; Alfa Aesar) dissolved in PBS. Upon dissection, brains were fixed for a further 3.5 hours in 4% PFA at 4°C. PFA-fixed brains were moved into a 30% (weight/volume – w/v) sucrose (VWR Chemicals) solution (dissolved in PBS) and kept at 4°C for 3 days. Then, the brains were embedded in optimal cutting temperature (OCT) medium (VWR International) in plastic moulds and frozen in an isopentane bath immersed in liquid nitrogen. Embedded brains were stored at -80°C.

Embedded brains were sectioned either coronally or sagittally as needed, using an NX70 ThermoFisher cryostat. 18-µm sections were collected on Superfrost Plus glass slides (Thermo Scientific) and stored at -80°C.

All activities involving mice were performed in accordance with all applicable regulations under the following Home Office licences: Grant lab (holder: Prof Seth Grant) project licence PPL 70/8140, Dr Melissa Cizeron personal licence PIL 60/13357 (revoked in March 2017) and Vlad Anton personal licence PIL IC5F0E467 (revoked in February 2018).

2.3 Immunohistochemistry and slide preparation

TAP-tagged GluN1 was labelled using a FLAG primary antibody (Sigma F1804 – mouse immunoglobulin G1) and a far-red dye-conjugated secondary antibody (Cy5-conjugated donkey anti-mouse immunoglobulin G1). Mouse brain sections were brought to room temperature (RT) by rinsing in PBS. The sections were incubated in blocking solution, consisting of 5% w/v bovine serum albumin (BSA; Sigma-Aldrich) and 0.5% w/v Triton X-100 detergent (Sigma-Aldrich) dissolved in tris-buffered saline (TBS; Sigma-Aldrich), for one hour at RT. The blocking solution was removed and replaced with the primary antibody (FLAG diluted 1:4000) dissolved in antibody

solution (3% BSA, 0.5% Triton X-100 in tris-buffered saline – TBS; Sigma-Aldrich). After 1 hour of primary antibody incubation at RT, three 10-minute washes were performed with washing solution (0.5% Triton X-100 in TBS). Secondary antibody (Cy5 diluted 1:3000) in antibody solution was added and incubated for 1 hour at RT. After three final 10-minute washing steps with washing solution, all liquid was removed and number 1.5 glass coverslips (0.17 mm thick; from VWR International) were mounted using MOWIOL (Calbiochem) mounting medium containing 2.5% w/v anti-fading agent DABCO (1,4-diazabicyclo[2.2.2]octane from Sigma-Aldrich). Mounting medium was allowed to set for 24 hours at room temperature and mounted slides were stored at -20°C before imaging. During imaging, Zeiss Immersol immersion oil with a refractive index (RI) of 1.518 was used.

Fluorescent beads (TetraSpeck 0.2 µm diameter; ThermoFisher) slides were prepared as follows. Number 1.5 coverslips were coated with a 5 µg/ml solution of Poly-D-lysine hydrobromide (PDL; Sigma-Aldrich) dissolved in distilled water by incubating for 20 minutes at RT. PDL-coated coverslips were lightly rinsed with distilled water and fluorescent beads, diluted 1:100 in distilled water, were added on for 10 minutes at RT. Bead-coated coverslips were lightly rinsed again and then mounted on glass slides using the same procedure as outlined above.

2.4 Spinning Disk Confocal Microscopy

An Andor Revolution XDi spinning disk confocal microscope (SDM) system with an Olympus UPlanSAPO 100x oil immersion lens with a numerical aperture (NA) of 1.4 were used for acquiring all fluorescence microscopy images in this study. The UPlanSAPO (Super Apochromat) objective fully compensates for both spherical and chromatic aberrations from the visible to the near-infrared region of the light spectrum according to Olympus, its manufacturer. The microscope was equipped with an Andor iXon Ultra EMCCD (electron multiplying charged coupled device) camera generating 16-bit 512 x 512 pixel images (tiles), with a pixel size of 84 nm.

Synaptic proteins often form puncta smaller than the resolution of a diffraction-limited microscope (Broadhead *et al.*, 2016). As a result, their images (point spread functions – PSFs) cannot have diameters (or full widths at half maximum – FWHMs) smaller than what Abbe's diffraction limit dictates, ranging from approximately 250 nm for green fluorophores (PSD95-eGFP) to approximately 350 nm for far-red

fluorophores (GluN1 labelled with Cy5-conjugated secondary antibodies) (Keller, 2006). The Nyquist sampling theorem states that the sampling frequency of a detector should be at least twice as high as the frequency of the signal being sampled. When imaging diffraction-limited puncta, this would translate to a pixel size of at most 125 nm (for green light). The 84 nm pixel size of the system used here is thus sufficient for imaging diffraction-limited puncta.

Three excitation wavelengths were used during imaging: 488 nm (for PSD95-eGFP), 561 nm (for SAP102-mKO2) and 640 nm (for Cy5-antibody stained GluN1). A fourth excitation wavelength of 405 nm was used to image 4′,6-diamidino-2-phenylindole (DAPI), a fluorescent stain that binds to deoxyribonucleic acids (DNA) and enables the visualisation of cell nuclei in fluorescence microscopy. The system employs a quadruple dichroic mirror and a quadruple bandpass emission filter transmitting light from the following wavelength intervals (in nm): 415-460, 505-533, 584-625 and 671-730. This quadruple bandpass filter allows light emitted by excited fluorophores in the sample to pass through to the camera while blocking excitation light wavelengths and any wavelengths not expected to originate from the fluorophores in the sample. As both the dichroic mirror and the emission filter work on four different wavelengths or wavelength intervals, they remove the need for physically switching filters between different channel image acquisitions, thus shortening imaging times. An illustrative diagram of the optical setup is shown in Figure 2-1.

The microscope uses a Yokogawa confocal scanning unit (CSU) (Gräf, Rietdorf and Zimmermann, 2005). In a confocal microscope, the pinholes block out-of-focus light from reaching the detector (EMCCD camera in the current setup), thus reducing the thickness of the optical section imaged and improving the microscope's axial resolution compared to wide-field microscopes. In effect, the CSU functions as a large group of single beam scanning confocal microscopes by having multiple pinholes arranged in a specific pattern (Nipkow disk), such that they uniformly cover the whole field of view as the disk spins (Gräf, Rietdorf and Zimmermann, 2005). The collector disk along the excitation light path contains microlenses aligned with the pinholes on the Nipkow disk. The microlenses help focus the excitation light onto the individual pinholes, allowing greater excitation efficiency and reducing image acquisition times. While excitation light wavelengths pass straight through the quadruple dichroic mirror, all other wavelengths (i.e. emitted light) are reflected towards the EMCCD camera.

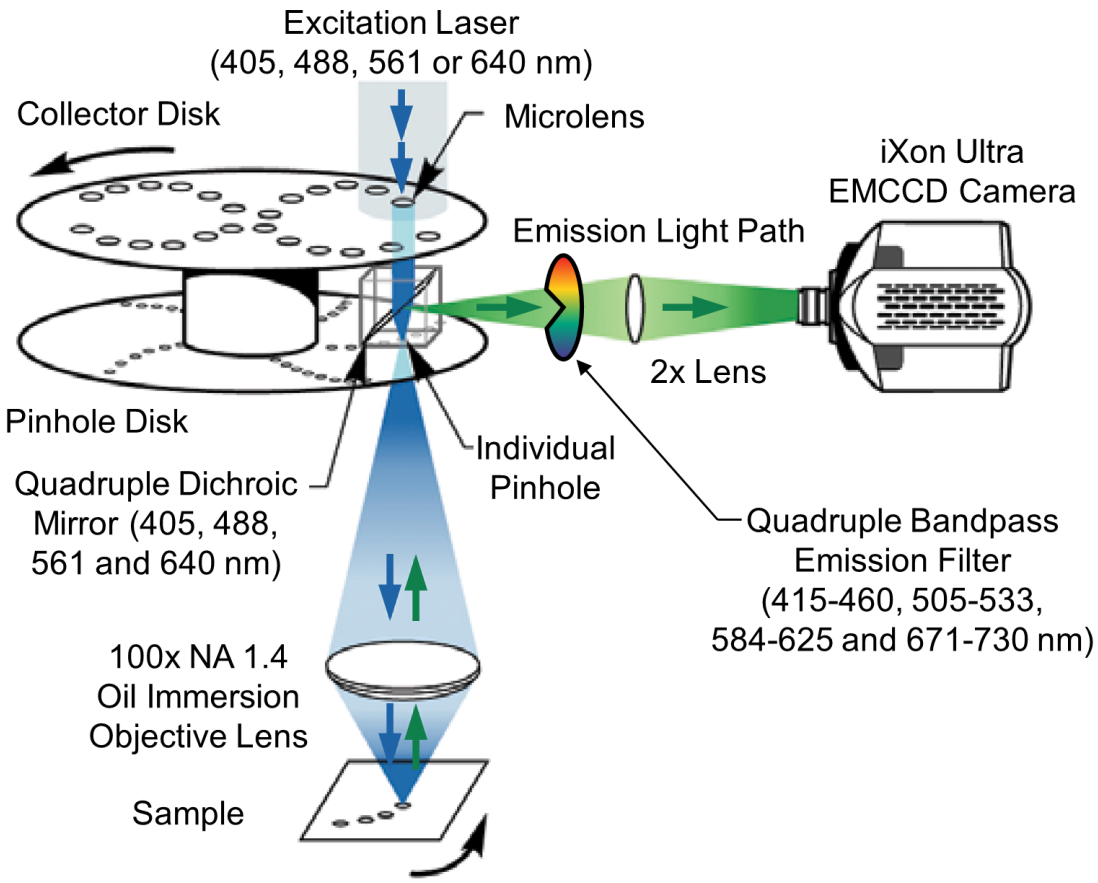

Figure 2-1. Diagram of optical setup. The left hand side of the diagram shows the double disk design of the Yokogawa CSU. The blue cones and arrows represent the excitation light path and the green cones and arrows the emission light path. The excitation and emission light paths coincide between the dichroic mirror and the sample. Adapted from (Andor, no date).

Excitation laser power and exposure were optimised to maximise the signal obtained while not excessively bleaching the fluorophores imaged. In practice, to optimally use the entire dynamic range of the camera, exposure was set so that images from age group and hippocampal area where expression is known to be highest for each protein (CA1 Stratum Radiatum for PSD95 and GluN1 and the dentate gyrus molecular layer for SAP102, all at postnatal day 21) would contain a small portion (0.001 to 0.01 % or between 2 and 25 pixels per tile) of saturated pixels. 2x frame averaging was used for all images. Once chosen, image acquisition settings were maintained constant throughout the entire data set.

The following table contains all acquisition settings, with approximate values for sample illumination power:

Fluorophore	Excitation Wavelength (nm)	Laser Power Setting (%)	Illumination Power (W/cm^2)	Exposure (ms)
PSD95-eGFP	488	19	84.6	120
SAP102-mKO2	561	23	94.9	180
GluN1-Cy5	640	28	140.7	240

Thanks to a motorised stage (Prior), whole brain regions such as the hippocampus could be imaged as mosaics of non-overlapping tiles (512 x 512 pixel images). From each hippocampal section, a single optical plane was imaged. The imaged plane was located at a depth of 3-5 µm from the surface of the brain tissue to minimise light scattering.

Fluorescent beads were imaged using a similar procedure with different excitation power and exposure settings.

2.5 Image analysis

All image analysis tasks were performed in the open-source software Fiji (Schindelin *et al.*, 2012) unless otherwise specified. Matlab (MathWorks) and Python (Python Software Foundation) scripts were used to automate image analysis.

The Fiji version used (including all plugins) is available in the electronic appendix image analysis folder, in the ‘Fiji Version Used’ subfolder.

2.5.1 Pixel-based intensity correlation

Pixel-based intensity correlation was analysed using the Colocalization Threshold Fiji plugin. This was used strictly as a qualitative method for confirming that no signal bleed-through exists between the different channels (wavelengths) imaged.

2.5.2 Puncta detection using TrackMate

Puncta images of synaptic proteins or fluorescent beads were detected with the TrackMate Fiji plugin v2.8.1 (Tinevez *et al.*, 2017) with the Difference of Gaussians

setting. The Quality and Mean Intensity parameters were used for puncta detection. Optimal parameter thresholds were chosen as described in the next chapter.

A Matlab script written by Dr Zhen Qiu was used for batch image analysis, running TrackMate on the raw image data and outputting the xy coordinates of all punctum centres (localisations assigned with sub-pixel accuracy). From every tile (512 x 512 pixel image) of a hippocampus scan, xy coordinates of the localisations of PSD95, SAP102 and GluN1 were stored as separate sets of puncta.

The batch TrackMate detection script developed by Dr Zhen (Ricky) Qiu (ZQ) is available in the electronic appendix image analysis folder, in the 'Batch Trackmate Detection (ZQ)' subfolder. Relevant instructions are provided in the 'Image Analysis Instructions' Microsoft Word document (.docx).

2.5.3 Signal-to-background ratio and photon measurements and simulations using ThunderSTORM

The Fiji ThunderSTORM plugin (Ovesný *et al.*, 2014) was used to estimate the number of photons per detected punctum and the signal-to-background ratio (SBR) of detected puncta. It was also used to generate simulated puncta with varying SBRs to test the ability of TrackMate to detect puncta in varying background conditions.

Based on manufacturer specifications, the following values were input into the ThunderSTORM camera setup section: pixel size – 84 nm; photoelectrons per A/D (analog-to-digital) count – 4.85; base level A/D counts – 11; EM gain: 250. When ThunderSTORM detection was applied to TrackMate sample data, the Difference-of-Gaussians filter with radii of 1.2 and 1.8 pixels was used. The local maximum thresholding method was used, with peak intensity thresholds of 0.715, 0.78 and 0.587 x std(Wave.F1) (plugin-specific syntax) for PSD95, SAP102 and GluN1, respectively, to match the total number of puncta detected with optimised TrackMate parameters. Then, for each punctum, the useful outputs were detected photons and SBR (defined here as detected photons / square standard deviation of the background or intensity/bkgstd^2).

The ThunderSTORM simulated data generator was used to create simulated puncta with different SBRs. Camera setup settings were the same, except for base level A/D counts, which was set to zero for simulated data. Simulated puncta were

created with full widths at half maximum (FWHMs) between 252 and 336 nm (3-4 pixels) at a density of 1 punctum per μm^2. Simulated punctum intensity was fixed at 2000 photons (representative of median photon counts for detected puncta in sample images for PSD95, SAP102 and GluN1) and mean photon background was varied from 1000 to 200 to provide an SBR range from 2 to 10. When TrackMate was used to detect the simulated puncta at varying SBRs, its quality threshold was set at the antimode (point of maximum separation) of the bimodal punctum quality distributions obtained.

2.5.4 Nearest neighbour distance measurements

Within each tile, nearest neighbour (NN) distances up to 1200 nm were measured between two sets of puncta at a time using a Matlab-based graphical user interface application developed by Dr Zhen Qiu. Localisations less than 2 pixels away from the edge of each tile (1.56% of the total surface area of each tile) were excluded from further analysis due to a technical challenge that will be addressed in future refinements of this application. At this step, the input consisted of pairs of sets of xy coordinates and the output was, for each protein in relation to all other colocalisation partners (including merged sets of coordinates, as described in the following chapter), a separate list of NN distances in each tile. A NN distance distribution is obtained by binning the NN distances into 10-nm bins and plotting the number of distances at each bin.

The NN distance measuring tool developed by Dr Zhen (Ricky) Qiu (ZQ) is available in the electronic appendix image analysis folder, in the ‘Nearest Neighbour Distance Measurement (ZQ)’ subfolder. Relevant instructions are provided in the ‘Image Analysis Instructions’ Microsoft Word document (.docx).

2.5.5 Hippocampal subregion delineation

Anatomical regions were delineated in accordance to the Allen Reference Atlas (Lein *et al.*, 2007) on stitched, downsampled montage images using the Fiji Polygon selections tool. The stitched, 16x downsampled montages were created using a Matlab script written by Dr Zhen Qiu.

A Python script written by Dr Zhen Qiu was then used to map (attribute) puncta numbers and measured nearest neighbour distances to delineated regions of interest (ROIs).

A tile was mapped to an ROI if more than 50% of its surface was included in the delineation on the corresponding downsampled stitched montage. This resulted in moderately distorted punctum density and colocalisation measurements in those regions with relatively large perimeter-to-surface ratios and those bordering significantly different regions. This impacted colocalisation measurements in the dentate gyrus polymorphic layer (DGpo) and the CA3 Stratum Lucidum (CA3slu), regions bordering cell body layers with high, probably extra-synaptic punctate GluN1 expression that were included in the NN distance measurements, leading to sub-optimal curve fitting during colocalisation analysis (introduced later). This shortcoming could be overcome in future refinements of this method by using the xy coordinates of individual puncta to assign them to different ROIs rather than including or excluding whole tiles from ROIs.

The output of this step consisted of NN distance distributions form each ROI (delineated anatomical region) for each protein relative to all other colocalisation partners. In total, from each ROI, 9 NN distance distributions were obtained (for each of the three proteins – P_0 – colocalisation with P_1, P_2 and merged P_{1+2}).

The downsampled montage stitching script and the ROI mapping script developed by Dr Zhen (Ricky) Qiu (ZQ) are available in the electronic appendix image analysis folder, in the ‘Montage Stitching Script (ZQ)’ and ‘Nearest Neighbour Distance Distribution Mapping (ZQ)’ subfolders, respectively. Relevant instructions are provided in the ‘Image Analysis Instructions’ Microsoft Word document (.docx).

2.6 Colocalisation analysis

The Vicinity-based Localisation Adjacency Determination (VLAD) colocalisation analysis method was implemented in Origin (OriginPro v9.5 from OriginLab Corporation) and Microsoft Excel 2013 (Microsoft Corporation).

2.6.1 VLAD curve fitting

The basis of the VLAD method is curve fitting on NN distance distributions, as described in detail in the following chapter. In the bimodal NN distance distributions, Peak 1 (at shorter NN distances) is fit with a Gaussian distribution and Peak 2 (at longer NN distances, sometimes lacking the conventional appearance of a sharp peak) with an adapted version of **Equation 1** describing the distribution of NN distances under spatial randomness (Torquato, Lu and Rubinstein, 1990).

Curve fitting was performed in Origin using the Multiple Peak Fit tool. While Origin can perform single peak fitting with any equation, Multiple Peak Fit requires that all equations used have a 'peak function' format with at least four parameters denoting peak baseline (y_0), area (scaling factor A), centre (m) and width (w; full width at half maximum equivalent for the Gaussian distribution). In this format, x refers to NN distance bins and y refers to the number of NN distances at a certain x (10-nm interval).

For fitting Peak 1, the following form of the Gaussian distribution was used:

$$y = y_0 + A \cdot \frac{e^{\frac{-4\ln(2)(x-m)^2}{w^2}}}{w\sqrt{\frac{\pi}{4\ln(2)}}}$$

Origin format: y=y0+A/(w*sqrt(pi/(4*ln(2)))) * exp(-4*ln(2)*(x-xc)^2/w^2)

This is an adaptation of the normal distribution probability density function (pdf) with variance σ^2 and mean μ, to which y_0 (baseline) and A (scaling factor) were added, and where m (peak) is μ and w is the full width at half maximum (FWHM), with $w = 2\sqrt{2\ln(2)}\,\sigma$. Below is the standard form of the normal distribution pdf:

$$y = \frac{1}{\sqrt{2\pi\sigma^2}} \cdot e^{-\frac{(x-\mu)^2}{2\sigma^2}}$$

To create the function for fitting Peak 2, the density (d) parameter of Equation 1 was split into two parameters (m and w) to permit its use in Origin's Peak Analyzer. Furthermore, two constants were also included to make m and w approximately numerically equal to the apparent centre and width of Peak 2, respectively. These adaptations did not negatively affect the quality of curve fitting but, in the future prospect of creating a streamlined VLAD application, the superfluous parameter could be removed.

The following adaptation of Equation 1 was used for fitting Peak 2:

$$y = y_0 + A \cdot \pi \frac{x \cdot w}{579{,}572{,}190} \cdot e^{\left(-\pi \frac{m \cdot x^2}{289{,}786{,}095}\right)}$$

Origin format: y=y0+A*((w/579572190)*pi*x*exp(-pi*(m/289786095)*(x^2)))

The following table contains the starting values and boundaries of all parameters:

	Parameter	Initial value	Lower bound	Upper bound
Peak 1 Gaussian Distribution	y_0	0	0	10^{-9}
	A	auto	1	N/A
	m	80	10	150
	w	auto	30	200
Peak 2 Equation 1	y_0	0	0	10^{-9}
	A	10	1	N/A
	m	330	50	800
	w	800	1	1350

The parameter values and boundaries above were used in all curve fitting steps except when testing VLAD in simulated data with varying peak colocalisation distances (PCDs), where the upper bounds of Peak 1 m and w were raised to 270 and 350, respectively. When fitting each NN distance distribution, a maximum of 100 Levenberg-Marquardt algorithm (damped least-squares) iterations were performed. For each NN distance distribution, the output at this stage consisted of the values of the parameters A, m and w of Peak 1 and Peak 2 and the Adjusted R-squared goodness-of-fit measure.

The Origin fitting function files are available in the electronic appendix image analysis folder, in the 'Origin User Files (VA)' subfolder. Relevant instructions are provided in the 'Image Analysis Instructions' Microsoft Word document (.docx).

2.6.2 VLAD colocalisation measurements

VLAD determines colocalisation by attributing a probability of true colocalisation to NN distances in every 10-nm bin and multiplying the probabilities of true colocalisation with the number of NN distances in every 10-nm bin to obtain the distribution of colocalising distances, as described in the following chapter. In practice, this is equivalent to the difference between all NN distances and the fitted value of Peak 2 at every point (based on the parameters of Peak 2 obtained from curve fitting). If the difference is negative, it is replaced by zero. Although VLAD-measured colocalisation is largely threshold-insensitive, a threshold of 230 nm was chosen nonetheless and applied to all protein pairs analysed. Peak colocalisation distance (PCD) and peak full width at half maximum (FHWM) were longest for the GluN1-PSD95 pair. In adult mice, median uncorrected PCD was 91 nm and median uncorrected FWHM 117 nm. 230 nm is equivalent to the GluN1-PSD95 PCD + 2.8 standard deviations, a point below which 99.7% of all values in the normal distribution of colocalising distances are found. Virtually all GluN1-SAP102 and PSD95-SAP102 colocalising distances are included below this threshold too. At the same time, an appropriate threshold limits the potential for error in cases with sub-optimal curve fitting.

Colocalisation in simulated data was determined in the same fashion, but the threshold for colocalising distances was 190 nm for all simulated data with a PCD of 97 nm, with two exceptions. First, when testing the ability of VLAD to measure colocalisation at different PCDs (**Figure 3-16**), the threshold was chosen automatically as PCD + 3 standard deviations (based on the fitted centre and FWHM of Peak 1) to avoid any bias and to demonstrate the ability of VLAD to measure colocalisation when no *a priori* knowledge is available. Second, when comparing VLAD and SODA (Statistical Object Distance Analysis) in **Figure 3-20**, a threshold of 210 nm was chosen to match the equivalent default setting of SODA, which measured colocalisation in 0.5-pixel steps (42 nm; 2.5 pixels = 210 nm).

In the developmental study of PSD95, SAP102 and GluN1, the presence of puncta of each protein in either non-colocalising, paired or TRIPLE subtypes was determined as described above and as illustrated in **Figure 3-10**. Colocalisation was determined for each of the three proteins and, due to slight deviations from a 1:1 colocalisation ratio in some cases of colocalising puncta, colocalising punctum densities of two colocalisation partners did not always match. Densities of

colocalising punctum subtypes were always reported as the minimum of the densities of the proteins involved. For example, colocalisation measurements in a region could show the following densities of individual proteins as triply colocalised: PSD95 – 12.2/100 μm^2, SAP102 – 14.3/100 μm^2 and GluN1 – 11.7/100 μm^2. In this example, TRIPLE punctum density would be reported as 11.7/100 μm^2, the smallest of the three, as this is most representative of the number of distinct TRIPLE assemblies in that region. For simplicity, and because differences in the densities of colocalising proteins were generally small, the minimum density of colocalising subtypes was reported for each individual protein as well.

An Excel file showing the final computations of VLAD is available in the electronic appendix image analysis folder, in the 'VLAD-measured Colocalisation (VA)' subfolder. Relevant instructions are provided in the 'Image Analysis Instructions' Microsoft Word document (.docx).

2.6.3 Simulated data generation

Simulated data with different punctum densities, levels of colocalisation and peak colocalisation distances were generated using a Python script written by Dr Babis Koniaris. Simulated data consisted of sets of xy coordinates generated as described in the following chapter and colocalisation was analysed as described above.

The simulated colocalisation data generator developed by Dr Babis Koniaris (BK) is available in the electronic appendix image analysis folder, in the 'Simulated Colocalisation Data Generator (BK)' subfolder. Relevant instructions are provided in the 'Image Analysis Instructions' Microsoft Word document (.docx).

2.6.4 SODA colocalisation measurements

The creators of SODA (Statistical Object Distance Analysis) (Lagache *et al.*, 2018), the object-based colocalisation analysis method used here as a benchmark, integrated SODA into the freely available image analysis platform Icy (De Chaumont *et al.*, 2012). This made the comparison of VLAD and SODA possible. The input of the SODA STORM 2D Icy protocol consists of sets of xy coordinates of localisations, same as the input for the VLAD method (for measuring NN distances). The outputs of SODA used here, at an equivalent search radius (r max) to the threshold of VLAD, were the number of coupled (colocalised) objects (nb coupled),

mean coupling probability and coupling index (level of colocalisation). For the comparisons in **Figure 3-19** and **Figure 3-20**, SODA results at a search radius (r max) of 210 nm (2.5 pixels) were reported, with the SODA default setting of 0.5 pixel (42 nm) search steps. For **Figure 3-21**, SODA step size was reduced to 10 nm (0.119 pixels) and the distributions of coupled objects (SODA coupled distances in figure legend) and of coupling probabilities were reported for each 10-nm interval.

2.7 Data processing and statistical analysis

All data processing was performed in Microsoft Excel 2013. Statistical analysis was performed in Origin and Excel, using the Real Statistics Resource Pack (Realstats) v5.8 (developed by Dr Charles Zaiontz). All graphs were produced in Origin and some figures were created in Microsoft PowerPoint 2013 (Microsoft Corporation).

2.7.1 Scaled Euclidean distance-based similarity matrices

The similarity matrices in Figure 4-15 and Figure 4-16 are based on scaled Euclidean distances between regions' subtype densities (4-15) or proportions (4-16). The scaled Euclidean distance d between two regions R1 and R2 was calculated using the following formula:

$$d = \frac{\sqrt{\sum_{i=1}^{p} \frac{(v_{R1i} - v_{R2i})^2}{v_{i\,max}{}^2}}}{\sqrt{p}}$$

p is the number of parameters (p = 7 punctum subtypes), v_i is the value of parameter i (punctum density or proportion of subtype i) and $v_{i\,max}$ is the maximum value of that parameter in the entire set of data (across all regions and all ages). Dividing the expression by $\sqrt{p}$ brings all measurements on a zero-to-one scale but, because the minimum and maximum values of each parameter do not all occur in the same age group, no Euclidean distance exceeded 0.44 for subtype densities and 0.37 for subtype proportions.

Similarity matrices were calculated as described above for all individual mice, based on average parameter values (average subtype densities and proportions). The

matrices shown are the averages of the matrices of all mice in each age group. The same colour scale was used in all figures of this type.

2.7.2 Statistical analysis

The normal distribution of values in groups of data was probed using the Shapiro-Wilk (S-W) test and the Kolmogorov-Smirnov (KS) test for normality.

The parametric paired Student's t-test and the non-parametric Wilcoxon signed rank test were used to compare PSD95 punctum density between hemispheres (N = 5, Figure 4-2).

The Kruskal-Wallis test (non-parametric equivalent of analysis of variance – ANOVA) with a post-hoc Mann-Whitney U-test were used to compare subtype densities between age groups, in figures such as Figure 4-4. Significance of the Mann-Whitney U-test (performed if $p_{Kruskal\text{-}Wallis}<0.05$) comparing subtype density to the preceding age group was labelled as * for $p<0.05$ and ** for $p<0.01$.

Two-factor analyses of variance (ANOVAs) were performed to probe the dependence of peak colocalisation distances (PCDs) on region and age (Figure 4-19) due to the absence of an equivalent 2-factor non-parametric test.

Analysis of variance with a post-hoc Tukey test was used to compare PCDs between regions in adult mice (Figure 4-21, Figure 4-22 and Figure 4-23).

3 The Vicinity-based Localisation Adjacency Determination colocalisation analysis method

3.1 Brief Introduction

The continuous development of microscopy methods enables the visualisation of fluorescently labelled proteins in ever-greater detail. A spinning disk confocal microscope (SDM) has a diffraction-limited lateral resolution of 200-300 nm (depending on wavelength of light and objective used). The SDM enables high-throughput high-resolution imaging of mouse brain areas. For example, over 4 million puncta corresponding to three different fluorescently labelled synaptic proteins can be imaged in a single plane of the mouse hippocampus in just over one hour.

Measuring colocalisation between different proteins is important for understanding the spatial and functional relationships between them. There are two main categories of colocalisation analysis: pixel-based and object-based (Lagache *et al.*, 2015). Pixel-based methods – reviewed in (Bolte and Cordelières, 2006; Aaron, Taylor and Chew, 2018) – measure either the correlation between fluorescence intensity in two different channels of the same field (Pearson's coefficient) or the overlap of intensity-thresholded pixels (Manders' overlap coefficient). These methods are not optimally suited for studying colocalisation between spots (puncta) because they provide no information on spatial relationships (other than surface area overlap) and are influenced by the resolution of the microscope, noise and potential channel misalignment.

In object-based methods, the first step is detecting objects (e.g. spots/puncta) and assigning their position or boundary/surface in xy (2D) or xyz (3D) coordinates. Puncta (spots) may be detected using a variety of methods (Chenouard *et al.*, 2014). Here, they were detected with the TrackMate ImageJ plugin (Tinevez *et al.*, 2017). The positions of the centres of all detected puncta are further treated as points. The resulting set of points within a defined space (area or volume) is called a point process. When additional features are described for every point (e.g. diameter or fluorescence intensity of the corresponding punctum), the set of points and their features is called a marked point process. For simplicity, they will be referred to as sets of points, spots or puncta.

The most common ways to study the spatial relationships between points, either within the same set or, more commonly, between two separate sets, are nearest neighbour (NN) distances (or n^{th} neighbour, generally) (Clark and Evans, 1954), Ripley's K function (Ripley, 1976) and its derivative, the pair correlation function (Wiegand and Moloney, 2004). The NN distance is the Euclidean distance between a given point in one set and the closest one in the other set, and it is the metric on which the work in this thesis is based. Ripley's K function for an individual point in set 1 equals the number of points of set 2 found in a circle with a specified radius r around point 1. Ripley's K function may also be normalised by localisation density if used to measure colocalisation above what would be expected by chance at that given localisation density (Caetano *et al.*, 2015). A boundary correction is often applied to avoid under-counting points of set 2 near a specified boundary or near the border of the analysed space. The pair correlation function is the difference between the Ripley's K function for two different radii and it counts the number of points of set 2 within a ring around a point in set 1. It may also be normalised by localisation density in similar fashion to Ripley's K function. The recently published colocalisation analysis method SODA (Statistical Object Distance Analysis), which will be discussed in more detail later, is based on the pair correlation function (Lagache *et al.*, 2018).

The main challenge for object-based colocalisation analysis methods is separating true colocalisation from false positive colocalisation that occurs when the distance between two points is short due to chance and not biological organisation. A high density of points (number of points/surface or volume) will result in shorter distances between them, even under the colocalisation null hypothesis of random distribution. The longer the distance between truly colocalising points is, and the higher the point density, the harder it becomes to correctly identify true colocalisation.

In this chapter, a new method for determining adjacency (colocalisation) of localisations based on their vicinity (in terms of nearest neighbour distance) is introduced. The Vicinity-based Localisation Adjacency Determination (VLAD) method relies on model fitting to nearest neighbour distance distributions. Its performance was evaluated on simulated data and compared to the state-of-the-art SODA method. In the next chapter, it is applied to a vast data set comprised of GluN1, PSD95 and SAP102 puncta in the mouse hippocampus throughout early development.

The work presented in this chapter was done with technical assistance from Dr Babis Koniaris and Dr Zhen Qiu. Dr Koniaris created the Simulated Colocalisation Data Generator. Dr Qiu created the Nearest Neighbour Distance Measurement tool. These can be found in the electronic appendix of the thesis.

3.2 Fluorescence microscope imaging and puncta detection

3.2.1 Microscope Validation: No Bleed-Through between Channels

In multi-colour fluorescence microscopy, it is essential to confirm that the microscope set-up does not allow signal bleed-through from one channel (wavelength) to another. Bleed-through was assessed via non-thresholded pixel-based intensity correlation plots for relevant colour pairs: green (excitation – ex – 488 nm) to red (ex 561 nm) and red (ex 561 nm) to far red (ex 640 nm) in samples where the longer-wavelength fluorescent tag was absent. The pixel intensity correlation plots in Figure 3-1 clearly show no bright pixels detected in the channels without fluorescent tags despite the presence of shorter-wavelength fluorophores.

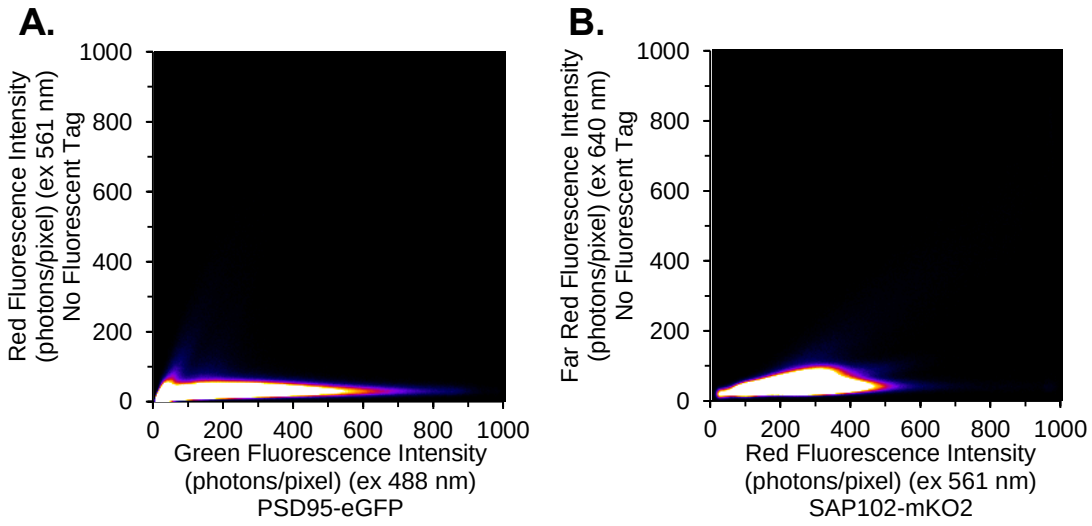

Figure 3-1. Pixel intensity correlation plots showing no signal bleed-through between channels. **A.** Sample containing PSD95 tagged with enhanced Green Fluorescent Protein (eGFP) with excitation wavelength (ex) 488 nm and no red fluorophore. An area of 244,200 μm^2 spanning multiple hippocampal sub-regions was imaged and no significant green-to-red signal bleed-through was detected. **B.** Sample containing SAP102 tagged with monomeric Kusabira Orange 2 (mKO2) with ex 561 nm and no far red fluorophore. An area of 333,000 μm^2 spanning multiple hippocampal sub-regions was imaged and no significant red-to-far red signal bleed-through was detected.

In addition to this control, the fact that detected GluN1, PSD95 and SAP102 puncta rarely coincide further suggests that, if present, potential bleed-through between channels is too low to be of significance.

3.2.2 Synaptic Puncta Detection using TrackMate

The Fiji image analysis software (Schindelin *et al.*, 2012) was used for visualising images obtained with the spinning disk microscope (SDM). The TrackMate plugin (Tinevez *et al.*, 2017) was used for puncta detection because of its good performance, speed and ease of use for large-scale batch data analysis. The Difference of Gaussians (DoG) detector was appropriate for detecting diffraction-limited puncta with diameters of 3-4 pixels (approximately 250-335 nm), and the Quality and Mean Intensity parameters were the most relevant for reliable puncta detection.

For each studied protein (PSD95, SAP102 and GluN1), a sample of images representing all main hippocampal regions in multiple mice at different ages was selected to train the puncta detector. Puncta in the training set images were manually counted to establish the ground truth. In the same images, puncta and their associated parameters were automatically detected by TrackMate. Figure 3-2 contains examples of the sample images used to train the TrackMate detector. The training set images, as well as associated Cell Counter (Fiji plugin) files with the coordinates of manually counted puncta, are available in the 'Sample Images' folder of the electronic appendix, in the 'TrackMate Detector Training Images' subfolder.

Automatically detected puncta were individually classified as true or false positive based on their proximity to manually counted puncta. A true positive (TP) is a manually counted (true) punctum that is also automatically detected. A false positive (FP) is a punctum that is automatically detected but is not manually counted (false). A false negative (FN) is a punctum that is manually counted (true) but is not automatically detected. Precision (Pr) refers to the proportion of all automatically detected puncta (true and false positives) that are true: $Pr = TP / (TP+FP)$. Recall (R) refers to the proportion of all true puncta (manually counted) that are automatically detected: $R = TP / (TP+FN)$.

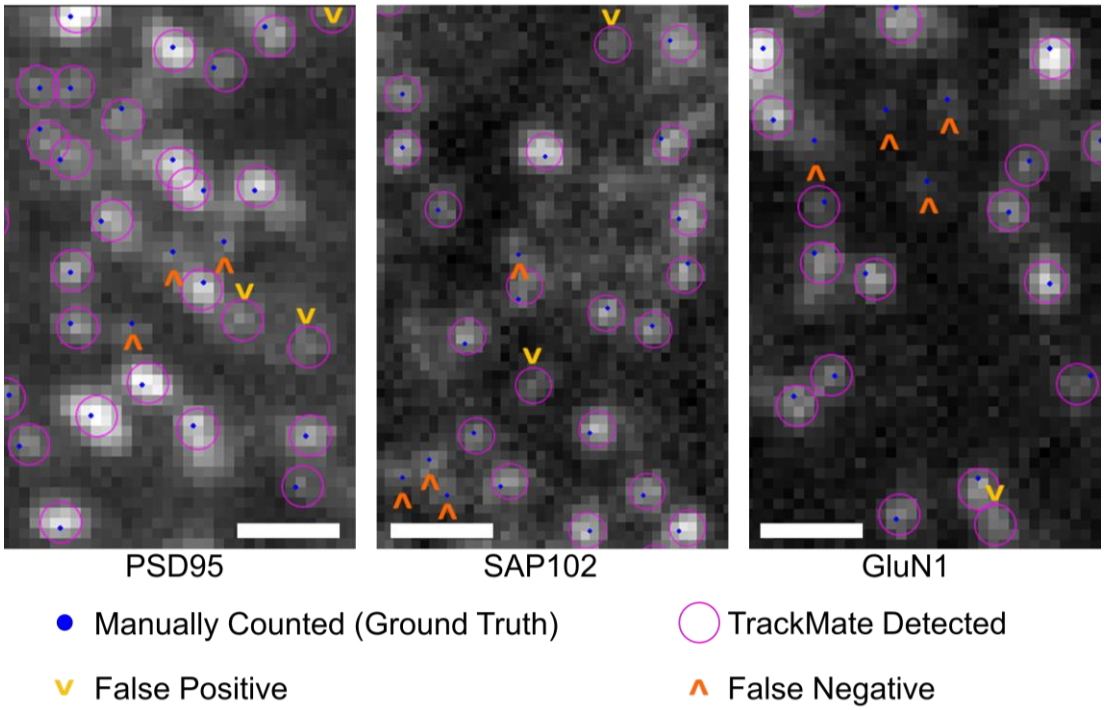

Figure 3-2. Sample images of manually counted and automatically detected PSD95, SAP102 and GluN1 puncta. The final set of TrackMate parameters (from Table 1) was used for automatic detection in these sample images. Magenta circles containing blue dots indicate true puncta that were successfully and automatically detected by TrackMate. False positives (not manually counted) and false negatives (not automatically detected) are indicated by chevrons. Scale bars: 1 µm.

For a perfect detector, both precision and recall would equal 1, i.e. no false positives and no false negatives would exist. For real detectors, there is an inverse relationship between precision and recall and a trade-off must be made. 99 pairs of TrackMate parameters (quality and mean intensity) were tested and precision and recall were measured for each pair. Choosing the pair of parameters that optimises detection can be done by plotting a precision-recall curve (Fawcett, 2006), as shown in Figure 3-3. Optimal detection occurs when both precision and recall are maximised (for parameter threshold pairs close to the top right corner of the graph in Figure 3-3). The optimal threshold combinations (maximising both precision and recall) for each protein detector are listed in Table 1.

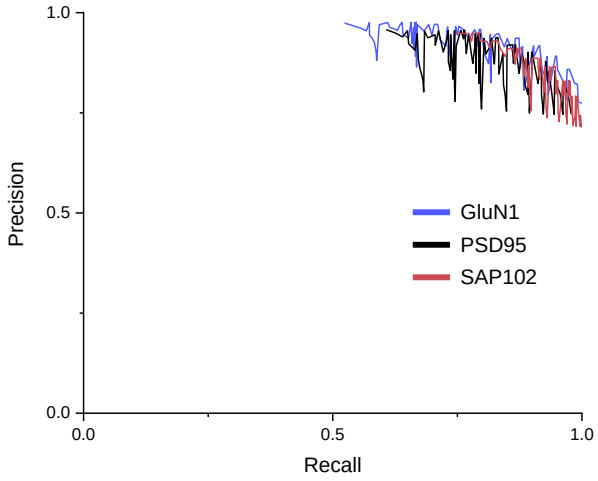

Figure 3-3. Puncta detector precision-recall curves for GluN1, PSD95 and SAP102. TrackMate proved itself a reliable puncta detector, with multiple parameter threshold combinations providing precision and recall values above 0.85 for all three sets of data analysed.

Protein	Manually Counted Puncta	TrackMate Parameter		Precision	Recall
		Quality	Mean Intensity		
GluN1	5,270	250	3000	0.918	0.915
PSD95	3,907	300	3000	0.902	0.900
SAP102	2,452	335	3000	0.887	0.917

Table 1. Optimal parameter thresholds and detector characteristics for each studied protein.

In the triple genetic knock-in mice used, PSD95 and SAP102 were fused to different fluorescent proteins and GluN1 was fused to a TAP-tag (tandem affinity purification tag) which, in turn, was labelled immunohistochemically with the specific FLAG antibody. With the detection settings used, no puncta were detected in the negative control (wild-type mouse brain sections) for PSD95 and SAP102 and very sparse punctate artefacts were detected for GluN1 in antibody-stained wild-type mouse brain control sections. Based on their density, it was estimated that up to 1.4% of detected GluN1 puncta may be falsely labelled artefacts. In summary, in the case of GluN1, 91.5% of all labelled puncta are detected and, of all detected puncta, 8.9% are false positive detections and up to 1.4% are detected staining artefacts.

The signal-to-background ratio (SBR) refers to the ratio between the intensity of wanted signals (puncta) and the intensity of the surrounding background. The higher the SBR, the greater the intensity difference between signals and background and the easier it is to detect signals. A SBR of 1 would mean there is no intensity difference between signals and background, making it impossible to distinguish signals from background. TrackMate's ability to detect puncta with varying SBRs

was tested on simulated puncta with fixed intensity (representative of punctum intensities in the training images set) and varying levels of background intensity. Figure 3-4 A shows that the performance of TrackMate rapidly drops at SBRs below 4. Above this level, TrackMate detects, on average, approximately 95% of all simulated puncta, continuing to improve slightly with higher SBRs. Figure 3-4 B, C and D show estimated SBR distributions for all detected PSD95, SAP102 and GluN1 puncta in their respective training image sets. 82% of PSD95 puncta, 84% of SAP102 puncta and 91% of GluN1 puncta have estimated SBRs greater than 4, a level above which TrackMate detection has been shown to be reliable. Figure 3-4 E also shows photon counts per detected punctum for the three proteins in the training images.

In summary, optimal detection parameter thresholds were determined by using a precision-recall curve based on manually counted puncta in a set of training images for each protein. Based on TrackMate's performance in relatively low SBR data (4 and higher) and on the generally higher SBRs measured in the training images, it is expected that TrackMate will be a sufficiently reliable puncta detector for this work.

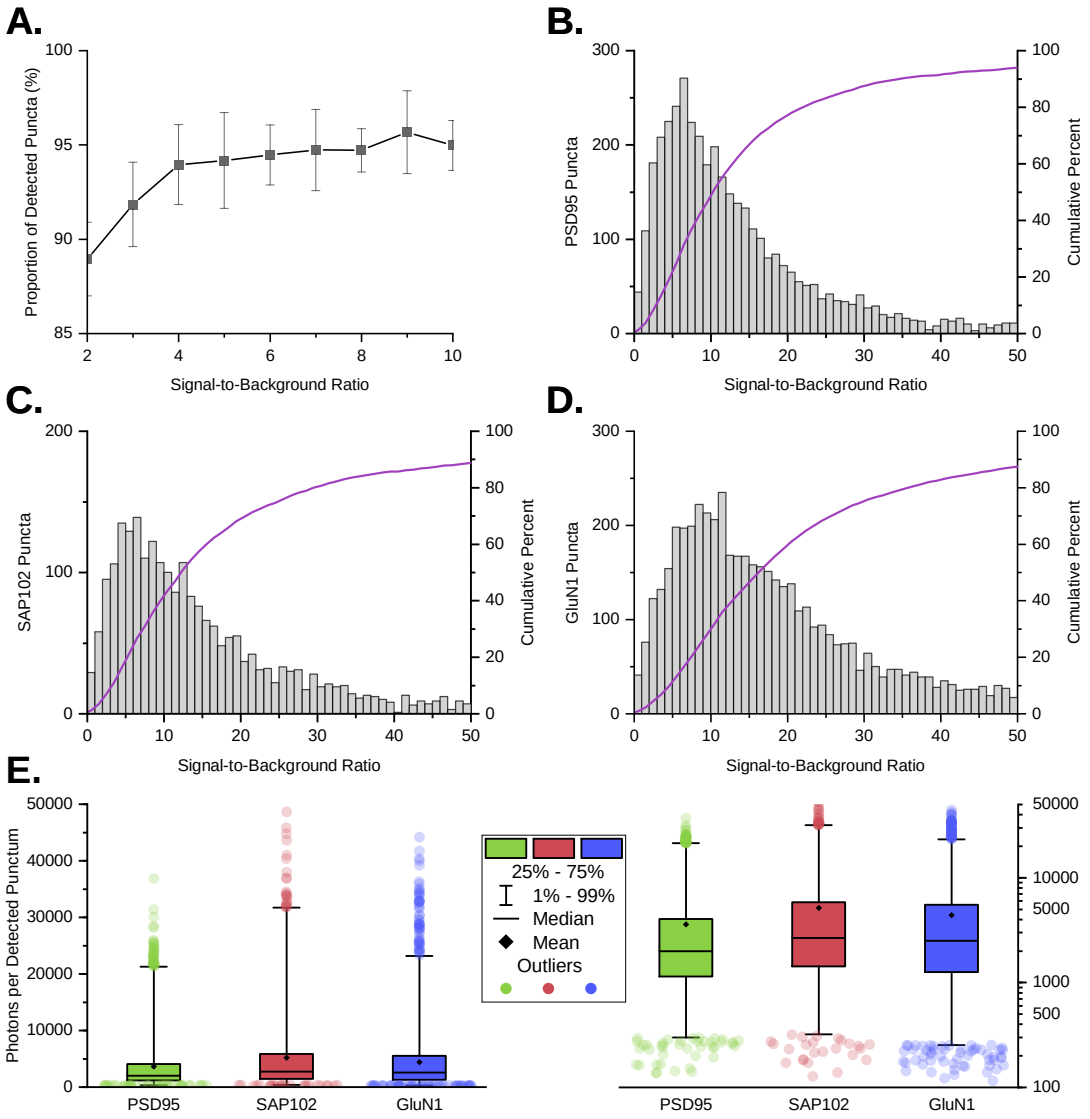

Figure 3-4. TrackMate performance at different signal-to-background ratios and signal-to-background ratio distributions in training images. A. TrackMate detection of simulated puncta at varying signal-to-background ratios (SBRs). 10 frames with 1,700 puncta each were generated at each SBR value. Mean proportion of detected puncta (of all simulated puncta) ± standard deviation was plotted (values at each SBR were normally distributed: $p_{Shapiro\text{-}Wilk} > 0.05$). **B, C and D.** Distributions of SBRs in TrackMate training images for PSD95, SAP102 and GluN1, respectively. Purple curves represent cumulative distributions (plotted on right y-axes). **E.** Box-and-whisker plots of photons per detected puncta for PSD95, SAP102 and GluN1 in the TrackMate training images. Left: linear scale. Right: logarithmic scale (same data). Boxes show the 25th-75th percentile range and whiskers extend from the 1st to the 99th percentile, with outliers individually plotted. Median photons per punctum are: PSD95 – 1,979; SAP102 – 2,654 and GluN1 – 2,488.

3.2.3 Optical aberrations and colocalisation analysis

In an ideal optical system, the light waves emitted by a point source in focus emerge from the rear aperture of the objective and, through constructive and destructive interference, give rise to a sharp and symmetrical diffraction image, or point spread function (PSF). Optical aberrations of multiple types arise from imperfections in an optical system and can lead to blurred or distorted images (Keller, 2006; Goodwin, 2007; Abramowitz *et al.*, 2012). There are two categories of optical aberrations: monochromatic (the same for light of any colour – wavelength) and polychromatic (different wavelengths of light are affected differently).

Spherical aberration is the most common type of monochromatic optical aberration. It consist of a point source having asymmetrical images above and below the plane of best focus. Typically, sharp diffraction rings are seen on one side of the plane of best focus and a blurred, indistinct image on the other (Goodwin, 2007). Another common monochromatic aberration is astigmatism. Astigmatism results in elongations of the PSF along perpendicular directions when defocusing in opposite directions (Goodwin, 2007). A third type of monochromatic aberration, the comatic aberration leads to asymmetrical, comet-shaped (hence the name comatic) PSFs and this is typically more pronounced towards the edges of the field of view (FOV) (Abramowitz *et al.*, 2012).

Polychromatic aberrations arise when different wavelengths of light are focussed at different points, leading to misalignments or shifts between the different colours imaged (Goodwin, 2007).

Field curvature is an aberration caused by the curvature of the image plane created by a lens with a curved surface. Its manifestation is that the centre and edges of the FOV cannot simultaneously be in focus, and either one or the other will be defocused (blurred) (Abramowitz *et al.*, 2012).

Image distortion can generally take two forms: barrel (positive) or pincushion (negative). In barrel distortion, the corners of a square object appear closer to the centre of the FOV and the image of a square appears rounded, as if forming a bulge in the centre of the FOV. In pincushion distortion, the sides of a square are closer to the centre of the FOV, while the corners appear to be stretched away from the centre. Less commonly, a combination of the two (sometimes called moustache distortion) can also occur (Abramowitz *et al.*, 2012).

All of these aberrations should be accounted for, as they can potentially negatively affect colocalisation measurements. The experimental setup used (high end microscope objective in conjunction with correct sample preparation) aimed to minimise optical aberrations. The Olympus UplanSAPO objective used in this study fully compensates for spherical and chromatic aberrations, as well as field curvature, according to its manufacturer. Aberrations can also be caused by using microscope coverslips with the wrong specifications and by mismatches in the refractive indices of the different media between the sample and the objective. In this study, all coverslips used were precision-cut 0.17 mm thick number 1.5 glass coverslips. The Immersion oil used had a refractive index (RI) of 1.518, matching the RI of glass. The RI of Mowiol, the mounting medium used, also approaches the RI of glass as it hardens (Wurm *et al.*, 2010).

To probe whether the system used allows colocalisation measurements to be made for punctate objects, a positive control experiment was performed. The positive control consisted of imaging multi-colour 200 nm fluorescent beads. The beads were imaged in the green, red and far red channels (excitation wavelengths – ex – 488 nm, 561 nm and 640 nm respectively). A qualitative analysis of z-stack images of beads revealed some degree of spherical aberration, as expected, but no comatic aberration (PSF shapes were round and of consistent sizes across the FOV) or chromatic aberration (the PSFs of the different channels overlapped). The effect of out-of-focus light was not assessed here, even though out-of-focus projections may falsely shorten apparent distances between the images of different objects in a sample.

Then, puncta were detected using TrackMate and nearest neighbour (NN) distances were measured for all three channel pairs. Gaussian distributions were fitted to the NN distance distributions for all pairs shown in Figure 3-5. The properties of the fitted peaks are listed in Table 2. Unsurprisingly, longer wavelengths lead to larger point spread functions (PSFs) which, in turn, lead to higher uncertainty when assigning the PSF centre (localisation). This explains why, although the physical locations of the three imaged fluorophores coincide within the multi-colour beads, the centres of their PSFs do not. However, the greatest peak shift measured (40 nm between green and far red) is still just under half a pixel (84 nm).

The number of detected photons per PSF is inversely correlated with the centre localisation uncertainty. The photon counts for detected protein puncta (GluN1,

PSD95 and SAP102; Figure 3-4) in the sample images used for detector optimisation were measured using the ThunderSTORM Fiji plugin (Ovesný *et al.*, 2014). For all three proteins, numbers of photons detected per punctum were high enough to allow localisation uncertainties of less than 10 nm in over 90% of cases.

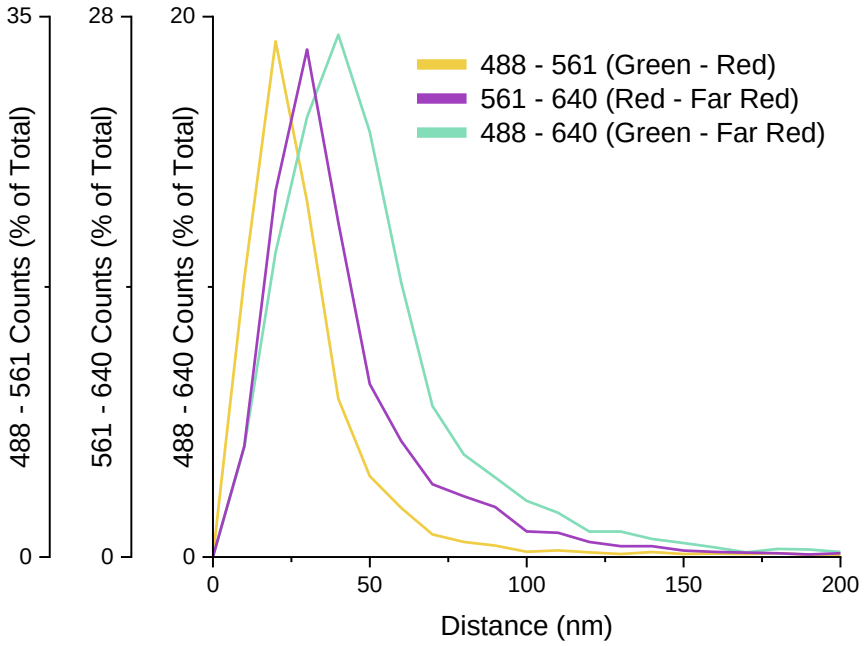

Figure 3-5. Colocalisation positive control: nearest neighbour distance distributions between separate channels in multi-colour 200 nm fluorescent beads. 5,442 beads were imaged with three excitation wavelengths: 488, 561 and 640 nm.

Channel Pair (ex nm)	Peak Centre (nm)	FWHM (nm)	σ (Sigma) (nm)	Adjusted R-squared
488 – 561	22	25	11	0.972
561 – 640	30	30	13	0.959
488 – 640	40	44	19	0.978

Table 2. Properties of Gaussian peaks fitted to nearest neighbour distance distributions between separate channels in multi-colour 200 nm fluorescent beads. σ (Sigma) is based on the fitted Gaussian FWHM. Adjusted R-squared is the goodness-of-fit measure.

Although this control experiment does not aim to separate and quantify the effects of all optical aberrations in addition to localisation uncertainty, their combined effect is sufficiently small to allow confident use of this image acquisition and analysis set-up. Eliscovich et al. have recently developed a method to computationally correct chromatic aberrations by imaging multi-colour fluorescent beads, measuring the displacement between their assigned centres and creating a vector map to correct

localisation positions for each wavelength across the field of view (Eliscovich, Shenoy and Singer, 2017). This correction was not applied to our data. Instead, based on the assumption of uniform distribution of localisations in the field of view, the Gaussian inter-bead-centre distance distributions were subtracted from the Gaussian inter-colocalising-protein distance distributions to obtain a population-level approximation of the true peak colocalisation distance for each pair of proteins imaged.

3.3 Development of a Vicinity-based Localisation Adjacency Determination method

3.3.1 Colocalisation Null Hypothesis (negative control): Randomly Distributed Localisations

One of the main challenges for colocalisation measurements is colocalisation (or clustering / coincidence / coupling) – occurring by chance. Indeed, in colocalisation analysis, the null hypothesis (H_0) occurs under random distribution of pixels (pixel-based methods) or localisations (object-based methods). The analysis method developed here relies on NN distance distributions – histogram-like sets of data where all NN distances in a sample are binned and their occurrence frequency (count or percent of total number of distances) plotted on the Y-axis. These were measured between sets of simulated randomly distributed (Poisson-distributed) (Illian *et al.*, 2008) localisations at multiple densities (points per surface area). Simulated data is representative of the used imaging setup and of recorded experimental values. Randomly distributed localisation data (random data, for brevity) was generated as pairs of random numbers between 0 and 512 as xy coordinates in a 512 x 512 pixel square, also referred to as a tile or field. The number of xy coordinate pairs divided by area is the punctum density. Throughout this thesis, metric units will be used for distances (nanometres instead of pixels) and areas (μm^2 instead of $pixels^2$), based on the imaging setup used here: 84 nm per pixel and a field of view of 1,849 μm^2 (512 x 512 pixels). The metric units represent the data more truthfully and do not depend on the imaging system – a nanometre is a nanometre irrespective of the number of pixels used to sample it.

When analysing two sets of puncta S1 and S2, when S2 contains randomly distributed puncta (simulated), the characteristics of the S1-S2 NN distance

distribution normalised to the total number of puncta in S1 only depend on the density of puncta in S2 (confirmed for punctum densities greater than 54/100 μm^2). The Kolmogorov-Smirnov test showed no significant differences (α = 0.05) between the S1-S2 NN distance distributions in all of the following cases (despite its tendency to classify even modest differences as highly significant for high n numbers). There was no difference when, for the same S2, S1 was replaced with randomly distributed puncta at different densities or with non-random experimental data. There also was no difference when, for the same S1, S2 was obtained either directly (simulated at the desired density) or by combining two lower density sets whose sum of densities matched that of the directly simulated one. This is relevant in the case of merging sets of points to measure triple colocalisation (introduced later).

In the random localisation simulations presented here, S1 (the set of puncta for which the NN distance distribution is displayed) was always of randomly distributed puncta at a density of 95/100 μm^2 and punctum density in S2 was varied from 54/100 μm^2 to 190/100 μm^2 in steps of 13.5/100 μm^2 and then up to 350/100 μm^2 in steps of 27/100 μm^2. In total, 17 different punctum densities were simulated, with one thousand 1,850 μm^2-fields (512 x 512 pixel) for each set of conditions, and the normalised (to total number of distances measured) NN distance distributions were plotted as illustrated in Figure 3-6 A. In all NN distance distributions presented, distances were grouped into bins of 10 nm for analysis and plotting.

German physicist Paul Hertz first described the probability density function (pdf) for NN distances between molecules in a volume in 1909 (Hertz, 1909). Later, Torquato et al. built on that work and generalised NN distance pdfs for penetrable and impenetrable spheres in D-dimensional spaces (Torquato, Lu and Rubinstein, 1990). A function describing NN distance distributions in 2D has been used (Equation 1) where x is the distance form a given point and d is a parameter that represents punctum density and A is the total area under the curve, allowing this equation to fit distributions irrespective of the unit of measurement used.

$$f(x) = A * 2\pi dx * e^{-\pi dx^2}$$ **Equation 1**

This equation closely matches NN distance distributions at different simulated punctum densities and allows predicting the NN distance distribution for any given density of puncta. Four examples of fitted distributions and their residuals are shown

in Figure 3-6 B and C, respectively. The linear dependency of the density parameter d on the actual density of randomly distributed puncta is shown in Figure 3-6 D.

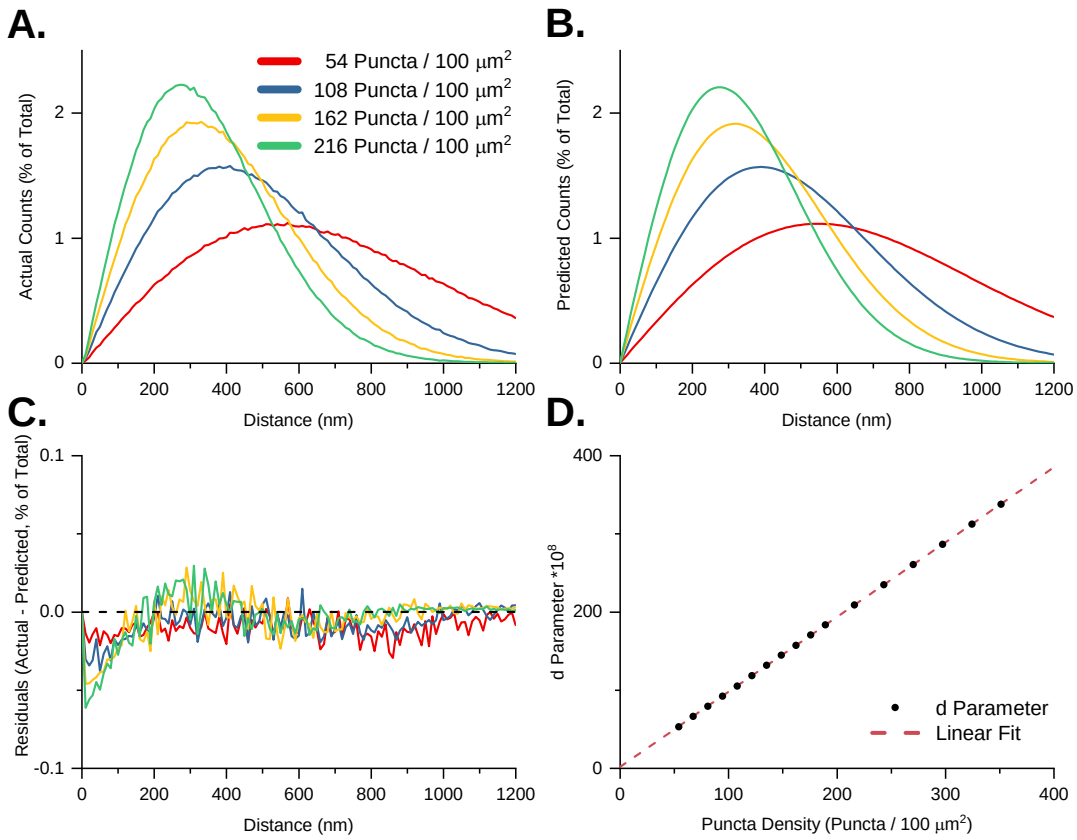

Figure 3-6. Nearest neighbour (NN) distance distributions under the null hypothesis of random localisations. A. NN distance distributions (normalised to total number of puncta) between randomly distributed puncta at four different punctum densities. **B.** Predicted NN distance distributions for the same punctum densities as in A. **C.** Residuals of fitting predicted curves in B. to simulated data in A. **D.** Linear dependence of 2D NN distance probability distribution function parameter d (multiplied by 10^8) on actual punctum density.

The ability to predict NN distance distributions for any given punctum density is useful, as the statistical significance of colocalisation is often compared to a randomised control. Generating a series of simulations of randomly distributed puncta to compare with actual data is time consuming but this step can be replaced by a compact equation. This model holds in cases where the region of interest (ROI) and the number of points within are large enough that its borders do not have a significant impact on the finding of nearest neighbours and on the overall NN distance distribution. Boundary corrections are frequently used in Ripley-based analysis methods (Lagache *et al.*, 2015) but not in NN-based ones. Although the model would become sub-optimal for very low punctum densities, false positive colocalisation due to crowding would also be reduced to an insignificant level. This model is appropriate for the data in this thesis because the field of view (FOV) of the

microscope is a 43 x 43 µm square and, in all cases, over 80% of NN distances measured between synaptic proteins were shorter than 1 µm.

To conclude, an accurate model was adopted for characterising the NN distance distributions resulting from randomly distributed puncta at various densities.

3.3.2 Statistical significance and false positives in colocalisation analysis

Statistical significance of colocalisation is assessed by comparing colocalisation measured in real data with colocalisation in matching randomised data (randomly distributed localisations at equal density). The two-sample Kolmogorov-Smirnov (KS) test is a commonly used non-parametric statistical test for comparing cumulative distributions of variables and deciding whether they are statistically significantly different. However, for large n numbers (e.g. many distance measurements), the KS test yields highly significant p-values even for small differences between two cumulative distributions. For example, when comparing the cumulative distribution of NN distances between GluN1 and PSD95 in the CA1 Radiatum (CA1rad) (n=300,000 measurements) with that of randomly distributed localisations, the KS test p-value is lower than 10^{-300}. Apart from indicating that the distribution of GluN1 relative to PSD95 in the CA1rad is not random, this test is of little use for actually quantifying colocalisation. Some colocalisation analysis methods (DiAna – Distance Analysis) do not even compute the KS-test p-value and are complacent with the fact that the distribution of NN distances falls outside the 95% confidence interval (CI) of randomised data (Gilles *et al.*, 2017). Other studies propose more elaborate Ripley's K function-based methods for assessing the statistical significance of colocalisation is presented without an actual measure of colocalisation (such as a percentage of colocalised points) (Lagache, Meas-Yedid and Olivo-Marin, 2013). The more advanced method SODA (Lagache *et al.*, 2018) incorporates a different way for assessing the significance of colocalisation and it commonly reports p-values lower than 10^{-20}, even in low colocalisation data, and extends to values as low as $10^{-2,900}$. While there is nothing wrong with this, these p-values are not informative, as they can occur even when a colocalisation measure includes a significant proportion of false positives that result from crowding (high punctum densities). A good colocalisation analysis method must have the ability to statistically separate true colocalisation from false positives.

The coordinate-based colocalisation (CBC) method of (Malkusch *et al.*, 2012) contains a distance-based weighting of colocalisation but does not tackle the issue of false positive short inter-object (clusters) distances occurring due to crowding. (Eliscovich, Shenoy and Singer, 2017) propose choosing a distance threshold for NN-based colocalisation corresponding to a randomised control that contains an arbitrary 10% false positives. This is a step in the right direction but it exposes the method to a potentially high rate of false negatives while still including a low and unknown amount of false positives in the final colocalisation measure.

The False Discovery Rate method of (Zhang and Chenouard, 2008) relies on statistically comparing the distances between all pairs of points of two sets in a sample with those in a corresponding randomised control and then selecting those above an arbitrary significance level as representing true colocalisation. Their method is not supported convincingly and its output is an unintuitive colocalisation ratio reflecting a portion of all possible distance measurements that indicate true colocalisation. The interaction strength measure of (Helmuth, Paul and Sbalzarini, 2010) contains an analytical way of estimating H_0 for comparison with experimental data but their colocalisation measure is also difficult to interpret in biological contexts. The Interaction Factor method of (Bermudez-Hernandez *et al.*, 2017) is a more intuitive measure of colocalisation, reflecting the proportion of colocalised objects in a population. It corrects for false positives by determining H_0 through a specific object randomisation procedure but has significant errors when tested on simulated data.

The Statistical Object Distance Analysis (SODA) method (Lagache *et al.*, 2018) appears to be the most advanced colocalisation analysis method to date and will be used as a benchmark in the following sections. SODA relies on thresholding the value of the first derivative of the pair correlation function in a puncta-density-dependent, adaptable way. Its meaningful outputs are an overall coupling (colocalisation) index and, for every potentially coupled pair of objects, a probability of true coupling. The high performance of SODA was demonstrated by extensive testing on simulated data under various conditions.

3.3.3 Model fitting to nearest neighbour distance distributions enables the determination of true colocalisation

For the three synaptic proteins studied here (GluN1, PSD95 and SAP102), NN distances were measured for every possible pair (3 pairs) and, separately, for every protein in each pair, in 15 brain regions across 7 age groups (N=30 mice in total). For example, in a given region, in the case of GluN1 and PSD95, distances were measured from every GluN1 punctum to the nearest PSD95 punctum (GluN1-PSD95) and vice-versa, from every PSD95 punctum to the nearest GluN1 punctum (PSD95-GluN1). Six (3 x 2) sets of NN distances were obtained from every region analysed. For every pair, the measured NN distances up to 1,200 nm were binned in 10 nm intervals and plotted as frequency distributions (NN distance distributions). Inspecting hundreds of NN distance distributions for all pairs of proteins analysed led to the observation that virtually all distributions were bimodal (contained 2 peaks). An example of such a distribution is shown in Figure 3-7 A (further examples in Figure 3-9 A). Peak 1, relatively sharp and occurring at short NN distances, resembles the peak formed by NN distances in multi-colour fluorescent beads – the positive control of colocalisation (Figure 3-5). Peak 2, broader and occurring at longer NN distances, resembles the distribution of NN distances under the null hypothesis of spatial randomness (Figure 3-6).

It is reasonable to infer that the short NN distances under Peak 1 correspond to colocalising puncta, with the longer NN distances (Peak 2) corresponding to non-colocalising puncta, and that puncta in any given region are made up of two populations: colocalising and non-colocalising. Indeed, the NN distance distribution can be fitted by combining two peak functions (Peak 1: Gaussian and Peak 2: NN distance distribution for randomly distributed puncta – Equation 1) as shown in Figure 3-7 A.

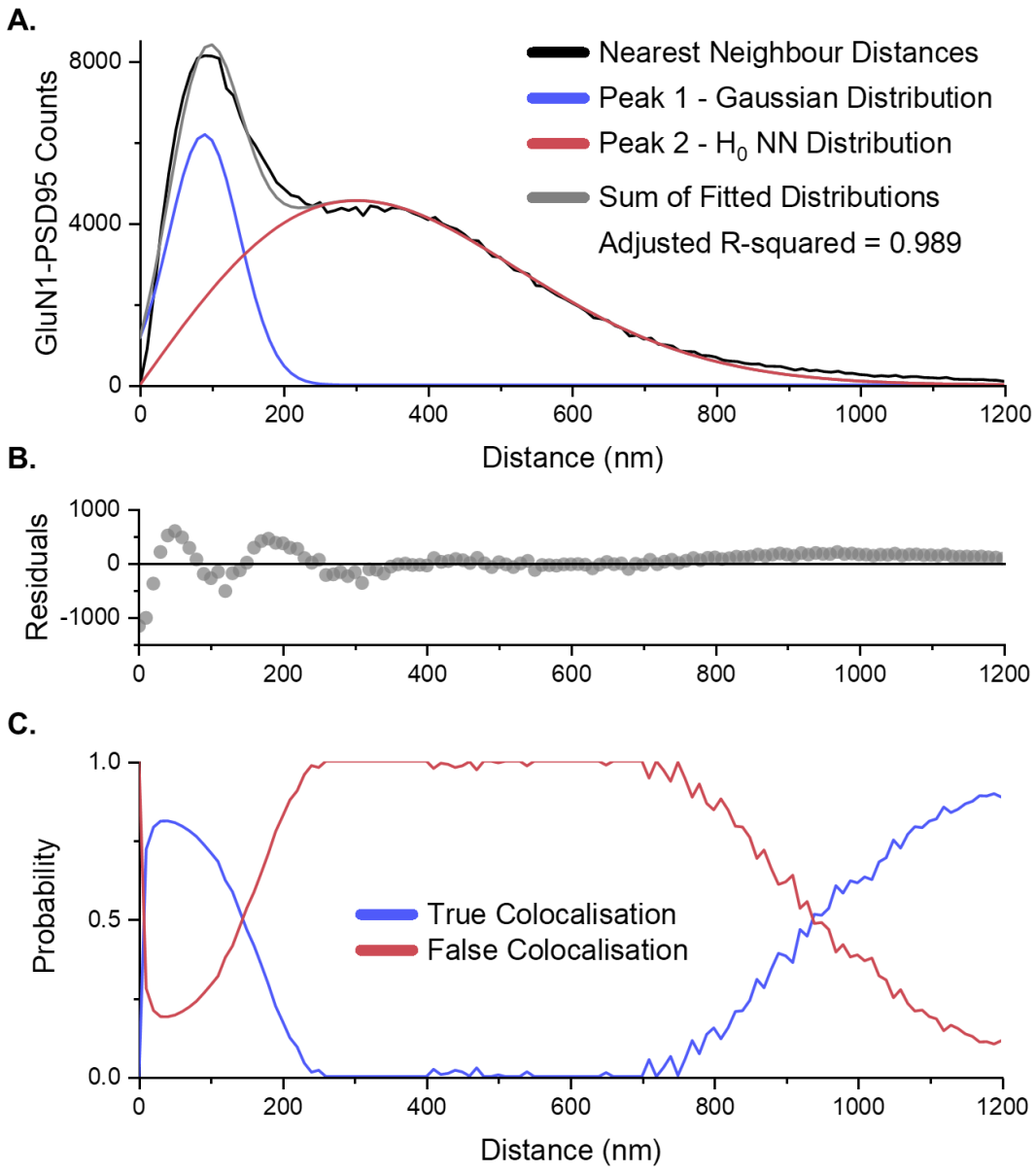

Figure 3-7. Curve fitting of nearest neighbour (NN) distance distributions and determination of probability of true colocalisation. A. Representative distribution of GluN1 puncta NN distances (317,700 distances) to PSD95 puncta in the CA1 Stratum Radiatum of an adult (P94) mouse. Peak 1 (Gaussian) of the bimodal NN distribution contains distances at which true colocalisation occurs. Peak 2 contains non-colocalising distances and is fitted by the equation describing NN distance distribution under the null hypothesis (H_0) of spatial randomness of puncta. **B.** Residual plot (actual - predicted) of curve fitting in A. (same units). **C.** Probability of true colocalisation is computed at every distance by dividing the number of measurements above fitted Peak 2 by the total number of measurements at that distance. The probability of true colocalisation equals zero when, at a given distance, all measurements fall under fitted Peak 2.

Adjusted R-squared (Adj. R-sq) can never be greater than the less conservative R-squared (coefficient of determination) and has been reported here as a measure of goodness of fit. Adj. R-sq is a semi-quantitative indicator of curve fitting quality but it is not a reliable criterion for choosing a nonlinear model (Spiess and Neumeyer, 2010). Therefore, Adj. R-sq values were not the deciding factor in choosing the

proposed model. Instead, the model was chosen based on the reasoning presented earlier and on the assumption that, in the majority of cases, non-colocalising puncta are close to randomly distributed relative to the puncta for which colocalisation is measured. In fact, substituting the equation describing Peak 2 with either a Type I Extreme Value distribution (also known as a Gumbel distribution) (Gumbel, 1935) or a Gaussian distribution yields similarly high Adj. R-sq values. The Gumbel distribution provides a relatively good approximation of NN distance distributions under spatial randomness and, as a result, would be similar to Equation 1 used here. On the other hand, the Gaussian distribution, due to its symmetric nature, clearly cannot describe the NN distance distributions under spatial randomness.

The fit residuals in Figure 3-7 B show some degree of error autocorrelation due to the fact that colocalising distances in experimental data do not form a perfect Gaussian distribution. The Gaussian distribution of best fit often has a non-zero value at a distance of 0 nm despite the fact that negative distances cannot exist. NN distances were measured from single-plane confocal microscope images, where the thickness of the optical slice imaged (and axial resolution) depends on the wavelength of light, characteristics of the tissue and mounting medium, depth of imaging and other, more subtle influencing factors. The 2D images obtained are projections from fluorescently labelled puncta within the optical slice imaged (approximately 250 – 400 nm both above and below the focal plane) and this will probably lead to a slight overestimation of colocalisation and an underestimation of peak colocalising distances (Peak 1 centre). Despite these caveats, the Gaussian model remains useful in describing colocalising distances. Lagache et al. used a Gaussian model to describe distances between colocalising puncta in structured illumination microscopy (SIM) and 3D stochastic optical reconstruction microscopy (STORM) images analysed with the SODA method (Lagache *et al.*, 2018). Peak 2 is closely, but not perfectly described by the formal expression of the NN distance distribution under spatial randomness (non-colocalisation). This is likely because non-colocalising puncta are not perfectly randomly distributed in relation to the reference set of puncta and may form clusters instead, occasionally leading to significant deviations from randomness. In the vast majority of cases, however, the deviation from perfect randomness is minor.

Since the observed NN distance distribution in an experimental setting is the combination of two populations of NN distances (colocalising and non-colocalising), they can be separated to reveal the distances corresponding to true colocalisation in

any given setting. In practice, this is achieved by subtracting, at every distance, the value of fitted Peak 2 from the observed NN distance distribution and substituting with zero at every point where the value of fitted Peak 2 is greater than the number of observed NN distances. At the level of individual NN distance measurements (corresponding to individual detected puncta), for a given interval (10-nm bin), the probability of true colocalisation can be defined as the number of NN distances above Peak 2 divided by all NN distances in that interval (zero when all NN distances fall under Peak 2), as shown in Figure 3-7 C. The probability of false positive colocalisation is simply 1 - probability of true colocalisation. The increase of the true colocalisation probability at distances beyond 800 nm is an undesired behaviour resulting from imperfect curve fitting. However, less than 5% of all distances in this example are above 800 nm, and excluding distances above a threshold set anywhere between 250 and 700 nm would easily exclude these from the colocalisation measurement. This constitutes the basis of the Vicinity-based Localisation Adjacency Determination (VLAD) method used in this project.

A visual illustration of VLAD is shown in Figure 3-8. For GluN1 puncta, the probability of true colocalisation with PSD95 is determined by first subtracting fitted Peak 2 from the initial NN distance distribution. The probability of true colocalisation itself varies with distance. In this case, distances between 30 and 40 nm have the highest likelihood of being associated with truly colocalising GluN1 puncta, with a probability of true colocalisation of 0.81 in this range. The probability of true colocalisation falls below 0.5 beyond 150 nm and reaches zero at 260 nm. In the bottom right image of Figure 3-8, detected GluN1 puncta are coloured based on their probability of true colocalisation, according to the red-to-blue colour scale next to the probability distribution in the graph above. This colour mapping provides a helpful visualisation of how probabilities are assigned to individual puncta.

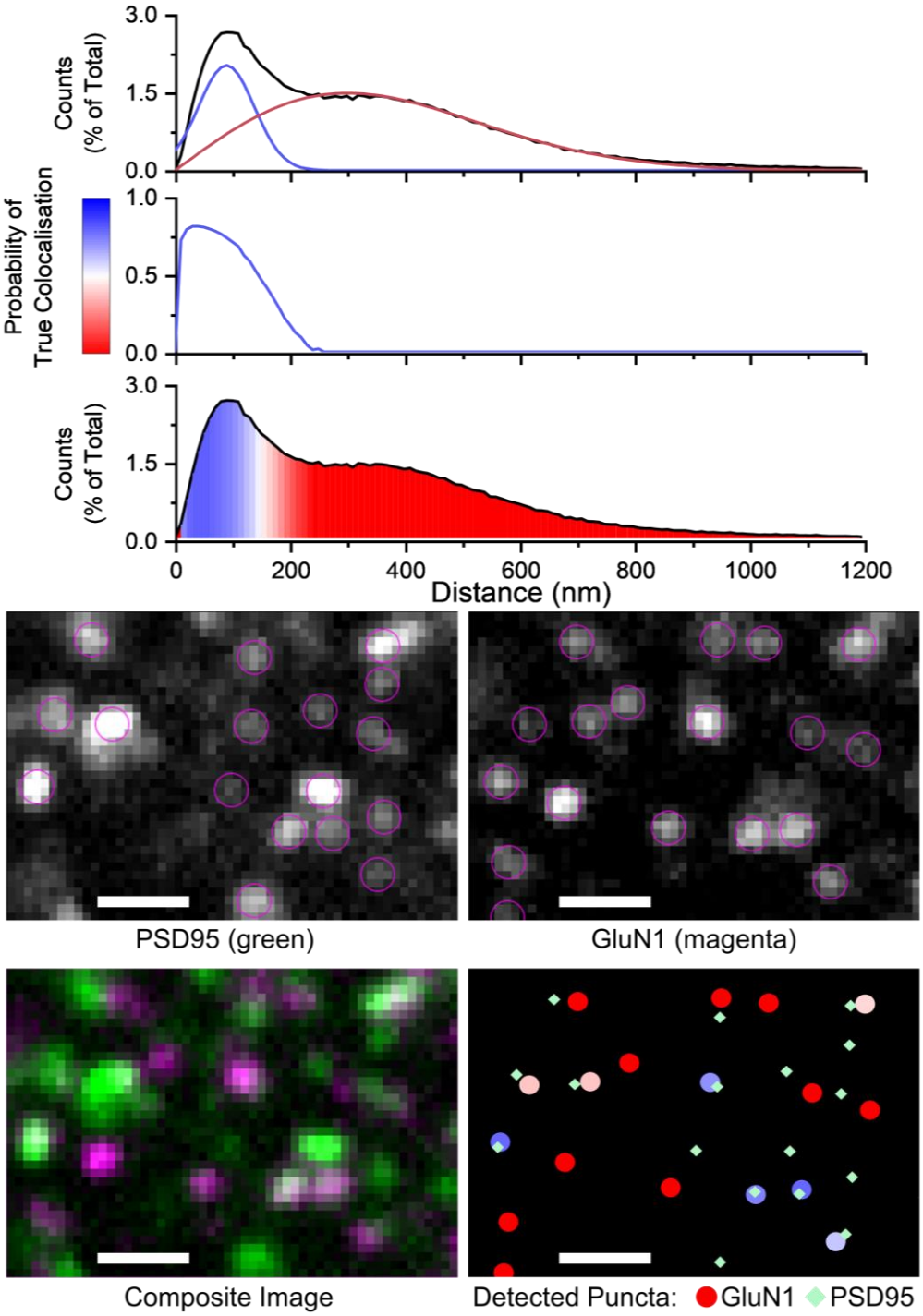

Figure 3-8. Measuring the colocalisation of GluN1 and PSD95 in the CA1 Stratum Radiatum of an adult mouse using the VLAD method. Graphs (from top to bottom): GluN1-PSD95 nearest neighbour (NN) distance distribution with fitted Peaks 1 and 2. Data from the CA1Rad of a P94 mouse, containing 317,700 GluN1 puncta and 351,500 PSD95 puncta (same as in **Figure** 3-7); Distribution of probability of true colocalisation for GluN1 puncta, mapped to a 0-to-1 colour scale (and set to zero beyond 300 nm); GluN1-PSD95 NN distance distribution coloured by probability of true colocalisation for every 10-nm bin. **Images:** Individual channel and composite images of PSD95 and GluN1 puncta. Magenta circles in individual channel images indicate TrackMate-detected puncta. Their locations are shown in the bottom right image, where GluN1 puncta (circles) are coloured by their probability of true colocalisation with PSD95 (colour scale same as above). Overall, 24.1% of GluN1 puncta in this region colocalised with PSD95 and the average probability of true colocalisation for NN distances under 230 nm was 0.57. Scale bars: 1 µm.

A step-wise illustration of the VLAD method used to measure colocalisation between synaptic protein puncta in the CA1 Stratum Radiatum (CA1rad) of another adult mouse (postnatal day 94) is shown in Figure 3-9. A total surface area of 0.28 mm2 of the CA1Rad was imaged and the following numbers of puncta were detected: GluN1 – 278,000; PSD95 – 355,000; SAP102 – 234,000 (average punctum densities of 100, 127 and 84 puncta/100 µm2, respectively). NN distances for each protein in each pair were pooled and their distributions plotted in Figure 3-9 A. Applying a simple distance threshold to define colocalisation is problematic because, for any threshold, an unknown but often significant amount of false positives will be included in the measurement. Figure 3-9 B. shows the cumulative distributions of the NN distances in A., normalised to the total number of puncta for each protein. It can be interpreted as the threshold-based colocalisation (percentage of colocalised puncta) of each protein at every distance threshold. This colocalisation measure is highly sensitive to the choice of threshold (changes at every distance), plateaus at different distances for different puncta pairs and relies on the arbitrary choice of a threshold, rendering it unreliable.

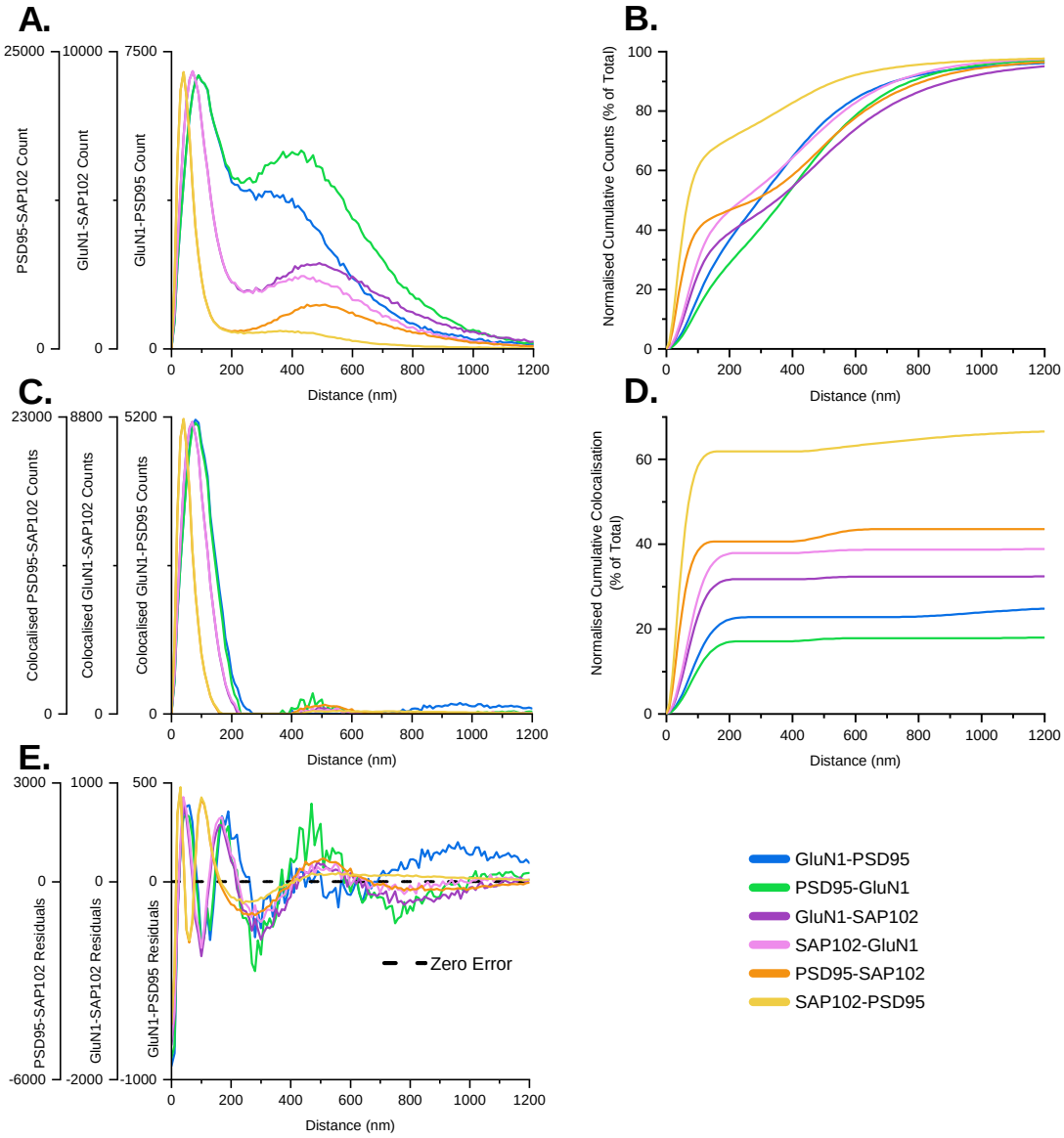

Figure 3-9. Application of the Vicinity-based Localisation Adjacency Determination (VLAD) method on synaptic protein puncta in the adult (P94) CA1 Stratum Radiatum. A. Nearest neighbour (NN) distance distributions for all pairs between GluN1, PSD95 and SAP102. For each pair, the NN distances of each member of the pair are plotted on the same axis (3 axes total). **B.** Cumulative distribution of NN distances in A., normalised to the total number of puncta for each protein. Value at every distance is equivalent to the uncorrected distance-threshold-based colocalisation up to that distance. Choosing an appropriate distance threshold is difficult and will always result in the inclusion of false positive colocalisation. **C.** Distribution of true colocalising distances determined by the VLAD method. For each pair, the colocalising distances of each member of the pair are plotted on the same axis (3 axes total). Peak colocalisation distances, from left to right, occur at 46, 76 and 90 nm. **D.** Cumulative distribution of colocalising distances in C., normalised to the total number of puncta for each protein. Value at every distance is equivalent to true colocalisation up to that distance measured by VLAD. For each protein, colocalisation reaches a plateau beyond 200 nm and the VLAD colocalisation measure is distance-threshold-insensitive over a significant distance range (200 – 400 nm) for all three pairs analysed, enabling the straightforward selection of a distance threshold. **E.** Residuals (actual - fitted) of the bimodal curve fitting of the data in A., necessary for applying the VLAD method. For each pair, residuals of each member of the pair are plotted on the same axis (3 axes total). **All.** Analysed surface area of the CA1 Stratum Radiatum: 0.28 mm^2. Number of puncta detected: GluN1 – 278,000; PSD95 – 355,000; SAP102 – 234,000.

By applying the VLAD method – curve fitting of the bimodal NN distance distributions – and subtracting Peak 2 from the overall distributions in A., the distributions of truly colocalising NN distances are obtained (Figure 3-9 C.).

The distances corresponding to true colocalisation form a Gaussian distribution and, within each pair, the numbers of colocalising puncta are close, implying an overall 1:1 colocalisation stoichiometry ratio. Figure 3-9 D. shows the cumulative distribution of colocalising distances, normalised to the total number of puncta for each protein. It can be interpreted as the VLAD-measured colocalisation of each protein at every distance threshold. Although colocalisation occurs in a 1:1 ratio for all three pairs analysed, the levels of colocalisation (%) of each protein in a pair differ, due to different total numbers of puncta.

In stark contrast to the cumulative NN distance distributions in panel B., VLAD-measured colocalisation plateaus at 200 nm and shows very little change beyond this point (owed to imperfect curve fitting). VLAD-measured colocalisation is almost completely insensitive to threshold between 200 and 400 nm, since non-colocalising distances occurring in this range are consistently accounted for (Peak 2 subtracted from NN distances). Between 200 and 400 nm, the smallest difference in threshold-based colocalisation is 11.7% in the case of PSD95-SAP102 and the largest is 28% for GluN1-PSD95 (average change of 18.4%). Over the same range, VLAD-measured colocalisation varies by less than 0.6% in all cases (average 0.2%). This greatly simplifies choosing a threshold for VLAD colocalisation. Choosing a universal threshold for all three pairs is desirable for ease of analysis and for quantifying triple colocalisation (introduced later).

The GluN1-PSD95 pair showed the longest colocalising distances, with an overall peak colocalisation distance of 90 nm and a standard deviation (of fitted Gaussian) of 54 nm. To include over 99% of these distances in the colocalisation measurement, a threshold of 230 nm was chosen (peak colocalisation distance plus 2.5 standard deviations). This threshold is sufficiently high to include all colocalising distances while excluding the noise resulting from imperfect curve fitting above this distance. Figure 3-9 E. shows the residuals of the VLAD curve fitting. The sum of residuals (positive and negative) above 30 nm falls between -3.1 and 6% of all fitted data. The sum of absolute residuals above 30 nm ranges from 4.3 to 8.7% of fitted data for the pairs containing GluN1. For the PSD95-SAP102 pair, the sum of absolute residuals over the same range makes up 17.3 – 20.7% of the fitted data.

This is due to a moderate deviation from randomness in non-colocalising puncta, and probably results in a slight underestimation of VLAD-measured colocalisation due to the overestimation of the component of Peak 2 at short distances. The more conservative colocalisation measure is arguably preferable to the uncorrected threshold-based colocalisation, making this an acceptable compromise.

VLAD assigns a probability of true colocalisation for each punctum based on its NN distance to a punctum from another partner set. Three proteins (GluN1, PSD95 and SAP102) were studied here and determining triple colocalisation was of great interest. When analysing colocalisation with two partner sets of puncta, the probability of true triple colocalisation for each punctum is the product of the probabilities of colocalisation with each of the two partners ($p_{Triple} = p_{Colocalisation\text{-}1} \times p_{Colocalisation\text{-}2}$). This principle can be extended to any number of colocalisation partners ($p_{Multiple} = p_1 \times p_2 \times \ldots \times p_n$), though, in practice, it is challenging to simultaneously image more than 3 or 4 distinct proteins in a sample.

Here, because individual punctum data was unavailable (a technical limitation, not theoretical), the approach illustrated in Figure 3-10 was employed for assessing triple colocalisation. For two colocalisation partners (P1 and P2), three quantities are desired: colocalisation with P1-only ($C_{1\text{-}only}$), colocalisation with P2-only ($C_{2\text{-}only}$) and triple colocalisation (with P1 and P2 – C_{Triple}). Colocalisation with an individual partner is comprised of colocalisation with that partner only and triple colocalisation, and can be measured directly (C_1 and C_2). Colocalisation with P1 or P2 is determined by measuring colocalisation with the merged sets of coordinates of P1 and P2 (C_{Merged}). The overlap between C_1 and C_2 (representing triple colocalisation) is illustrated in the bottom section of Figure 3-10. $C_{1\text{-}only}$, $C_{2\text{-}only}$ and C_{Triple} can be determined from the measured quantities C_1, C_2 and C_{Merged} as shown by the system of three equations below.

$$\begin{cases} C_1 = C_{1-only} + C_{Triple} \\ C_2 = C_{2-only} + C_{Triple} \\ C_{Merged} = C_{1-only} + C_{2-only} + C_{Triple} \end{cases} \Rightarrow \begin{cases} C_{1-only} = C_{Merged} - C_2 \\ C_{2-only} = C_{Merged} - C_1 \\ C_{Triple} = C_1 + C_2 - C_{Merged} \end{cases}$$

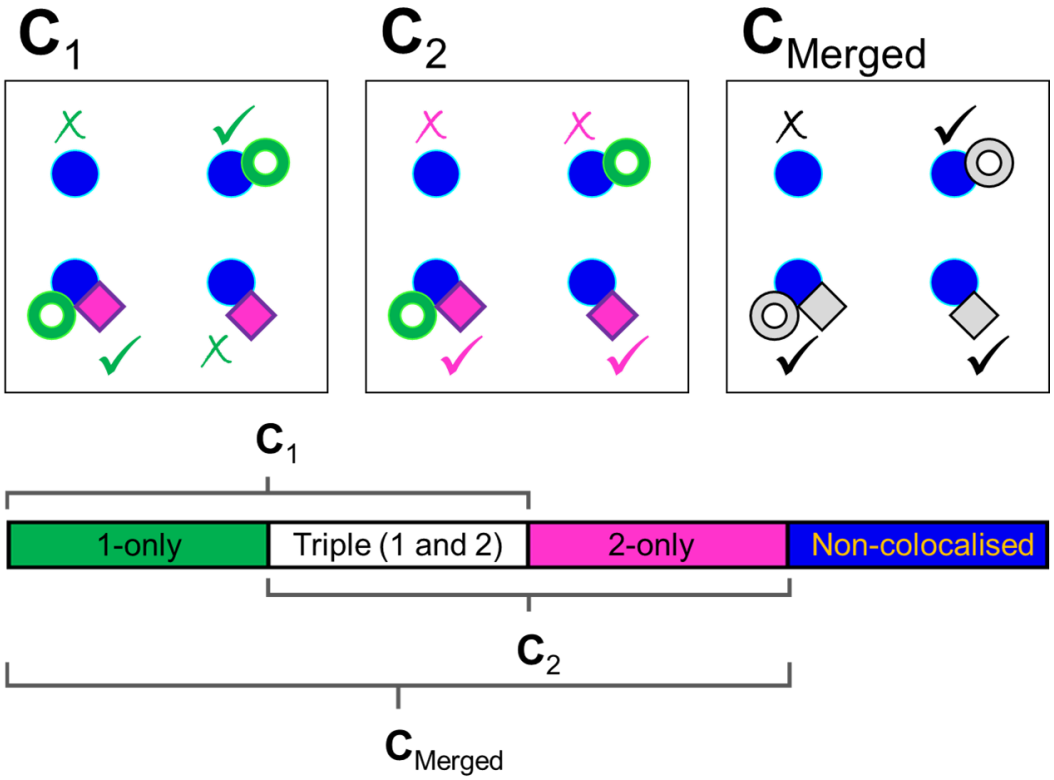

Figure 3-10. Determining triple colocalisation at a population level. In this illustration, colocalisation is measured for the blue circles with Partner 1 – green doughnuts – and Partner 2 – purple diamonds. In each square panel, the four blue circles represent four possible populations: non-colocalised (top left), colocalised with Partner 1 only (top right), colocalised with both – Triple colocalisation (bottom left) and colocalised with Partner 2 only (bottom right). 'X' represents non-colocalisation and a tick mark (✓) represents colocalisation. The first two panels show colocalisation with Partner 1 and with Partner 2, respectively. The third panel shows colocalisation with the merged sets of puncta of Partner 1 and Partner 2 – colocalisation with 1 OR 2. The bottom section shows the relationships between the measured quantities C_1, C_2 and C_{Merged} and the quantities of interest $C_{1\text{-only}}$, $C_{2\text{-only}}$ and C_{Triple}.

In summary, the VLAD colocalisation analysis method and its underlying principles were introduced here. It is an attractive colocalisation analysis method because it assigns probabilities of true colocalisation to individual puncta (thus appropriately accounting for false positive colocalisation) and is threshold-insensitive over a significant range of distances.

3.3.4 Validation of the Vicinity-based Localisation Adjacency Determination method

The accuracy of VLAD was tested in simulated localisation data with pre-determined levels of colocalisation across a wide range of conditions. Input data for VLAD consists of localisations that can be obtained with any object detection method. The purpose of the simulated data was to test the ability of VLAD to detect colocalisation

irrespective of the puncta detection method used. Therefore, simulated data was generated in the form of sets of localisations (pairs of xy coordinates) and not synthetic images.

Simulated data was generated in square fields (tiles) of 512 x 512 pixels (1850 μm^2). To ease computational burden, localisations were placed at intersections between pixels in a 4,096 x 4,096 pixel grid (no sub-pixel localisation at this level) that was subsequently downsampled 8 times. Each tile contained two sets with equal numbers of simulated localisations (puncta). For all simulated data in this chapter, density (puncta/100 μm^2) refers to the density of both sets of puncta in a given setting. This represents a sufficiently good approximation of experimental data, where, in most cases, the densities of two proteins in the same area differ by a factor smaller than 2. Simulated puncta within the same set were never allowed to be closer than 170 nm to each other, mimicking the shortest resolvable distance of approximately 210 nm for green light in experimental data. In each tile of simulated data, puncta in one set (S1) were placed randomly within the tile and puncta in the second set (S2), for which colocalisation was measured, were placed according to the chosen level of colocalisation. Colocalising S2 puncta were placed such that the distance to S1 puncta followed a Gaussian distribution with the mean at a chosen peak colocalisation distance and a standard deviation equal to a third of the peak colocalisation distance (normally distributed between zero and 2x peak colocalisation distance). This model was based on observations from experimental data where colocalising NN distances are closely described by a Gaussian distribution. Lagache et al. also used a Gaussian process for colocalised (coupled) spots in simulated data (without a fixed relationship between the peak colocalisation distance and the standard deviation) used for testing SODA (Lagache *et al.*, 2018), based on their own observation that colocalising distances in experimental data are normally distributed. A limit of 3 colocalising S2 puncta per 1 S1 punctum was imposed. Non-colocalising S2 puncta were randomly placed within the tile. Simulated colocalisation refers to the percentage of S2 puncta chosen to be colocalised (not randomly placed). Measured colocalisation refers to S2 colocalisation. Peak colocalisation distance was 97 nm in all simulations (similar to the peak colocalisation distance of GluN1-PSD95), unless otherwise specified, and the VLAD distance threshold was always equal to the peak colocalisation distance plus 3 standard deviations (190 nm in most cases, unless otherwise specified).

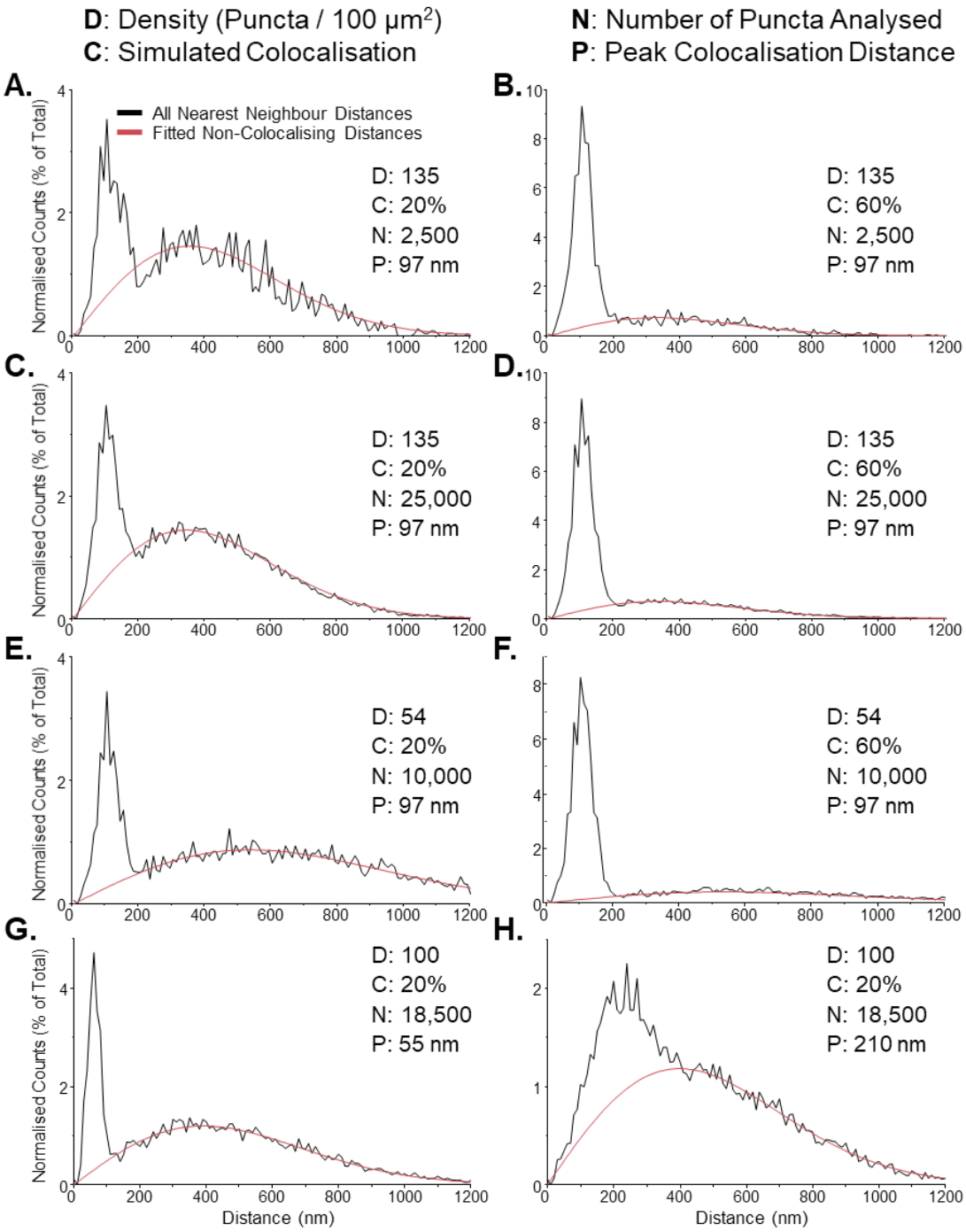

Figure 3-11. Nearest neighbour distance distributions in simulated data with defined punctum densities, colocalisation levels and peak colocalisation distances. All panels show NN distance distributions for simulated data with chosen punctum density (D), colocalisation level (C), total number of puncta analysed (N) and peak colocalisation distance (P). The red lines correspond to non-colocalising distances, as determined by VLAD fitting of Peak 2, to be subtracted from the overall distribution for the measurement of true colocalisation. **A and B.** NN distance distributions in a single 1850 µm² tile at high punctum density (135/100 µm²) with low and high simulated colocalisation (20% and 60%, respectively). **C and D.** Data from 10 tiles with all other parameters as in A. and B., respectively. The distributions are similar to those in A. and B., but less noisy, as they are comprised of more data points. **E and F.** Data from 10 tiles with puncta at low density (54/100 µm²), with all other parameters as in C. and D., respectively. **G and H.** Data from 10 tiles with puncta at intermediate density (100/100 µm²), 20% simulated colocalisation and different peak colocalisation distances (55 and 210 nm, respectively). Longer peak colocalisation distances result in NN distance distributions that are harder to distinguish from those of randomly distributed puncta.

Figure 3-11 contains examples of NN distance distributions in simulated data with various parameters (level of colocalisation, punctum density, total area analysed and peak colocalisation distance). For each NN distance distribution, Peak 2 fitted by VLAD is also shown in red. Subtracting fitted Peak 2 essentially reveals true colocalisation on a population (NN distance distribution) level.

The jagged appearance of Peak 1 in simulated data is a result of the discrete nature of NN distances measured between puncta placed in a downsampled 4,096 x 4,096 pixel grid. The impact of the grid-like nature of simulated data on VLAD and SODA performance was negligible, confirmed by identical colocalisation measurements from both methods in equivalent simulated data with finer sub-pixel localisation (32-times downsampled grid of 16,384 x 16,384 pixels).

VLAD was tested in simulated data with an intermediate punctum density of 100/100 μm^2, representative of the average punctum densities in the majority of experimental data. At each simulated level of colocalisation (ranging from 0 to 100%), VLAD-measured colocalisation closely matched the simulated value (99% confidence interval within ±2 percentage points), as shown in Figure 3-12.

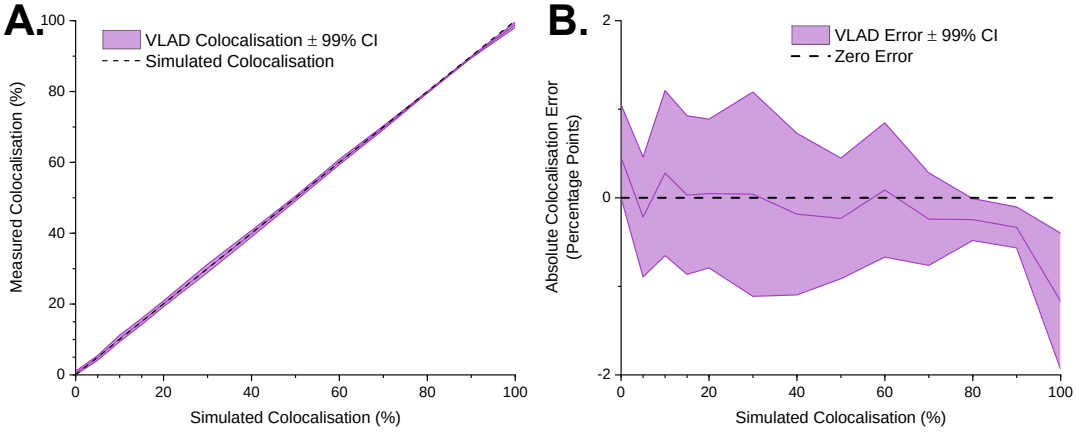

Figure 3-12. VLAD performance in simulated data at 100 puncta/100 µm² and varying levels of colocalisation. A. VLAD-measured colocalisation in simulated data with different levels of colocalisation. Colocalisation was varied from 0 to 20% in 5% steps and from 20 to 100% in 10% steps (ticks on x-axis; 13 conditions total). At every level, colocalisation was measured in 10 individual 1,850-µm² tiles and the average measured colocalisation ±99% confidence interval (CI – equivalent to 1.03 standard deviations) was plotted. Within every group (except 0% colocalisation), measurements were normally distributed ($p_{Shapiro\text{-}Wilk} > 0.05$). **B.** Error of VLAD colocalisation measurements in simulated data with different levels of colocalisation. From the data in A., the error was calculated as the difference between the measured value and the simulated one, and was plotted as average error ±99% CI. VLAD displays remarkable accuracy across all levels of colocalisation, with the 99% CI contained within ±1.2 percentage points (%) of the simulated level between 0 and 90% colocalisation.

The VLAD method relies on curve fitting and benefits from analysing large sets of data, where NN distance distributions are less noisy (see Figure 3-11 A. and C.).

The precision of VLAD (spread of measured values) was evaluated by analysing simulated data at low and high density (54 and 135 puncta/100 µm^2, respectively), low and high colocalisation (20% and 60%, respectively) and different total area (groups of varying numbers of 1,850-µm^2 tiles). Figure 3-13 shows the precision of VLAD improving with increasing numbers of puncta analysed. Curve fitting is more accurate when more data points (NN distances) are available – either from a higher punctum density or from a larger area. Measurements spread over a 2.1 percentage point range for data sets of 5,000 NN distances (5 tiles of 54 puncta/100 µm^2).

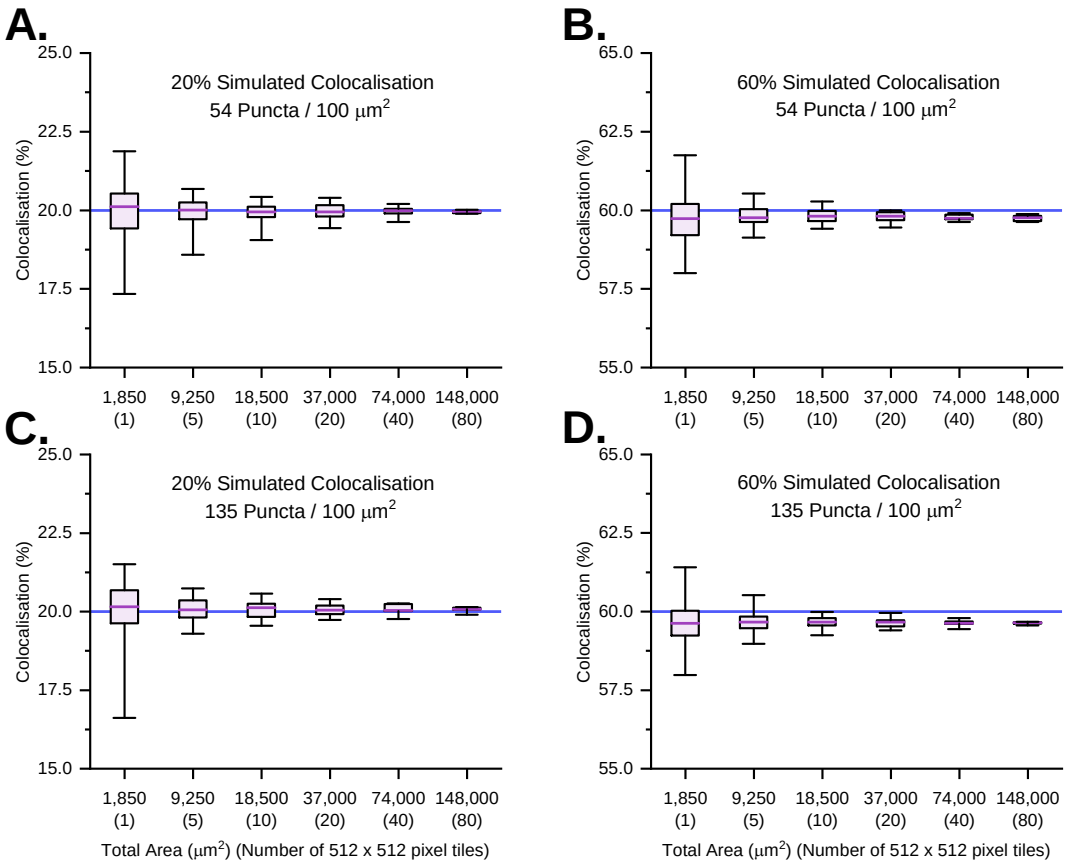

Figure 3-13. VLAD precision improves with increasing numbers of puncta analysed. A. 20% simulated colocalisation at 54 puncta/100 µm^2. **B.** 60% simulated colocalisation at 54 puncta/100 µm^2. **C.** 20% simulated colocalisation at 135 puncta/100 µm^2. **D.** 60% simulated colocalisation at 135 puncta/100 µm^2. **All.** VLAD colocalisation measurements plotted as boxes (25th-75th percentile range and median) and whiskers (extending to minimum and maximum values). Blue lines indicated levels of simulated colocalisation in each panel. The following numbers of different simulations were generated for each total area (in number of tiles) group: $n_{1\ tile}$ = 100; $n_{5\ tiles}$ = 80; $n_{10\ tiles}$ = 40; $n_{20\ tiles}$ = 20; $n_{40\ tiles}$ = 10; $n_{80\ tiles}$ = 5.

89.3% of all experimental data analysed with the VLAD method contained over 5,000 NN distance measurements. For groups of 40 tiles or more (total area > 74,000 µm^2), measurement spreads were negligible, falling below 0.6 percentage points in all cases presented in Figure 3-13.

While the curve fitting step of VLAD benefits from pooling NN distance data, it was important to test VLAD on individual 1,849-µm^2 tiles at various punctum densities and colocalisation levels. To this end, simulated data with punctum densities between 13.5 and 270 puncta/µm^2 and simulated colocalisation levels between 20 and 80% was generated. Punctum densities were varied from 13.5/100 µm^2 to 54/100 µm^2 in increments of 13.5/100 µm^{2}and from 54/100 µm^2 to 270/100 µm^2 in increments of 27/100 µm^2. For each density, colocalisation was set between 20% and 80% in 20% increments. In total, VLAD was tested on 10 tiles in each condition (48 different conditions in total) and the results are shown in Figure 3-14.

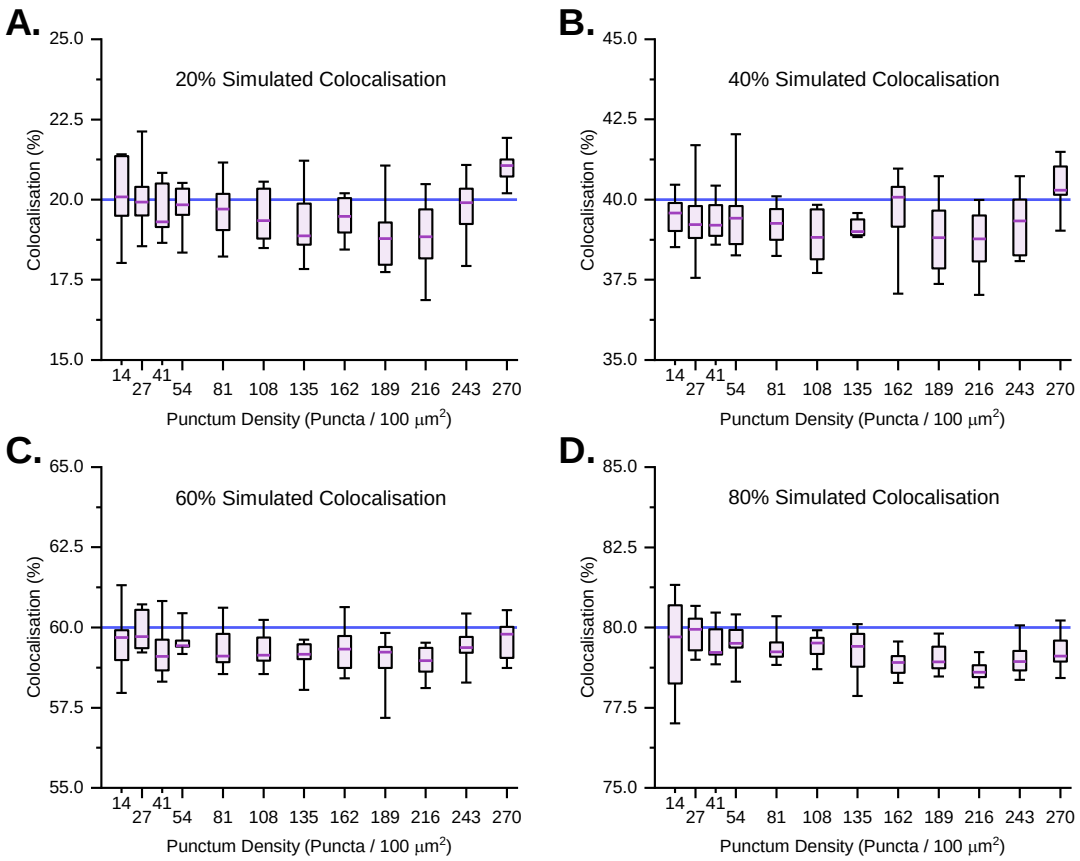

Figure 3-14. VLAD performance in simulated data at various punctum densities and levels of colocalisation. VLAD was applied on simulated data with 20% (**A**), 40% (**B**), 60% (**C**) and 80% (**D**) colocalisation. For every punctum density and colocalisation level, n=10 1,850-µm^2 tiles of simulated data were generated. VLAD colocalisation measurements are displayed as box plots. Boxes: 25th-75th percentile range and median. Whiskers extend to minimum and maximum values. Blue lines indicated levels of simulated colocalisation in each panel.

VLAD colocalisation measurements consistently match simulated levels, with median measured colocalisation always falling within 1.4 percentage points from simulated values in all conditions. VLAD is relatively precise, with 25th-75th inter-percentile ranges below 2.1 percentage points in all cases and minimum-to-maximum ranges under 4.3 percentage points. Based on this data, the precision of

VLAD appears superior to the precision of SODA (Lagache *et al.*, 2018), although this is an imperfect comparison. A direct comparison of VLAD and SODA will be presented at the end of this chapter. VLAD shows a slight tendency to underestimate colocalisation, with median measured values being 0.6 percentage points below simulated values on average. VLAD was tested here on punctum densities up to 270 puncta/100 μm^2 but, in all experimental data analysed in this study, synaptic protein punctum densities never exceeded 210 puncta/100 μm^2.

Experimental data in the following chapter was analysed at the level of entire hippocampal subregions (data was pooled for each subregion). Although VLAD can accurately measure colocalisation in heterogeneous data sets, an important consideration needs to be made regarding probabilities of true colocalisation assigned to individual puncta (individual NN distances). Figure 3-15 shows the NN distance distributions in two sets of simulated data (A. and B.) with equal densities and total surface area and the combined set created by pooling S1 and S2 (C.). The same sets of data are characterised in further detail in Table 3. S1 has a low level of colocalisation (20%) and non-colocalising puncta contribute significantly to short NN distances (below 190 nm): in S1, 29.3% of all NN distances fall below 190 nm. VLAD correctly assigns an average probability of true colocalisation (p_{True}) of 0.67 to all NN distances below 190 nm (only 67% of these distances correspond to true colocalisation), leading to a final colocalisation measurement of 19.8%. In contrast, S2 has high colocalisation (80%) and, as a result, 97% of all distances below 190 nm correspond to true colocalisation (average $p_{True} = 0.97$ below 190 nm). When S1 and S2 are pooled and analysed as a combined set, the average probability of true colocalisation for distances below 190 nm becomes 0.89 (average p_{True} of S1 and S2 weighted by the number of distances below 190 nm). While this accurately depicts the average p_{True} for the entire combined data set, it inevitably misrepresents p_{True} for the individual components. In general, although VLAD maintains its ability to accurately measure colocalisation in heterogeneous data sets, the accuracy of probabilities of true colocalisation assigned to individual puncta decreases with increasing heterogeneity. VLAD curve fitting, on the other hand, is more reliable when analysing more data points (i.e. pooled regions). It is worth noting that experimental data rarely exerts such extreme intra-regional variability (e.g. 20% colocalisation in one sub-region and 80% in another). Ultimately, the decision on whether to analyse small sets of data separately or to pool them should be guided by the desired data output on a case-by-case basis. It is also important to note that

low colocalisation data will always contain a higher proportion of statistically non-colocalising short NN distances, limiting the certainty with which individual puncta can be classified as colocalising or non-colocalising. 33% of NN distances below 190 nm correspond to false-positive colocalisation in 20% colocalisation data, compared to only 3% in 80% colocalisation data.

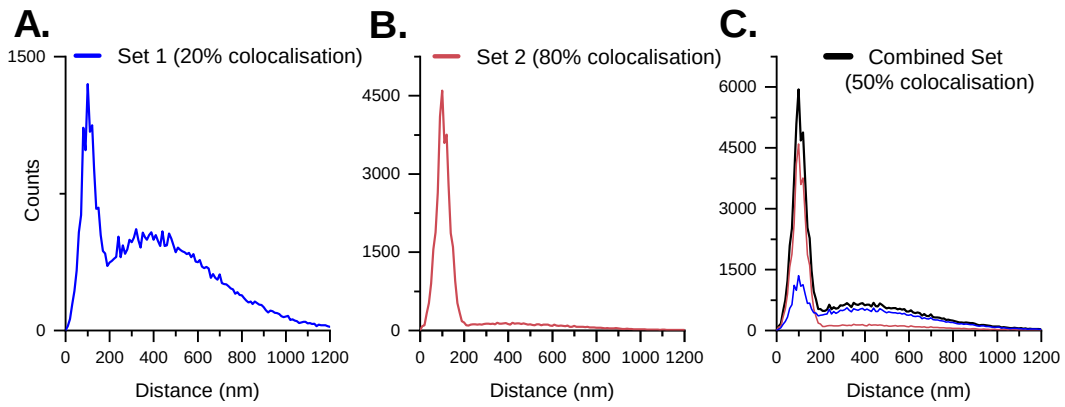

Figure 3-15. Nearest neighbour distance distributions in combined simulated data sets. A. Nearest neighbour (NN) distance distribution of Set 1: 37,000 µm² (20 tiles) of simulated data with 108 puncta/100 µm² and 20% colocalisation. **B.** NN distance distribution of Set 2: same total area and density as Set 1 and 80% colocalisation. **C.** NN distance distribution of combined sets 1 and 2: 74,000 µm² (40 tiles) with 108 puncta/100 µm² and 50% average colocalisation. Analysing pooled sets of data (Sets 1 and 2) is equivalent to adding their NN distance distributions together.

Data Set (Total Puncta)	$C_{Simulated}$	$C_{Measured}$	NN Distances <190 nm (% of Total)	p_{True} <190 nm	Colocalising NN Distances <190 nm (% of Total)
S_1 (20,000)	20%	19.8%	11,721 (29.3%)	0.67	7,910 (19.8%)
S_2 (20,000)	80%	79.3%	32,761 (81.9%)	0.97	31,719 (79.3%)
$S_{Combined}$ (40,000)	50%	49.5%	44,482 (55.6%)	0.89	39,640 (49.5%)

Table 3. VLAD colocalisation measurements in combined simulated data sets. Two sets of simulated data S_1 and S_2 with equal punctum density (108 puncta/100 µm²) and total area (37,000 µm² – 20 tiles) and different levels of colocalisation (20% and 80%, respectively) were analysed separately, then pooled and analysed as a combined set. For each set (S_1, S_2 and $S_{Combined}$), the simulated level of colocalisation ($C_{Simulated}$) and the following VLAD measurements are provided: measured colocalisation ($C_{Measured}$), nearest neighbour (NN) distances below 190 nm (number and % of all distances in each data set), average probability of true colocalisation (p_{True}) for NN distances below 190 nm and NN distances corresponding to true colocalisation below 190 nm (number and % of all distances in each data set – equal to $C_{Measured}$).

Next, the ability of VLAD to measure colocalisation at various peak colocalisation distances (PCDs) was tested in simulated data with 100 puncta/100 µm², 20% and 60% colocalisation and different PCDs, ranging from 55 to 210 nm. At each

simulated PCD, VLAD-measured colocalisation closely matched the simulated value (99% confidence interval between -3.5 and +1.4 percentage points), as shown in Figure 3-16. Precision declines with longer PCDs but allows sufficient reliability over the range of physiological colocalisation distances between postsynaptic proteins (95% of PCDs in experimental data were shorter than 100 nm).

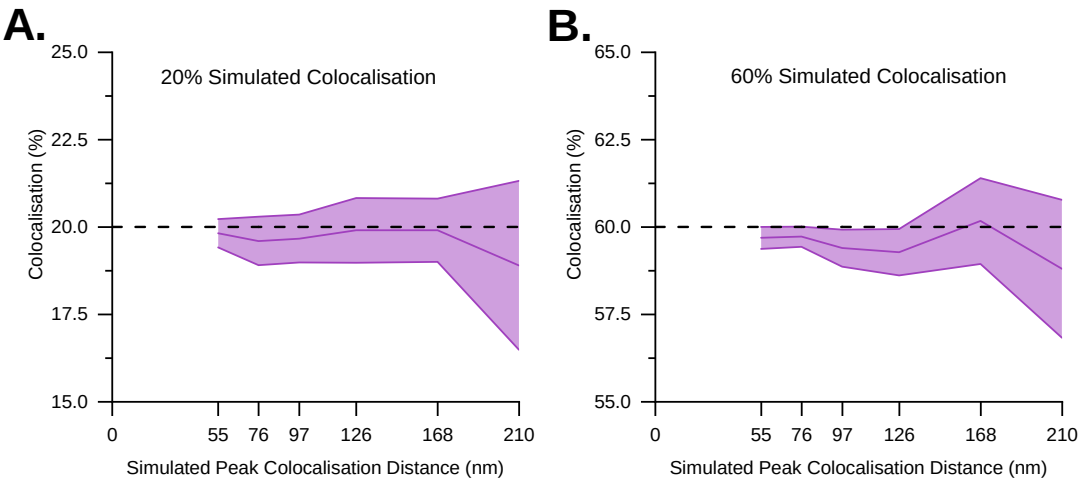

Figure 3-16. VLAD performance in simulated data at different peak colocalisation distances. VLAD-measured colocalisation in simulated data with 100 puncta/100 µm^2, colocalisation of 20% (**A**) or 60% (**B**) and various peak colocalisation distances (labels on x-axis). For each distance, colocalisation was measured in n=10 individual 1,850-µm^2 tiles and the average measured colocalisation ± 99% confidence interval (CI – equivalent to 1.03 standard deviations) was plotted. Within every group, colocalisation measurements were normally distributed ($p_{Shapiro\text{-}Wilk} > 0.05$). VLAD displays remarkable accuracy at multiple peak colocalisation distances, with the 99% CI contained within ±1.4 percentage points (%) of the simulated level between 55 and 168 nm peak colocalisation distance.

Lastly, the ability of VLAD to measure peak colocalisation distances (PCDs) and the full widths at half maximum (FWHMs) of normally distributed colocalising distances was tested on simulated data with 100 puncta/100 µm^2, 20% colocalisation and different PCDs, ranging from 55 to 210 nm. In all simulated data, the normally distributed colocalising distances spanned the range between zero and 2x PCD. This implies a fixed relationship between the PCD, SD and FWHM of the distribution of colocalising distances (PCD = 3*SD, FWHM = 2.35*SD, FWHM = 0.783*PCD). Figure 3-17 shows the errors of VLAD when measuring PCDs (A.) and FWHMs (B.). The 99% confidence intervals (CIs) of PCD measurements fell between -10 and +10 nm from actual simulated values but showed a systematic overestimation of PCDs between 55 and 126 nm and decreasing precision with longer PCDs. Below 100 nm, VLAD overestimates PCDs by 6 nm on average (+ 5-10% of actual value). FWHM measurements closely follow simulated values up to 99 nm but measurement precision quickly deteriorates with increasing FWHMs thereafter. This is, at least in part, due to the fact that, at longer PCDs, the distribution of colocalising distances

becomes less well separated from the distribution of NN distances corresponding to randomly distributed, non-colocalising pairs of puncta (see Figure 3-11 G. and H.).

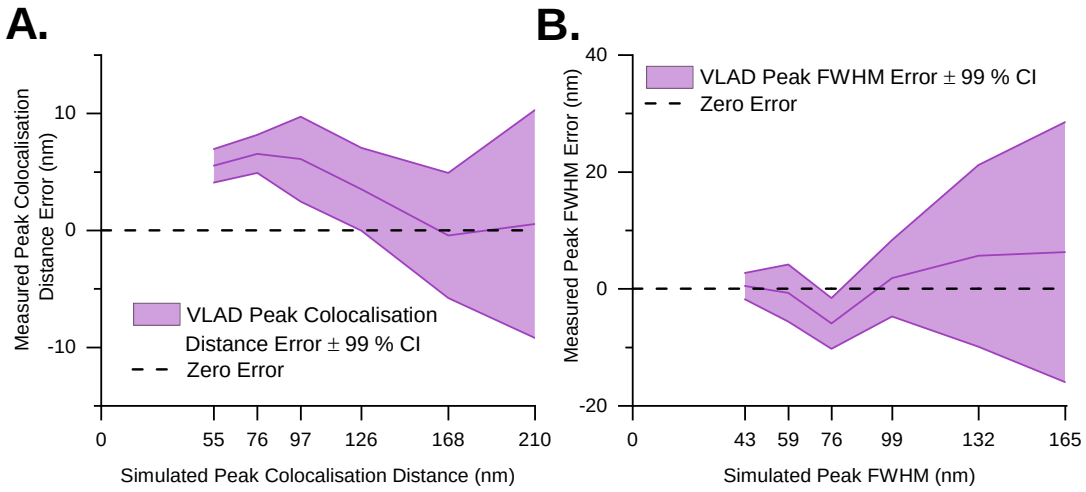

Figure 3-17. VLAD performance in colocalisation distance measurements. A. Error of VLAD peak colocalisation distance (PCD) measurements in simulated data with different PCDs. At each simulated PCD (labels on x-axis), the distance was measured in n=10 individual 1,850-µm^2 tiles with 100 puncta/100 µm^2 and 20% colocalisation. Average error (measurement–simulated value) ±99% confidence interval (CI – equivalent to 1.03 standard deviations) was plotted. At every PCD, VLAD measurements were normally distributed ($p_{Shapiro\text{-}Wilk} > 0.05$). **B.** Error of VLAD peak full width at half maximum (FWHM) measurements in simulated data with different peak FWHMs. Same simulated data and plot type as in A. In each set of simulated data, FWHM = 0.78 x PCD.

VLAD was confidently applied to experimental data after it proved its ability to accurately measure colocalisation in simulated data. While the performance of VLAD in experimental data is difficult to evaluate without knowing the ground truth, the model goodness-of-fit (Adjuster R-squared for VLAD curve fitting of NN distance distributions) can serve as a proxy for this. The distribution of Adjusted R-squared values from applying VLAD to 4,674 NN distance distributions (all experimental data analysed) is shown in Figure 3-18. Curve fitting was reliable in most experimental data, with Adjusted R-squared values above 0.7 in 98.6% of all cases. VLAD may be seen as an adjusted-threshold-based colocalisation analysis method. For simplicity, a universal threshold of 230 nm was used in all experimental data analysed. As a result, all VLAD-measured colocalisation values will occur between zero and the total portion of NN distances below 230 nm (uncorrected threshold-based colocalisation) in any given set of data, limiting the potential for significant errors, even in cases where curve fitting is sub-optimal.

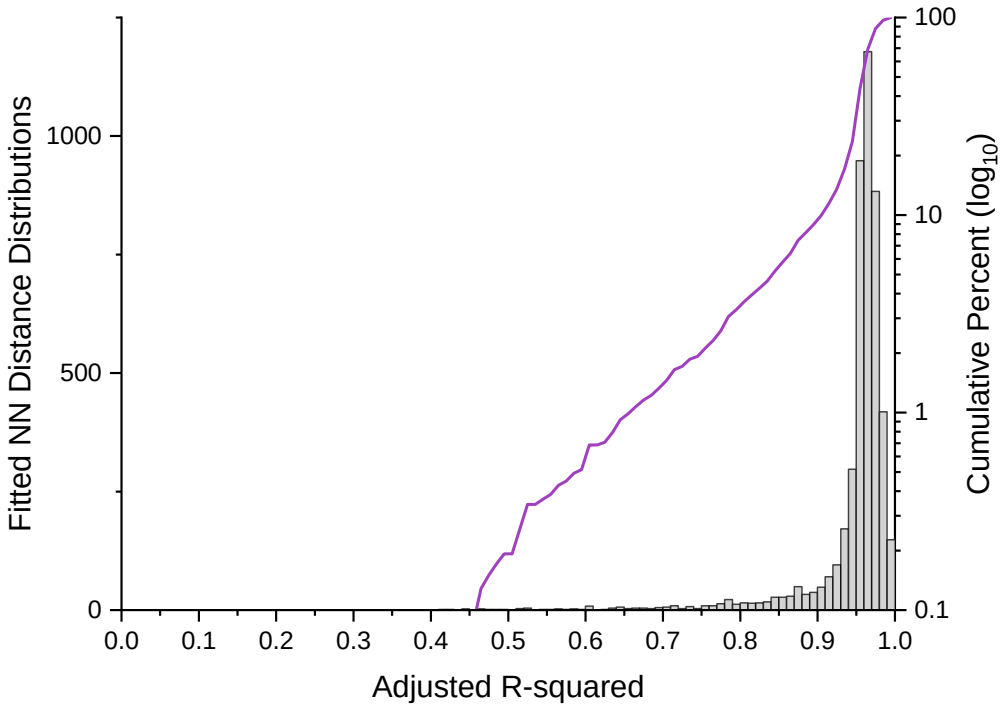

Figure 3-18. Quality of VLAD curve fitting in experimental data. Curve fitting of nearest neighbour (NN) distance distributions is central to the VLAD colocalisation analysis method. The Adjusted R-squared goodness-of-fit measures (albeit imperfect for non-linear curve fitting) from 4,674 NN distance distributions in experimental data analysed with VLAD are shown here as a histogram (left axis) and cumulative histogram (right axis, logarithmic scale). Smallest Adjusted R-squared value = 0.41, median = 0.96, 99% of values > 0.66 and 95% of values > 0.84.

In summary, VLAD was validated by testing on simulated data with pre-defined parameters (punctum density, colocalisation level and colocalisation distance). VLAD colocalisation measurements showed high accuracy and precision when tested on simulated data with over 170 distinct parameter combinations.

3.3.5 Comparison of VLAD and the state-of-the-art alternative SODA

After developing and validating the VLAD colocalisation analysis method, its performance was compared to that of SODA, the state-of-the-art colocalisation analysis method developed by Lagache et al. (Lagache *et al.*, 2018). In order to meaningfully compare the two methods, they were both tested on the same set of simulated data used in Figure 3-12 (punctum density of 100 puncta/100 µm2 and colocalisation levels ranging from 0% to 100%). Figure 3-19 shows the performance of the two methods in the same set of simulated data, with VLAD significantly outperforming SODA at colocalisation levels above 20%. Interestingly, SODA measurements increasingly underestimate true colocalisation with increasing

colocalisation levels, while VLAD measurements remain centred around simulated values across the entire range.

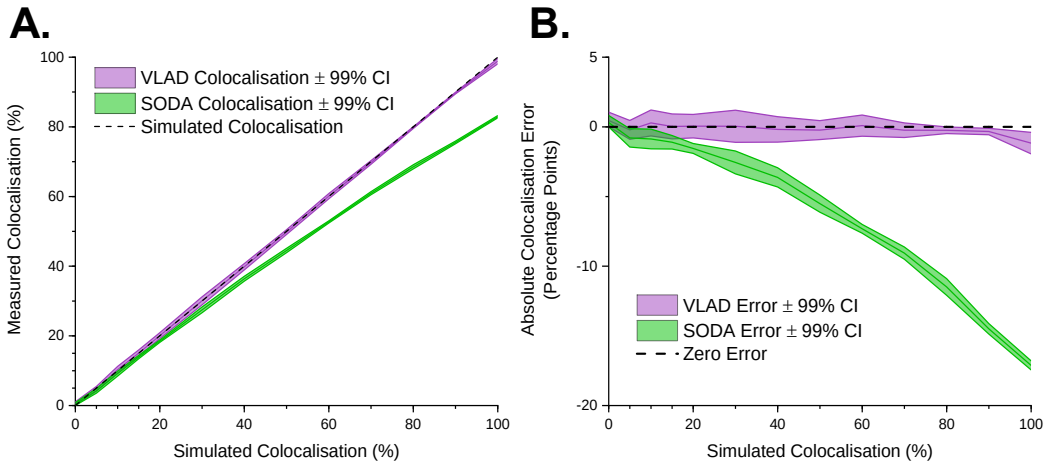

Figure 3-19. Comparative performance of VLAD and SODA in simulated data at 100 puncta/100 µm² and varying levels of colocalisation. A. Colocalisation measured by VLAD and SODA in simulated data with different levels of colocalisation. Colocalisation was varied from 0 to 20% in 5% steps and from 20 to 100% in 10% steps (ticks on x-axis; 13 conditions total; same data as in Figure 3-12). At every level, colocalisation was measured in n=10 individual 1,850-µm² tiles and the average measured colocalisation ±99% confidence interval (CI – equivalent to 1.03 standard deviations) was plotted. Within every group (except 0% colocalisation), measurements from each method were normally distributed ($p_{Shapiro\text{-}Wilk} > 0.05$). **B.** Error of VLAD and SODA colocalisation measurements in simulated data with different levels of colocalisation. From the data in A., the error was calculated as the difference between the measured value and the simulated one, and was plotted as average error ±99% CI. VLAD colocalisation measurements are within ±2 percentage points from the simulated values across all colocalisation levels. SODA measurements show comparable accuracy up to 20% colocalisation but increasingly underestimate true values with increasing colocalisation, with significant errors above 50% colocalisation.

VLAD and SODA measure colocalisation based on fundamentally different principles but share equivalent intermediate outputs. In a given data set, both methods identify potentially colocalised objects: NN distances (VLAD) and coupled objects (SODA). To these potentially colocalised objects, each method assigns a probability of true colocalisation to obtain the final measure of colocalisation: true colocalisation probability (VLAD) and coupling probability (SODA). For the previously mentioned set of simulated data, the intermediate outputs underlying the colocalisation measurements in Figure 3-19 were extracted and plotted for both methods in Figure 3-20. Although neither method requires the arbitrary choice of a distance threshold, 210 nm (VLAD – NN distance threshold; SODA – search radius) was chosen purely to illustrate a quantity of potentially colocalised objects. The probabilities measured by both methods refer to the average probabilities to be applied to all potentially colocalised objects (puncta) in a 210 nm radius from the reference set of puncta (with which colocalisation is measured). Both methods

assign probabilities to objects at different NN distances (SODA – search radii) in a threshold-independent manner.

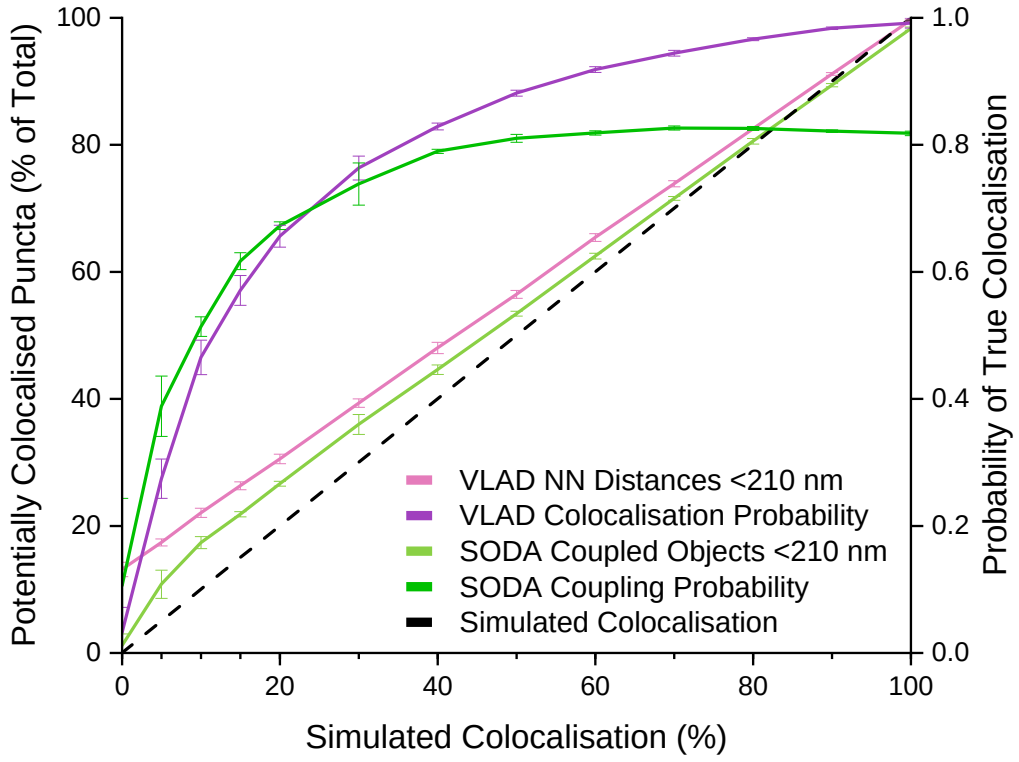

Figure 3-20 VLAD and SODA potentially colocalising puncta and probabilities of true colocalisation in simulated data at 100 puncta/100 µm² and varying levels of colocalisation. VLAD and SODA produce two comparable intermediate outputs: potentially colocalised objects (left axis, % of total objects in data set) and probability of true colocalisation (right axis). Neither method requires the arbitrary choice of a nearest neighbour (NN) distance threshold but a threshold of 210 nm was used here purely to illustrate potentially colocalised objects. For VLAD, these are NN Distances <210 nm and Colocalisation Probability. For SODA, these are Coupled Objects <210 nm and Coupling Probability. With each method, overall colocalisation is obtained by multiplying the number (% of Total) of potentially colocalised objects with the probability of true colocalisation. Simulated data colocalisation was varied from 0 to 20% in 5% steps and from 20 to 100% in 10% steps (ticks on x-axis; 13 conditions total; same data as in Figure 3-19). At every level, the percentage of potentially colocalising objects and the probability of true colocalisation was measured with each method in n=10 individual 1,850-µm² tiles. All measured values were plotted as averages ±standard deviation. Above 0% colocalisation, all VLAD measurements, 9/12 SODA Coupled Objects measurements and 11/12 SODA Coupling Probability measurements were normally distributed ($p_{Shapiro\text{-}Wilk}<0.05$). All groups passed the less stringent Kolmogorov-Smirnov test for normality.

Potentially colocalised objects always overestimate true colocalisation because they include varying degrees of false positives to be accounted for through the probability of true colocalisation. For VLAD, they are determined here by a simple 210 nm threshold. SODA identifies coupled objects differently but, above 10% colocalisation, they closely resemble the proportion of NN distances below a 170 nm threshold. Up to 20% colocalisation, VLAD identifies more potentially colocalised objects than SODA and this is offset by lower probabilities of true colocalisation, yielding similar overall results. Above 20%, SODA potentially colocalised objects and probability of

true colocalisation are both smaller than VLAD-determined values, leading to the overall underestimation of colocalisation. SODA coupled objects match actual simulated colocalisation better than VLAD NN distances but the method is let down by the coupling probability estimates which seem to plateau just above 0.8 for colocalisation levels above 50%, leading to significant underperformance in this range. This may be an undesirable result of the statistical threshold employed by SODA, which only takes punctum density into account based on the null hypothesis of spatial randomness, blind to the actual distribution of puncta in the analysed set of data.

In the original publication, SODA was shown to accurately measure all levels of colocalisation (from 0% to 100%) in simulated data with100 localisations per 256x256 pixel tile, agnostic of real pixel dimensions (400 localisations per 512x512 pixel tile, equivalent to 22 puncta/100 μm^2 for the pixel dimensions used here). This may be representative of synaptic punctum densities in neuronal cultures but not in densely packed dendritic areas in the brain. Another difference between the simulated data presented here and that of Lagache et al. is that, although colocalising (coupled) distances followed a normal distribution in both, in the SODA study, the colocalising distances were, in many cases, normally distributed between 2 and 4 pixels away from reference puncta (mean 3 pixels, standard deviation 0.3 pixels in most supplementary information simulated data). However, all observations in experimental data (here and in the SODA study) indicate that the distribution of colocalising distances always starts at zero and not at a non-zero minimum colocalisation distance limit. The simulated data presented here, where colocalising distances span the range from zero to 2x peak colocalisation distance, arguably approximate experimental data more closely. This difference in the generation of simulated data may, at least in part, account for the difference between the performance of SODA evaluated here and that reported in the SODA study.

A detailed comparison of VLAD and SODA was performed on a set of 10 1,850-μm^2 tiles with 100 puncta/100 μm^2 and 40% colocalisation, a setting where both methods yielded comparable results. Figure 3-21 shows that VLAD and SODA produced similar intermediate outputs and final results, with VLAD ultimately coming closer to the actual simulated colocalisation level. Above all else, VLAD and SODA validate each other through the similarity between the two methods' intermediate outputs (especially the distribution of the probability of true colocalisation) in a setting with comparable final outputs that closely match the simulated ground truth.

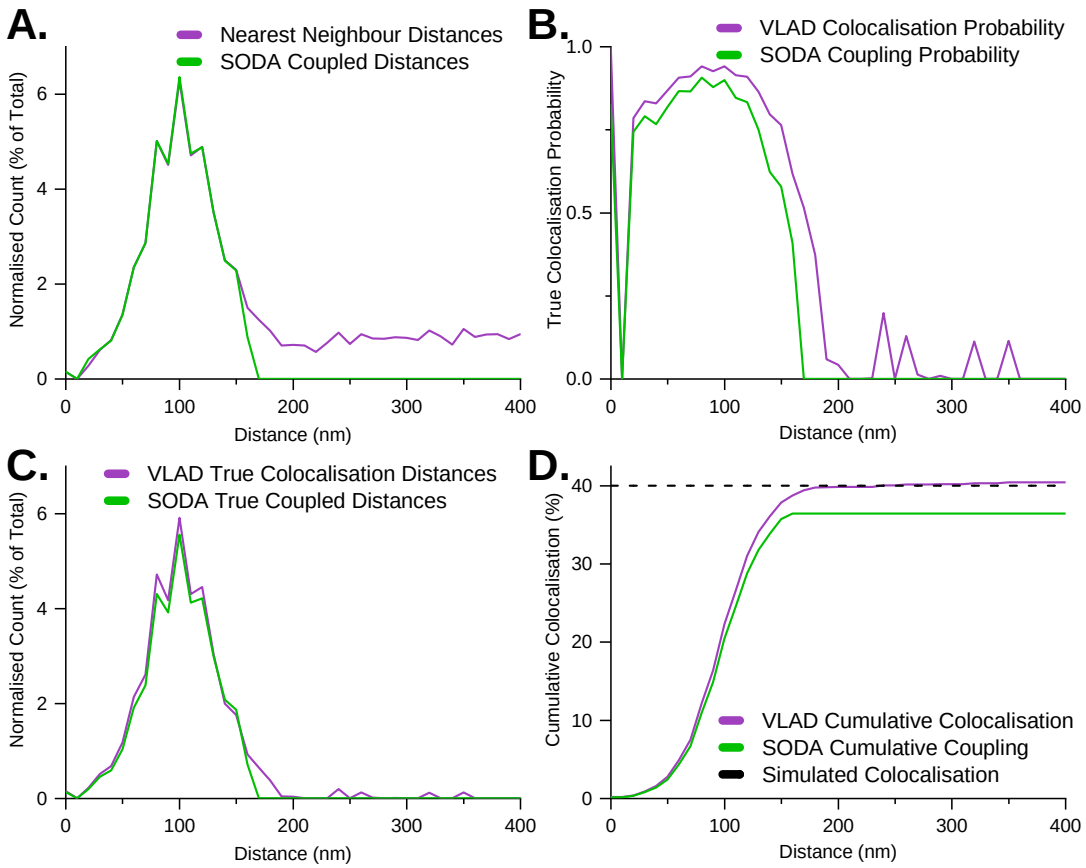

Figure 3-21. Comparison of the intermediate and final outputs of VLAD and SODA in simulated data at 100 puncta/100 µm² and 40% colocalisation. Both methods produced comparable results when analysing n=10 1,850-µm² tiles of simulated data. **A.** VLAD Nearest neighbour (NN) distances and SODA coupled distances. The values coincide almost perfectly up to 150 nm, with SODA values rapidly falling to zero beyond this distance. **B.** VLAD and SODA probabilities of true colocalisation (coupling) assigned to 10-nm distance intervals. Probabilities from both methods have a similar distribution between 0 and 200 nm, with SODA probabilities of true colocalisation being, on average, 10% smaller than VLAD probabilities. **C.** VLAD and SODA distribution of distances corresponding to true colocalisation (product of multiplying data in A and B). **D.** Cumulative distribution of data in C. Value at every point equivalent to measured colocalisation by each method up to that distance (VLAD distance threshold; SODA search radius). Colocalisation measured by both methods plateaus beyond 180 nm and is virtually threshold-insensitive between 200 and 400 nm. VLAD and SODA are based on fundamentally different principles but produce very similar intermediate and final outputs, with VLAD more closely matching the simulated colocalisation level.

VLAD was developed based on sound theoretical principles and numerous observations in vast amounts of experimental data, and was validated by extensive testing in simulated data, showing exceptional accuracy. Still, the reliance of VLAD on a model (curve fitting to NN distance distributions) may limit its use in cases that are poorly described by this model. A further compromise is required as curve fitting benefits from pooling sets of data at the expense of the accuracy of individual probabilities of true colocalisation.

SODA is more flexible than VLAD because it is model-free and its performance is not affected by the size of the set of data analysed. However, this flexibility comes at

the cost of decreased accuracy due to the over-conservative treatment of false positive colocalisation in form of a puncta-density-dependent but distribution-blind statistical threshold.

VLAD and SODA both have strengths and weaknesses but, based on testing in simulated data, VLAD outperforms SODA, especially in high colocalisation data. At the same time, the similarity between the intermediate outputs of these two radically different methods supports both of them.

3.4 Brief chapter summary and conclusions

The technical aspects of imaging the three fluorescently labelled proteins – GluN1, PSD95 and SAP102 – were addressed. The effects of signal bleed-through between channels and optical aberrations were sufficiently low in the imaging setup used, allowing the simultaneous imaging of the three proteins for the purpose of colocalisation measurements. Then, it was shown that the TrackMate puncta detector performed well in low signal-to-background settings, enabling its use on the experimental data presented here. The detector was trained using manually counted training data to enable optimal detection of synaptic protein puncta (maximising precision and recall).

The Vicinity-based Localisation Adjacency Determination (VLAD) object-based colocalisation analysis method was introduced, with a focus on accounting for false-positive colocalisation. This is an area where previous methods showed lacklustre performance, either by not appropriately discounting colocalisation arising due to chance, or by over-compensating for false positives and underestimating true colocalisation in high-colocalisation settings.

VLAD is based on observations in vast sets of experimental data suggesting that nearest neighbour (NN) distances between colocalising puncta are normally distributed, and on the assumption that the distribution of non-colocalising NN distances can be described by the theoretically-derived equation describing this distribution for randomly distributed (non-colocalising) puncta.

The outputs of VLAD answer the three basic colocalisation questions: what proportion of puncta from a group A colocalise with puncta from group B? what is the probability of true colocalisation for each punctum of group A? and what is the spatial relationship between A and B when they colocalise?

The high performance of VLAD was demonstrated by extensive testing in simulated data spanning a wide range of conditions (punctum densities, colocalisation levels and peak colocalisation distances) mimicking experimental data. VLAD compared favourably with the state-of-the-art SODA (Statistical Object Distance Analysis) colocalisation analysis method and a few considerations regarding the strengths and limitations of each method were made.

The accuracy of VLAD in determining true colocalisation without over- or under-compensating for colocalisation arising due to chance makes it an ideal tool for measuring colocalisation in the context of brain mapping.

4 Synaptic Diversity in the Developing Hippocampus

4.1 Brief introduction

In vertebrate excitatory synapses, the postsynaptic neuron contains a postsynaptic density (PSD) – a protein dense region attached to the postsynaptic membrane and apposed to the active zone of the presynaptic neuron. The PSD proteome contains more than 1,000 different proteins that are conserved across vertebrates (humans, mice, zebrafish) (Bayés *et al.*, 2012, 2017). Their importance is underscored by their involvement (when mutated) in over 130 neuropsychiatric disorders in humans (Bayés *et al.*, 2010; Kaizuka and Takumi, 2018).

The various PSD components, including neurotransmitter receptors, signalling proteins and cell adhesion molecules, are organised by scaffolding proteins (Won *et al.*, 2017). Postsynaptic Density 95 (PSD95 or DLG4) is one of the most abundant proteins of the PSD by copy number (Gold, 2012) and it is part of the Discs Large Homolog (DLG) family of membrane-associated guanylate kinases (MAGUKs). Two whole genome duplications early in the vertebrate lineage gave rise to four DLG paralogs (Ryan and Grant, 2009). The four paralogs share a common structure comprised of three PDZ (PSD95, DLG1 and zona occludens-1 protein) peptide binding domains, an SH3 (Src homology 3) protein-protein interaction domain and a catalytically inactive GK (guanylate kinase-like) domain (Kim and Sheng, 2004). In spite of their structural similarity, the four DLG paralogs evolved separate specialised functions, highlighted by the fact that, when mutated, they affect different behaviours. Even more notable is the fact that this specialisation seems to be conserved in mice and humans, indicated by the fact that loss of DLG2 (PSD93) leads to comparable cognitive phenotypes in both species (Nithianantharajah *et al.*, 2013). This resemblance supports the use of mice as model organisms in the study of DLG proteins.

PSD proteins can assemble in a combinatorial fashion and their differential expression at individual synapses gives rise to significant synaptic diversity (Grant, 2007; Emes *et al.*, 2008; O'Rourke *et al.*, 2012). Currently, no technique can identify the presence of hundreds of different proteins at individual synapses across the entire brain. Proteomic studies have identified separate protein complexes present at the PSD (Frank *et al.*, 2016) and differences in the PSD proteome between brain regions (Roy, Sorokina, McLean, *et al.*, 2018) but forewent the ability to characterise

individual synapses. Conjugate Light-Electron Array Tomography detects synapses with exquisite reliability and can identify 7 (potentially more) separate proteins at individual synapses (Collman *et al.*, 2015) but its low throughput limits its use to relatively small brain volumes. Recent efforts in synaptome mapping are an attempt to bring separate protein identification at individual synapses at the whole-brain scale by using fluorescently labelled synaptic proteins and high-throughput spinning disc confocal microscopy (Zhu *et al.*, 2018).The work in this thesis is a proof-of-concept extension of synaptome mapping to three proteins, with an emphasis on the accurate determination of their colocalisation in the hippocampus – a region of high synaptic density. The hippocampus has well-established roles in learning and memory and is one of the few brain regions where neurogenesis is continued in adulthood (Cameron and Glover, 2015).

The current study focusses on PSD95 (DLG4) and SAP102 (Synapse-Associated Protein 102, also known as DLG3) – two PSD scaffolding proteins essential for different aspects of cognition (Nithianantharajah and Grant, 2013) – and the N-Methyl-D-Aspartate (NMDA) receptor (NMDAR) subunit 1 (GluN1, also NR1 or GRIN1) – an obligatory subunit of all NMDARs, receptors with key roles in development and synaptic plasticity (Traynelis *et al.*, 2010). These three proteins play key roles at excitatory synapses and studying their colocalisation may reveal interesting aspects of their functional roles.

In this chapter, the novel object-based colocalisation analysis method VLAD (Vicinity-based Localisation Adjacency Determination, introduced in the previous chapter) is used to study PSD95, SAP102 and GluN1 in the mouse hippocampus in early development, from birth to postnatal day 94 (P94) at 7 different ages. Through different colocalisation combinations, the three proteins define 7 synaptic protein punctum or assembly subtypes. The densities (puncta per surface area) of these 7 subtypes were quantified across 13 hippocampal subregions and in parts of two adjacent brain regions (part of layer 6 of the motor cortex and part of the dorsal thalamus). The developmental trajectories of the 7 subtypes were described and the subregions were compared in terms of subtype composition and spatial relationships between the three proteins.

The 30 mouse brain sections in the developmental study in this chapter were provided by Dr Melissa Cizeron. The work presented in this chapter was done with technical assistance from Dr Zhen Qiu, who created the Batch Trackmate Detection

script, the Montage Stitching Script, the Nearest Neighbour Distance Measurement tool and the Nearest Neighbour Distance Distribution Mapping code. These can be found in the electronic appendix of the thesis.

4.2 PSD95, SAP102 and GluN1 define 7 synaptic punctum subtypes

PSD95, SAP102 and GluN1 (NMDARs) are all highly expressed in the mouse hippocampus. It is widely accepted that PSD95 is almost exclusively expressed at synapses and it is believed that punctate accumulations of SAP102 are located synaptically, with diffuse SAP102 expression present in dendrites (Kim and Sheng, 2004). NMDARs, on the other hand, are known to be present at extrasynaptic sites, as reviewed in (Papouin and Oliet, 2014). In cultured rat hippocampal neurons, extrasynaptic NMDARs may even associate with PSD95 and SAP102 (Petralia *et al.*, 2010). NMDARs were also found at presynaptic sites in young (P12) but not adult mice (in synaptosome preparations), suggesting that NMDARs are involved in synaptic development on both sides of the synaptic cleft (Gill *et al.*, 2015). Furthermore, NMDARs can form silent synapses (synapses lacking α-amino-3-hydroxy-5-methyl-4-isoxazolepropionic acid receptors – AMPARs) and it has been shown that PSD95 is required for the activity-dependent maturation (inclusion of AMPARs) of silent synapses during development (Huang *et al.*, 2015).

Taken together, these findings imply that a small fraction of detected SAP102 puncta and a potentially significant portion of GluN1 puncta may be non-synaptic. The gold standard for identifying whether a protein is part of a synapse is correlative fluorescence and electron microscopy (CFEM), where the signal from a fluorescently labelled protein is superimposed on electron micrographs, where pre- and postsynaptic membranes, PSD and neurotransmitter vesicles are readily identifiable (Schirra and Zhang, 2014). The labouriosness and low throughput of CFEM render it impractical for large-scale synaptome mapping. Analysing colocalisation with known immunolabelled presynaptic molecules could provide additional information on synaptic localisation. In the current study, immunostaining of vesicular glutamate transporter 1 (VGluT1), synaptophysin and synaptic vesicle protein 2 A (SV2A) – known presynaptic markers (Weingarten *et al.*, 2014) – was attempted with limited success. Colocalisation of PSD95 and SAP102 with either

presynaptic protein appeared almost indistinguishable from colocalisation with randomly distributed puncta (data not shown), rendering that analysis inconclusive. Elucidating the synaptic localisation of PSD95, SAP102 and GluN1 puncta was not the focus of this study. Still, all of the above considerations must be taken into account when interpreting the data presented in this chapter.

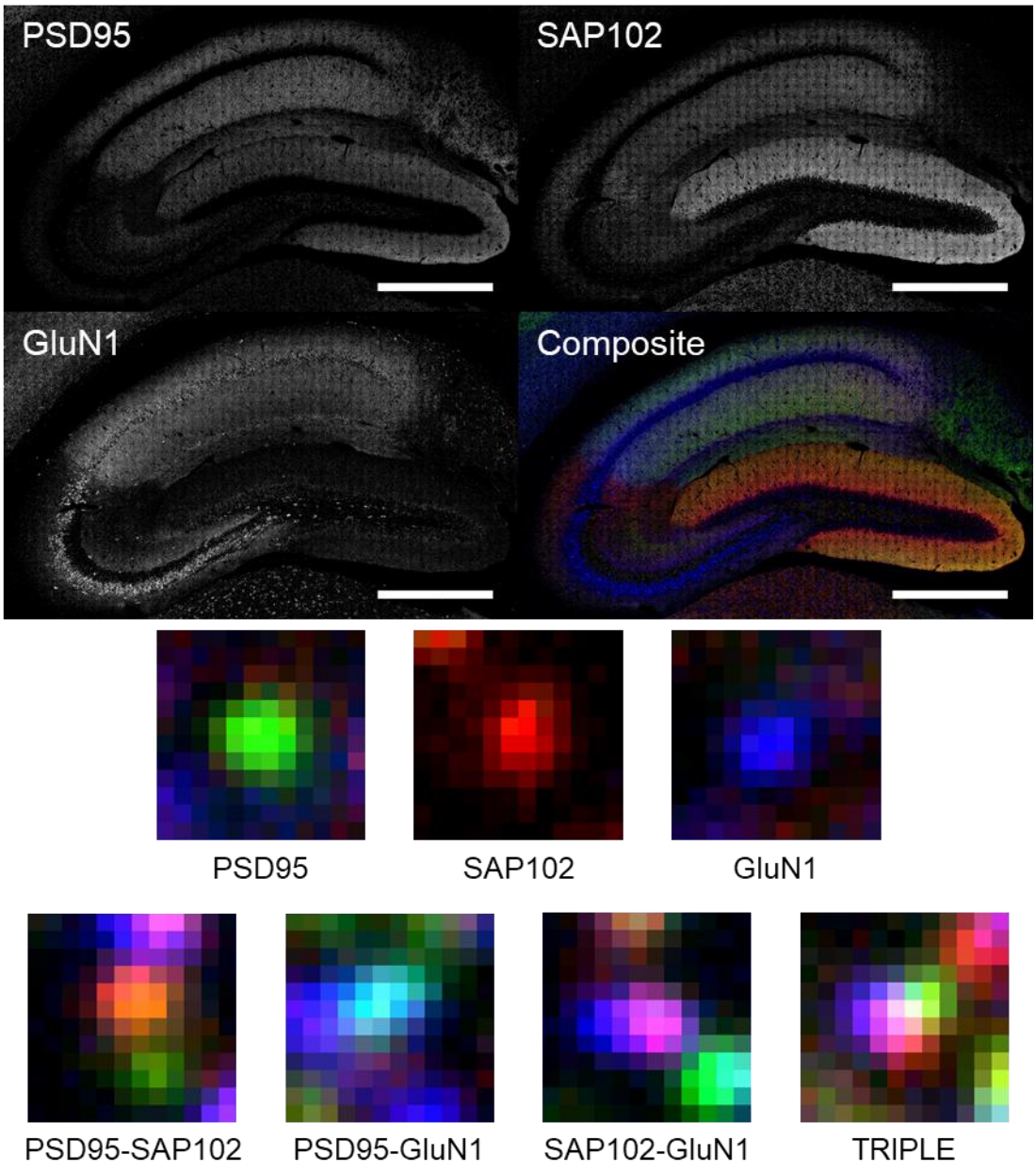

Figure 4-1. PSD95, SAP102 and GluN1 expression in the mouse hippocampus. Top: Sagittal section of the dorsal hippocampus of a P94 mouse, approximately 1.2 mm from the brain midline. Composite image lookup table colours (whole figure): PSD95 – green; SAP102 – red; GluN1 – blue. Scale bars: 500 µm.
Bottom: representative images of 7 synaptic punctum subtypes (in the centre of each square) – 3 individual, 3 pairs and 1 TRIPLE assembly. The sides of each square are 1 µm (12 84-nm pixels). Images are of raw data with enhanced contrast.

PSD95, SAP102 and GluN1 have distinct expression profiles in the hippocampus, as seen in Figure 4-1, but all three form detectable puncta. The puncta appear either individually (non-colocalised PSD95, SAP102 or GluN1), in pairs (3 possible pairs: PSD95-SAP102, PSD95-GluN1 or SAP102-GluN1) or in TRIPLE assemblies (all 3 puncta colocalised).

Examples of these 7 combinations (3 individual protein puncta and 4 colocalising assemblies) are shown in Figure 4-1. Going forward, these 7 combinations will be referred to as synaptic punctum subtypes, or punctum subtypes for brevity. Pairwise and TRIPLE assemblies will be counted as individual puncta of the colocalised type for consistency. For example, one PSD95-SAP102 punctum is composed of one PSD95 punctum and one SAP102 punctum, and will only be counted once.

Representative images of the whole hippocampus (as downsampled montages) and full resolution images of GluN1, PSD95 and SAP102 in the CA1rad, CA3rad, DGmo and DGpo across the 7 age groups analysed are included in the electronic appendix of this thesis, in the ‘Sample Images’ folder.

4.3 Synaptic punctum diversity in the hippocampus

4.3.1 Synaptic punctum subtype trajectories in the developing hippocampus

It is reasonable to assume that the 7 punctum subtypes defined by PSD95, SAP102 and GluN1 are functionally different, irrespective of whether they are part of a synapse or not. This prompted a detailed study into the distribution of these 7 subtypes across the mouse hippocampus in development. Puncta were detected and their colocalisation was quantified with the VLAD method detailed in the previous chapter. For the developmental study, the left dorsal hippocampus was imaged in sagittal sections, approximately 1.2 mm away from the midline in adults, and at equivalent positions in younger mice. In total, hippocampal sections from 30 male mice across 7 age groups were analysed. For each age group, the ages – in days – of individual mice are shown in brackets: P1 (5x1), P7 (4x7, 8), P15 (14, 2x15), P21 (4x21), P30 (4x30, 31), P61 (2x60, 61, 62) and P94 (4x94). In these mice, PSD95 was tagged with enhanced green fluorescent protein (eGFP – all heterozygous), SAP102 with monomeric Kusabira Orange 2 (mKO2 – all hemizygous; SAP102 gene is on the X chromosome) (Zhu *et al.*, 2018). The N-

terminal, extracellular terminus of the GluN1 subunit was fused to a tandem affinity purification tag (TAP-tag – all homozygous) (Frank *et al.*, 2016) that was subsequently immunolabelled with the highly specific FLAG antibody (Hopp *et al.*, 1988) and a far-red secondary antibody. The following hippocampal regions were analysed, delineated in accordance with the Allen Reference Atlas (Lein *et al.*, 2007): the dentate gyrus molecular layer (DGmo) and polymorphic layer (DGpo), within the Cornu Ammonis (CA) regions 1, 2 and 3, Stratum Oriens (CA1/2/3ori), Stratum Radiatum (CA1/2/3rad) and Stratum Lacunosum-Moleculare (CA1/2/3slm), the CA3 Stratum Lucidum (CA3slu) and the subiculum (SUB). Incomplete portions of the motor cortex layer 6 adjacent to the hippocampus (CTX) and the dorsal thalamus (TH) were also included for reference.

To verify that the left hemisphere is representative of the distribution of synaptic protein puncta, PSD95 punctum density in the hippocampus was compared between both brain hemispheres in a separate cohort of adult mice. Figure 4-2 shows PSD95 punctum density data across 12 hippocampal regions from both hemispheres in coronal brain sections (approximately Bregma -1.8 mm) from 5 adult mice (P113). Some variability exists between individual mice but no statistically significant differences were found between the two hemispheres in any of the 12 regions analysed here after the Wilcoxon signed-rank test and paired Student's t-test without correction for multiple comparisons at the 0.05 level. The same tests also showed no statistically significant differences between consecutive coronal sections (20 µm apart) in individual mice. Mean P113 PSD95 densities from the left hemisphere in coronal sections strongly correlate with those measured in the P94 group in sagittal sections (introduced later), with Pearson's correlation coefficient $R=0.972$.

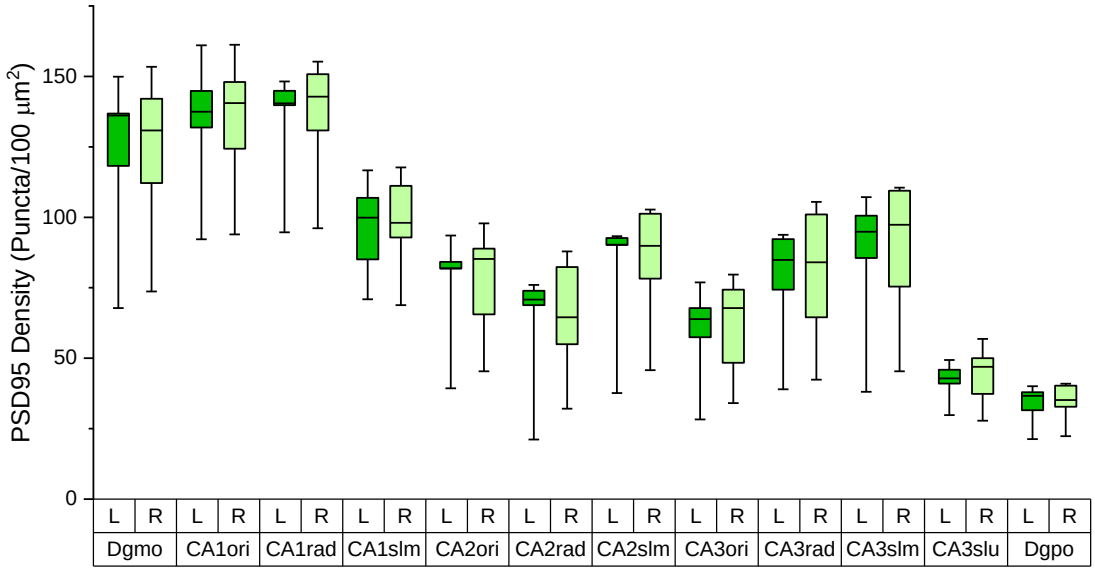

Figure 4-2. PSD95 punctum density in the left and right hippocampus in adult (P113) mice. Boxes represent median values and 25th–75th percentile range. Whiskers extend to minimum and maximum values, respectively. Data from all regions in coronal sections of N=5 adult mice. L – left hemisphere; R – right hemisphere. In all regions, the difference between the left and the right hemisphere is not statistically significant at the 0.05 level according to the Wilcoxon signed-rank test and paired Student's t-test without correction for multiple comparisons

Furthermore, PSD95 punctum density in the hippocampus appears unchanged in mice that underwent electric foot shock contextual fear conditioning 2 hours post-treatment, though subtle left-right asymmetries in PSD95 density may arise in the basomedial amygdala (data not shown). Overall, PSD95 density shows no notable left-right asymmetry and appears unaffected even by intense experiences such as contextual fear conditioning. Some studies report left-right asymmetries in dendritic spine morphology and synaptic glutamate receptor content – reviewed in (Shinohara, 2009) – but they are often based on the quantification of only a few hundred synapses (Shinohara *et al.*, 2008) and no such effects were recorded here on a whole-region level, where tens or hundreds of thousands of puncta are typically quantified in every region. While left-right asymmetry cannot be ruled out, the above findings suggest that synaptic punctum distributions in the hippocampus in one hemisphere are likely to be representative of both hemispheres.

The DGmo is the first part of the hippocampal trisynaptic circuit and receives excitatory inputs from the entorhinal cortex (EC) through perforant path axons. Its function is pattern separation (amplifying differences or reducing overlap between similar input patterns before generating an output), an essential part of memory formation (Yassa and Stark, 2011; Neunuebel and Knierim, 2014). Figure 4-3 shows the developmental trajectories of PSD95-, SAP102- and GluN1-containing puncta in

the DGmo. For each protein, the puncta densities (left side, in puncta/100 µm^2) and proportions (right side, in %) of all puncta (for the same protein) are shown. For the same protein, the subtypes are non-overlapping (e.g. a detected PSD95 fluorescent spot can only be part of one subtype, colocalising or not) and the total height of the stacked columns indicates the density of all puncta for a given protein. In all upcoming graphs of this type, the Y-axis scales for all puncta densities will be equal within the same graph to facilitate a direct comparison between puncta densities (expression levels) of the three different proteins at every age.

In the DGmo, PSD95-containing puncta are almost entirely absent at P1 and among the few PSD95-containing puncta present at P7, 83% are colocalised with SAP102 (50% PSD95-SAP102 and 33% TRIPLE). PSD95 density manifests the fastest growth from P7 to P15 and reaches adult-like levels by P21. Interestingly, virtually all PSD95 puncta colocalised with GluN1 are part of TRIPLE puncta, and the PSD95-GluN1 subtype makes up less than 2% of all PSD95-containing puncta at all ages. From P21 onwards, densities of colocalised PSD95 puncta (PSD95-SAP102 and TRIPLE) stay constant, while the density and overall proportion of non-colocalising PSD95 steadily increase, contributing to the overall growth of PSD95-containing puncta density into adulthood.

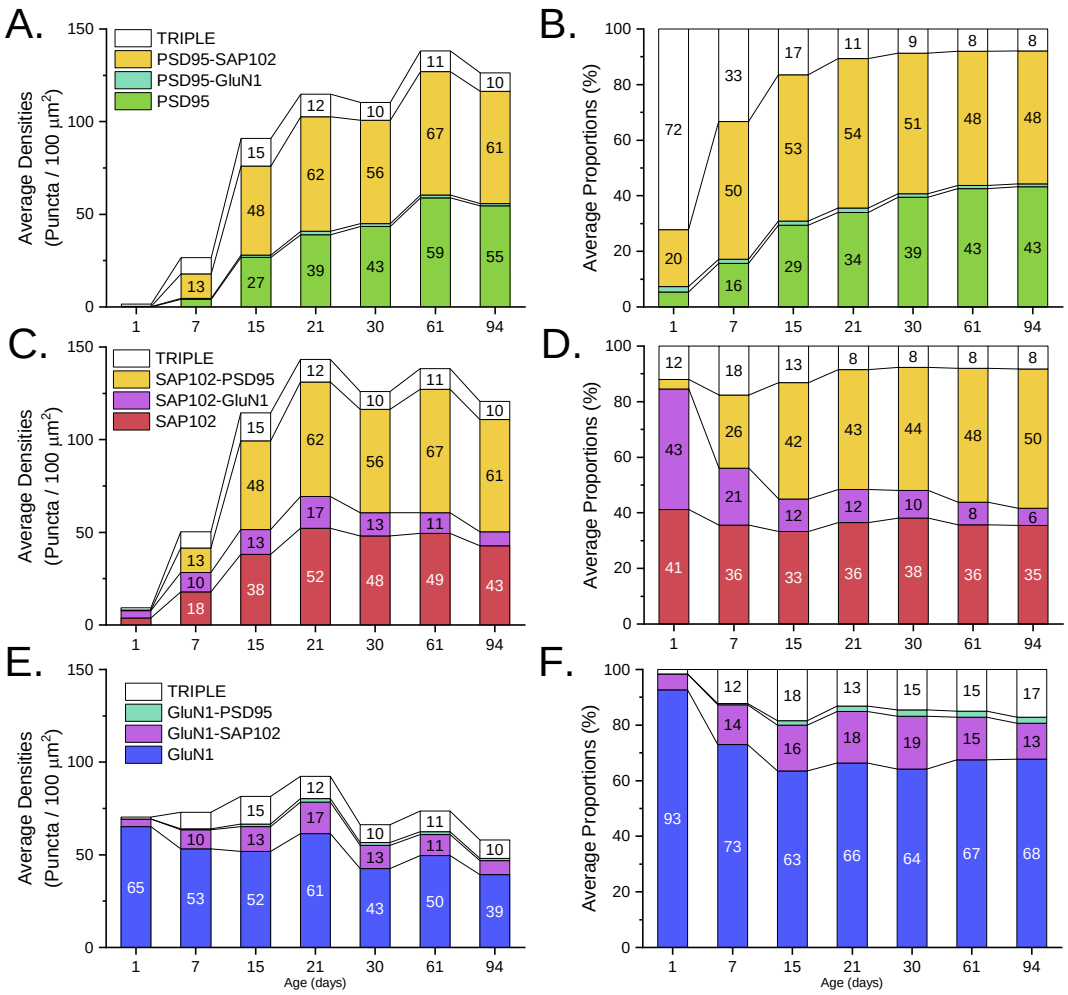

Figure 4-3. Developmental trajectories of PSD95, SAP102 and GluN1 in the dentate gyrus molecular layer (DGmo). A and B. Average PSD95-containing synaptic punctum densities (A) and proportions (B).
C and D. Average SAP102-containing synaptic punctum densities (C) and proportions (D).
E and F. Average GluN1-containing synaptic punctum densities (E) and proportions (F).

The highest SAP102 expression levels (in terms of SAP102-containing puncta density) occur in the DGmo at all ages. The density of SAP102-containing puncta at P1, although small (9/100 µm^2), is over 4 times higher than that of PSD95-containing puncta. Similar to PSD95, SAP102 expression rapidly increases from P1 to P15, reaching adult-like levels by P21. SAP102-containing puncta outnumber PSD95-containing puncta from P1 to P61, but they show a slow decline after peaking at P21, and become fewer than PSD95-containing puncta at P94. The proportion of non-colocalising SAP102 puncta appears constant from P1 to P94, at approximately 36% on average. The DGmo contains the highest densities of non-colocalised SAP102 puncta among all regions analysed and at all ages. 55% of SAP102-containing puncta colocalise with GluN1 at P1 and this proportion drops below 25% from P15 onward, as more SAP102-PSD95 puncta emerge. While total

SAP102 density slowly declines after P21, SAP102 subtype proportions are maintained almost constant, with a slight decline of the SAP102-GluN1 subtype in favour of SAP102-PSD95.

Unlike PSD95 and SAP102, high numbers of GluN1-containing puncta are present in the DGmo at P1 (70/100 μm^2), mostly of the non-colocalising GluN1 subtype, since few colocalisation partners are available. GluN1-containing puncta gradually increase in number up to P21 and gradually decrease thereafter. At P94, there are fewer GluN1-containing puncta than at P1. GluN1 colocalises with PSD95 almost exclusively in the presence of SAP102, forming TRIPLE puncta. Remarkably, GluN1-containing puncta proportions show little change after P7 and the vast majority of GluN1 puncta are not colocalised with PSD95 or with SAP102.

A comprehensive overview of all 7 punctum subtypes in the DGmo is shown in Figure 4-4. In all upcoming figures of this type, panel A contains a stacked column chart with the densities of all 7 subtypes in a region (in puncta/100 μm^2) and panel B shows the subtype proportions, this time of the total number of puncta (from all 7 subtypes) in the region. The total height of the stacked columns in panel A represents the overall density of distinct puncta or assemblies. For example, if a 100 μm^2 area contained one TRIPLE punctum, TRIPLE density would be reported as 1/100 μm^2 even though a TRIPLE punctum is an assembly of all three proteins. Panels C through I show the developmental trajectories of the densities of each subtype, plotted as averages and individual data points due to the small sample sizes within each age group (3 to 5 mice per group). Unlike in the column charts, the X-axis (mouse age) is linear in these panels, providing a clearer representation of the rate of change of subtype densities between time points. Panel J shows the total numbers of distinct puncta quantified for every age group (puncta density x region surface area), displaying the often vast numbers of synaptic puncta on which subtype density measurements are based.

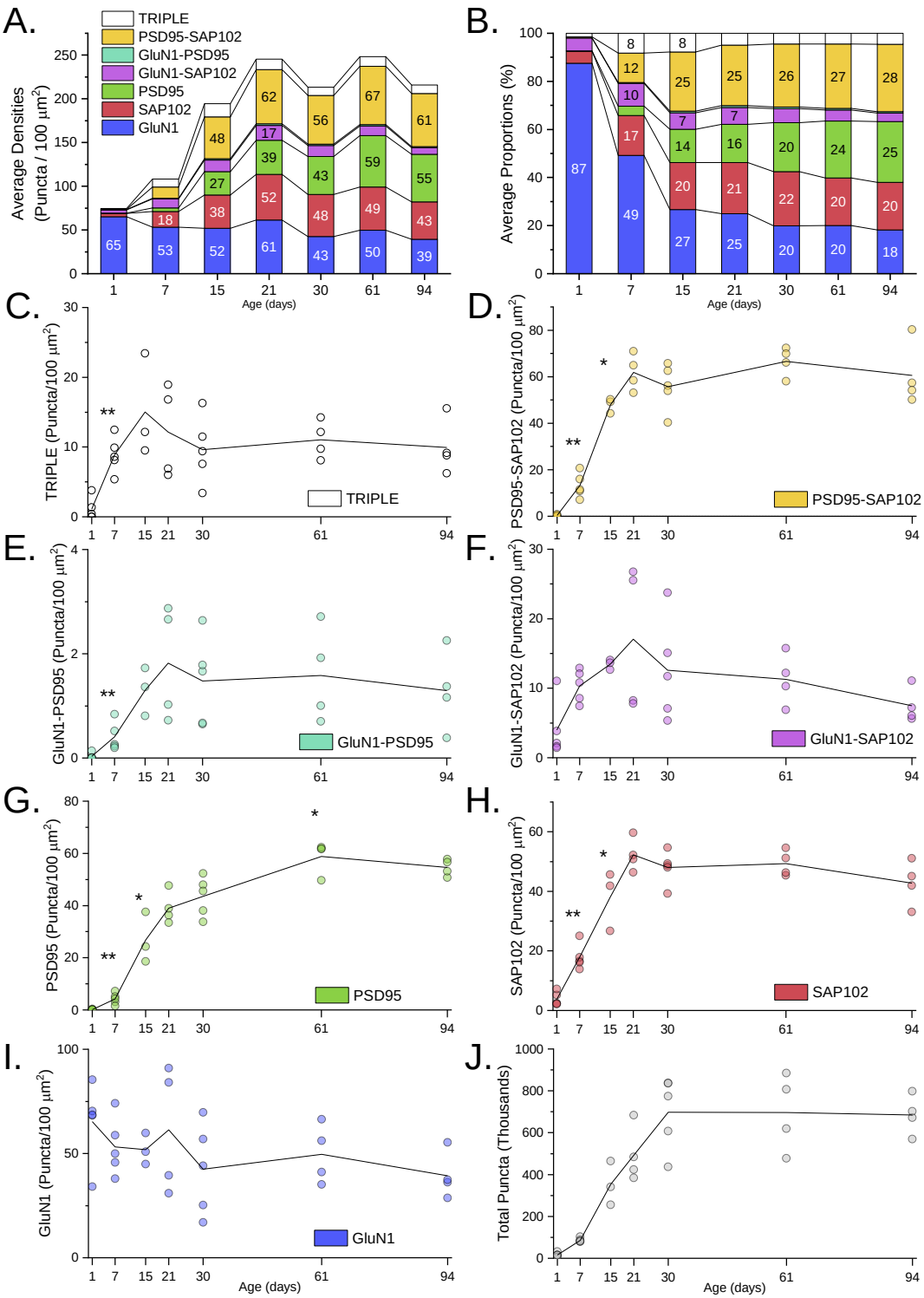

Figure 4-4. Developmental trajectories of 7 synaptic punctum subtypes in the dentate gyrus molecular layer (DGmo). A and B. Average subtype densities (A) and proportions of all puncta (B). **C to I.** Developmental trajectories of individual subtype densities (circles – subtype density measurements in individual mice; black lines – average values). Y-axis scales vary. For each subtype, asterisks indicate p-values of the Mann-Whitney test comparing its density at one age with that at the preceding age (* $p<0.05$, ** $p<0.01$). **J.** Total number of synaptic puncta (density x region surface area) analysed at every age (circles – total puncta numbers in individual mice; black line – average). In total, across all ages, 12.6 M distinct synaptic protein puncta were analysed in the DGmo.

Average overall synaptic punctum density in the DGmo increases more than 3-fold from P1 to P21. From P1 to P7, subtype composition shifts from predominantly GluN1 to a mixture, primarily made up of GluN1 and SAP102-containing puncta. By P15, following a marked increase in PSD95 expression, the DGmo reaches an adult-like subtype composition that is broadly maintained into adulthood. Overall synaptic punctum density initially peaks at P21 and fluctuates between 248/100 μm^2 and 213/100 μm^2 thereafter. From P15 onward, the DGmo contains the second highest (after the CA1rad) total density of synaptic protein puncta of all regions analysed. After P15, there is a gradual shift from colocalising subtypes to non-colocalised synaptic protein puncta, driven almost entirely by increasing proportions of the PSD95 subtype. The majority of colocalising puncta after P15 are of the PSD95-SAP102 subtype.

The CA3 field is the second part of the hippocampal circuit, receiving its primary excitatory input from mossy fibres originating in the dentate gyrus (DG). It also receives direct input from layer 2 of the EC via the perforant path and from CA3 recurrent collaterals (Yassa and Stark, 2011). In contrast to the DGmo, the CA3 performs pattern completion (retrieving stored output patterns when only partial inputs are provided), a crucial step in memory recall (Neunuebel and Knierim, 2014).

Figure 4-5 shows the developmental trajectories of PSD95-, SAP102- and GluN1-containing puncta in the CA3 Stratum Radiatum (CA3rad). In similar fashion to the DGmo, PSD95-containing puncta are almost entirely absent at P1 and low in number at P7. They manifest a rapid increase from P7 to P15 but, unlike in the DGmo, PSD95-containing punctum density in the CA3rad remains almost constant from P15 until P94. Subtype proportions do resemble the DGmo more closely – the proportions at P15 are broadly maintained at later ages, with a gradual increase in PSD95 puncta, a reduction in TRIPLE puncta and negligible amounts of PSD95-GluN1 puncta. From P15 to P94, overall PSD95-containing punctum density in the CA3rad is lower than in the DGmo (average 82/100 μm^2 compared to 115/100 μm^2 in the DGmo) and shows little change over that period.

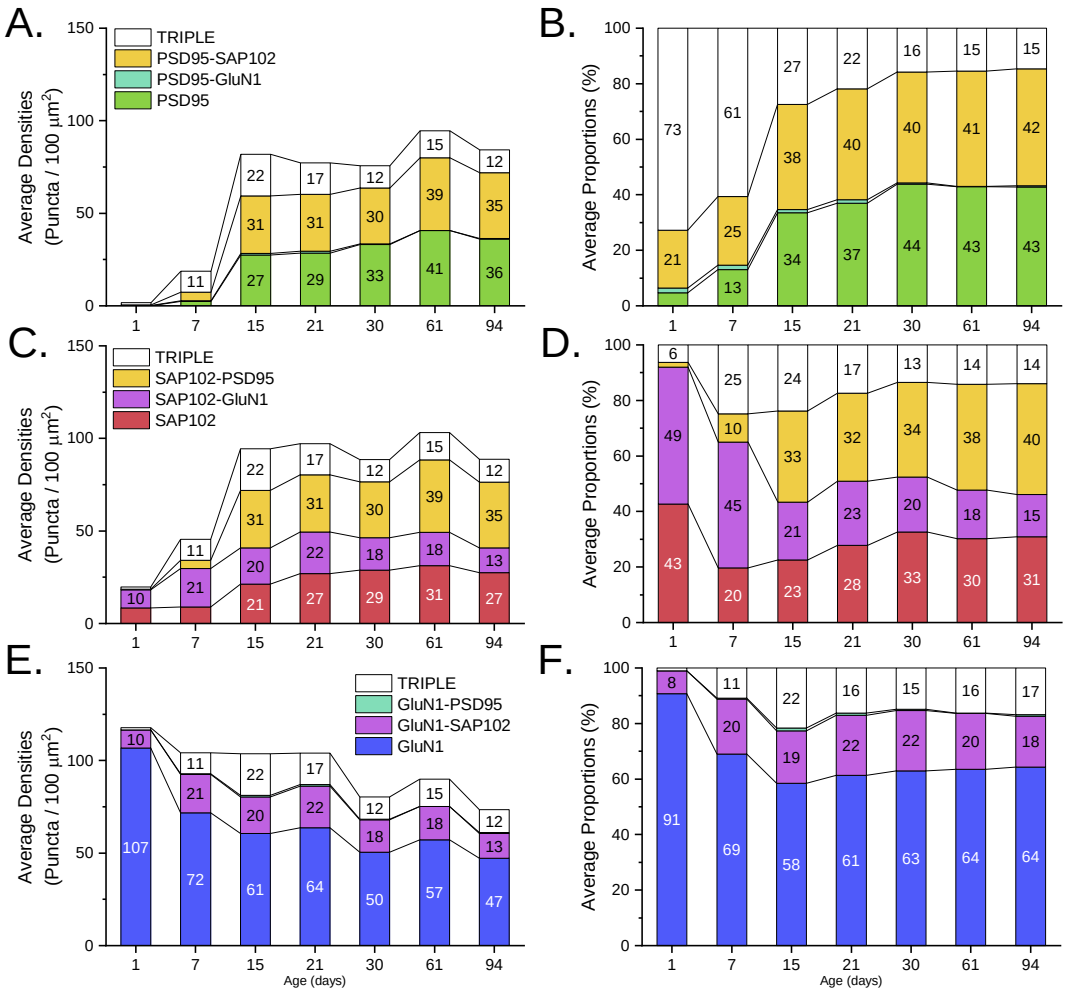

Figure 4-5. Developmental trajectories of PSD95, SAP102 and GluN1 in the CA3 Stratum Radiatum (CA3rad). A and B. Average PSD95-containing synaptic punctum densities (A) and proportions (B).
C and D. Average SAP102-containing synaptic punctum densities (C) and proportions (D).
E and F. Average GluN1-containing synaptic punctum densities (E) and proportions (F).

SAP102-containing puncta are more numerous than PSD95-containing puncta at P1 and P7 in the CA3rad. Their density also grows most rapidly from P7 to P15, showing little change beyond that age. As PSD95 expression increases from P1 to P15, so do the proportions of TRIPLE and SAP102-PSD95 puncta. SAP102-containing punctum subtype proportions are maintained from P15 onward, with a slight expansion of SAP102-PSD95 and a slight reduction of TRIPLE and SAP102-GluN1 puncta.

GluN1-containing puncta are abundant in the CA3rad at P1 (118/100 µm^2) and decrease in number in two successive steps, first from P1 to P7 and second from P21 to P30. GluN1-containing punctum subtype proportions in the CA3rad closely follow those in the DGmo despite the different trend in overall GluN1-containing punctum density.

Figure 4-6 shows the comprehensive overview of all 7 subtypes in the developing CA3rad. Similar to the DGmo, the CA3rad undergoes the most significant changes from P1 to P15, when a marked increase in PSD95 and SAP102 coupled with a slight decrease in GluN1 gives rise to a subtype composition at P15 that is broadly maintained into adulthood. After P15, the CA3rad expresses fewer PSD95- and SAP102-containing puncta and more GluN1-containing puncta than the DGmo, and the 7 different subtypes are more evenly represented (apart from GluN1-PSD95, which is practically absent from both regions). Colocalising subtypes, the majority of which are PSD95-SAP102 puncta, make up just over a third of all puncta, and non-colocalising GluN1 puncta take up almost one third as well.

The pyramidal neurons of the CA1 field are the final component of the hippocampal trisynaptic circuit, receiving their main input from the Schaffer collaterals originating in the CA3. Through the fornix, the output of CA1 pyramidal neurons is projected to the deeper layers of the EC (layer 5). The CA1 is neither pattern separating (like the DGmo) nor pattern completing (like the CA3), instead performing linear transformations of activity patterns (Yassa and Stark, 2011).

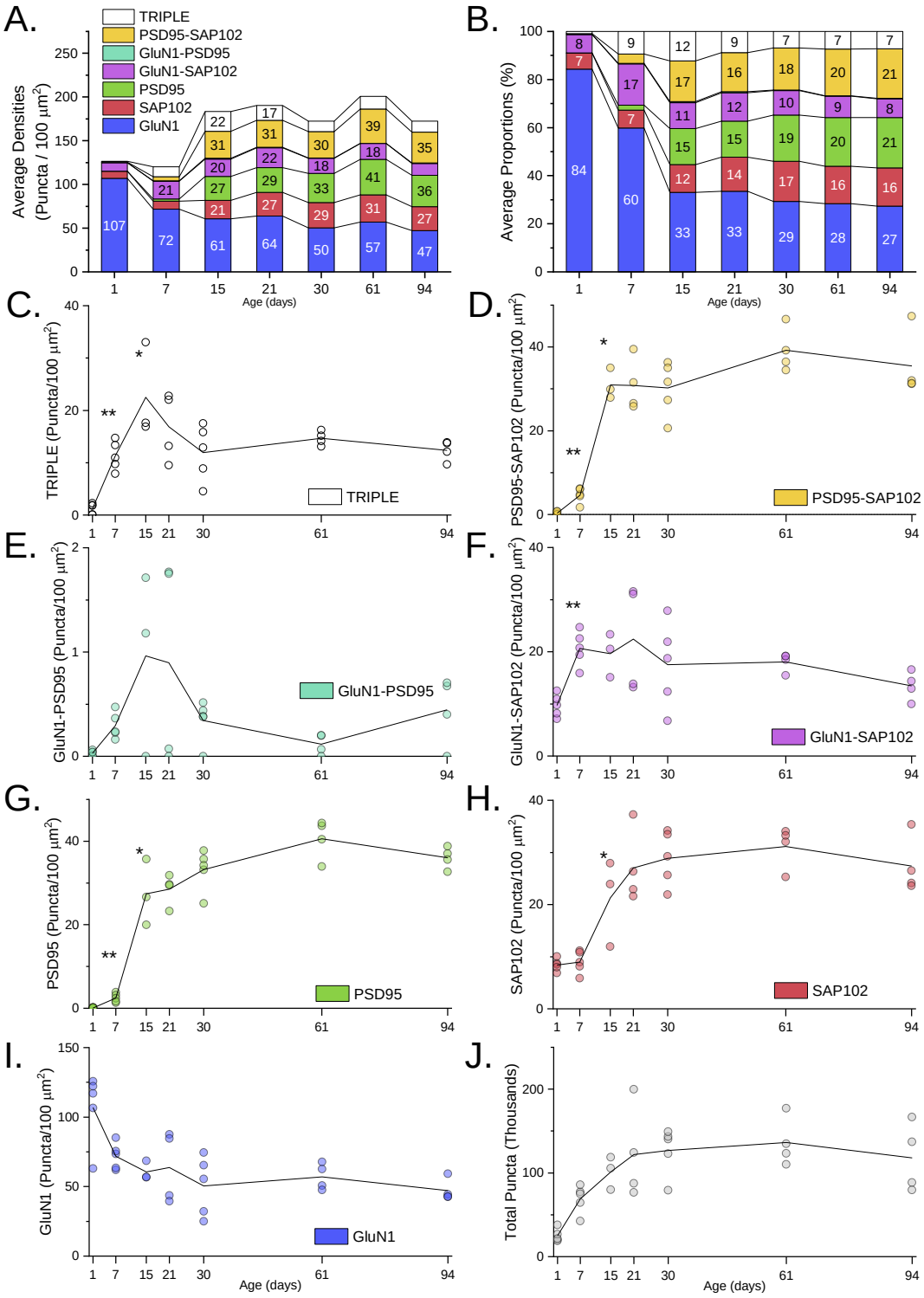

Figure 4-6. Developmental trajectories of 7 synaptic punctum subtypes in the CA3 Stratum Radiatum (CA3rad). A and B. Average subtype densities (A) and proportions of all puncta (B). **C to I.** Developmental trajectories of individual subtype densities (circles – subtype density measurements in individual mice; black lines – average values). Y-axis scales vary. For each subtype, asterisks indicate p-values of the Mann-Whitney test comparing its density at one age with that at the preceding age (* p<0.05, ** p<0.01). **J.** Total number of synaptic puncta (density x region surface area) analysed at every age (circles – total puncta numbers in individual mice; black line – average). In total, across all ages, 2.9 M distinct synaptic protein puncta were analysed in the CA3rad.

Figure 4-7 shows the developmental trajectories of PSD95-, SAP102- and GluN1-containing puncta in the CA1 Stratum Radiatum (CA1rad). Both PSD95 and GluN1 are most highly expressed in the CA1rad (among all regions analysed). Just like in the DGmo and CA3rad, PSD95 expression in the CA1rad ramps up from P7 to P15. From P15 to P94 (apart from a peak at P61), non-colocalising PSD95 density increases, PSD95-SAP102 density is mostly maintained, while TRIPLE density gradually decreases. Even though both PSD95 and GluN1 are most highly expressed in the CA1rad, the PSD95-GluN1 subtype makes up less than 3% of all PSD95-containing puncta at all ages. The CA1rad contains the highest density of TRIPLE puncta of all analysed regions.

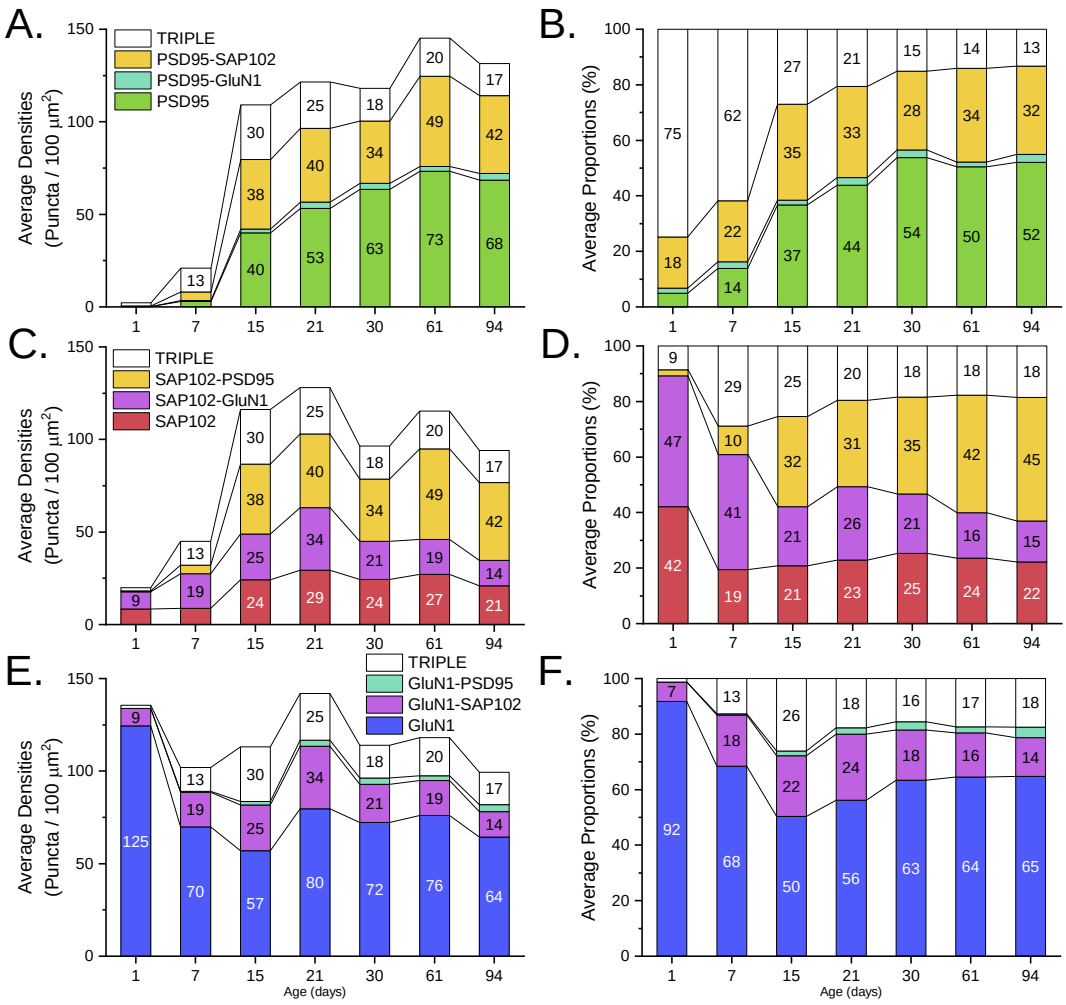

Figure 4-7. Developmental trajectories of PSD95, SAP102 and GluN1 in the CA1 Stratum Radiatum (CA1rad). A and B. Average PSD95-containing synaptic punctum densities (A) and proportions (B).
C and D. Average SAP102-containing synaptic punctum densities (C) and proportions (D).
E and F. Average GluN1-containing synaptic punctum densities (E) and proportions (F).

SAP102-containing puncta densities in the CA1rad show the fastest growth from P7 to P15 (just as in the DGmo and CA3rad) and peak at P21. Unlike in the DGmo and the CA3rad, where SAP102-containing puncta densities fluctuate around the P21 peak, they decrease in the CA1rad towards adulthood. Trends in SAP102-containing puncta proportions are broadly similar to those in the CA3rad.

The CA1rad contains a high density of GluN1-containing puncta at P1 (135/100 μm^2) that dips at P7 and P15, then peaks at a maximum of 141/100 μm^2 at P21 before starting a gradual decrease towards adulthood. At P15, 50% of all GluN1-containing puncta are colocalised, the highest proportion among all analysed regions across all ages (the other CA1 subfields show a similar trend). The high degree of GluN1 colocalisation occurs at the end of P7-P15 period of accelerated growth of PSD95 and SAP102 expression, but reverts to under 37% after P30.

Figure 4-8 provides an overview of the developmental trajectories of all 7 subtypes in the CA1rad. From P15 onward, the CA1rad contains the highest total density of synaptic protein puncta of all regions analysed. The trajectory of overall synaptic punctum density in the CA1rad is similar to that in the DGmo and the CA3rad: total density initially peaks at P21, dips at P30 and reaches its maximum value at P61 before dropping again at P94. In the adult CA1rad (from P30 onward), about one third of all puncta are colocalising subtypes, predominantly PSD95-SAP102. Lone PSD95 and GluN1 make up almost one third each, and less than 11% of all puncta are lone SAP102 puncta across all ages. In similar fashion to the other regions, subtype proportions are mostly unchanged between P15 and P94, with most significant changes occurring in the first 15 postnatal days.

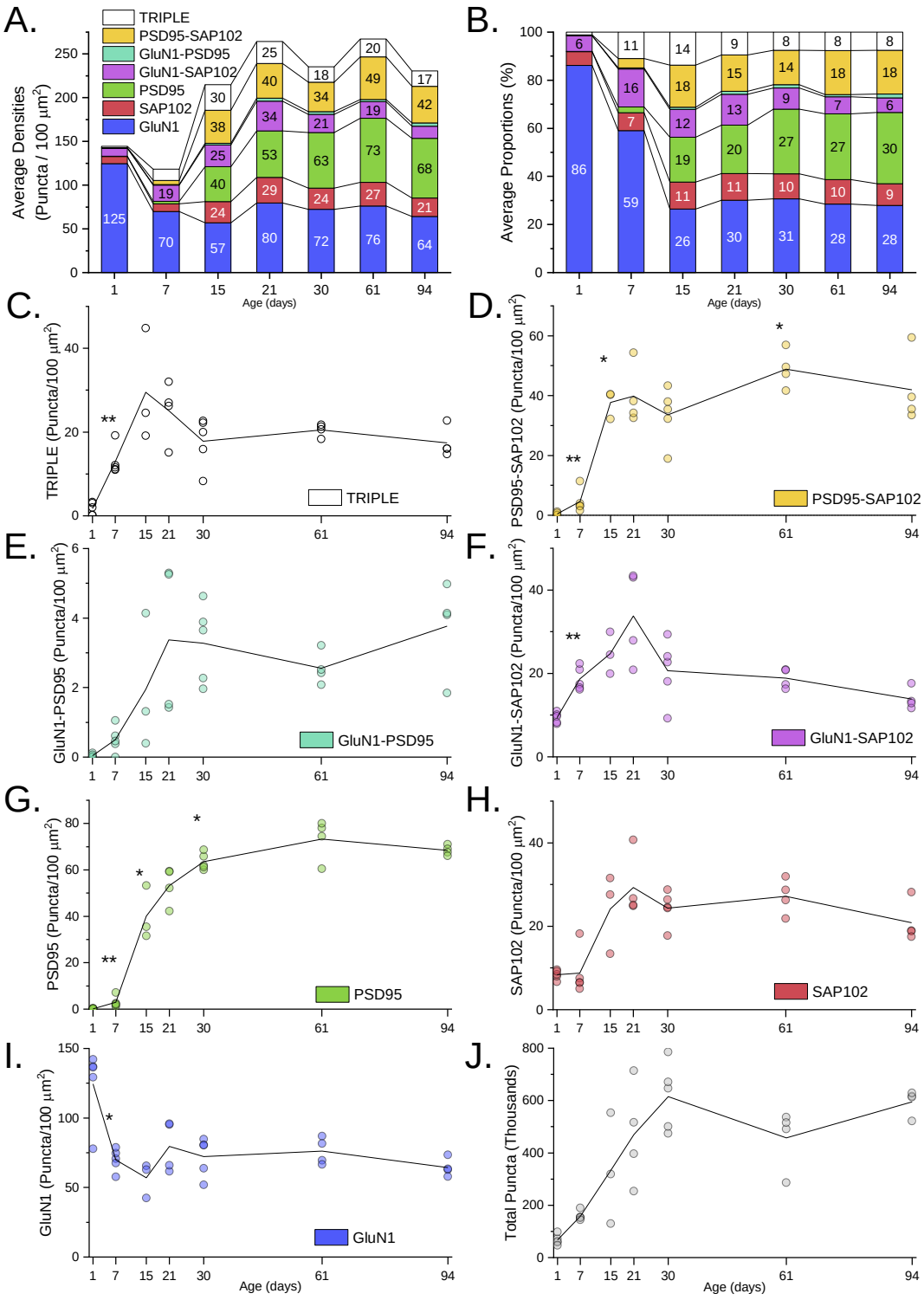

Figure 4-8. Developmental trajectories of 7 synaptic punctum subtypes in the CA1 Stratum Radiatum (CA1rad). A and B. Average subtype densities (A) and proportions of all puncta (B). **C to I.** Developmental trajectories of individual subtype densities (circles – subtype density measurements in individual mice; black lines – average values). Y-axis scales vary. For each subtype, asterisks indicate p-values of the Mann-Whitney test comparing its density at one age with that at the preceding age (* p<0.05, ** p<0.01). **J.** Total number of synaptic puncta (density x region surface area) analysed at every age (circles – total puncta numbers in individual mice; black line – average). In total, across all ages, 11.3 M distinct synaptic protein puncta were analysed in the CA1rad.

It should be noted that, although the three main components of the hippocampal circuit have specified predominant functions, these are also context-dependent. For example, although the CA3 mainly performs pattern completion, it can also function as a pattern separator under certain circumstances (Vazdarjanova, 2004). Nevertheless, differences in synaptic punctum subtype compositions between the DGmo, CA3rad and CA1rad may underlie some of the known functional differences. Of these three regions, the DGmo has the lowest number of GluN1-containing puncta, potentially limiting NMDAR-dependent synaptic strengthening (Hunt and Castillo, 2012), a useful feature for pattern separation. In contrast, the CA3rad and especially the CA1rad have higher contents of GluN1, possibly enhancing overall synaptic strength, thus facilitating pattern completion and memory recall. Still, NMDARs are involved in the opposing processes of synaptic long-term potentiation (LTP) and long-term depression (LTD) in an activity-dependent manner (Hunt and Castillo, 2012) and their presence at a particular synapse is insufficient for predicting their functional role. The high levels of SAP102 expression in the DGmo are another notable feature, distinguishing the DGmo from all other hippocampal areas. Adult neurogenesis takes place in the DG and a host of hippocampus-dependent behaviours appear to rely on the continuous addition of new neurons to the DG (Cameron and Glover, 2015). SAP102 expression is generally higher than PSD95 expression in early development (up to P15) across all regions analysed here. Indeed, a Western blot study of the developing rat hippocampus shows that SAP102 expression reaches adult-like levels at P10, far sooner than PSD95, which is barely detectable at early ages. Perhaps this trait of the early postnatal brain is maintained in the DG to a certain degree due to adult neurogenesis.

The main functions of the hippocampus are spatial navigation and memory. Some CA1 pyramidal neurons are place cells – neurons that fire when an animal is at specific places in its environment – contributing to an internal representation of space (Moser, Rowland and Moser, 2015). Recent studies of memory employing engram labelling and manipulation – the activity-dependent labelling of neurons active during a task and their subsequent optogenetic activation or inhibition – have shed some light onto the mechanisms underlying memory storage and recall (Tonegawa *et al.*, 2015). Following various learning paradigms, labelled engram neurons have been identified in the dentate gyrus (Liu *et al.*, 2012), CA1 (Ryan *et al.*, 2015) or the basolateral amygdala (especially involved in fear processing) (Gore *et al.*, 2015). Taken together, these studies suggest that engrams are made up of

sparse individual neurons (not entire brain regions) that are distributed in a potentially brain-wide network. Interestingly, despite the unidirectional sequence between the components of an engram, activating any segment seemingly elicits memory recall. While the current study aims to provide insights into the organisation of synaptic proteins in the hippocampus, one of its limitations, shared by a recent, brain-wide synaptome mapping effort (Zhu *et al.*, 2018), is the lack of neuron-specific information. Dye filling or sparsely expressing cytoplasmic fluorescent proteins in conjunction with synaptome mapping could provide neuron-specific data at the expense of using part of the light spectrum for labelling a neuron's cytoplasm instead of a synaptic protein.

All punctum densities reported here are /100 μm^2 because a single plane was imaged in brain sections. However, given the axial resolution of a confocal microscope, each image likely contains the projections of puncta within a 600 nm-thick optical slice (300 nm above and below the focal plane). Based on this, each imaged surface of 100 μm^2 could be approximated by a volume of 60 μm^3 (100 μm^2 x 0.6 µm). Hence, punctum densities reported here per 100 μm^2 could be converted to densities per 1 μm^3 by dividing by 60 (e.g. a density of 100/100 μm^2 is approximately equivalent to 1.66/μm^3) to aid comparisons to other studies reporting synaptic densities per volume, rather than surface area. The CTX region (part of layer 6 of the motor cortex) at P61 contains a total of 131 puncta/100 μm^2 (or approximately 2.2μm^3), of which 33% are GluN1 puncta. Other studies measured excitatory synapse densities of 1/μm^3 (Simhal *et al.*, 2017) and 0.64/μm^3 (Schüz and Palm, 1989) in other cortical areas of adult mice. Assuming that none of the non-colocalised GluN1 puncta represent synapses in the adult cortex helps reconcile the values (1.5/μm^3 excluding GluN1) but the puncta densities reported here still exceed excitatory synapse densities measured by electron microscopy.

Detailed data of the sort included in this section (individual protein and overall punctum subtype developmental trajectories) is also available for the other 12 analysed regions and is included in the appendix. Three regions of particular functional significance (DGmo, CA3rad and CA1rad) were presented here in detail. The next section will present an analysis of synaptic punctum subtype composition gradients along the radial and tangential axes of the CA1 field in the adult hippocampus.

4.3.2 Synaptic punctum subtype distributions in the CA1

Numerous studies have established that the hippocampus plays crucial roles in multiple aspects of memory and spatial navigation, reviewed in (Strange *et al.*, 2014). It is generally accepted that the dorsal hippocampus (analysed in this thesis) is involved in memory (Jackson and Beevor, 1889) and spatial navigation (Morris, 1982) and the ventral hippocampus plays a role in emotional (especially fear) memory, due to its enhanced connectivity to the amygdala (Van Groen and Wyss, 1990). More recently, it was shown that differences in connectivity to extra-hippocampal regions along the dorsoventral axis of the hippocampus are gradual (Kjelstrup *et al.*, 2008). Patterns of gene expression along the same axis, however, reveal multiple discrete domains with well-defined boundaries (Thompson *et al.*, 2008). The following section explores the distributions of the 7 synaptic protein puncta defined by PSD95, SAP102 and GluN1 along the radial and tangential axes (illustrated in Figure 4-9) in the CA1 field of the adult (P94) hippocampus.

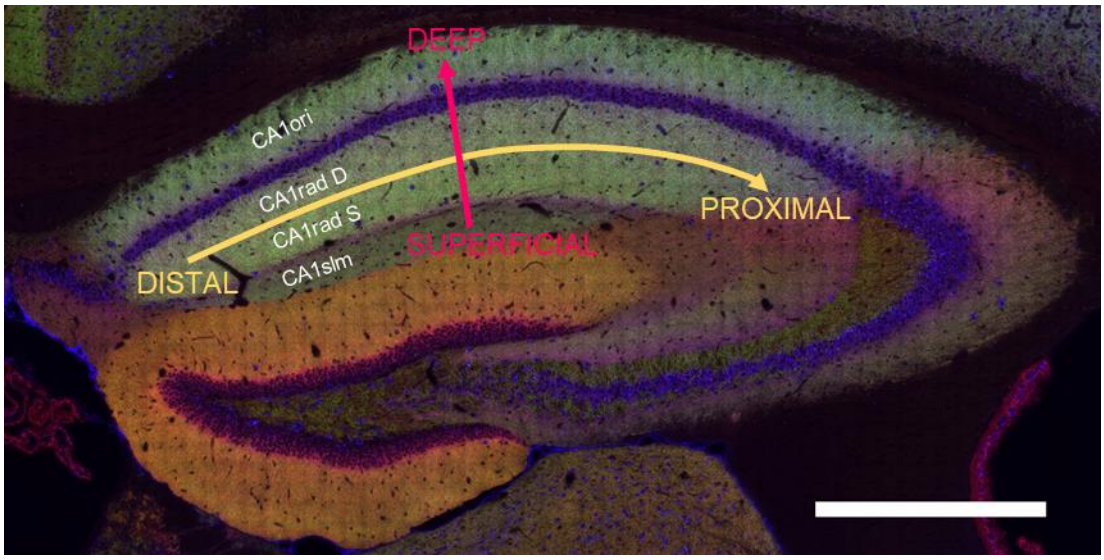

Figure 4-9. Coronal section of the dorsal hippocampus of an adult (P94) mouse. Sectioning plane approximately at Bregma -1.8 mm. Two perpendicular axes are described in the CA1 field: the tangential axis (yellow arrow, from distal to proximal) and the radial axis (red arrow, from superficial to deep). CA1rad D and S – deep and superficial areas of the CA1rad. Composite image lookup table colours: PSD95 – green; SAP102 – red; GluN1 – blue. Scale bar: 500 µm

The basal dendrites of CA1 pyramidal neurons extend into the CA1ori. The proximal (proximal to the pyramidal cell layer, not to be confused with the proximal end of the tangential hippocampal axis) apical dendrites of these cells extend into the CA1rad and the distal apical dendrites are positioned in the CA1slm. The CA1rad was divided into two segments: deep (CA1rad D – closest to the pyramidal cell layer)

and superficial (CA1rad S). The CA1 pyramidal neurons receive weak inputs from the EC layer 3 onto their distal apical dendrites (CA1slm) and strong inputs from the CA3 onto proximal apical dendrites (CA1rad). The CA1rad and CA1ori also receive inputs from the CA2, which, in turn, receives its input from either the CA3 or the EC (Amaral and Witter, 1989). It is thought that the CA1 primarily receives input from the EC during memory encoding and from the CA3 during memory retrieval and consolidation (Carr and Frank, 2012). Synaptic protein punctum subtype distributions in the CA1 were analysed to determine whether these functional differences are reflected in subtype compositions.

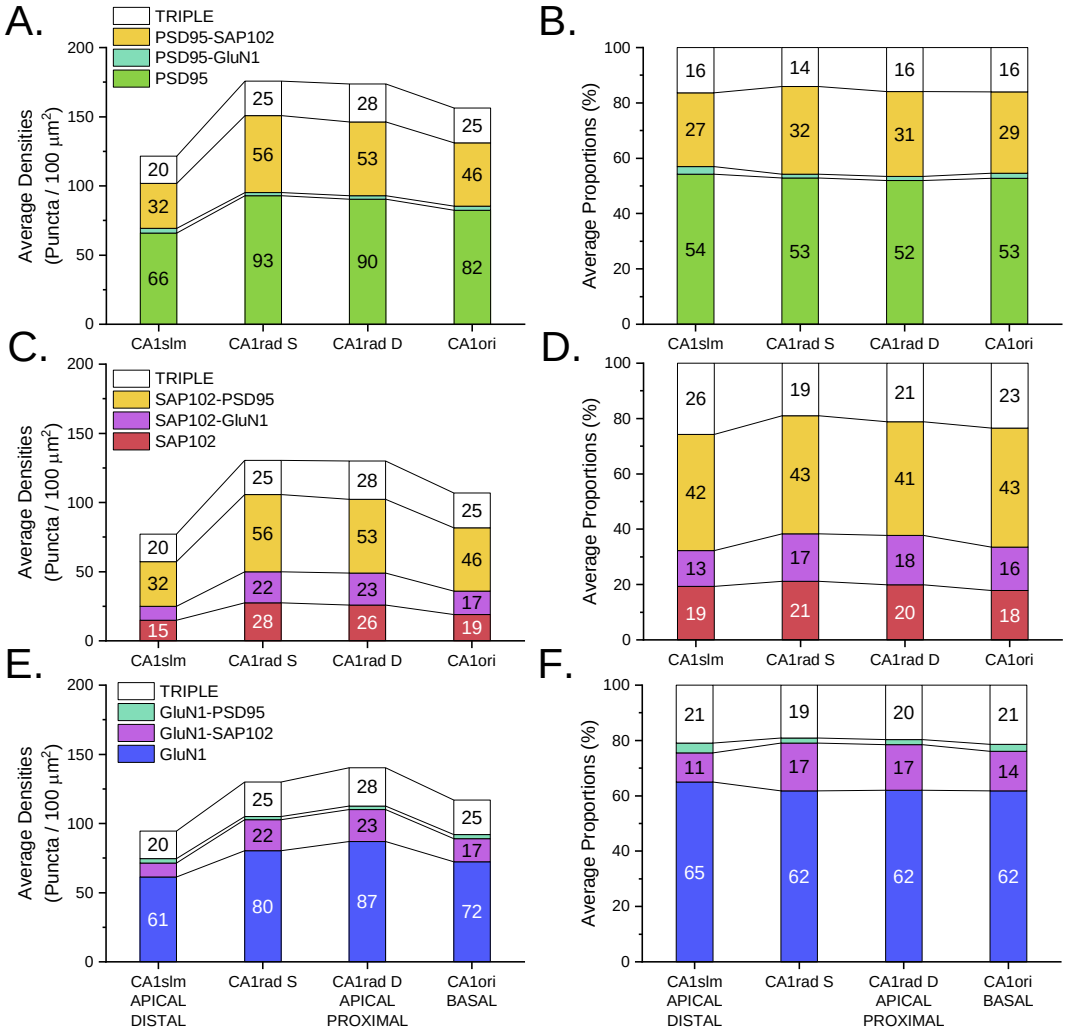

Figure 4-10. PSD95, SAP102 and GluN1 along the radial axis of hippocampal field CA1. A and B. Average PSD95-containing synaptic punctum densities (A) and proportions (B). **C and D.** Average SAP102-containing synaptic punctum densities (C) and proportions (D). **E and F.** Average GluN1-containing synaptic punctum densities (E) and proportions (F). **All.** Distal and Proximal annotations refer to the location along the apical dendrites of the CA1 pyramidal neurons, not to be confused with the distal-to-proximal tangential axis. CA1rad D and S – deep and superficial areas of the CA1rad. Data are averages from left and right hemispheres in coronal sections (Bregma -1.8 mm) from N=2 P94 mice.

Figure 4-10 shows the distributions of PSD95-, SAP102- and GluN1-containing puncta in 4 segments along the radial axis of the CA1 field in the coronal plane. The dorsal hippocampus was imaged in both hemispheres in coronal sections (Bregma -1.8 mm) from two male adult (P94) mice and same-region data from both hemispheres were averaged.

All three proteins show similar expression patterns along the radial axis, with the lowest puncta densities in the CA1slm, intermediate densities in the CA1ori and highest densities in the CA1rad. Within the CA1rad, there is little difference between the deep and superficial layers in PSD95- and SAP102-containing puncta, and there are slightly more (9% more) GluN1-containing puncta in the deep layer (near the pyramidal neuron cell bodies) than in the superficial one.

Figure 4-11 provides a detailed overview of the distributions of the 7 subtypes along the radial axis in the CA1. Within each coronal section imaged, subtype densities were nearly equal in the same region in both hemispheres, but values differed between the two mice, resulting in the pairwise grouping of subtype density values. Overall punctum densities vary between the four regions but subtype proportions are remarkably similar within the CA1. The dendrites of the same pyramidal neurons span all regions and subtype proportions may be regulated on a whole-cell level, whereas total synaptic protein punctum density is determined in the context of broader neural circuits. While this seems plausible based on a whole-region view, punctum subtype data from the dendritic trees of individual neurons (perhaps dye filled neurons) would be required to verify this hypothesis.

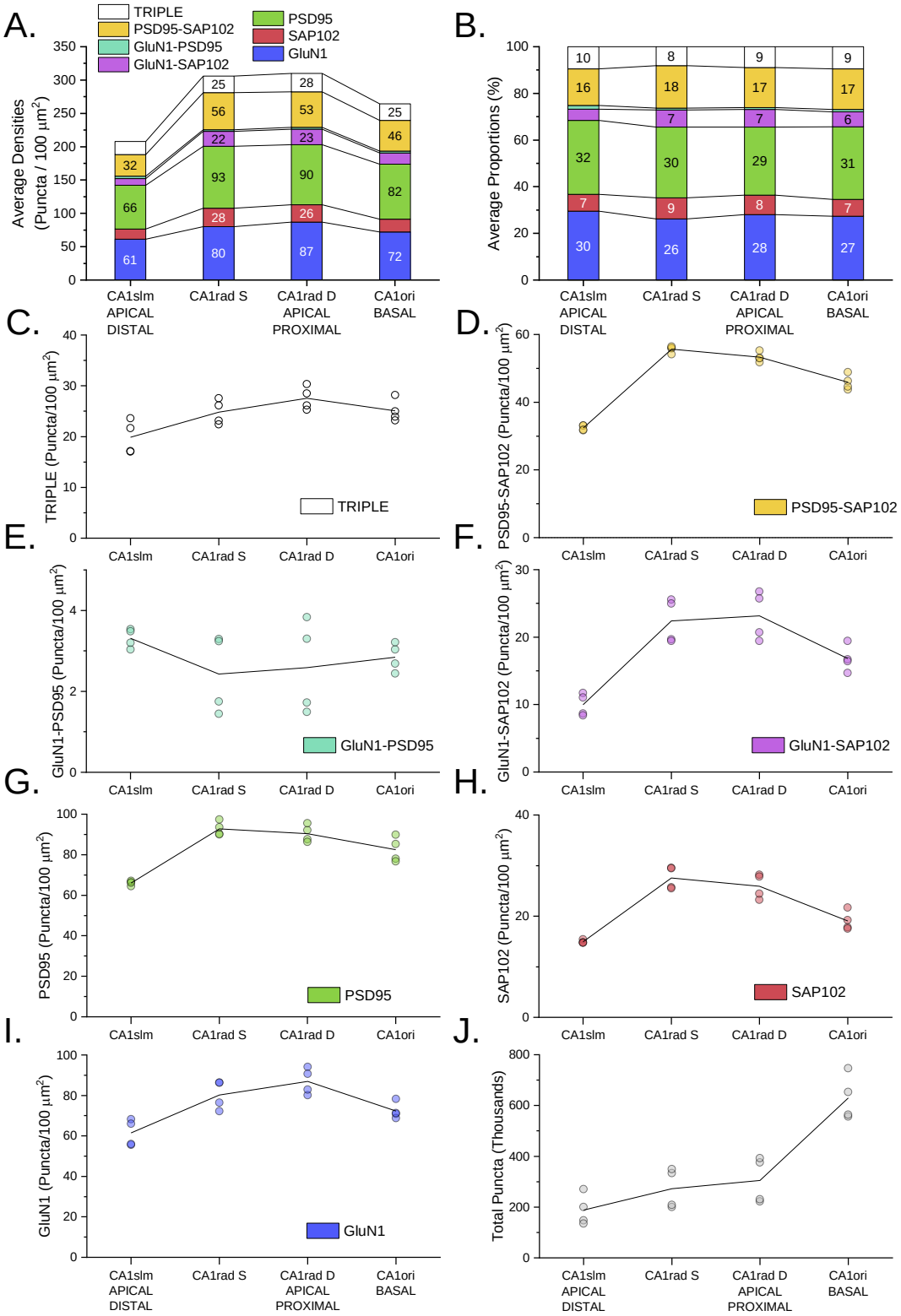

Figure 4-11. Distribution of 7 synaptic punctum subtypes along the radial axis of hippocampal field CA1. A and B. Average subtype densities (A) and proportions of all puncta (B). CA1rad D and S – deep and superficial areas of the CA1rad. **C to I.** Punctum densities of individual subtypes (circles – subtype density measurements in individual regions; black lines – average values). Y-axis scales vary. **J.** Total number of synaptic puncta (density x region surface area) analysed in every region (circles – total puncta numbers in individual regions; black line – average). In total, across all regions, 5.6 M distinct synaptic protein puncta were analysed along the radial axis of the CA1. Data from left and right hemispheres in coronal sections (Bregma -1.8 mm) from N=2 P94 mice.

Along the CA1 tangential axis, multiple studies identified differences in the type of processed spatial information, connectivity to the EC or gene expression profiles, all reviewed in (Igarashi *et al.*, 2014). To probe whether these differences influence subtype compositions along the tangential axis of the CA1, the CA1rad was divided into 5 equal segments (1 – distal; 5 – proximal) that were analysed individually in the coronal and sagittal planes. Both hemispheres of two mice were imaged in the coronal plane (Bregma -1.8 mm) and the data averaged. In the sagittal plane (1.2 mm from midline), N=4 P94 mice were imaged (same as in the previous section). The average subtype densities in the CA1rad along the tangential axis in both planes (sagittal and coronal) are shown in the 3D stacked column graph in Figure 4-12. Average punctum densities in the coronal sections were uniformly greater (by 33%) than those in the sagittal sections, a possible result of the small sample size and mouse-to-mouse variability. In order to match total punctum densities at the intersection between the two planes, density values from the coronal plane were multiplied by 0.75 for display purposes. Detailed CA1rad tangential axis data from both planes are included in the appendix.

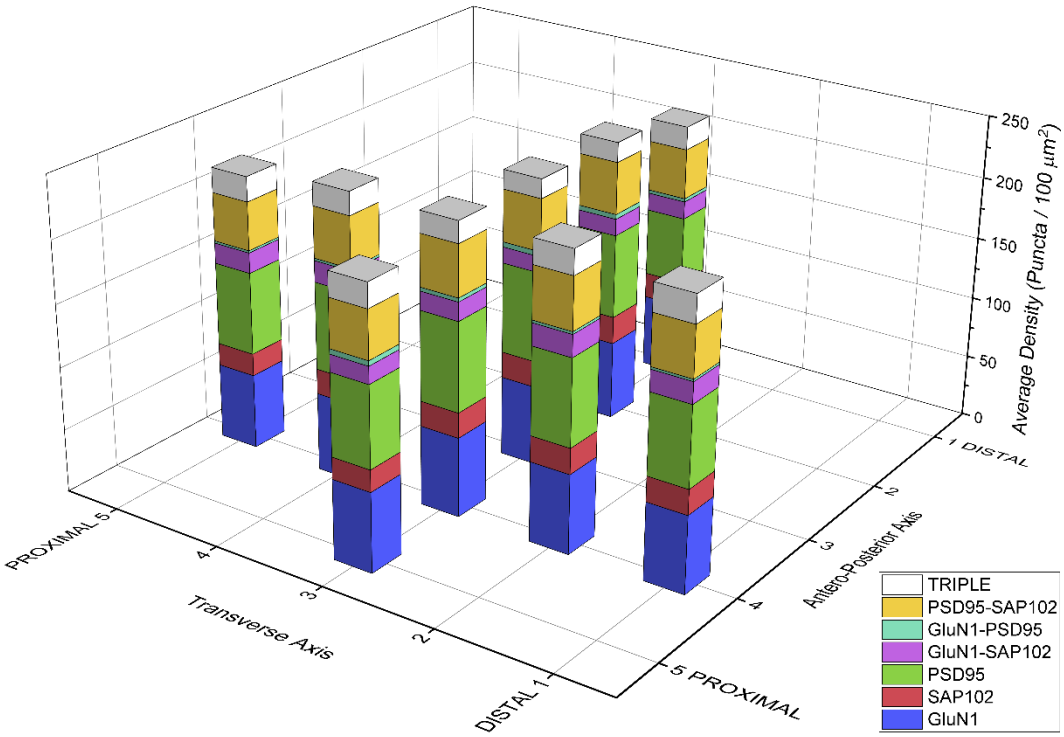

Figure 4-12. Distribution of 7 synaptic punctum subtypes along the tangential axis of the CA1 Stratum Radiatum (CA1rad) in the coronal (transverse axis) and sagittal (antero-posterior axis) planes. The CA1rad was subdivided into 5 equal segments along the tangential axis (1-Distal; 5-Proximal). Coronal section plane approximately at Bregma -1.8 mm (averages of both hemispheres from N=2 P94 mice). Sagittal section plane approximately at 1.2 mm from midline (averages from left hemisphere of N=4 P94 mice, same as in the previous section). All average densities in the coronal plane were multiplied by 0.75 to match total puncta density at the point of intersection (coronal segment 3 with sagittal segment 4).

CA1rad subtype distribution profiles along the tangential axis are similar in both planes. The CA1rad contains slightly fewer synaptic protein puncta at the extremities (segments 1 and 5) compared to the central segments. In the coronal plane, subtype proportions were virtually identical along the entire axis. In the sagittal plane, segments 1 and 5 have a marginally higher proportion of TRIPLE puncta (9% compared to 7% in segments 2 - 4) and correspondingly fewer non-colocalising PSD95 puncta (28% average compared to 31% average in segments 2 - 4). Still, these differences are unlikely to be of any real significance.

In summary, synaptic protein punctum distributions do not seem to show meaningful differences along either gradient analysed, apart from the difference in overall punctum density, but not proportions, between the CA1 Strata Oriens, Radiatum and Lacunosum-Moleculare. This may be a result of whole-cell level regulation of synaptic protein expression. While no gradients were identified over relatively short distances (approximately 1.2 mm along the tangential axis and 0.4 mm along the radial axis), it is possible that heterogeneity exists at a larger scale (e.g. differences between the dorsal and the ventral hippocampus). Thus, the functional gradients present along these axes are neither a consequence, nor a determinant of synaptic protein punctum distribution. Instead, these functional differences likely arise due to differential connectivity to other regions inside and out of the hippocampus. The next section will present all analysed hippocampal regions for a direct inter-regional comparison of synaptic punctum subtype densities and proportions.

4.3.3 Inter-regional comparison of synaptic punctum subtype composition

This section provides an overview of the developing hippocampus, facilitating direct inter-regional comparisons of synaptic protein punctum subtype compositions (densities and proportions). For each region, the average densities and proportions of the 7 synaptic protein punctum subtypes were plotted in Figure 4-13 (early postnatal development, from P1 to P21) and Figure 4-14 (adolescence and early adulthood, from P21 to P94). The scale of the Y-axis is the same across all punctum density plots (left side) in both figures. In 11 of the 15 analysed regions, overall punctum density reaches an initial peak at P21. The exceptions are the CA2ori and CA3slm, where overall punctum density first peaks at P15, and the DGpo and CA3slu, where the highest overall punctum density occurs at P1, mainly made up of GluN1 puncta. While overall punctum density generally follows the same developmental trajectory in all regions (rapid increase from P1 to P21, followed by small fluctuations around the peak value), the absolute density values of different regions diverge from P15 onward. Little change takes place after P21 in every analysed region.

The main components of the hippocampal trisynaptic circuit (DGmo, CA3 Radiatum and Lacunosum-Moleculare and CA1 Radiatum and Oriens) appear to contain the highest overall punctum densities. Remarkably, subtype proportions seem to differ less than subtype densities across regions. To investigate this further, Euclidean distance-based similarity matrices were generated to visualise all pairwise region comparisons of subtype densities and proportions.

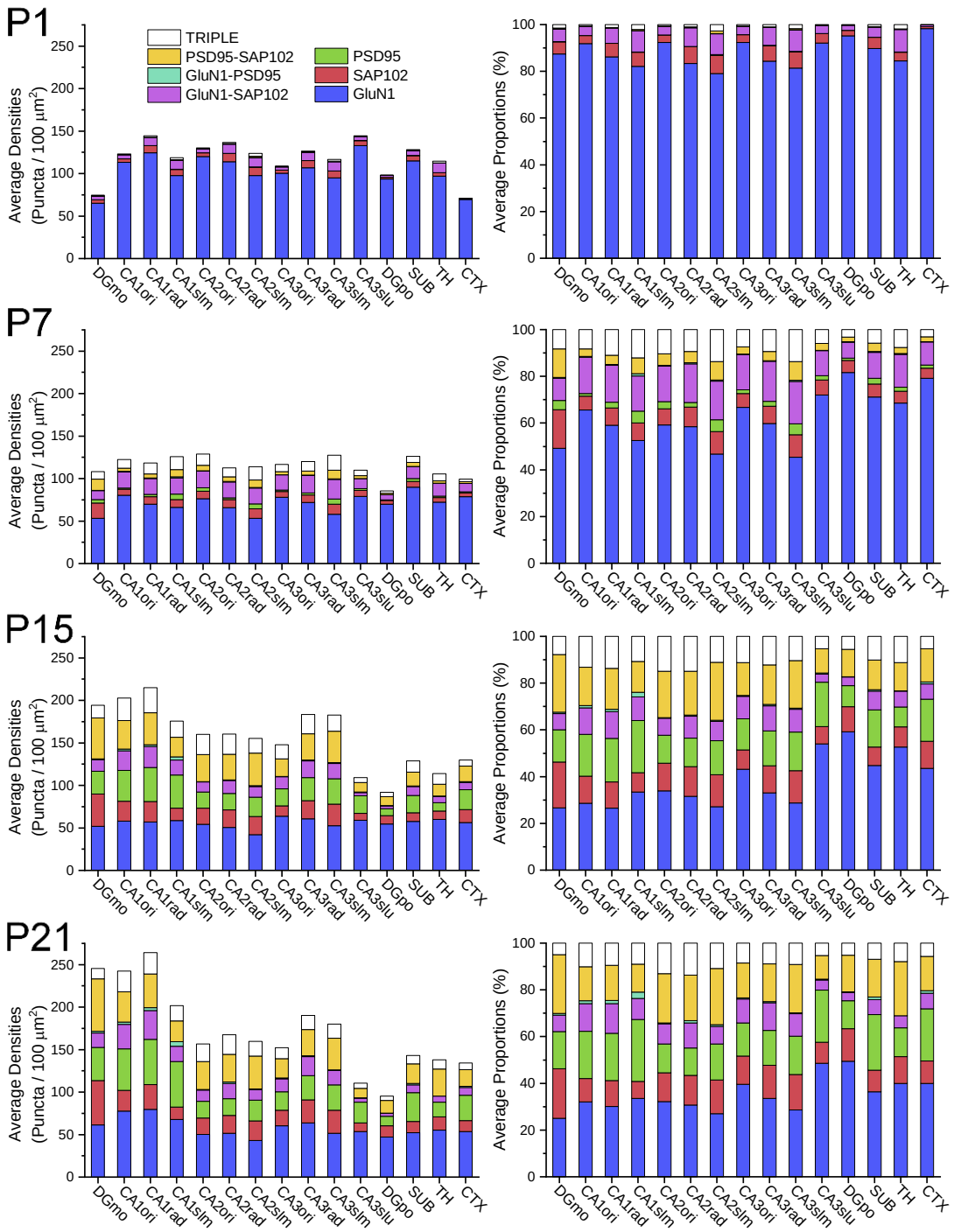

Figure 4-13. Synaptic punctum subtype compositions in the hippocampus in early postnatal development (P1-P21). Left. Average densities of 7 synaptic protein punctum subtypes. Same Y-axis scale for all age groups. **Right.** Average proportions of 7 synaptic protein punctum subtypes.

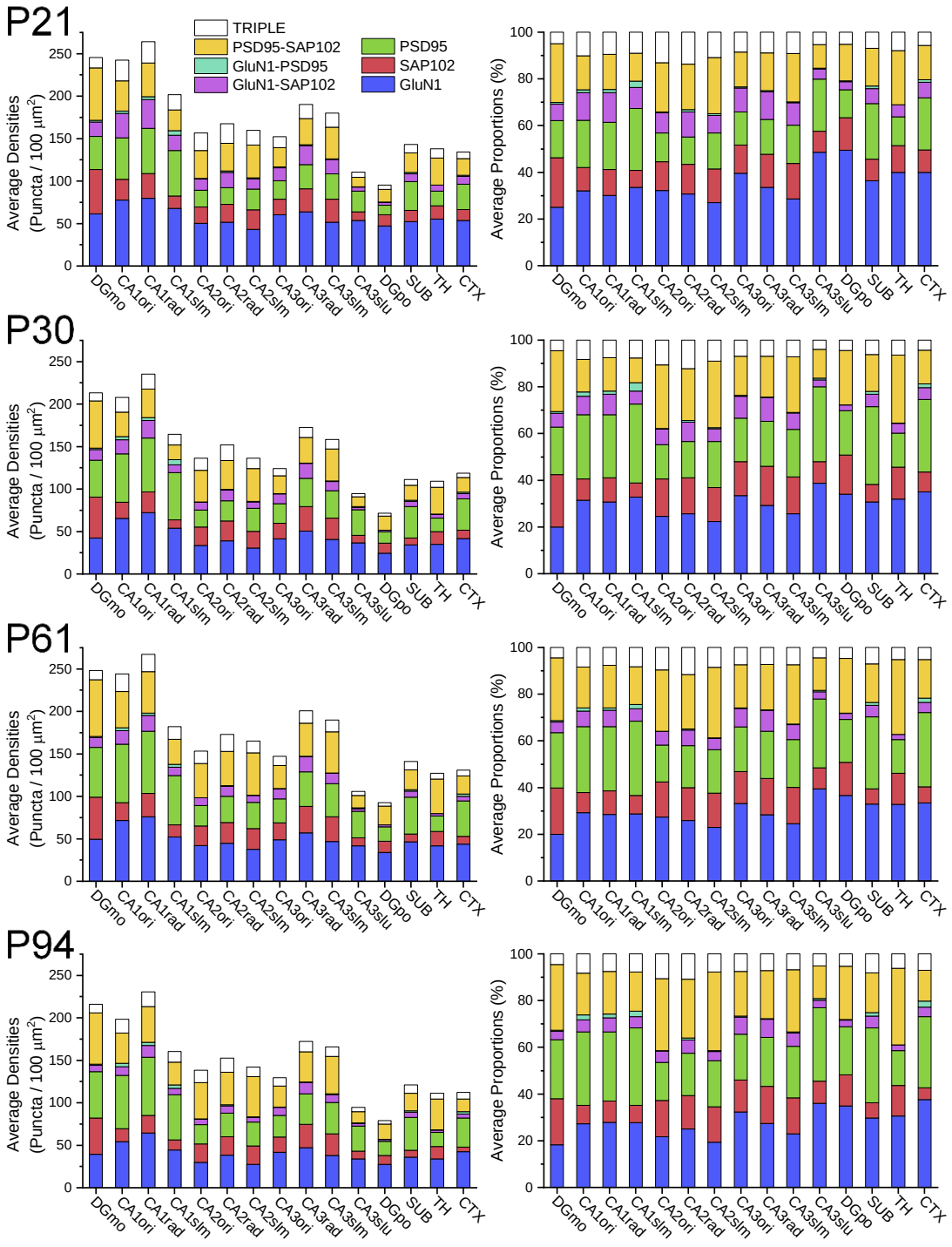

Figure 4-14. Synaptic punctum subtype compositions in the hippocampus in adolescence and early adulthood (P21-P94). Left. Average densities of 7 synaptic protein punctum subtypes. **Right.** Average proportions of 7 synaptic protein punctum subtypes.

Figure 4-15 contains similarity matrices for region subtype densities throughout development and Figure 4-16 contains similarity matrices for region subtype proportions. In each age group, the matrix displayed is an average of the matrices from individual mice within that group. Each Euclidean distance component (i.e. squared difference of a subtype density/proportion between two regions) was normalised to the squared maximum value of that component in the data set (i.e. the maximum value taken by the corresponding subtype density/proportion across the entire data set). This normalisation was performed to balance the weight of each subtype, irrespective of its absolute value. The final Euclidean distance was further normalised to the square root of the number of components ($\sqrt{7}$) to obtain a zero-to-one scale, mapped onto a single colour scale. Euclidean distance-based similarity matrices can provide insights into the relationships between regions and reveal clusters of similar regions but these should be viewed as primarily qualitative descriptions due to the arbitrary (if reasonable) normalisations performed.

Figure 4-15 shows that all analysed regions are undifferentiated from each other at P1 and P7 (indicated by small overall Euclidean distances) in terms of subtype densities. There is a sharp increase in average Euclidean distances across the matrix from P7 to P15 (bottom right graph in Figure 4-15), indicating that the rapid increase in PSD95 and SAP102 expression in that period is not uniform across all analysed regions, leading to their divergence in terms of synaptic protein punctum subtype content. From P15 to P94, inter-regional density relationships appear constant and overall diversity (matrix-wide average Euclidean distance) only manifests a slight decrease over that period. In line with overall punctum densities, overall Euclidean distances peak at P21 and P61. As regions diversify in development, two clusters of similar regions emerge in the hippocampus: the CA1 (Oriens, Radiatum and Lacunosum-Moleculare) and the CA2 and CA3 (Oriens, Radiatum and Lacunosum-Moleculare), highlighted by the dotted squares in each matrix.

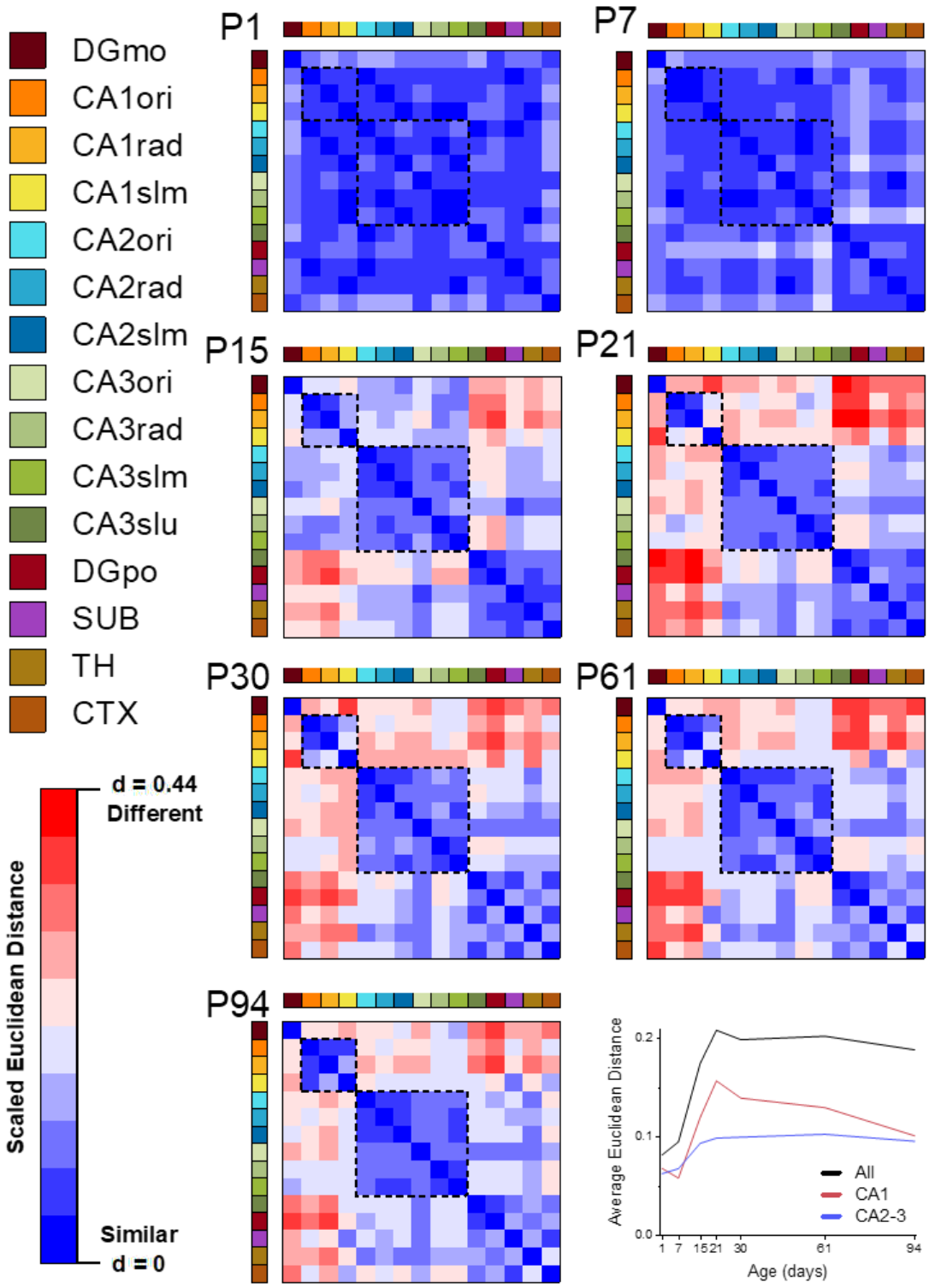

Figure 4-15. Euclidean distance-based similarity matrices comparing synaptic protein punctum subtype densities between hippocampal sub-regions. Each matrix is an average of the matrices of individual mice within an age group. In each matrix, the small dotted square (3x3) delineates the CA1 field and the large dotted square (6x6) delineates the CA2 and CA3 fields. The plot in the bottom right shows average Euclidean distances within the entire matrix (All), the CA1 cluster (CA1) and the CA2 and CA3 cluster (CA2-3) at every age. A marked increase in inter-regional diversity (increase in average Euclidean distances) occurs from P1 to P21.

The average Euclidean distance across the CA2 and CA3 increases far less than the average for all regions from P1 to P15 and plateaus at approximately half of the all-regions average value. In the CA1, the CA1slm diverges slightly from the two other CA1 regions between P15 and P61. Intra-CA1 similarity is at its lowest at P21. At P94, intra-CA1 similarity is comparable to the CA2-CA3 cluster.

At P94, the average inter-regional subtype density Euclidean distance is 0.188. For every region, the average Euclidean distance to all other regions can be calculated and regions can be ranked in terms of uniqueness (the larger the average distance to all other regions, the more differentiated or unique a region becomes). At P94, the top 3 most differentiated regions by subtype density are the DGmo (0.263), CA1rad (0.247) and the CA1ori (0.219). These are also the regions with the 3 highest overall punctum densities.

Euclidean distances based on subtype proportions (Figure 4-16) calculated in the same fashion are numerically smaller than subtype density-based distances. Overall proportion-based distances increase more slowly than density-based distances from P1 to P21, and they peak at P30, later than density-based distances and not synchronised with overall punctum densities. The same CA1 and CA2-CA3 clusters emerge in the proportions-based matrices too, but they are less differentiated from the other analysed regions in terms of proportions (especially the CA1 cluster).

The proportion-based uniqueness ranking at P94 is also different form the density-based one. The DGmo is 4th (0.178) under the CTX (0.222), CA1slm (0.186) and TH (0.180). The CA1ori (0.162) and CA1rad (0.144) fall below the all-region average (0.164). The proportions ranking is partly skewed by the larger (but small, in absolute terms) proportion of GluN1-PSD95 puncta in the CTX and the CA1slm. The DGmo is differentiated from the other regions both through its subtype densities and proportions (primarily due to the increased proportion of SAP102 puncta). The CA1ori and CA1rad, on the other hand, appear to differentiate themselves from the other regions primarily through their higher overall puncta density, with subtype proportions close to the all-regions average.

Taken together, these observations raise the interesting possibility that overall synaptic punctum density may be the main factor in regional differentiation, since density-based Euclidean distances between regions are generally larger than proportion-based distances, (subtype proportions appear to be more similar between regions than do subtype densities).

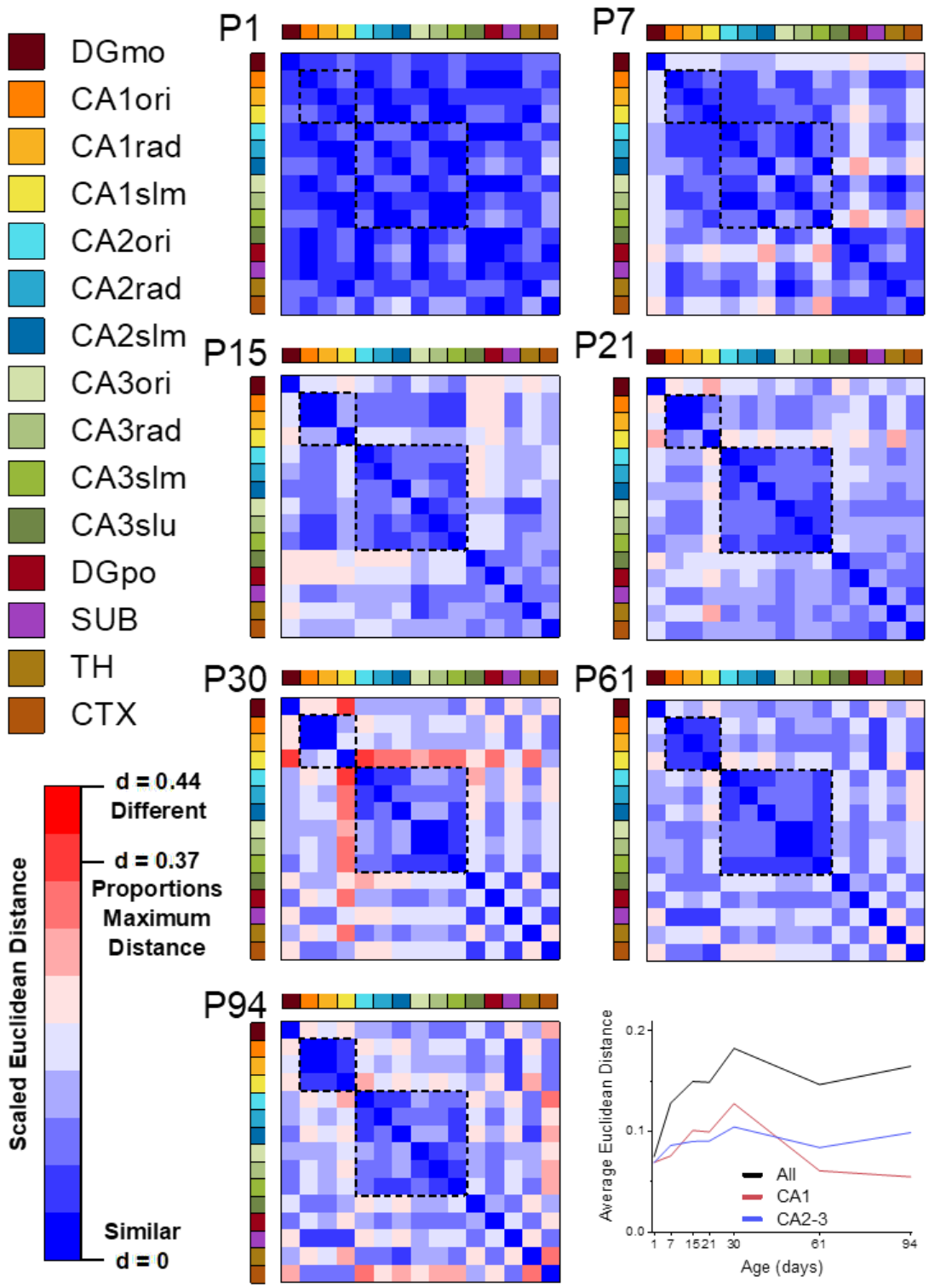

Figure 4-16. Euclidean distance-based similarity matrices comparing synaptic protein punctum subtype proportions between hippocampal sub-regions. Each matrix is an average of the matrices of individual mice within an age group. In each matrix, the small dotted square (3x3) delineates the CA1 field and the large dotted square (6x6) delineates the CA2 and CA3 fields. The plot in the bottom right shows average Euclidean distances within the entire matrix (All), the CA1 cluster (CA1) and the CA2 and CA3 cluster (CA2-3) at every age.

The synaptome mapping study of Zhu et al. (2018) generated Euclidean distance-based similarity matrices between multiple regions in the adult (P80) mouse brain, based on PSD95 and SAP102 punctum densities, overall colocalisation and other punctum intensity and shape parameters. In this study, colocalisation was determined via an error-prone nearest neighbour distance threshold. Furthermore, recording punctum shape features may be of limited use, since super-resolution microscopy studies have revealed that the vast majority of PSD95 puncta (65-78%) are, in fact, PSD95 nanoclusters smaller than the diffraction limit of the confocal microscope used (Broadhead *et al.*, 2016) (and SAP102 is likely to follow similar organisational principles). Nevertheless, the inter-regional relationships reported in the synaptome mapping study are in agreement with those measured here based on the densities of 7 synaptic punctum subtypes, as shown in Figure 4-17. The CA1 and CA2-CA3 clusters are apparent in both studies, and the two matrices show moderately high correlation, with a Pearson's correlation coefficient r = 0.61.

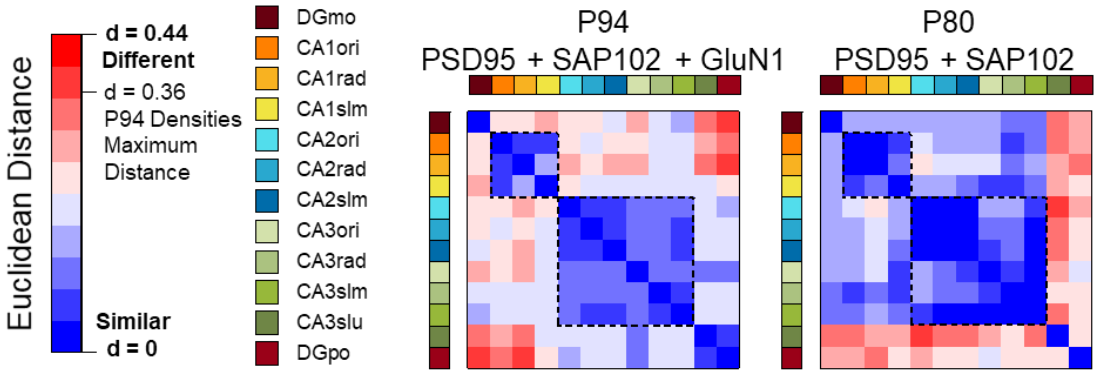

Figure 4-17. 2-protein and 3-protein hippocampal region similarity matrices. Left matrix: Subtype density-based similarity matrix (same as in Figure 4-15) at P94. **Right matrix:** Similarity matrix from left hemisphere dorsal hippocampus at P80, from (Zhu *et al.*, 2018). Right matrix is based on PSD95 and SAP102 density, overall colocalisation and multiple punctum intensity and shape parameters. The reported similarity values (S) were converted to distances (D) via the transformation D = -(S-1) and were normalised to the maximum distance value from the P94 matrix. Pearson's correlation coefficient between the two matrices is r = 0.61.

The agreement between the two studies may be regarded from different perspectives. One possibility is that GluN1 is, for the most part, uniformly involved in assemblies with PSD95 and SAP102 across the different regions, such that its inclusion in the similarity analysis does not result in a marked change from a similarity matrix determined solely by PSD95 and SAP102. Another, more tempting possibility, may be that the organisation of PSD95 and SAP102 determines that of GluN1, such that the distribution of GluN1 may be predicted based only on the features of PSD95 and SAP102 puncta. Then, it would be of great interest to identify other synaptic proteins with a similar organisational dependence on DLG proteins.

Generally, it is possible that the number of degrees of freedom of PSD molecular composition is smaller than the number of known postsynaptic proteins. Hypothetically, if verified, this could enable the indirect mapping of multiple synaptic proteins, unrestricted by the technical limitation to a maximum of three or four proteins labelled and imaged simultaneously. Still, such an exciting prospect would require extensive validation and would be contingent on discovering strong correlations between the features of a 'core' set of proteins (such as the DLG scaffolding proteins) and those of other synaptic proteins, ideally on an individual punctum basis.

To summarise, differential distributions of synaptic protein punctum subtypes lead to inter-regional diversity in the hippocampus and two clusters of similarity – the CA1 and the CA2-CA3 regions – are apparent. Interestingly, inter-regional relationships defined by PSD95, SAP102 and GluN1 resemble those defined by PSD95 and SAP102 only, potentially indicating their importance as synaptic organisers.

4.3.4 Average synaptic punctum subtype composition in the hippocampus

Notwithstanding the inter-regional diversity within the hippocampus, characterising its average synaptic punctum composition will enable a more relevant comparison to proteomic studies of the PSD proteome which, for the most part, represent averages of entire brain sub-regions (Roy, Sorokina, McLean, *et al.*, 2018) or segments (e.g. whole forebrain) (Frank *et al.*, 2016). Figure 4-18 shows the developmental trajectory of the average subtype composition of all 15 analysed regions (weighted by total number of puncta within each region). Average trends are representative of most individual regions.

The trajectories of PSD95-containing puncta and SAP102-containinc puncta are in agreement with Western blot studies of protein expression (continued increase in PSD95 after P35 and early plateauing of SAP102 at P10) (Sans *et al.*, 2000). GluN1-containing puncta, on the other hand, show a steady decline from P1 to P94, despite protein levels doubling form P1 to P10 and remaining constant thereafter, as the developmental NMDAR subunit switch from GluN2B (NR2B) to GluN2A (NR2A) occurs (Sans *et al.*, 2000). Extrasynaptic and even presynaptic NMDARs are involved in a host of developmental processes (Petralia, 2012). NMDARs are

expressed at axonal growth cones in early development but this type of presynaptic expression is greatly reduced after 14 days in vitro in cultured hippocampal neurons (Wang *et al.*, 2011), at least partly explaining the reduction in GluN1-containing puncta observed here from P1 to P15. NMDARs are not required for synaptogenesis (Sytnyk *et al.*, 2006) but are recruited to newly formed synapses.

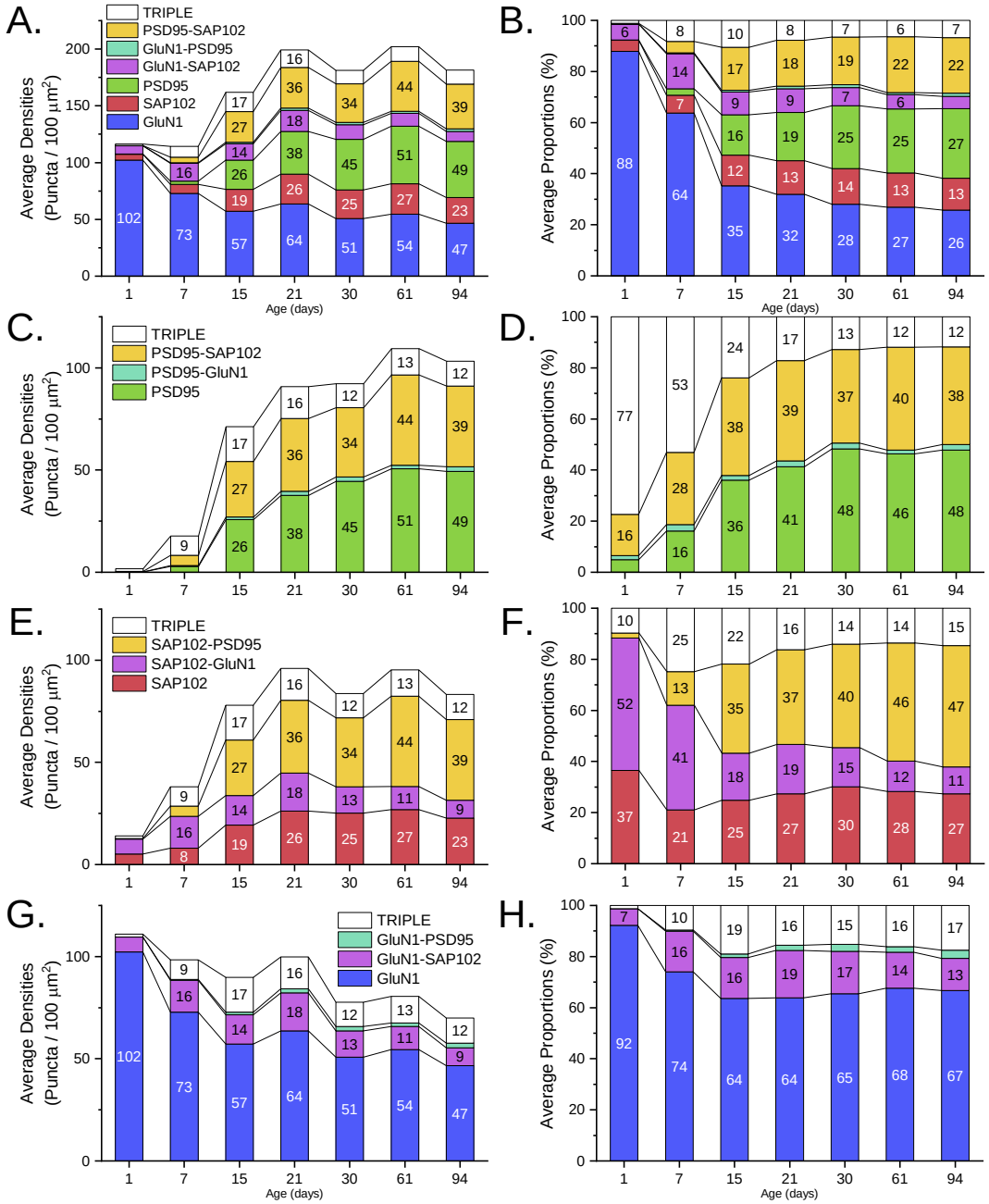

Figure 4-18. Average developmental trajectories of synaptic punctum subtypes. A and B. Average subtype densities (A) and proportions of all puncta (B). **C and D.** Average PSD95-containing synaptic punctum densities (C) and proportions (D). **E and F.** Average SAP102-containing synaptic punctum densities (E) and proportions (F). **G and H.** Average GluN1-containing synaptic punctum densities (G) and proportions (H). **All.** The values displayed are total puncta-weighted averages from all 13 hippocampal and 2 non-hippocampal regions analysed.

From P1 to P15, the density of colocalising GluN1 puncta (primarily TRIPLE and GluN1-SAP102) more than triples (from 9/100 μm^2 to 33/100 μm^2) and it is likely that colocalising GluN1 puncta contain higher amounts of GluN1. A series of studies on PSD protein complexes, reviewed in (Frank and Grant, 2017) revealed that 50% of GluN1 subunits in the adult mouse forebrain are found in large, 1.5 MDa (mega Daltons) protein supercomplexes. Here, only 18% of GluN1 puncta are colocalised with PSD95 (predominantly in TRIPLE puncta). If both studies are correct, this would imply that TRIPLE and GluN1-PSD95 puncta contain, on average, 4 times more GluN1 than lone GluN1 puncta. Indeed, this would be consistent with the contribution of PSD95 to the clustering of NMDARs at synapses (Kim and Sheng, 2004). Furthermore, it was found that PSD95 and SAP102 are present in distinct, biochemically separable supercomplexes (Frank *et al.*, 2016). Nevertheless, 60% of SAP102 puncta colocalise with PSD95 in the hippocampus on average. This would suggest that the PSD contains densely packed, spatially overlapping yet independent protein interaction networks.

Nearly one third of GluN1 puncta colocalise with SAP102 (split evenly between TRIPLE and GluN1-SAP102 puncta) from P15 onwards. SAP102 is known to associate with NMDARs as they are being transported to newly formed synapses (Washbourne, 2004) and also as they are removed from synapses (Chen *et al.*, 2012). This may explain the population of GluN1-SAP102 puncta present at virtually all ages. SAP102 is known to be capable of rapid diffusion in and out of the PSD (Zheng *et al.*, 2010), a feature that may aid its role in trafficking NMDARs. Furthermore, just as SAP102 precedes PSD95 on a developmental time scale, it also does so on the time scale of new synapse formation – SAP102 is incorporated in newly formed dendritic spines 3 hours after formation, whereas PSD95 is expressed at mature levels much later, 12 to 20 hours after spine formation (Lambert *et al.*, 2017). While it is tempting to infer that the SAP102-containing puncta from early time points end up incorporating PSD95 to form mature, permanent synapses, this cannot be verified with the current set of data, as that would require the continuous tracking of individual puncta throughout development. Still, the developmental increase in the proportion of SAP102 colocalising with PSD95 and the decrease in the proportion (but not absolute density) of PSD95 colocalising with SAP102 support a model of synaptogenesis whereby SAP102 is initially required for synapse formation, followed by recruitment of PSD95 and

potential removal of SAP102, resulting in mature synapses containing PSD95 but not SAP102.

To recapitulate, although trends in subtype densities and proportions mostly corroborate known functional aspects of PSD95, SAP102 and GluN1, the basic question of when synaptic protein puncta represent actual synapses still remains. A recently developed method assigns a probability for a structure to be a true synapse based on the number of known synaptic markers it incorporates (Simhal *et al.*, 2017). Although this approach can reasonably identify true synapses, it goes against the fundamental concept of synaptic diversity. The evident heterogeneity of synaptic protein puncta and their distribution across different brain regions requires a more profound appreciation of synaptic diversity.

4.4 Developmental trajectories of spatial relationships between PSD95, SAP102 and GluN1

Nearest neighbour (NN) distances between colocalising puncta are normally distributed around a peak colocalisation distance (PCD) for all three colocalising pairs studied here (PSD95-SAP102, PSD95-GluN1 and SAP102-GluN1). The colocalisation analysis method VLAD provides the PCD and full width at half maximum (FWHM) of the normal distribution of colocalising NN distances for every puncta pair in every analysed region.

Chromatic aberrations caused by microscope lens imperfections can result in shifts of puncta images (Eliscovich, Shenoy and Singer, 2017). In the previous chapter, these shifts were recorded for each pair of wavelengths by imaging multi-colour fluorescent beads and measuring NN distances between the puncta of the three wavelengths subsequently used for imaging synaptic proteins (Figure 3-3 and Table 2). Colocalising NN distances were normally distributed in fluorescent beads and between synaptic proteins. Although chromatic aberrations affect the field of view (FOV) unevenly, based on the reasonable assumption that synaptic puncta were uniformly distributed within the FOV, a population-level correction was applied by subtracting the distribution of colocalising distances of fluorescent beads from those of synaptic proteins. When subtracting one Gaussian distribution from another, the resulting mean (peak colocalisation distance here) is the difference of the means. The FWHM of the resulting distribution, however, increases to become

the square root of the sum of squared initial FWHMs. Naturally, NN distances are zero-bound (cannot be negative) but applying the previously mentioned correction results in corrected distributions with smaller means (shorter PCDs) and increased FWHMs, which do not make physical sense. Still, this correction was necessary for removing the effect of chromatic aberrations to reveal the biologically determined spatial relationships between colocalising PSD95, SAP102 and GluN1. As a result, this section will mainly focus on PCDs. All PCDs and FWHMs shown in this section were obtained through this correction.

VLAD measures the PCD and FWHM of the distribution of colocalising distances through a curve fitting step. PCD and FWHM measurements are more strongly affected by sub-optimal curve fitting than actual colocalisation measurements. To avoid distorted measurements, PCDs and FWHMs were excluded from analysis if the quality of the curve fitting was insufficient. A conservative threshold of 0.9 was chosen for the Adjusted R-squared (Adj-R^2) value (a measure of the goodness of fit). In total, from the three protein pairs, 58 values were excluded from a total of 1,200 (4.8%). 49 of the 58 excluded measurements were of colocalisation between GluN1-PSD95 and GluN1-SAP102 in the DGpo and CA3slu, regions with sparse, uniquely shaped multi-PSD synapses and dense punctate GluN1 expression in the neighbouring cell body layers that could not be excluded from the initial NN distance analysis. In every region, for each protein pair, PCD and FWHM were measured twice – once from the NN distance distribution of each protein relative to the other. The Adj-R^2-weighted average of both PCD and FWHM measurements was used for each pair, though values within a pair were generally very similar.

Measurements for GluN1-SAP102 were made for all 7 age groups. Because of the low expression levels of PSD95 at P1, the pairs including PSD95 were included from P7 onward. 2-factor ANOVA tests (factors: region and age) of all protein pairs showed a significant effect of age but not region on PCDs in the entire set of data (for GluN1-SAP102, both factors had a significant effect). Within each age group, measurements from all regions from all mice were pooled and the developmental trajectories of median PCDs and FWHMs for all three pairs of proteins are shown in Figure 4-19. GluN1 PCDs increase by approximately 20 nm from P7 to P30 (and plateau from P30 to P94) and the PSD95-SAP102 PCD shows a more modest increase of only 7 nm over the same period (also plateauing from P30 to P94). Median FWHM trajectories broadly follow their respective PCDs but have a less pronounced relative increase from P7 to P30.

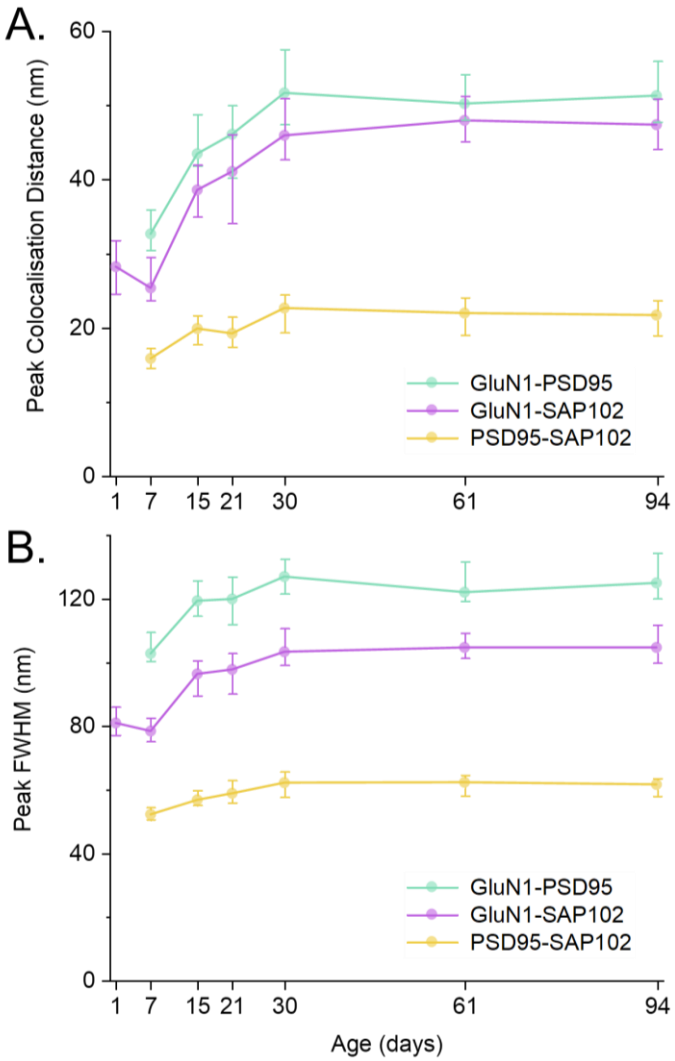

Figure 4-19. Developmental trajectories of spatial relationships between PSD95, SAP102 and GluN1. **A.** Peak colocalisation distances (PCDs) of the three protein punctum pairs in development. **B.** Full width at half maximum (FWHM) of colocalising distances of the three protein punctum pairs in development. **All.** Median values of all regions of all mice in each age group are plotted; error bars extend from the 25th to the 75th percentile. PCDs and FWHMs were excluded from analysis if VLAD curve fitting was of insufficient quality (Adjusted R-squared < 0.9). Excluded individual region measurements (/of all regions x mice): GluN1-PSD95 32/375; GluN1-SAP102 25/450; PSD95-SAP102 1/375. Of the 58 excluded measurements, 49 were from the DGpo or CA3slu.

Based on the median PCDs and FWHMs measured at P7 and P94, an illustration of the 'average synapse' containing all three proteins was created, shown in Figure 4-20. Colocalising GluN1 puncta are located further away from PSD95 and SAP102 in the adult hippocampus compared to earlier developmental time points, while the distance between the two scaffolding proteins stays almost unchanged from birth to adulthood. FWHMs do not increase as much as PCDs over the same period, suggesting that GluN1 puncta are truly distributed around a larger radius relative to the scaffolding proteins and this is not simply a consequence of a broader distribution.

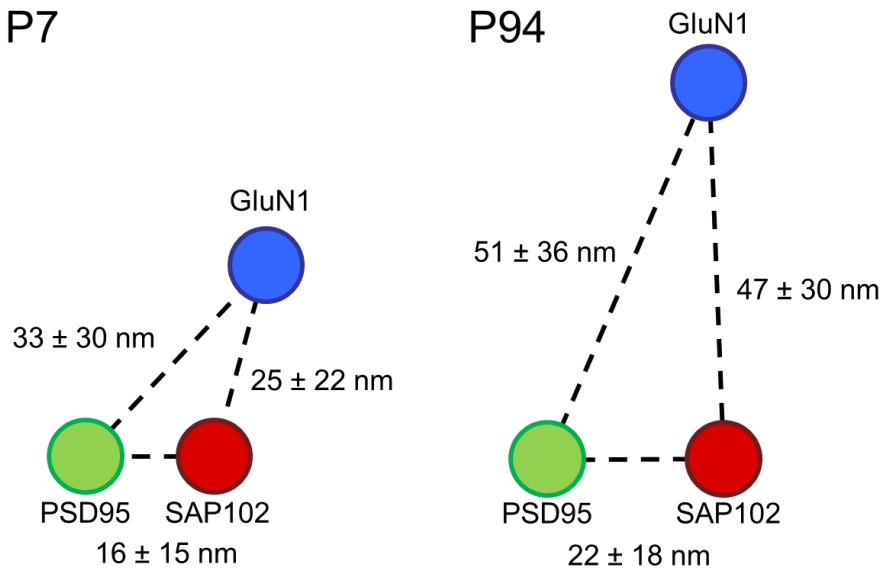

Figure 4-20. Spatial relationships between PSD95, SAP102 and GluN1 at P7 (early postnatal development) and P94 (adulthood). Circles represent punctum centres and dashed lines illustrate median peak colocalisation distances (PCDs). Values shown are median PCDs ± 0.675 standard deviations based on median FWHMs of colocalising distances (equivalent to the range where the middle 50% of values are found).

The relatively short distance between colocalising PSD95 and SAP102 maintained throughout development is consistent with their spatially overlapping presence within the PSD, even if they are involved in biochemically separable protein complexes (Frank *et al.*, 2016).

In synaptogenesis, thin processes called filopodia emerge from the dendritic shaft to later form mature dendritic spines (Hotulainen and Hoogenraad, 2010). It is possible that the shorter distance between GluN1 and the two scaffolding proteins at earlier time points is due to the fact that a larger proportion of synapses are located in small filopodia compared to the adult brain. In the adult brain, GluN1 colocalises with the two scaffolding proteins over a large range of distances. Two factors may contribute to this. First, dendritic spine head shapes are diverse and spine head volumes and diameters can both vary over orders of magnitude (Bourne and Harris, 2008), providing multiple spine head conformations where GluN1 may colocalise with PSD proteins at different distances. Second, NMDARs are capable of diffusion into synapses from extrasynaptic and perisynaptic locations (Tovar and Westbrook, 2002; Dupuis *et al.*, 2014), further increasing the range of distances over which GluN1 may colocalise with the PSD.

Multiple studies have characterised the spatial distribution of proteins at the sub-synaptic level using either immuno-electron microscopy (immuno-EM) or fluorescence microscopy (Gold, 2012). Of the fluorescence microscopy studies, to which the data in this study are more directly comparable, a prominent one performed triple colour 3D stochastic optical reconstruction microscopy (STORM) on fixed mouse brain tissue (Dani *et al.*, 2010). Imaging known synaptic scaffolding proteins (presynaptic Bassoon and postsynaptic Homer1) provided a reference for the position of the synaptic cleft, allowing the authors to determine the position of a third protein of interest along the pre-postsynaptic axis. They found PSD95 located 44 nm away from the synaptic cleft and the C-terminal tail of the NMDAR GluN2B (NR2B) subunit 21 nm away from the cell membrane within the postsynaptic neuron. It is worth noting that immuno-EM studies place PSD95 even closer to the postsynaptic membrane, just 12 nm away (Valtschanoff and Weinberg, 2001). Here, PSD95 was determined to be at a median distance of 51 nm from the extracellular N-terminus of the GluN1 subunit in the adult brain (Figure 4-20). This is in good agreement with the 3D STORM study, considering that the extracellular N-terminus of the GluN1 subunit protrudes approximately 13 nm away from the cell membrane (44+13=57 nm from PSD95), based on the crystal structure of the NMDAR (Karakas and Furukawa, 2014).

The 3D STORM study, as well as most immuno-EM ones, determined the location of synaptic proteins in relation to the synaptic cleft (or cell membrane) within relatively narrow bands (with standard deviations rarely exceeding 20 nm). The current study, however, attributes no directionality to its distance measurements, resulting in significantly broader distributions (median standard deviation of GluN1-PSD95 distance at P94 is 53 nm). Because confocal microscope images are projections of puncta from an approximately 600 nm-thick optical slice onto a single plane, puncta separated along the axial direction may, in fact, appear to overlap, contributing to shorter inter-protein distances. The relatively broad distribution of colocalising distances may also be a consequence of the large number of synaptic puncta analysed. Similarly broad distributions of colocalising distances were observed between PSD95 and Homer1 (64 nm with a standard deviation of 48 nm) using structured illumination microscopy (SIM) by the researchers who developed the SODA (Statistical Object Distance Analysis) colocalisation analysis method (Lagache *et al.*, 2018). Their measurement, despite revealing a broader distribution, was in agreement with the 3D STORM measure of 36 nm and with the observation

that Homer1 is often located outside of the PSD, at its periphery (Tao-Cheng *et al.*, 2014). Lagache et al. (2018) also produced triangle-like figures (similar to Figure 4-20) representing average colocalisation distances between three synaptic proteins (1 pre- and 2 postsynaptic) based on distance measurements lacking directionality. That study surveyed approximately 38,000 distinct puncta (16,000 in colocalising assemblies) in cultured hippocampal neurons and found that the distribution of distances between every two colocalising proteins are virtually identical in pairwise and triple assemblies of those proteins. The measurements in this thesis are based on the analysis of over 61.5 million distinct puncta, of which approximately 20 million were colocalising assemblies. No distinction was made between pairwise and TRIPLE assemblies with regard to colocalising distance measurements.

Changing PCDs throughout development and small sample sizes in individual age groups precluded an inter-regional comparison of PCDs across all ages. However, PCDs for all three protein pairs studied remained constant from P30 onward (p_{ANOVA}>0.19 for all 3 pairs when pooling regions and comparing age groups). Pooling PCD data from the three adult age groups (P30, P61 and P94, N=13 mice total) provided higher statistical power and permitted the meaningful comparison of PCDs between all analysed regions for all protein pairs. Despite small deviations from normality of PCD values in 5/44 cases (according to the Shapiro-Wilk test for normality, none according to the less stringent Kolmogorov-Smirnov test), an ANOVA was performed to compare PCDs from multiple regions. In every case, the ANOVA result stated that the PCDs in the different regions were statistically significantly different, prompting a post-hoc Tukey test for pairwise region comparisons.

Figure 4-21 shows the GluN1-PSD95 PCDs in 13 hippocampal and 2 non-hippocampal regions in adult mice (P30-P94). The majority of values fall between 45 and 55 nm but some outliers exist. The table at the bottom of the figure shows the $-\log_{10}$ - transformed p-values of the post-hoc Tukey test, highlighted whenever a p-value was smaller than 0.05. The table can be viewed as a similarity matrix, where statistically significant differences between regions are highlighted. Due to the relatively broad distributions of GluN1-PSD95 PCDs within regions, few comparisons yielded statistical significance. The DGpo is an outlier, but with only three PCD measurements, little confidence can be attributed to the post-hoc comparisons. Of note are the TH and CTX, where GluN1-PSD95 PCDs are statistically significantly greater than in most other hippocampal regions (TH median

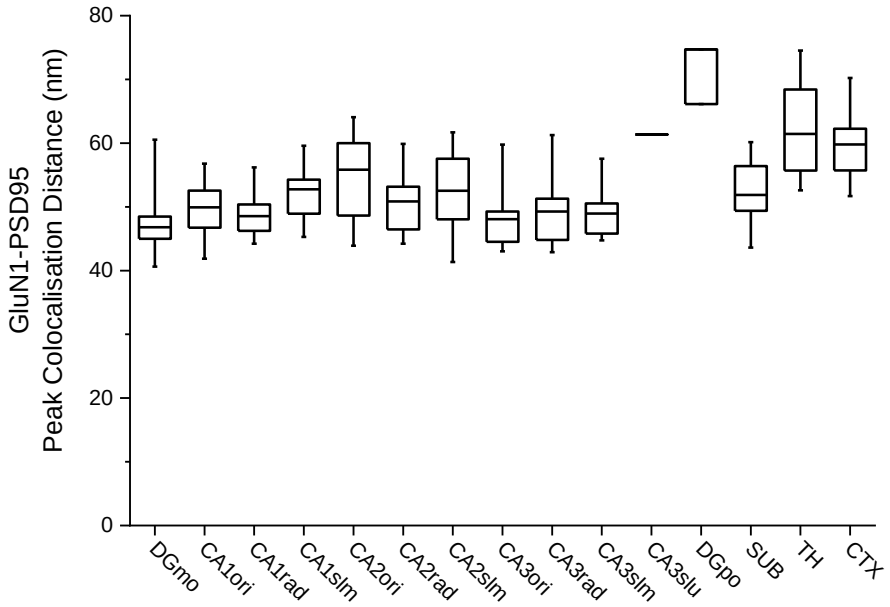

S-W	N		DGmo	CA1ori	CA1rad	CA1slm	CA2ori	CA2rad	CA2slm	CA3ori	CA3rad	CA3slm	CA3slu	DGpo	SUB	TH	CTX
0.022	13	DGmo	**0.0**	**0.0**	**0.0**	**0.2**	**1.5**	**0.0**	**0.2**	**0.0**	**0.0**	**0.0**	**0.5**	**7.6**	**0.3**	**7.6**	**6.1**
	13	CA1ori	**0.0**	**0.0**	**0.0**	**0.0**	**0.4**	**0.0**	**0.0**	**0.0**	**0.0**	**0.0**	**0.2**	**7.5**	**0.0**	**7.1**	**4.0**
	13	CA1rad	**0.0**	**0.0**	**0.0**	**0.0**	**0.7**	**0.0**	**0.0**	**0.0**	**0.0**	**0.0**	**0.3**	**7.5**	**0.1**	**7.6**	**4.7**
	13	CA1slm	**0.2**	**0.0**	**0.0**	**0.0**	**0.0**	**0.0**	**0.0**	**0.2**	**0.0**	**0.0**	**0.0**	**6.2**	**0.0**	**4.6**	**1.9**
	13	CA2ori	**1.5**	**0.4**	**0.7**	**0.0**	**0.0**	**0.1**	**0.0**	**1.4**	**0.7**	**0.7**	**0.0**	**4.5**	**0.0**	**2.1**	**0.3**
	13	CA2rad	**0.0**	**0.0**	**0.0**	**0.0**	**0.1**	**0.0**	**0.0**	**0.0**	**0.0**	**0.0**	**0.1**	**7.1**	**0.0**	**6.0**	**3.0**
	12	CA2slm	**0.2**	**0.0**	**0.0**	**0.0**	**0.0**	**0.0**	**0.0**	**0.2**	**0.0**	**0.0**	**0.0**	**6.0**	**0.0**	**4.2**	**1.6**
0.017	13	CA3ori	**0.0**	**0.0**	**0.0**	**0.2**	**1.4**	**0.0**	**0.2**	**0.0**	**0.0**	**0.0**	**0.4**	**7.6**	**0.3**	**7.6**	**5.9**
	13	CA3rad	**0.0**	**0.0**	**0.0**	**0.0**	**0.7**	**0.0**	**0.0**	**0.0**	**0.0**	**0.0**	**0.3**	**7.5**	**0.1**	**7.6**	**4.7**
	12	CA3slm	**0.0**	**0.0**	**0.0**	**0.0**	**0.7**	**0.0**	**0.0**	**0.0**	**0.0**	**0.0**	**0.3**	**7.7**	**0.1**	**7.4**	**4.5**
N/A	1	CA3slu	**0.5**	**0.2**	**0.3**	**0.0**	**0.0**	**0.1**	**0.0**	**0.4**	**0.3**	**0.3**	**0.0**	**0.1**	**0.0**	**0.0**	**0.0**
0.001	3	DGpo	**7.6**	**7.5**	**7.5**	**6.2**	**4.5**	**7.1**	**6.0**	**7.6**	**7.5**	**7.7**	**0.1**	**0.0**	**5.9**	**0.7**	**1.8**
	13	SUB	**0.3**	**0.0**	**0.1**	**0.0**	**0.0**	**0.0**	**0.0**	**0.3**	**0.1**	**0.1**	**0.0**	**5.9**	**0.0**	**4.1**	**1.5**
	13	TH	**7.6**	**7.1**	**7.6**	**4.6**	**2.1**	**6.0**	**4.2**	**7.6**	**7.6**	**7.4**	**0.0**	**0.7**	**4.1**	**0.0**	**0.0**
	13	CTX	**6.1**	**4.0**	**4.7**	**1.9**	**0.3**	**3.0**	**1.6**	**5.9**	**4.7**	**4.5**	**0.0**	**1.8**	**1.5**	**0.0**	**0.0**

Figure 4-21. GluN1-PSD95 peak colocalisation distances in the adult mouse. Top. Box plots of peak colocalisation distances (PCDs) across 15 regions in adult mice (P30, P61 and P94, N=13 mice total). $p_{ANOVA} = 0$. Boxes represent median values and 25th–75th percentile range. Whiskers extend to minimum and maximum values, respectively. **Bottom.** Table of statistical significance of post-hoc pairwise comparisons between regions. Values are $-\log_{10}(p_{Tukey\ post\text{-}hoc\ test})$ and all values above 1.3 ($-\log_{10}(0.05)$) are coloured. N refers to the number of PCDs available from each region. PCD values were included if VLAD curve fitting was of sufficient quality (Adjusted R-squared > 0.9). S-W refers to the p-value of the Shapiro-Wilk test for normality, provided wherever lower than 0.05. PCD values from all regions passed the less stringent Kolmogorov-Smirnov test for normality ($p > 0.05$).

PCD: 61 nm; CTX: 60 nm; overall median: 51 nm). This difference may be caused by a larger portion of perisynaptic NMDARs in these two regions compared to the hippocampus, or dendritic spines may be slightly larger, or of different shapes. Either way, it would be difficult to assign functional meaning to this PCD difference. The NMDAR GluN2B subunit interacts with PSD95 via a PDZ domain close to the C-terminus of a long (over 500 amino acid) disorganised C-terminal domain with a

theoretical maximum linear length of approximately 160 nm (Traynelis *et al.*, 2010). Thus, NMDAR-PSD95 interactions could theoretically occur over a distance range far greater than the PCDs measured in any of the 15 analysed regions.

Figure 4-22 shows the inter-regional comparisons of GluN1-SAP102 PCDs in adult mice. Unlike the GluN1-PSD95 post-hoc comparison matrix, the statistically significant differences here are not concentrated around three outlier regions. Instead, a higher degree of PCD-based inter-regional diversity is apparent. The CA1, CA2 and CA3 clusters of similarity revealed by punctum subtype compositions also have GluN1-SAP102 PCDs in common, as pairwise comparisons show statistically significant differences between but not within them. The TH and CTX differ from the overall median PCD of 47 nm in opposite ways (TH: 57 nm; CTX: 41 nm), unlike in the case of GluN1-PSD95, where PCDs in both regions were greater than the overall median. This would suggest that different dendritic spine shapes or sizes are unlikely to explain the differences in GluN1 PCDs seen in the CTX, since the distance between PSD95 and SAP102 in the CTX is similar to most other regions analysed.

Figure 4-23 shows inter-regional comparisons of PSD95-SAP102 PCDs. Although PSD95-SAP102 PCDs vary over a smaller range than GluN1 PCDs, the narrow distributions of values within each region lead to highly statistically significant, albeit small differences between most region pairs. With the largest difference in median PCDs of only 8 nm (TH: 17 nm; CA1slm: 25 nm; overall median: 22 nm), it is unlikely that this could have meaningful functional consequences. Still, it is remarkable that the CA1, CA2 and CA3 clusters of similarity are also preserved in the case of PSD95-SAP102 PCDs.

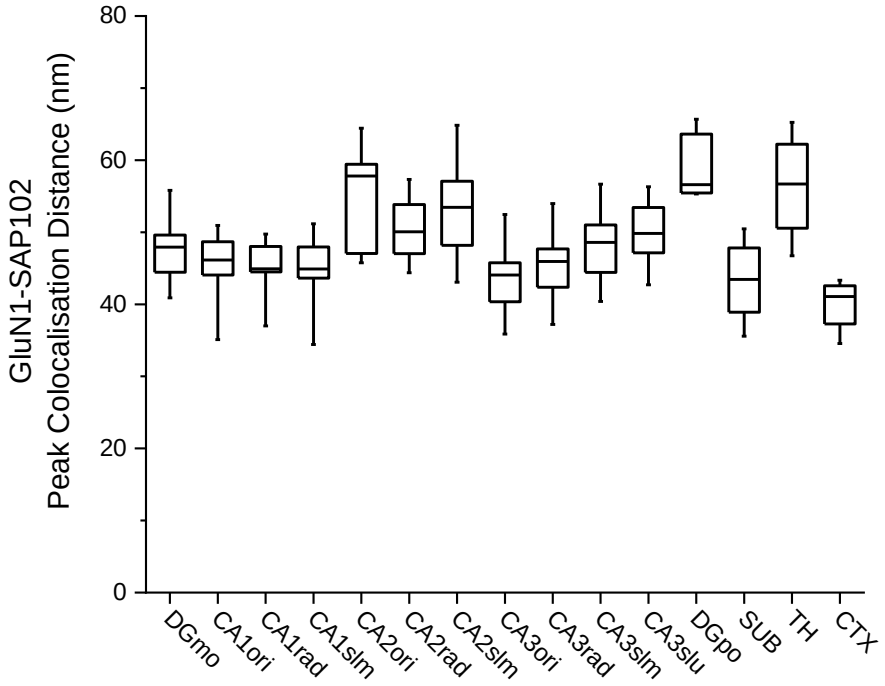

S-W	N		DGmo	CA1ori	CA1rad	CA1slm	CA2ori	CA2rad	CA2slm	CA3ori	CA3rad	CA3slm	CA3slu	DGpo	SUB	TH	CTX
	13	DGmo	0.0	0.0	0.0	0.0	2.3	0.0	0.9	0.1	0.0	0.0	0.0	2.4	0.1	3.9	1.9
	13	CA1ori	0.0	0.0	0.0	0.0	3.8	0.4	2.0	0.0	0.0	0.0	0.2	3.5	0.0	5.7	0.8
	13	CA1rad	0.0	0.0	0.0	0.0	4.2	0.5	2.3	0.0	0.0	0.0	0.2	3.7	0.0	6.1	0.6
	13	CA1slm	0.0	0.0	0.0	0.0	4.8	0.8	2.8	0.0	0.0	0.1	0.4	4.1	0.0	6.7	0.4
0.032	13	CA2ori	2.3	3.8	4.2	4.8	0.0	0.3	0.0	6.3	4.3	1.4	0.3	0.0	6.1	0.0	8.3
	13	CA2rad	0.0	0.4	0.5	0.8	0.3	0.0	0.0	1.7	0.6	0.0	0.0	0.8	1.6	1.2	4.9
	13	CA2slm	0.9	2.0	2.3	2.8	0.0	0.0	0.0	4.2	2.4	0.4	0.0	0.1	4.0	0.1	7.6
	13	CA3ori	0.1	0.0	0.0	0.0	6.3	1.7	4.2	0.0	0.0	0.5	1.0	5.1	0.0	7.8	0.0
	13	CA3rad	0.0	0.0	0.0	0.0	4.3	0.6	2.4	0.0	0.0	0.0	0.3	3.8	0.0	6.2	0.5
	13	CA3slm	0.0	0.0	0.0	0.1	1.4	0.0	0.4	0.5	0.0	0.0	0.0	1.8	0.4	2.9	2.8
	9	CA3slu	0.0	0.2	0.2	0.4	0.3	0.0	0.0	1.0	0.3	0.0	0.0	0.8	0.9	1.0	3.5
	4	DGpo	2.4	3.5	3.7	4.1	0.0	0.8	0.1	5.1	3.8	1.8	0.8	0.0	5.0	0.0	7.5
	13	SUB	0.1	0.0	0.0	0.0	6.1	1.6	4.0	0.0	0.0	0.4	0.9	5.0	0.0	7.7	0.1
	13	TH	3.9	5.7	6.1	6.7	0.0	1.2	0.1	7.8	6.2	2.9	1.0	0.0	7.7	0.0	7.9
	13	CTX	1.9	0.8	0.6	0.4	8.3	4.9	7.6	0.0	0.5	2.8	3.5	7.5	0.1	7.9	0.0

Figure 4-22. GluN1-SAP102 peak colocalisation distances in the adult mouse. Top. Box plots of peak colocalisation distances (PCDs) across 15 regions in adult mice (P30, P61 and P94, N=13 mice total). $p_{ANOVA} = 0$. Boxes represent median values and 25th–75th percentile range. Whiskers extend to minimum and maximum values, respectively. **Bottom.** Table of statistical significance of post-hoc pairwise comparisons between regions. Values are $-\log_{10}(p_{Tukey\ post\text{-}hoc\ test})$ and all values above 1.3 ($-\log_{10}(0.05)$) are coloured. N refers to the number of PCDs available from each region. PCD values were included if VLAD curve fitting was of sufficient quality (Adjusted R-squared > 0.9). S-W refers to the p-value of the Shapiro-Wilk test for normality, provided wherever lower than 0.05. PCD values from all regions passed the less stringent Kolmogorov-Smirnov test for normality ($p > 0.05$).

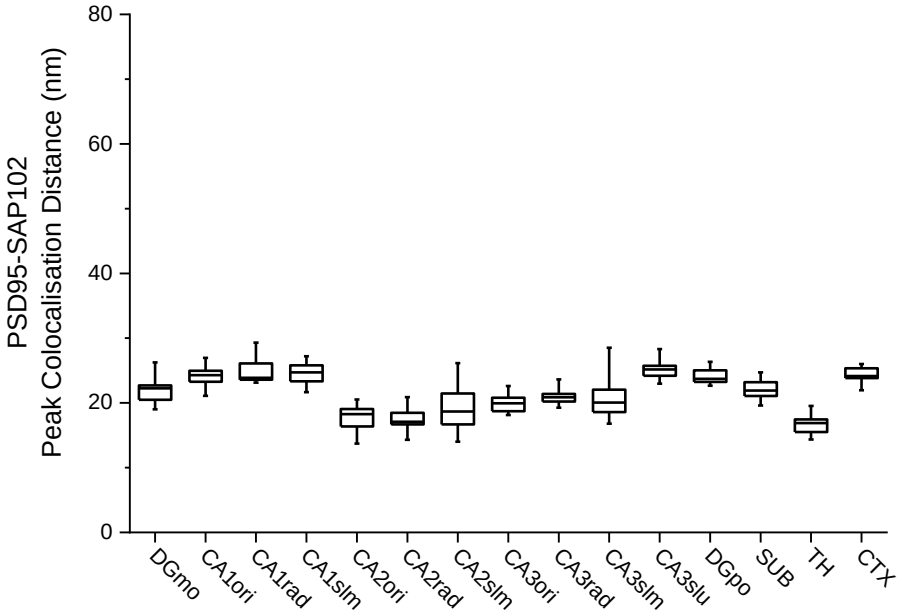

S-W	N		DGmo	CA1ori	CA1rad	CA1slm	CA2ori	CA2rad	CA2slm	CA3ori	CA3rad	CA3slm	CA3slu	DGpo	SUB	TH	CTX
	13	DGmo	0.0	0.8	2.0	1.3	5.6	6.5	1.5	0.5	0.0	0.0	2.7	0.8	0.0	8.2	1.2
	13	CA1ori	0.8	0.0	0.0	0.0	8.0	8.2	7.2	5.3	2.4	3.3	0.0	0.0	0.6	10.0	0.0
0.011	13	CA1rad	2.0	0.0	0.0	0.0	8.6	9.2	8.3	7.3	4.1	5.2	0.0	0.0	1.7	10.0	0.0
	13	CA1slm	1.3	0.0	0.0	0.0	8.2	10.0	7.9	6.3	3.2	4.2	0.0	0.0	1.1	10.0	0.0
	13	CA2ori	5.6	8.0	8.6	8.2	0.0	0.0	0.2	0.9	3.2	2.3	9.4	8.0	6.0	0.0	8.1
	13	CA2rad	6.5	8.2	9.2	10.0	0.0	0.0	0.4	1.4	4.0	3.0	10.0	8.2	6.9	0.0	9.4
	13	CA2slm	1.5	7.2	8.3	7.9	0.2	0.4	0.0	0.0	0.3	0.1	7.8	7.3	1.8	1.8	7.8
	13	CA3ori	0.5	5.3	7.3	6.3	0.9	1.4	0.0	0.0	0.0	0.0	7.9	5.4	0.7	3.3	6.1
	13	CA3rad	0.0	2.4	4.1	3.2	3.2	4.0	0.3	0.0	0.0	0.0	5.1	2.5	0.0	6.4	3.0
	13	CA3slm	0.0	3.3	5.2	4.2	2.3	3.0	0.1	0.0	0.0	0.0	6.2	3.3	0.1	5.3	4.0
	13	CA3slu	2.7	0.0	0.0	0.0	9.4	10.0	7.8	7.9	5.1	6.2	0.0	0.0	2.4	8.4	0.0
	13	DGpo	0.8	0.0	0.0	0.0	8.0	8.2	7.3	5.4	2.5	3.3	0.0	0.0	0.6	10.0	0.0
	13	SUB	0.0	0.6	1.7	1.1	6.0	6.9	1.8	0.7	0.0	0.1	2.4	0.6	0.0	8.3	1.0
	13	TH	8.2	10.0	10.0	10.0	0.0	0.0	1.8	3.3	6.4	5.3	8.4	10.0	8.3	0.0	10.0
	13	CTX	1.2	0.0	0.0	0.0	8.1	9.4	7.8	6.1	3.0	4.0	0.0	0.0	1.0	10.0	0.0

Figure 4-23. PSD95-SAP102 peak colocalisation distances in the adult mouse. Top. Box plots of peak colocalisation distances (PCDs) across 15 regions in adult mice (P30, P61 and P94, N=13 mice total). $p_{ANOVA} = 0$. Boxes represent median values and 25th–75th percentile range. Whiskers extend to minimum and maximum values, respectively. **Bottom.** Table of statistical significance of post-hoc pairwise comparisons between regions. Values are $-\log_{10}(p_{Tukey\ post\text{-}hoc\ test})$ and all values above 1.3 ($-\log_{10}(0.05)$) are coloured. A value of 10 was assigned to fields where $p_{Tukey\ post\text{-}hoc\ test} < 10^{-10}$. N refers to the number of PCDs available from each region. PCD values were included if VLAD curve fitting was of sufficient quality (Adjusted R-squared > 0.9). S-W refers to the p-value of the Shapiro-Wilk test for normality, provided wherever lower than 0.05. PCD values from all regions passed the less stringent Kolmogorov-Smirnov test for normality ($p > 0.05$).

To summarise, PCDs between GluN1, PSD95 and SAP102 have distinct developmental trajectories. From P7 to P94, PCDs of GluN1-PSD95 increase by 54%, GluN1-SAP102 by 88% and PSD95-SAP102 by only 38%. PCDs remain constant in adulthood (from P30 onward) and, for each protein pair, they show small but statistically significant differences between analysed regions. Interestingly, the pairwise region PCD comparisons revealed the same clusters of similarity (CA1, CA2 and CA3) as defined by synaptic protein punctum compositions.

4.5 Brief chapter summary and conclusions

The combinatorial assembly of GluN1, PSD95 and SAP102 gives rise to 7 synaptic protein punctum subtypes. Over 61.5 million distinct puncta or punctum assemblies were analysed in the hippocampus across 7 age groups, making this the largest scale analysis of these three proteins and their colocalisation in the mouse hippocampus to date. This vast dataset revealed the organisational patterns of these proteins throughout early development.

These subtypes, quantified with the VLAD colocalisation analysis method, are differentially distributed across hippocampal subregions, giving rise to intra- and inter-regional synaptic diversity. The distinct subtype compositions of the dentate gyrus molecular layer, the CA3 and the CA1 subfields may underlie their different functions in the hippocampal circuit. However, no discernible subtype composition gradients were identified within the CA1 subfield, suggesting that known functional gradients in this region are likely a consequence of connectivity gradients.

GluN1, PSD95 and SAP102 are known to interact directly within the PSD, but an unexpectedly high proportion of their puncta remain non-colocalised in the adult hippocampus: 67% of GluN1, 48% of PSD95 and 27% of SAP102. While it was not possible to determine whether all of these are synaptic (and indeed, many of them are not expected to be), this observation highlights the need to develop new ways to determine whether synaptic protein puncta are actually located in synapses. In the context of synaptic diversity, it also opens the possibility that these proteins give rise to different synaptic properties depending on their colocalisation.

The GluN1-PSD95 subtype, on average, made up fewer than 1.3% of all puncta across all ages. This would not be expected if the three proteins could interact with each other independently. Instead, it appears that NMDA receptors colocalise with

PSD95 only when also in the presence of SAP102, raising interesting questions about the functional roles of these two scaffolding in their interactions with NMDARs.

Synaptic protein punctum densities and proportions in 13 hippocampal and 2 non-hippocampal regions were then compared across 7 age groups, from birth (P1) to adulthood (P94). The regions undergo significant differentiation (from each other) between P7 and P15, as PSD95 and SAP102 expression rises. Subtype density-based Euclidean distances (measure of dissimilarity) between regions were greater than subtype proportion-based ones, raising the interesting hypothesis that total synaptic density may be the primary factor leading to regional differentiation.

The developmental trajectories of peak colocalisation distances (PCDs) of the three protein pairs were characterised, revealing a larger increase of GluN1 PCDs compared to PSD95-SAP102 PCDs in early postnatal development, consistent with the size of dendritic spines increasing more than that of PSDs during development. In adulthood, subtle differences between PCDs in different regions displayed patterns similar to synaptic protein punctum composition differences.

5 General Discussion

5.1 Summary of findings

The findings of this thesis are two-fold: methodological and biological. On the methodological side, the Vicinity-based Localisation Adjacency Determination (VLAD) method was developed in order to address the limitations of previously existing colocalisation analysis methods. VLAD can answer the three basic colocalisation questions: what proportion of puncta from a group A colocalise with puncta from a group B? what is the probability of true colocalisation for each punctum of group A? and what is the spatial relationship between A and B when they colocalise? Furthermore, it was shown through extensive testing in simulated data that VLAD colocalisation measurements are accurate across a wide range of conditions, and especially under conditions representative of experimental data of the kind included in this thesis. Unlike previous colocalisation methods, including the Statistical Object Distance Analysis (SODA) method of Lagache et al., VLAD achieves minimal false positives and false negatives as a result of its curve-fitting step in nearest neighbour (NN) distance distributions, fully adapting to every dataset without any prior assumptions or thresholds of any sort.

On the biological side, VLAD was applied to brain mapping in the first large-scale triple colocalisation study of GluN1, PSD95 and SAP102 in the mouse hippocampus in development. In total, over 62.5 million puncta or puncta assemblies of these key synaptic proteins were analysed. This analysis captured the synaptic diversity arising from the combinatorial assembly of the three proteins into seven punctum (or assembly) subtypes and their differential distribution across hippocampal subregions. It was shown that the subtype compositions of the hippocampal subregions diverge during development and the differences in subtype compositions in the adult hippocampus may underlie the distinct functions performed by each component of the hippocampal circuit. The findings of this project invite further work to provide a detailed proteomic and electrophysiological characterisation of every synaptic subtype.

An unexpectedly high proportion of the puncta of each protein were non-colocalising in the adult mouse (67% of GluN1, 48% of PSD95 and 27% of SAP102) despite their known involvement in the postsynaptic density protein network. Another unexpected finding was the low representation of the GluN1-PSD95 subtype, which

never made up more than 1.3% of all puncta in the hippocampus in development. This hints at the possibility that the three proteins interact with each other in a co-dependent manner – it seems that, for the most part, NMDA receptors (GluN1) only interact with PSD95 when also in the presence of SAP102. The potential functional implications would have to be investigated further.

Lastly, the spatial relationships between the colocalising puncta were described, and it was found that the distance between colocalising scaffolding proteins (PSD95 and SAP102) remains shorter than the distance between each scaffolding protein and GluN1 during development.

The wealth of data generated during this project poses the new challenge of integrating large datasets in the context of brain mapping.

5.2 Imaging and colocalisation analysis

The focal point of this thesis was the development of the VLAD object-based colocalisation analysis method. A few aspects of fluorescence microscopy imaging will be discussed before reviewing future directions regarding the VLAD method.

The images analysed in this thesis were obtained with a spinning disc confocal microscope (SDM), with an axial resolution of approximately 500-800 nm. As a result, the focal plane imaged also contained projections from out-of-focus (OOF) puncta about 250-400 nm either side of the imaged plane. This means that the image data analysed here was not purely 2D, but instead a 2D projection of a relatively thin optical slice. OOF puncta projections come from a distance range highly relevant to true colocalisation (0-250 nm) and may skew the data obtained towards containing more short nearest neighbour (NN) distances.

Two alternatives exist for addressing this issue at the level of image acquisition. The first option would be acquiring small z-stacks (multiple planes imaged for the same field of view – FOV) made up of 3-5 imaging planes and spanning no more than 800 nm along the z-axis. Following the detection of puncta (and projections of OOF puncta) in all images, this would allow the exclusion of OOF puncta from the central plane, resulting in a true 2D image. This would benefit the VLAD colocalisation analysis, as VLAD is based on the theoretical description of NN distance distributions in 2D space without taking into account NN distances occurring between OOF puncta (and without accounting for any other optical aberrations,

even though some, such as chromatic shifts, could be mitigated by additional calibrations and image processing steps).

The second option would be acquiring ‘tall’ z-stacks to generate true 3D images. In the PSD95, SAP102 and GluN1 NN data analysed in this thesis, more than 80% of NN distances (sometimes closer to 95%) measured less than 1 µm in virtually every hippocampal region analysed. Assuming that, on the scale of a few micrometres, synaptic puncta are uniformly distributed in space, this would require imaging a z-stack spanning 2.5 µm to obtain a 500 nm-thick central section of true 3D data. With currently available microscopes and fluorescent proteins, this presents difficult technical challenges. First, image acquisition times would become prohibitively long for sampling whole brains or even just brain regions. Second, few currently available fluorophores (fluorescent proteins or synthetic molecules) could withstand the necessary amount of illumination in the same FOV without bleaching (losing their ability to fluoresce), imposing a hard limit on the thickness and sampling rate of any z-stack.

As neither of the z-stack options seems appealing in the context of whole-brain mapping, given the limited FOVs of current microscopes and the resilience of most available fluorophores, the prospect of accounting for OOF puncta at the image analysis level becomes more compelling. It may be possible to develop an analysis method that could appropriately account for OOF puncta based on a microscope’s measured axial resolution and, perhaps, observed puncta distribution patterns in single-plane images. Until such advancements are made, all of the above observations must be recognised as caveats inherent to the imaging system used.

Qualitative observations were made stating that both increased punctum densities and increased peak colocalisation distances (PCDs – NN distances at which ‘true’ colocalisation occurs) make colocalisation analysis more difficult, as the distribution of colocalised puncta becomes less and less distinguishable from randomness. These factors preclude colocalisation analysis as combinations and not individually. For example, colocalisation could still be measured between partners with long PCDs, provided that overall punctum densities were sufficiently low. A theoretical description of all combinations of densities and PCDs preventing colocalisation analysis could be made, to be used at the start of experiments in combination with statistical tests for the non-randomness of punctum distributions in experimental data.

5.3 VLAD: Future directions

The foundation and novelty of the VLAD method lie in its treatment of non-colocalising puncta and the NN distances measured between them in a completely adaptable way. VLAD successfully separates the contribution of non-colocalising puncta from its colocalisation measure in low colocalisation data without making any assumptions on the effect of punctum density, thus preserving its ability to accurately measure high colocalisation as well. This is perhaps the area where VLAD best differentiates itself from SODA (Statistical Object Distance Analysis), a colocalisation analysis method with seemingly similar performance (Lagache *et al.*, 2018). As shown in the comparison of VLAD and SODA, the latter underestimates colocalisation in high-colocalisation simulated data, possibly as a consequence of the 'statistical threshold' it employs, which only takes punctum density but not actual punctum distribution into account.

A strong case has been made for VLAD in its current form. However, multiple areas of future development still remain. The first, to be used in conjunction with correctly acquired 3D image data, would be an extension of VLAD to 3D colocalisation analysis, based on the same principles and on the available theoretical description of NN distance distributions between randomly distributed points in 3D (Torquato, Lu and Rubinstein, 1990).

Another area of improvement, and one where SODA is proficient, is measuring the stoichiometry of colocalisation (ratio between the numbers of colocalising puncta of different colocalisation partners). In the absence of a thorough exploration of this area, it is yet unclear whether the approach should include the analysis of 2^{nd}, 3^{rd} and n^{th} neighbour distance distributions (and whether applicable descriptions of n^{th} neighbour distance distributions between randomly distributed puncta exist) or whether it should be based on identifying clusters of points belonging to the same population and subsequently treating clusters as single points whose colocalisation could be readily measured.

Regarding technical (not theoretical) aspects, a first step should be an implementation of VLAD where the equation used for fitting Peak 2 (the NN distance distribution corresponding to non-colocalised puncta) is not over-parametrised. It should only include a scaling factor and a punctum density parameter, as described in This would also open the possibility of limiting the punctum density parameter to the observed punctum density in analysed data, potentially allowing the

measurement of colocalisation with markedly longer PCDs by facilitating the separation between Peaks 1 (colocalising NN distances) and 2 (non-colocalising NN distances) during the curve-fitting step of VLAD. However, imposing an upper limit for a parameter used in fitting should only be used following rigorous testing.

Another unexplored area of VLAD is finding an optimum between pooling a sufficient amount of data to allow reliable curve fitting while maintaining data heterogeneity to a minimum to allow the accurate assignment of probabilities of true colocalisation to individual NN distances (and pairs of puncta). A measure of the uniformity of colocalisation measured in different segments of a set of data could guide VLAD towards including more segments (if colocalisation is uniform) or towards separating the segments (if colocalisation differs significantly) to enable a better estimation of probabilities of true colocalisation. This should be performed without compromising the quality of curve fitting or dividing the data into segments so small that the presence of boundaries would negatively impact the measurement of NN distances. The nature of the experimental data analysed and the prioritisation of outcomes (measuring population-level colocalisation versus determining individual punctum colocalisation probabilities) would all need to be taken into account for such an optimisation.

Finally, VLAD could be turned into an application or a plugin for existing image analysis software and distributed to the wider scientific community. By standardising the inputs and outputs (sets of localisations and colocalisation measurements, respectively), VLAD could become a colocalisation analysis module ready to be integrated in pre-existing workflows and image analysis pipelines, from the colocalisation of molecules in single-particle tracking experiments to the colocalisation of synaptic protein puncta in brain mapping and potentially many more experiments.

5.4 Colocalisation analysis and brain mapping

The experimental data presented in this thesis, of the distribution and colocalisation of PSD95, SAP102 and GluN1 in the mouse hippocampus in development, was generated as part of an exploratory, non-hypothesis-driven study. Its analysis was in agreement with recently published mouse synaptome data (Zhu *et al.*, 2018) and also revealed novel organisational aspects of these synaptic proteins.

For example, the observation that GluN1 colocalises with PSD95, a well-known interaction partner, almost exclusively in the presence of SAP102 (as part of TRIPLE punctum assemblies and rarely GluN1-PSD95), had not been previously documented in this way.

Hippocampal inter-regional similarity relationships revealed by PSD95, SAP102 and GluN1 were in close agreement with those determined solely by PSD95 and SAP102 in the separate study of Zhu et al. (2018), raising the interesting possibility that a subset of synaptic proteins are sufficient for determining the protein composition of postsynaptic densities (PSDs). Furthermore, it was observed that many inter-regional relationships determined by synaptic protein punctum subtype composition were mirrored by inter-protein spatial relationships (PCDs) in those regions.

Lastly, the fact that no substantial gradients of punctum subtype composition exist within the Cornu Ammonis 1 Stratum Radiatum (CA1rad) over short distances (1-2 µm) despite documented functional gradients was unexpected. Furthermore, the differences in total punctum densities but not punctum subtype compositions along the radial axis of the CA1rad point to several possibilities on the organisation of brain networks. It is likely, based on the data presented in this study, that subtype composition (i.e. proportions of expressed punctum subtypes) is determined at a whole-cell level while synaptic protein punctum density may be determined by the density of inputs from a wider neural network.

All of these observations, enabled by a rigorous colocalisation analysis, open up new avenues of research. If executed well, large-scale non-hypothesis-driven brain mapping studies could have great power in guiding future research and formulating new hypotheses.

5.5 Concluding remarks

Colocalisation is of great relevance in the context of brain mapping, as demonstrated here and in the recently published synaptome maps of Zhu et al. (2018). The VLAD colocalisation analysis method is well-suited for such studies and my hope is that its adoption by neuroscientists will push the boundaries of our understanding of the brain ever further.

References

Aaron, J. S., Taylor, A. B. and Chew, T.-L. (2018) 'Image co-localization – co-occurrence versus correlation', *Journal of Cell Science*, 131(3), p. jcs211847. doi: 10.1242/jcs.211847.

Abramowitz, M. (Olympus A. *et al.* (2012) *Olympus Microscopy Resource Center*, *Introduction to Fluorescence*. Available at: http://www.olympusmicro.com/primer/lightandcolor/fluorointroduction.html%5Cnhttp://www.olympusmicro.com/primer/techniques/fluorescence/anatomy/fluoromicroanatomy.html.

Amaral, D. G. and Witter, M. P. (1989) 'The three-dimensional organization of the hippocampal formation: A review of anatomical data', *Neuroscience*. United States, 31(3), pp. 571–591. doi: 10.1016/0306-4522(89)90424-7.

Andor (no date) *Oxford Instruments*. Available at: https://www.oxinst.com/learning/.

Azevedo, F. A. C. *et al.* (2009) 'Equal numbers of neuronal and nonneuronal cells make the human brain an isometrically scaled-up primate brain', *Journal of Comparative Neurology*. United States, 513(5), pp. 532–541. doi: 10.1002/cne.21974.

Bayés, Á. *et al.* (2010) 'Characterization of the proteome, diseases and evolution of the human postsynaptic density', *Nature Neuroscience*, 14(1), pp. 19–21. doi: 10.1038/nn.2719.

Bayés, À. *et al.* (2012) 'Comparative Study of Human and Mouse Postsynaptic Proteomes Finds High Compositional Conservation and Abundance Differences for Key Synaptic Proteins', *PLoS ONE*, 7(10). doi: 10.1371/journal.pone.0046683.

Bayés, À. *et al.* (2017) 'Evolution of complexity in the zebrafish synapse proteome', *Nature Communications*, 8. doi: 10.1038/ncomms14613.

Bermudez-Hernandez, K. *et al.* (2017) 'A Method for Quantifying Molecular Interactions Using Stochastic Modelling and Super-Resolution Microscopy', *Scientific Reports*, 7(1), pp. 1–13. doi: 10.1038/s41598-017-14922-8.

Berry, K. P. and Nedivi, E. (2017) 'Spine Dynamics: Are They All the Same?', *Neuron*. Elsevier Inc., 96(1), pp. 43–55. doi: 10.1016/j.neuron.2017.08.008.

Bolte, S. and Cordelières, F. P. (2006) 'A guided tour into subcellular colocalization

analysis in light microscopy', *Journal of Microscopy*, 224(3), pp. 213–232. doi: 10.1111/j.1365-2818.2006.01706.x.

Bourne, J. N. and Harris, K. M. (2008) 'Balancing Structure and Function at Hippocampal Dendritic Spines', *Annual Review of Neuroscience*, 31(1), pp. 47–67. doi: 10.1146/annurev.neuro.31.060407.125646.

Broadhead, M. J. *et al.* (2016) 'PSD95 nanoclusters are postsynaptic building blocks in hippocampus circuits', *Scientific Reports*. Nature Publishing Group, 6, pp. 1–14. doi: 10.1038/srep24626.

Caetano, F. A. *et al.* (2015) 'MIiSR : Molecular Interactions in Super- Resolution Imaging Enables the Analysis of Protein Interactions , Dynamics and Formation of Multi-protein Structures', pp. 1–30. doi: 10.1371/journal.pcbi.1004634.

Cameron, H. A. and Glover, L. R. (2015) 'Adult neurogenesis: beyond learning and memory.', *Annual review of psychology*. United States, 66, pp. 53–81. doi: 10.1146/annurev-psych-010814-015006.

Carlisle, H. J. *et al.* (2008) 'Opposing effects of PSD-93 and PSD-95 on long-term potentiation and spike timing-dependent plasticity', *Journal of Physiology*, 586(24), pp. 5885–5900. doi: 10.1113/jphysiol.2008.163469.

Carr, M. F. and Frank, L. M. (2012) 'A single microcircuit with multiple functions: State dependent information processing in the hippocampus', *Current Opinion in Neurobiology*. Elsevier Ltd, 22(4), pp. 704–708. doi: 10.1016/j.conb.2012.03.007.

De Chaumont, F. *et al.* (2012) 'Icy: An open bioimage informatics platform for extended reproducible research', *Nature Methods*. United States, 9(7), pp. 690–696. doi: 10.1038/nmeth.2075.

Chen, B. S. *et al.* (2012) 'SAP102 Mediates Synaptic Clearance of NMDA Receptors', *Cell Reports*. The Authors, 2(5), pp. 1120–1128. doi: 10.1016/j.celrep.2012.09.024.

Chen, L. *et al.* (2000) 'Stargazin regulates synaptic targeting of AMPA receptors by two distinct mechanisms.', *Nature*. England, 408(6815), pp. 936–943. doi: 10.1038/35050030.

Chen, X. *et al.* (2011) 'PSD-95 Is Required to Sustain the Molecular Organization of the Postsynaptic Density', *Journal of Neuroscience*, 31(17), pp. 6329–6338. doi: 10.1523/JNEUROSCI.5968-10.2011.

Chenouard, N. *et al.* (2014) ‘Objective comparison of particle tracking methods’, *Nature Methods*, 11(3), pp. 281–289. doi: 10.1038/nmeth.2808.

Clark, P. J. and Evans, F. C. (1954) ‘Distance to Nearest Neighbor as a Measure of Spatial Relationships in Populations’, *Ecology*, 35(4), pp. 445–453. doi: 10.2307/1931034.

Collingridge, G. L., Kehl, S. J. and McLennan, H. (1983) ‘The antagonism of amino acid-induced excitations of rat hippocampal CA1 neurones in vitro.’, *The Journal of Physiology*, 334(1), pp. 19–31. doi: 10.1113/jphysiol.1983.sp014477.

Collman, F. *et al.* (2015) ‘Mapping Synapses by Conjugate Light-Electron Array Tomography’, *Journal of Neuroscience*, 35(14), pp. 5792–5807. doi: 10.1523/JNEUROSCI.4274-14.2015.

Costes, S. V. *et al.* (2004) ‘Automatic and quantitative measurement of protein-protein colocalization in live cells’, *Biophysical Journal*. Elsevier, 86(6), pp. 3993–4003. doi: 10.1529/biophysj.103.038422.

Craven, S. E., El-Husseini, A. E. and Bredt, D. S. (1999) ‘Synaptic targeting of the postsynaptic density protein PSD-95 mediated by lipid and protein motifs.’, *Neuron*. United States, 22(3), pp. 497–509.

Cuthbert, P. C. *et al.* (2007) ‘Synapse-Associated Protein 102/dlgh3 Couples the NMDA Receptor to Specific Plasticity Pathways and Learning Strategies’, *Journal of Neuroscience*, 27(10), pp. 2673–2682. doi: 10.1523/JNEUROSCI.4457-06.2007.

Dani, A. *et al.* (2010) ‘Superresolution Imaging of Chemical Synapses in the Brain’, *Neuron*. Elsevier, 68(5), pp. 843–856. doi: 10.1016/j.neuron.2010.11.021.

Dupuis, J. P. *et al.* (2014) ‘Surface dynamics of GluN2B-NMDA receptors controls plasticity of maturing glutamate synapses’, *EMBO Journal*, 33(8), pp. 842–861. doi: 10.1002/embj.201386356.

El-Husseini, A., Schnell, E. and Chetkovich, D. (2000) ‘PSD-95 involvement in maturation of excitatory synapses’, *Science*, 290(5495), pp. 1364–8. doi: 10.1126/science.290.5495.1364.

Elias, G. M. *et al.* (2006) ‘Synapse-Specific and Developmentally Regulated Targeting of AMPA Receptors by a Family of MAGUK Scaffolding Proteins’, *Neuron*, 52(2), pp. 307–320. doi: 10.1016/j.neuron.2006.09.012.

Eliscovich, C., Shenoy, S. M. and Singer, R. H. (2017) ‘Imaging mRNA and protein

interactions within neurons', *Proceedings of the National Academy of Sciences*, 114(10), pp. E1875–E1884. doi: 10.1073/pnas.1621440114.

Emes, R. D. *et al.* (2008) 'Evolutionary expansion and anatomical specialization of synapse proteome complexity', *Nature Neuroscience*, 11(7), pp. 799–806. doi: 10.1038/nn.2135.

Emes, R. D. and Grant, S. G. N. (2012) 'Evolution of Synapse Complexity and Diversity', *Annual Review of Neuroscience*, 35(1), pp. 111–131. doi: 10.1146/annurev-neuro-062111-150433.

Fawcett, T. (2006) 'An introduction to ROC analysis', *Pattern Recognition Letters*, 27(8), pp. 861–874. doi: 10.1016/j.patrec.2005.10.010.

Fernández, E. *et al.* (2009) 'Targeted tandem affinity purification of PSD-95 recovers core postsynaptic complexes and schizophrenia susceptibility proteins', *Molecular Systems Biology*, 5(269). doi: 10.1038/msb.2009.27.

Feyder, M. *et al.* (2010) 'Association of mouse Dlg4 (PSD-95) gene deletion and human DLG4 gene variation with phenotypes relevant to autism spectrum disorders and Williams' syndrome.', *The American journal of psychiatry*. United States, 167(12), pp. 1508–1517. doi: 10.1176/appi.ajp.2010.10040484.

Frackowiak, R. and Markram, H. (2015) 'The future of human cerebral cartography: A novel approach', *Philosophical Transactions of the Royal Society B: Biological Sciences*, 370(1668), pp. 20140171–20140171. doi: 10.1098/rstb.2014.0171.

Frank, R. A. and Grant, S. G. (2017) 'Supramolecular organization of NMDA receptors and the postsynaptic density', *Current Opinion in Neurobiology*, 45, pp. 139–147. doi: 10.1016/j.conb.2017.05.019.

Frank, R. A. W. *et al.* (2016) 'NMDA receptors are selectively partitioned into complexes and supercomplexes during synapse maturation', *Nature Communications*, 7. doi: 10.1038/ncomms11264.

Frank, R. A. W. *et al.* (2017) 'Hierarchical organization and genetically separable subfamilies of PSD95 postsynaptic supercomplexes', *Journal of Neurochemistry*, 142(4), pp. 504–511. doi: 10.1111/jnc.14056.

Gill, I. *et al.* (2015) 'Presynaptic NMDA receptors - dynamics and distribution in developing axons in vitro and in vivo', *Journal of Cell Science*, 128(4), pp. 768–780. doi: 10.1242/jcs.162362.

Gilles, J. F. *et al.* (2017) 'DiAna, an ImageJ tool for object-based 3D co-localization and distance analysis', *Methods*, 115, pp. 55–64. doi: 10.1016/j.ymeth.2016.11.016.

Gold, M. G. (2012) 'A frontier in the understanding of synaptic plasticity: Solving the structure of the postsynaptic density', *BioEssays*, 34(7), pp. 599–608. doi: 10.1002/bies.201200009.

Goodwin, P. C. (2007) 'Evaluating Optical Aberration Using Fluorescent Microspheres: Methods, Analysis, and Corrective Actions BT - Digital Microscopy', *Digital Microscopy*, 81(06), pp. 397–413. doi: 10.1016/S0091-679X(06)81018-6.

Gore, F. *et al.* (2015) 'Neural Representations of Unconditioned Stimuli in Basolateral Amygdala Mediate Innate and Learned Responses', *Cell*. Elsevier Inc., 162(1), pp. 134–145. doi: 10.1016/j.cell.2015.06.027.

Gräf, R., Rietdorf, J. and Zimmermann, T. (2005) 'Live cell spinning disk microscopy', *Advances in Biochemical Engineering/Biotechnology*, 95, pp. 57–75. doi: 10.1007/b102210.

Grant, S. G. N. (2007) 'Toward a molecular catalogue of synapses', *Brain Research Reviews*, 55(2 SPEC. ISS.), pp. 445–449. doi: 10.1016/j.brainresrev.2007.05.003.

Van Groen, T. and Wyss, J. M. (1990) 'Extrinsic projections from area CA1 of the rat hippocampus: Olfactory, cortical, subcortical, and bilateral hippocampal formation projections', *Journal of Comparative Neurology*. United States, 302(3), pp. 515–528. doi: 10.1002/cne.903020308.

Gumbel, E. (1935) 'Les valeurs extrêmes des distributions statistiques', *Annales de l'institut Henri Poincaré*, 2, pp. 115–158. doi: 10.2307/3205540.

Helmuth, J. A., Paul, G. and Sbalzarini, I. F. (2010) 'Beyond co-localization: Inferring spatial interactions between sub-cellular structures from microscopy images', *BMC Bioinformatics*, 11. doi: 10.1186/1471-2105-11-372.

Herculano-Houzel, S., Mota, B. and Lent, R. (2010) 'How to build a bigger brain: Cellular scaling rules for rodent brains', *Evolution of Nervous Systems*. United States, 3(32), pp. 155–166. doi: 10.1016/B0-12-370878-8/00345-1.

Hertz, P. (1909) ??'ber den gegenseitigen durchschnittlichen Abstand von Punkten, die mit bekannter mittlerer Dichte im Raume angeordnet sind', *Mathematische Annalen*, 67(3), pp. 387–398. doi: 10.1007/BF01450410.

Hogan-Cann, A. D. and Anderson, C. M. (2016) 'Physiological Roles of Non-

Neuronal NMDA Receptors', *Trends in Pharmacological Sciences*. Elsevier Ltd, 37(9), pp. 750–767. doi: 10.1016/j.tips.2016.05.012.

Hopp, T. P. *et al.* (1988) 'A Short Polpeptide Marker Sequence Useful For Recombinant Protein Identification And Purification', *Biotechnology*. Nature Publishing Group, 6, pp. 1204–1210. doi: 10.1038/nbt1088-1204.

Hotulainen, P. and Hoogenraad, C. C. (2010) 'Actin in dendritic spines: Connecting dynamics to function', *Journal of Cell Biology*, 189(4), pp. 619–629. doi: 10.1083/jcb.201003008.

Huang, X. *et al.* (2015) 'Progressive maturation of silent synapses governs the duration of a critical period', *Proceedings of the National Academy of Sciences*, 112(24), pp. E3131–E3140. doi: 10.1073/pnas.1506488112.

Hunt, D. L. and Castillo, P. E. (2012) 'Synaptic plasticity of NMDA receptors: Mechanisms and functional implications', *Current Opinion in Neurobiology*. Elsevier Ltd, 22(3), pp. 496–508. doi: 10.1016/j.conb.2012.01.007.

Husi, H. and Grant, S. G. N. (2001) 'Isolation of 2000-kDa complexes of N-methyl-D-aspartate receptor and postsynaptic density 95 from mouse brain', *Journal of Neurochemistry*, 77(1), pp. 281–291. doi: 10.1046/j.1471-4159.2001.t01-1-00248.x.

Igarashi, K. M. *et al.* (2014) 'Functional diversity along the transverse axis of hippocampal area CA1', *FEBS Letters*. Federation of European Biochemical Societies, 588(15), pp. 2470–2476. doi: 10.1016/j.febslet.2014.06.004.

Illian, J. *et al.* (2008) *Statistical Analysis and Modelling of Spatial Point Patterns*, *Statistical Analysis and Modelling of Spatial Point Patterns*. doi: 10.1002/9780470725160.

Iwabuchi, S. *et al.* (2014) 'Evaluation of the effectiveness of Gaussian filtering in distinguishing punctate synaptic signals from background noise during image analysis', *Journal of Neuroscience Methods*. Elsevier B.V., 223, pp. 92–113. doi: 10.1016/j.jneumeth.2013.12.003.

Jackson, J. H. and Beevor, C. E. (1889) 'Case of tumour of the right temporosphenoidal lobe bearing on the localisation of the sense of smell and on the interpretation of a particular variety of epilepsy', *Brain*. United States, 12(3), pp. 346–349. doi: 10.1093/brain/12.3.346.

Kaizuka, T. and Takumi, T. (2018) 'Postsynaptic density proteins and their

involvement in neurodevelopmental disorders', *Journal of Biochemistry*, 163(6), pp. 447–455. doi: 10.1093/jb/mvy022.

Karakas, E. and Furukawa, H. (2014) 'Crystal structure of a heterotetrameric NMDA receptor ion channel', *Science*. United States, 344(6187), pp. 992–997. doi: 10.1126/science.1251915.

Keller, H. E. (2006) 'Objective lenses for confocal microscopy', *Handbook of Biological Confocal Microscopy: Third Edition*, pp. 145–161. doi: 10.1007/978-0-387-45524-2_7.

Kim, E. and Sheng, M. (2004) 'PDZ domain proteins of synapses', *Nature Reviews Neuroscience*, 5(10), pp. 771–781. doi: 10.1038/nrn1517.

Kjelstrup, K. B. *et al.* (2008) 'Finite Scale of Spatial Represenation in the Hippocampus', *Science*, 321(July), pp. 140–143.

Komiyama, N. H. *et al.* (2018) 'Synaptic combinatorial molecular mechanisms generate repertoires of innate and learned behavior', *bioRxiv*, p. 500389. doi: 10.1101/500389.

Lagache, T. *et al.* (2015) 'Statistical analysis of molecule colocalization in bioimaging', *Cytometry Part A*, 87(6), pp. 568–579. doi: 10.1002/cyto.a.22629.

Lagache, T. *et al.* (2018) 'Mapping molecular assemblies with fluorescence microscopy and object-based spatial statistics', *Nature Communications*. Springer US, 9(1), pp. 102–108. doi: 10.1038/s41467-018-03053-x.

Lagache, T., Meas-Yedid, V. and Olivo-Marin, J. C. (2013) 'A statistical analysis of spatial colocalization using Ripley's K function', in *Proceedings - International Symposium on Biomedical Imaging*, pp. 896–901. doi: 10.1109/ISBI.2013.6556620.

Lambert, J. T. *et al.* (2017) 'Protracted and asynchronous accumulation of PSD95-family MAGUKs during maturation of nascent dendritic spines', *Developmental Neurobiology*, 77(10), pp. 1161–1174. doi: 10.1002/dneu.22503.

Lander, E. S. . L. *et al.* (2001) 'Initial sequencing and analysis of the human genome', *Nature*, 409(6822).

Lee, E. E. *et al.* (2015) 'Ketamine as a novel treatment for major depressive disorder and bipolar depression: A systematic review and quantitative meta-analysis', *General Hospital Psychiatry*. Elsevier B.V., 37(2), pp. 178–184. doi: 10.1016/j.genhosppsych.2015.01.003.

Lee, E. J., Choi, S. Y. and Kim, E. (2015) ‘NMDA receptor dysfunction in autism spectrum disorders’, *Current Opinion in Pharmacology*. Elsevier Ltd, 20, pp. 8–13. doi: 10.1016/j.coph.2014.10.007.

Lein, E. S. *et al.* (2007) ‘Genome-wide atlas of gene expression in the adult mouse brain’, *Nature*. England, 445(7124), pp. 168–176. doi: 10.1038/nature05453.

Lisman, J. (2017) ‘Glutamatergic synapses are structurally and biochemically complex because of multiple plasticity processes: Long-term potentiation, long-term depression, short-term potentiation and scaling’, *Philosophical Transactions of the Royal Society B: Biological Sciences*, 372(1715), p. 20160260. doi: 10.1098/rstb.2016.0260.

Lisman, J., Yasuda, R. and Raghavachari, S. (2012) ‘Mechanisms of CaMKII action in long-term potentiation’, *Nature Reviews Neuroscience*. Nature Publishing Group, 13(3), pp. 169–182. doi: 10.1038/nrn3192.

Liu, X. *et al.* (2012) ‘Optogenetic stimulation of a hippocampal engram activates fear memory recall’, *Nature*. Nature Publishing Group, 484(7394), pp. 381–385. doi: 10.1038/nature11028.

MacGillavry, H. D. *et al.* (2013) ‘Nanoscale scaffolding domains within the postsynaptic density concentrate synaptic ampa receptors’, *Neuron*. Elsevier, 78(4), pp. 615–622. doi: 10.1016/j.neuron.2013.03.009.

Malkusch, S. *et al.* (2012) ‘Coordinate-based colocalization analysis of single-molecule localization microscopy data’, *Histochemistry and Cell Biology*, 137(1), pp. 1–10. doi: 10.1007/s00418-011-0880-5.

Manders, E. M. M. *et al.* (1992) ‘Dynamics of three-dimensional replication patterns during the S-phase, analysed by double labelling of DNA and confocal microscopy’, *Journal of cell science*, 103 (Pt 3, pp. 857–862. Available at: c:%5CUsers%5CIvan_2%5CDocuments%5CReadCube Media%5CJ Cell Sci-1992-Manders-857-62 (1).pdf%5Cnhttp://www.ncbi.nlm.nih.gov/pubmed/1478975.

Manders, E. M. M., Verbeek, F. J. and Aten, J. A. (1993) ‘Measurement of co-localization of objects in dual-colour confocal images’, *Journal of Microscopy*. Wiley/Blackwell (10.1111), 169(3), pp. 375–382. doi: 10.1111/j.1365-2818.1993.tb03313.x.

Markram, H. (2006) ‘The Blue Brain Project’, *Nature Reviews Neuroscience*. Nature

Publishing Group, 7, p. 153. Available at: http://dx.doi.org/10.1038/nrn1848.

Migaud, M. *et al.* (1998) 'Enhanced long-term potentiation and impaired learning in mice with mutant postsynaptic density-95 protein', *Nature*, 396(6710), pp. 433–439. doi: 10.1038/24790.

Miller, S. L. and Yeh, H. H. (2016) *Neurotransmitters and Neurotransmission in the Developing and Adult Nervous System*, *Conn's Translational Neuroscience*. Elsevier Inc. doi: 10.1016/B978-0-12-802381-5.00004-X.

Morciano, M. *et al.* (2009) 'The proteome of the presynaptic active zone: From docked synaptic vesicles to adhesion molecules and maxi-channels', *Journal of Neurochemistry*. England, 108(3), pp. 662–675. doi: 10.1111/j.1471-4159.2008.05824.x.

Morris, R. G. M. (1982) 'Place navgation impaired in rats with hippocampal lesions', *Nature*. Nature Publishing Group, 297, p. 681. Available at: http://dx.doi.org/10.1038/297681a0.

Morris, R. G. M. *et al.* (1986) 'Selective impairment of learning and blockade of long-term potentiation by an N-methyl-D-aspartate receptor antagonist, AP5', *Nature*, 319(6056), pp. 774–776. doi: 10.1038/319774a0.

Morris, R. G. M. (2013) 'NMDA receptors and memory encoding', *Neuropharmacology*. Elsevier Ltd, 74, pp. 32–40. doi: 10.1016/j.neuropharm.2013.04.014.

Moser, M. B., Rowland, D. C. and Moser, E. I. (2015) 'Place cells, grid cells, and memory', *Cold Spring Harbor Perspectives in Biology*. United States, 7(2), p. a021808. doi: 10.1101/cshperspect.a021808.

Nair, D. *et al.* (2013) 'Super-Resolution Imaging Reveals That AMPA Receptors Inside Synapses Are Dynamically Organized in Nanodomains Regulated by PSD95', *Journal of Neuroscience*, 33(32), pp. 13204–13224. doi: 10.1523/JNEUROSCI.2381-12.2013.

Neunuebel, J. P. and Knierim, J. J. (2014) 'CA3 retrieves coherent representations from degraded input: Direct evidence for CA3 pattern completion and dentate gyrus pattern separation', *Neuron*. Elsevier Inc., 81(2), pp. 416–427. doi: 10.1016/j.neuron.2013.11.017.

Nithianantharajah, J. *et al.* (2013) 'Synaptic scaffold evolution generated

components of vertebrate cognitive complexity', *Nature Neuroscience*, 16(1), pp. 16–24. doi: 10.1038/nn.3276.

Nithianantharajah, J. and Grant, S. G. N. (2013) 'Cognitive components in mice and humans: Combining genetics and touchscreens for medical translation', *Neurobiology of Learning and Memory*. Elsevier Inc., 105, pp. 13–19. doi: 10.1016/j.nlm.2013.06.006.

O'Rourke, N. A. *et al.* (2012) 'Deep molecular diversity of mammalian synapses: Why it matters and how to measure it', *Nature Reviews Neuroscience*. Nature Publishing Group, 13(6), pp. 365–379. doi: 10.1038/nrn3170.

Oh, S. W. *et al.* (2014) 'A mesoscale connectome of the mouse brain', *Nature*. Nature Publishing Group, 508(7495), pp. 207–214. doi: 10.1038/nature13186.

Ovesný, M. *et al.* (2014) 'ThunderSTORM: A comprehensive ImageJ plug-in for PALM and STORM data analysis and super-resolution imaging', *Bioinformatics*, 30(16), pp. 2389–2390. doi: 10.1093/bioinformatics/btu202.

Paoletti, P., Bellone, C. and Zhou, Q. (2013) 'NMDA receptor subunit diversity: Impact on receptor properties, synaptic plasticity and disease', *Nature Reviews Neuroscience*. Nature Publishing Group, 14(6), pp. 383–400. doi: 10.1038/nrn3504.

Papouin, T. and Oliet, S. H. R. (2014) 'Organization, Control and function of extrasynaptic NMDA receptors', *Philosophical Transactions of the Royal Society B: Biological Sciences*, 369(1654), pp. 18–21. doi: 10.1098/rstb.2013.0601.

Van De Peer, Y., Maere, S. and Meyer, A. (2009) 'The evolutionary significance of ancient genome duplications', *Nature Reviews Genetics*. Nature Publishing Group, 10(10), pp. 725–732. doi: 10.1038/nrg2600.

Petralia, R. S. *et al.* (2010) 'Organization of NMDA receptors at extrasynaptic locations', *Neuroscience*. Elsevier Inc., 167(1), pp. 68–87. doi: 10.1016/j.neuroscience.2010.01.022.

Petralia, R. S. (2012) 'Distribution of extrasynaptic NMDA receptors on neurons', *The Scientific World Journal*, 2012, pp. 1–11. doi: 10.1100/2012/267120.

Ripley, B. D. (1976) 'The Second-Order Analysis of Stationary Point Processes', *Journal of Applied Probability*, 13(2), p. 255. doi: 10.2307/3212829.

Roy, M., Sorokina, O., Skene, N., *et al.* (2018) 'Proteomic analysis of postsynaptic proteins in regions of the human neocortex', *Nature Neuroscience*. Springer US,

21(1), pp. 130–141. doi: 10.1038/s41593-017-0025-9.

Roy, M., Sorokina, O., McLean, C., *et al.* (2018) 'Regional Diversity in the Postsynaptic Proteome of the Mouse Brain', *Proteomes*, 6(3), p. 31. doi: 10.3390/proteomes6030031.

Ryan, T. J. *et al.* (2015) 'Engram cells retain memory under retrograde amnesia', *Science*, 348(6238), pp. 1007–1013. doi: 10.1126/science.aaa5542.

Ryan, T. J. and Grant, S. G. N. (2009) 'The origin and evolution of synapses', *Nature Reviews Neuroscience*, 10(11), pp. 701–712. doi: 10.1038/nrn2748.

Sans, N. *et al.* (2000) 'A developmental change in NMDA receptor-associated proteins at hippocampal synapses.', *The Journal of neuroscience : the official journal of the Society for Neuroscience*, 20(3), pp. 1260–1271. doi: 10.1016/j.nlm.2011.01.004.Bidirectional.

Sanz-Clemente, A., Nicoll, R. A. and Roche, K. W. (2013) 'Diversity in NMDA receptor composition: Many regulators, many consequences', *Neuroscientist*, 19(1), pp. 62–75. doi: 10.1177/1073858411435129.

Schindelin, J. *et al.* (2012) 'Fiji: An open-source platform for biological-image analysis', *Nature Methods*, 9(7), pp. 676–682. doi: 10.1038/nmeth.2019.

Schirra, R. T. and Zhang, P. (2014) 'Correlative fluorescence and electron microscopy', *Current Protocols in Cytometry*, 2014, p. 12.36.1-12.36.10. doi: 10.1002/0471142956.cy1236s70.

Schluter, O. M., Xu, W. and Malenka, R. C. (2006) 'Alternative N-terminal domains of PSD-95 and SAP97 govern activity-dependent regulation of synaptic AMPA receptor function.', *Neuron*. United States, 51(1), pp. 99–111. doi: 10.1016/j.neuron.2006.05.016.

Schüz, A. and Palm, G. (1989) 'Density of neurons and synapses in the cerebral cortex of the mouse', *Journal of Comparative Neurology*, 286(4), pp. 442–455. doi: 10.1002/cne.902860404.

Sheng, M. and Hoogenraad, C. C. (2007) 'The Postsynaptic Architecture of Excitatory Synapses: A More Quantitative View', *Annual Review of Biochemistry*, 76(1), pp. 823–847. doi: 10.1146/annurev.biochem.76.060805.160029.

Shinohara, Y. *et al.* (2008) 'Left-right asymmetry of the hippocampal synapses with differential subunit allocation of glutamate receptors', *Proceedings of the National*

Academy of Sciences. United States, 105(49), pp. 19498–19503. doi: 10.1073/pnas.0807461105.

Shinohara, Y. (2009) 'Size and receptor density of glutamatergic synapses: a viewpoint from left-right asymmetry of CA3-CA1 connections', *Frontiers in Neuroanatomy*, 3(July), pp. 1–6. doi: 10.3389/neuro.05.010.2009.

Simhal, A. K. *et al.* (2017) 'Probabilistic fluorescence-based synapse detection', *PLoS Computational Biology*, 13(4), pp. 1–24. doi: 10.1371/journal.pcbi.1005493.

Spiess, A. N. and Neumeyer, N. (2010) 'An evaluation of R2as an inadequate measure for nonlinear models in pharmacological and biochemical research: A Monte Carlo approach', *BMC Pharmacology*, 10, pp. 1–11. doi: 10.1186/1471-2210-10-6.

Strange, B. A. *et al.* (2014) 'Functional organization of the hippocampal longitudinal axis', *Nature Reviews Neuroscience*. Nature Publishing Group, 15(10), pp. 655–669. doi: 10.1038/nrn3785.

Sytnyk, V. *et al.* (2006) 'NCAM promotes assembly and activity-dependent remodeling of the postsynaptic signaling complex', *Journal of Cell Biology*, 174(7), pp. 1071–1085. doi: 10.1083/jcb.200604145.

Tao-Cheng, J. H. *et al.* (2014) 'Homer is concentrated at the postsynaptic density and does not redistribute after acute synaptic stimulation', *Neuroscience*, 266(301), pp. 80–90. doi: 10.1016/j.neuroscience.2014.01.066.

Tarpey, P. *et al.* (2004) 'Mutations in the DLG3 gene cause nonsyndromic X-linked mental retardation.', *American journal of human genetics*. United States, 75(2), pp. 318–324. doi: 10.1086/422703.

Thompson, C. L. *et al.* (2008) 'Genomic Anatomy of the Hippocampus', *Neuron*. Elsevier Ltd, 60(6), pp. 1010–1021. doi: 10.1016/j.neuron.2008.12.008.

Tinevez, J. Y. *et al.* (2017) 'TrackMate: An open and extensible platform for single-particle tracking', *Methods*. The Author(s), 115, pp. 80–90. doi: 10.1016/j.ymeth.2016.09.016.

Tonegawa, S. *et al.* (2015) 'Memory engram storage and retrieval', *Current Opinion in Neurobiology*, 35, pp. 101–109. doi: 10.1016/j.conb.2015.07.009.

Torquato, S., Lu, B. and Rubinstein, J. (1990) 'Nearest-neighbor distribution functions in many-body systems', *Physical Review A*. American Physical Society,

41(4), pp. 2059–2075. doi: 10.1103/PhysRevA.41.2059.

Tovar, K. R. and Westbrook, G. L. (2002) ‘Mobile NMDA receptors at hippocampal synapses’, *Neuron*, 34(2), pp. 255–264. doi: 10.1016/S0896-6273(02)00658-X.

Traynelis, S. *et al.* (2010) ‘Glutamate Receptor Ion Channels : Structure , Regulation , and Function’, *Pharmacological Reviews*. Edited by D. Sibley, 62(3), p. 405 LP-496. doi: 10.1124/pr.109.002451.405.

Valtschanoff, J. G. and Weinberg, R. J. (2001) ‘Laminar organization of the NMDA receptor complex within the postsynaptic density.’, *The Journal of neuroscience : the official journal of the Society for Neuroscience*, 21(4), pp. 1211–7. doi: 21/4/1211 [pii].

Vazdarjanova, A. (2004) ‘Differences in Hippocampal Neuronal Population Responses to Modifications of an Environmental Context: Evidence for Distinct, Yet Complementary, Functions of CA3 and CA1 Ensembles’, *Journal of Neuroscience*, 24(29), pp. 6489–6496. doi: 10.1523/JNEUROSCI.0350-04.2004.

Wang, P. Y. *et al.* (2011) ‘Functional NMDA Receptors at Axonal Growth Cones of Young Hippocampal Neurons’, *Journal of Neuroscience*, 31(25), pp. 9289–9297. doi: 10.1523/JNEUROSCI.5639-10.2011.

Washbourne, P. (2004) ‘Cycling of NMDA Receptors during Trafficking in Neurons before Synapse Formation’, *Journal of Neuroscience*, 24(38), pp. 8253–8264. doi: 10.1523/JNEUROSCI.2555-04.2004.

Weingarten, J. *et al.* (2014) ‘The proteome of the presynaptic active zone from mouse brain’, *Molecular and Cellular Neuroscience*. Elsevier Inc., 59, pp. 106–118. doi: 10.1016/j.mcn.2014.02.003.

Wiegand, T. and Moloney, K. A. (2004) ‘Rings, circles, and null-models for point pattern analysis in ecology’, *Oikos*, pp. 209–229. doi: 10.1111/j.0030-1299.2004.12497.x.

Won, S. *et al.* (2017) ‘MAGUKs: multifaceted synaptic organizers’, *Current Opinion in Neurobiology*. Elsevier Ltd, 43, pp. 94–101. doi: 10.1016/j.conb.2017.01.006.

Wurm, C. A. *et al.* (2010) ‘Sample Preparation for STED Microscopy BT - Live Cell Imaging: Methods and Protocols’, in Papkovsky, D. B. (ed.). Totowa, NJ: Humana Press, pp. 185–199. doi: 10.1007/978-1-60761-404-3_11.

Yassa, M. A. and Stark, C. E. L. (2011) ‘Pattern separation in the hippocampus’,

Trends in Neurosciences. Elsevier Ltd, 34(10), pp. 515–525. doi: 10.1016/j.tins.2011.06.006.

Zhang, B. *et al.* (2008) 'Statistical colocalization in biological imaging with false discovery control', *2008 5th IEEE International Symposium on Biomedical Imaging: From Nano to Macro, Proceedings, ISBI*, pp. 1327–1330. doi: 10.1109/ISBI.2008.4541249.

Zhang, B. and Chenouard, N. (2008) 'STATISTICAL COLOCALIZATION IN BIOLOGICAL IMAGING WITH FALSE DISCOVERY CONTROL Unit ´ e Analyse d ' Images Quantitative Institut Pasteur 75015 Paris France', pp. 1327–1330.

Zheng, C. Y. *et al.* (2010) 'SAP102 Is a Highly Mobile MAGUK in Spines', *Journal of Neuroscience*, 30(13), pp. 4757–4766. doi: 10.1523/JNEUROSCI.6108-09.2010.

Zheng, C. Y. *et al.* (2011) 'MAGUKs, synaptic development, and synaptic plasticity', *Neuroscientist*, 17(5), pp. 493–512. doi: 10.1177/1073858410386384.

Zhu, F. *et al.* (2018) 'Architecture of the Mouse Brain Synaptome', *Neuron*, 99(4), p. 781–799.e10. doi: 10.1016/j.neuron.2018.07.007.

Zhu, J., Shang, Y. and Zhang, M. (2016) 'Mechanistic basis of MAGUK-organized complexes in synaptic development and signalling', *Nature Reviews Neuroscience*. Nature Publishing Group, 17(4), pp. 209–223. doi: 10.1038/nrn.2016.18.

Aaron, J. S., Taylor, A. B. and Chew, T.-L. (2018) 'Image co-localization – co-occurrence versus correlation', *Journal of Cell Science*, 131(3), p. jcs211847. doi: 10.1242/jcs.211847.

Abramowitz, M. (Olympus A. *et al.* (2012) *Olympus Microscopy Resource Center*, *Introduction to Fluorescence*. Available at: http://www.olympusmicro.com/primer/lightandcolor/fluorointroduction.html%5Cnhttp://www.olympusmicro.com/primer/techniques/fluorescence/anatomy/fluoromicroanatomy.html.

Amaral, D. G. and Witter, M. P. (1989) 'The three-dimensional organization of the hippocampal formation: A review of anatomical data', *Neuroscience*. United States, 31(3), pp. 571–591. doi: 10.1016/0306-4522(89)90424-7.

Andor (no date) *Oxford Instruments*. Available at: https://www.oxinst.com/learning/.

Azevedo, F. A. C. *et al.* (2009) 'Equal numbers of neuronal and nonneuronal cells make the human brain an isometrically scaled-up primate brain', *Journal of*

Comparative Neurology. United States, 513(5), pp. 532–541. doi: 10.1002/cne.21974.

Bayés, Á. *et al.* (2010) 'Characterization of the proteome, diseases and evolution of the human postsynaptic density', *Nature Neuroscience*, 14(1), pp. 19–21. doi: 10.1038/nn.2719.

Bayés, À. *et al.* (2012) 'Comparative Study of Human and Mouse Postsynaptic Proteomes Finds High Compositional Conservation and Abundance Differences for Key Synaptic Proteins', *PLoS ONE*, 7(10). doi: 10.1371/journal.pone.0046683.

Bayés, À. *et al.* (2017) 'Evolution of complexity in the zebrafish synapse proteome', *Nature Communications*, 8. doi: 10.1038/ncomms14613.

Bermudez-Hernandez, K. *et al.* (2017) 'A Method for Quantifying Molecular Interactions Using Stochastic Modelling and Super-Resolution Microscopy', *Scientific Reports*, 7(1), pp. 1–13. doi: 10.1038/s41598-017-14922-8.

Berry, K. P. and Nedivi, E. (2017) 'Spine Dynamics: Are They All the Same?', *Neuron*. Elsevier Inc., 96(1), pp. 43–55. doi: 10.1016/j.neuron.2017.08.008.

Bolte, S. and Cordelières, F. P. (2006) 'A guided tour into subcellular colocalization analysis in light microscopy', *Journal of Microscopy*, 224(3), pp. 213–232. doi: 10.1111/j.1365-2818.2006.01706.x.

Bourne, J. N. and Harris, K. M. (2008) 'Balancing Structure and Function at Hippocampal Dendritic Spines', *Annual Review of Neuroscience*, 31(1), pp. 47–67. doi: 10.1146/annurev.neuro.31.060407.125646.

Broadhead, M. J. *et al.* (2016) 'PSD95 nanoclusters are postsynaptic building blocks in hippocampus circuits', *Scientific Reports*. Nature Publishing Group, 6, pp. 1–14. doi: 10.1038/srep24626.

Caetano, F. A. *et al.* (2015) 'MIiSR : Molecular Interactions in Super- Resolution Imaging Enables the Analysis of Protein Interactions , Dynamics and Formation of Multi-protein Structures', pp. 1–30. doi: 10.1371/journal.pcbi.1004634.

Cameron, H. A. and Glover, L. R. (2015) 'Adult neurogenesis: beyond learning and memory.', *Annual review of psychology*. United States, 66, pp. 53–81. doi: 10.1146/annurev-psych-010814-015006.

Carlisle, H. J. *et al.* (2008) 'Opposing effects of PSD-93 and PSD-95 on long-term potentiation and spike timing-dependent plasticity', *Journal of Physiology*, 586(24),

pp. 5885–5900. doi: 10.1113/jphysiol.2008.163469.

Carr, M. F. and Frank, L. M. (2012) ‘A single microcircuit with multiple functions: State dependent information processing in the hippocampus’, *Current Opinion in Neurobiology*. Elsevier Ltd, 22(4), pp. 704–708. doi: 10.1016/j.conb.2012.03.007.

De Chaumont, F. *et al.* (2012) ‘Icy: An open bioimage informatics platform for extended reproducible research’, *Nature Methods*. United States, 9(7), pp. 690–696. doi: 10.1038/nmeth.2075.

Chen, B. S. *et al.* (2012) ‘SAP102 Mediates Synaptic Clearance of NMDA Receptors’, *Cell Reports*. The Authors, 2(5), pp. 1120–1128. doi: 10.1016/j.celrep.2012.09.024.

Chen, L. *et al.* (2000) ‘Stargazin regulates synaptic targeting of AMPA receptors by two distinct mechanisms.’, *Nature*. England, 408(6815), pp. 936–943. doi: 10.1038/35050030.

Chen, X. *et al.* (2011) ‘PSD-95 Is Required to Sustain the Molecular Organization of the Postsynaptic Density’, *Journal of Neuroscience*, 31(17), pp. 6329–6338. doi: 10.1523/JNEUROSCI.5968-10.2011.

Chenouard, N. *et al.* (2014) ‘Objective comparison of particle tracking methods’, *Nature Methods*, 11(3), pp. 281–289. doi: 10.1038/nmeth.2808.

Clark, P. J. and Evans, F. C. (1954) ‘Distance to Nearest Neighbor as a Measure of Spatial Relationships in Populations’, *Ecology*, 35(4), pp. 445–453. doi: 10.2307/1931034.

Collingridge, G. L., Kehl, S. J. and McLennan, H. (1983) ‘The antagonism of amino acid-induced excitations of rat hippocampal CA1 neurones in vitro.’, *The Journal of Physiology*, 334(1), pp. 19–31. doi: 10.1113/jphysiol.1983.sp014477.

Collman, F. *et al.* (2015) ‘Mapping Synapses by Conjugate Light-Electron Array Tomography’, *Journal of Neuroscience*, 35(14), pp. 5792–5807. doi: 10.1523/JNEUROSCI.4274-14.2015.

Costes, S. V. *et al.* (2004) ‘Automatic and quantitative measurement of protein-protein colocalization in live cells’, *Biophysical Journal*. Elsevier, 86(6), pp. 3993–4003. doi: 10.1529/biophysj.103.038422.

Craven, S. E., El-Husseini, A. E. and Bredt, D. S. (1999) ‘Synaptic targeting of the postsynaptic density protein PSD-95 mediated by lipid and protein motifs.’, *Neuron*.

United States, 22(3), pp. 497–509.

Cuthbert, P. C. *et al.* (2007) 'Synapse-Associated Protein 102/dlgh3 Couples the NMDA Receptor to Specific Plasticity Pathways and Learning Strategies', *Journal of Neuroscience*, 27(10), pp. 2673–2682. doi: 10.1523/JNEUROSCI.4457-06.2007.

Dani, A. *et al.* (2010) 'Superresolution Imaging of Chemical Synapses in the Brain', *Neuron*. Elsevier, 68(5), pp. 843–856. doi: 10.1016/j.neuron.2010.11.021.

Dupuis, J. P. *et al.* (2014) 'Surface dynamics of GluN2B-NMDA receptors controls plasticity of maturing glutamate synapses', *EMBO Journal*, 33(8), pp. 842–861. doi: 10.1002/embj.201386356.

El-Husseini, A., Schnell, E. and Chetkovich, D. (2000) 'PSD-95 involvement in maturation of excitatory synapses', *Science*, 290(5495), pp. 1364–8. doi: 10.1126/science.290.5495.1364.

Elias, G. M. *et al.* (2006) 'Synapse-Specific and Developmentally Regulated Targeting of AMPA Receptors by a Family of MAGUK Scaffolding Proteins', *Neuron*, 52(2), pp. 307–320. doi: 10.1016/j.neuron.2006.09.012.

Eliscovich, C., Shenoy, S. M. and Singer, R. H. (2017) 'Imaging mRNA and protein interactions within neurons', *Proceedings of the National Academy of Sciences*, 114(10), pp. E1875–E1884. doi: 10.1073/pnas.1621440114.

Emes, R. D. *et al.* (2008) 'Evolutionary expansion and anatomical specialization of synapse proteome complexity', *Nature Neuroscience*, 11(7), pp. 799–806. doi: 10.1038/nn.2135.

Emes, R. D. and Grant, S. G. N. (2012) 'Evolution of Synapse Complexity and Diversity', *Annual Review of Neuroscience*, 35(1), pp. 111–131. doi: 10.1146/annurev-neuro-062111-150433.

Fawcett, T. (2006) 'An introduction to ROC analysis', *Pattern Recognition Letters*, 27(8), pp. 861–874. doi: 10.1016/j.patrec.2005.10.010.

Fernández, E. *et al.* (2009) 'Targeted tandem affinity purification of PSD-95 recovers core postsynaptic complexes and schizophrenia susceptibility proteins', *Molecular Systems Biology*, 5(269). doi: 10.1038/msb.2009.27.

Feyder, M. *et al.* (2010) 'Association of mouse Dlg4 (PSD-95) gene deletion and human DLG4 gene variation with phenotypes relevant to autism spectrum disorders and Williams' syndrome.', *The American journal of psychiatry*. United States,

167(12), pp. 1508–1517. doi: 10.1176/appi.ajp.2010.10040484.

Frackowiak, R. and Markram, H. (2015) ‘The future of human cerebral cartography: A novel approach’, *Philosophical Transactions of the Royal Society B: Biological Sciences*, 370(1668), pp. 20140171–20140171. doi: 10.1098/rstb.2014.0171.

Frank, R. A. and Grant, S. G. (2017) ‘Supramolecular organization of NMDA receptors and the postsynaptic density’, *Current Opinion in Neurobiology*, 45, pp. 139–147. doi: 10.1016/j.conb.2017.05.019.

Frank, R. A. W. *et al.* (2016) ‘NMDA receptors are selectively partitioned into complexes and supercomplexes during synapse maturation’, *Nature Communications*, 7. doi: 10.1038/ncomms11264.

Frank, R. A. W. *et al.* (2017) ‘Hierarchical organization and genetically separable subfamilies of PSD95 postsynaptic supercomplexes’, *Journal of Neurochemistry*, 142(4), pp. 504–511. doi: 10.1111/jnc.14056.

Gill, I. *et al.* (2015) ‘Presynaptic NMDA receptors - dynamics and distribution in developing axons in vitro and in vivo’, *Journal of Cell Science*, 128(4), pp. 768–780. doi: 10.1242/jcs.162362.

Gilles, J. F. *et al.* (2017) ‘DiAna, an ImageJ tool for object-based 3D co-localization and distance analysis’, *Methods*, 115, pp. 55–64. doi: 10.1016/j.ymeth.2016.11.016.

Gold, M. G. (2012) ‘A frontier in the understanding of synaptic plasticity: Solving the structure of the postsynaptic density’, *BioEssays*, 34(7), pp. 599–608. doi: 10.1002/bies.201200009.

Goodwin, P. C. (2007) ‘Evaluating Optical Aberration Using Fluorescent Microspheres: Methods, Analysis, and Corrective Actions BT - Digital Microscopy’, *Digital Microscopy*, 81(06), pp. 397–413. doi: 10.1016/S0091-679X(06)81018-6.

Gore, F. *et al.* (2015) ‘Neural Representations of Unconditioned Stimuli in Basolateral Amygdala Mediate Innate and Learned Responses’, *Cell*. Elsevier Inc., 162(1), pp. 134–145. doi: 10.1016/j.cell.2015.06.027.

Gräf, R., Rietdorf, J. and Zimmermann, T. (2005) ‘Live cell spinning disk microscopy’, *Advances in Biochemical Engineering/Biotechnology*, 95, pp. 57–75. doi: 10.1007/b102210.

Grant, S. G. N. (2007) ‘Toward a molecular catalogue of synapses’, *Brain Research Reviews*, 55(2 SPEC. ISS.), pp. 445–449. doi: 10.1016/j.brainresrev.2007.05.003.

Van Groen, T. and Wyss, J. M. (1990) ‘Extrinsic projections from area CA1 of the rat hippocampus: Olfactory, cortical, subcortical, and bilateral hippocampal formation projections’, *Journal of Comparative Neurology*. United States, 302(3), pp. 515–528. doi: 10.1002/cne.903020308.

Gumbel, E. (1935) ‘Les valeurs extrêmes des distributions statistiques’, *Annales de l’institut Henri Poincaré*, 2, pp. 115–158. doi: 10.2307/3205540.

Helmuth, J. A., Paul, G. and Sbalzarini, I. F. (2010) ‘Beyond co-localization: Inferring spatial interactions between sub-cellular structures from microscopy images’, *BMC Bioinformatics*, 11. doi: 10.1186/1471-2105-11-372.

Herculano-Houzel, S., Mota, B. and Lent, R. (2010) ‘How to build a bigger brain: Cellular scaling rules for rodent brains’, *Evolution of Nervous Systems*. United States, 3(32), pp. 155–166. doi: 10.1016/B0-12-370878-8/00345-1.

Hertz, P. (1909) ??‘ber den gegenseitigen durchschnittlichen Abstand von Punkten, die mit bekannter mittlerer Dichte im Raume angeordnet sind’, *Mathematische Annalen*, 67(3), pp. 387–398. doi: 10.1007/BF01450410.

Hogan-Cann, A. D. and Anderson, C. M. (2016) ‘Physiological Roles of Non-Neuronal NMDA Receptors’, *Trends in Pharmacological Sciences*. Elsevier Ltd, 37(9), pp. 750–767. doi: 10.1016/j.tips.2016.05.012.

Hopp, T. P. *et al.* (1988) ‘A Short Polpeptide Marker Sequence Useful For Recombinant Protein Identification And Purification’, *Biotechnology*. Nature Publishing Group, 6, pp. 1204–1210. doi: 10.1038/nbt1088-1204.

Hotulainen, P. and Hoogenraad, C. C. (2010) ‘Actin in dendritic spines: Connecting dynamics to function’, *Journal of Cell Biology*, 189(4), pp. 619–629. doi: 10.1083/jcb.201003008.

Huang, X. *et al.* (2015) ‘Progressive maturation of silent synapses governs the duration of a critical period’, *Proceedings of the National Academy of Sciences*, 112(24), pp. E3131–E3140. doi: 10.1073/pnas.1506488112.

Hunt, D. L. and Castillo, P. E. (2012) ‘Synaptic plasticity of NMDA receptors: Mechanisms and functional implications’, *Current Opinion in Neurobiology*. Elsevier Ltd, 22(3), pp. 496–508. doi: 10.1016/j.conb.2012.01.007.

Husi, H. and Grant, S. G. N. (2001) ‘Isolation of 2000-kDa complexes of N-methyl-D-aspartate receptor and postsynaptic density 95 from mouse brain’, *Journal of*

Neurochemistry, 77(1), pp. 281–291. doi: 10.1046/j.1471-4159.2001.t01-1-00248.x.

Igarashi, K. M. *et al.* (2014) 'Functional diversity along the transverse axis of hippocampal area CA1', *FEBS Letters*. Federation of European Biochemical Societies, 588(15), pp. 2470–2476. doi: 10.1016/j.febslet.2014.06.004.

Illian, J. *et al.* (2008) *Statistical Analysis and Modelling of Spatial Point Patterns*, *Statistical Analysis and Modelling of Spatial Point Patterns*. doi: 10.1002/9780470725160.

Iwabuchi, S. *et al.* (2014) 'Evaluation of the effectiveness of Gaussian filtering in distinguishing punctate synaptic signals from background noise during image analysis', *Journal of Neuroscience Methods*. Elsevier B.V., 223, pp. 92–113. doi: 10.1016/j.jneumeth.2013.12.003.

Jackson, J. H. and Beevor, C. E. (1889) 'Case of tumour of the right temporosphenoidal lobe bearing on the localisation of the sense of smell and on the interpretation of a particular variety of epilepsy', *Brain*. United States, 12(3), pp. 346–349. doi: 10.1093/brain/12.3.346.

Kaizuka, T. and Takumi, T. (2018) 'Postsynaptic density proteins and their involvement in neurodevelopmental disorders', *Journal of Biochemistry*, 163(6), pp. 447–455. doi: 10.1093/jb/mvy022.

Karakas, E. and Furukawa, H. (2014) 'Crystal structure of a heterotetrameric NMDA receptor ion channel', *Science*. United States, 344(6187), pp. 992–997. doi: 10.1126/science.1251915.

Keller, H. E. (2006) 'Objective lenses for confocal microscopy', *Handbook of Biological Confocal Microscopy: Third Edition*, pp. 145–161. doi: 10.1007/978-0-387-45524-2_7.

Kim, E. and Sheng, M. (2004) 'PDZ domain proteins of synapses', *Nature Reviews Neuroscience*, 5(10), pp. 771–781. doi: 10.1038/nrn1517.

Kjelstrup, K. B. *et al.* (2008) 'Finite Scale of Spatial Represenation in the Hippocampus', *Science*, 321(July), pp. 140–143.

Komiyama, N. H. *et al.* (2018) 'Synaptic combinatorial molecular mechanisms generate repertoires of innate and learned behavior', *bioRxiv*, p. 500389. doi: 10.1101/500389.

Lagache, T. *et al.* (2015) 'Statistical analysis of molecule colocalization in

bioimaging', *Cytometry Part A*, 87(6), pp. 568–579. doi: 10.1002/cyto.a.22629.

Lagache, T. *et al.* (2018) 'Mapping molecular assemblies with fluorescence microscopy and object-based spatial statistics', *Nature Communications*. Springer US, 9(1), pp. 102–108. doi: 10.1038/s41467-018-03053-x.

Lagache, T., Meas-Yedid, V. and Olivo-Marin, J. C. (2013) 'A statistical analysis of spatial colocalization using Ripley's K function', in *Proceedings - International Symposium on Biomedical Imaging*, pp. 896–901. doi: 10.1109/ISBI.2013.6556620.

Lambert, J. T. *et al.* (2017) 'Protracted and asynchronous accumulation of PSD95-family MAGUKs during maturation of nascent dendritic spines', *Developmental Neurobiology*, 77(10), pp. 1161–1174. doi: 10.1002/dneu.22503.

Lander, E. S. . L. *et al.* (2001) 'Initial sequencing and analysis of the human genome', *Nature*, 409(6822).

Lee, E. E. *et al.* (2015) 'Ketamine as a novel treatment for major depressive disorder and bipolar depression: A systematic review and quantitative meta-analysis', *General Hospital Psychiatry*. Elsevier B.V., 37(2), pp. 178–184. doi: 10.1016/j.genhosppsych.2015.01.003.

Lee, E. J., Choi, S. Y. and Kim, E. (2015) 'NMDA receptor dysfunction in autism spectrum disorders', *Current Opinion in Pharmacology*. Elsevier Ltd, 20, pp. 8–13. doi: 10.1016/j.coph.2014.10.007.

Lein, E. S. *et al.* (2007) 'Genome-wide atlas of gene expression in the adult mouse brain', *Nature*. England, 445(7124), pp. 168–176. doi: 10.1038/nature05453.

Lisman, J. (2017) 'Glutamatergic synapses are structurally and biochemically complex because of multiple plasticity processes: Long-term potentiation, long-term depression, short-term potentiation and scaling', *Philosophical Transactions of the Royal Society B: Biological Sciences*, 372(1715), p. 20160260. doi: 10.1098/rstb.2016.0260.

Lisman, J., Yasuda, R. and Raghavachari, S. (2012) 'Mechanisms of CaMKII action in long-term potentiation', *Nature Reviews Neuroscience*. Nature Publishing Group, 13(3), pp. 169–182. doi: 10.1038/nrn3192.

Liu, X. *et al.* (2012) 'Optogenetic stimulation of a hippocampal engram activates fear memory recall', *Nature*. Nature Publishing Group, 484(7394), pp. 381–385. doi: 10.1038/nature11028.

MacGillavry, H. D. *et al.* (2013) ‘Nanoscale scaffolding domains within the postsynaptic density concentrate synaptic ampa receptors’, *Neuron*. Elsevier, 78(4), pp. 615–622. doi: 10.1016/j.neuron.2013.03.009.

Malkusch, S. *et al.* (2012) ‘Coordinate-based colocalization analysis of single-molecule localization microscopy data’, *Histochemistry and Cell Biology*, 137(1), pp. 1–10. doi: 10.1007/s00418-011-0880-5.

Manders, E. M. M. *et al.* (1992) ‘Dynamics of three-dimensional replication patterns during the S-phase, analysed by double labelling of DNA and confocal microscopy’, *Journal of cell science*, 103 (Pt 3, pp. 857–862. Available at: c:%5CUsers%5CIvan_2%5CDocuments%5CReadCube Media%5CJ Cell Sci-1992-Manders-857-62 (1).pdf%5Cnhttp://www.ncbi.nlm.nih.gov/pubmed/1478975.

Manders, E. M. M., Verbeek, F. J. and Aten, J. A. (1993) ‘Measurement of co-localization of objects in dual-colour confocal images’, *Journal of Microscopy*. Wiley/Blackwell (10.1111), 169(3), pp. 375–382. doi: 10.1111/j.1365-2818.1993.tb03313.x.

Markram, H. (2006) ‘The Blue Brain Project’, *Nature Reviews Neuroscience*. Nature Publishing Group, 7, p. 153. Available at: http://dx.doi.org/10.1038/nrn1848.

Migaud, M. *et al.* (1998) ‘Enhanced long-term potentiation and impaired learning in mice with mutant postsynaptic density-95 protein’, *Nature*, 396(6710), pp. 433–439. doi: 10.1038/24790.

Miller, S. L. and Yeh, H. H. (2016) *Neurotransmitters and Neurotransmission in the Developing and Adult Nervous System*, *Conn’s Translational Neuroscience*. Elsevier Inc. doi: 10.1016/B978-0-12-802381-5.00004-X.

Morciano, M. *et al.* (2009) ‘The proteome of the presynaptic active zone: From docked synaptic vesicles to adhesion molecules and maxi-channels’, *Journal of Neurochemistry*. England, 108(3), pp. 662–675. doi: 10.1111/j.1471-4159.2008.05824.x.

Morris, R. G. M. (1982) ‘Place navgation impaired in rats with hippocampal lesions’, *Nature*. Nature Publishing Group, 297, p. 681. Available at: http://dx.doi.org/10.1038/297681a0.

Morris, R. G. M. *et al.* (1986) ‘Selective impairment of learning and blockade of long-term potentiation by an N-methyl-D-aspartate receptor antagonist, AP5’, *Nature*,

319(6056), pp. 774–776. doi: 10.1038/319774a0.

Morris, R. G. M. (2013) 'NMDA receptors and memory encoding', *Neuropharmacology*. Elsevier Ltd, 74, pp. 32–40. doi: 10.1016/j.neuropharm.2013.04.014.

Moser, M. B., Rowland, D. C. and Moser, E. I. (2015) 'Place cells, grid cells, and memory', *Cold Spring Harbor Perspectives in Biology*. United States, 7(2), p. a021808. doi: 10.1101/cshperspect.a021808.

Nair, D. *et al.* (2013) 'Super-Resolution Imaging Reveals That AMPA Receptors Inside Synapses Are Dynamically Organized in Nanodomains Regulated by PSD95', *Journal of Neuroscience*, 33(32), pp. 13204–13224. doi: 10.1523/JNEUROSCI.2381-12.2013.

Neunuebel, J. P. and Knierim, J. J. (2014) 'CA3 retrieves coherent representations from degraded input: Direct evidence for CA3 pattern completion and dentate gyrus pattern separation', *Neuron*. Elsevier Inc., 81(2), pp. 416–427. doi: 10.1016/j.neuron.2013.11.017.

Nithianantharajah, J. *et al.* (2013) 'Synaptic scaffold evolution generated components of vertebrate cognitive complexity', *Nature Neuroscience*, 16(1), pp. 16–24. doi: 10.1038/nn.3276.

Nithianantharajah, J. and Grant, S. G. N. (2013) 'Cognitive components in mice and humans: Combining genetics and touchscreens for medical translation', *Neurobiology of Learning and Memory*. Elsevier Inc., 105, pp. 13–19. doi: 10.1016/j.nlm.2013.06.006.

O'Rourke, N. A. *et al.* (2012) 'Deep molecular diversity of mammalian synapses: Why it matters and how to measure it', *Nature Reviews Neuroscience*. Nature Publishing Group, 13(6), pp. 365–379. doi: 10.1038/nrn3170.

Oh, S. W. *et al.* (2014) 'A mesoscale connectome of the mouse brain', *Nature*. Nature Publishing Group, 508(7495), pp. 207–214. doi: 10.1038/nature13186.

Ovesný, M. *et al.* (2014) 'ThunderSTORM: A comprehensive ImageJ plug-in for PALM and STORM data analysis and super-resolution imaging', *Bioinformatics*, 30(16), pp. 2389–2390. doi: 10.1093/bioinformatics/btu202.

Paoletti, P., Bellone, C. and Zhou, Q. (2013) 'NMDA receptor subunit diversity: Impact on receptor properties, synaptic plasticity and disease', *Nature Reviews*

Neuroscience. Nature Publishing Group, 14(6), pp. 383–400. doi: 10.1038/nrn3504.

Papouin, T. and Oliet, S. H. R. (2014) 'Organization, Control and function of extrasynaptic NMDA receptors', *Philosophical Transactions of the Royal Society B: Biological Sciences*, 369(1654), pp. 18–21. doi: 10.1098/rstb.2013.0601.

Van De Peer, Y., Maere, S. and Meyer, A. (2009) 'The evolutionary significance of ancient genome duplications', *Nature Reviews Genetics*. Nature Publishing Group, 10(10), pp. 725–732. doi: 10.1038/nrg2600.

Petralia, R. S. *et al.* (2010) 'Organization of NMDA receptors at extrasynaptic locations', *Neuroscience*. Elsevier Inc., 167(1), pp. 68–87. doi: 10.1016/j.neuroscience.2010.01.022.

Petralia, R. S. (2012) 'Distribution of extrasynaptic NMDA receptors on neurons', *The Scientific World Journal*, 2012, pp. 1–11. doi: 10.1100/2012/267120.

Ripley, B. D. (1976) 'The Second-Order Analysis of Stationary Point Processes', *Journal of Applied Probability*, 13(2), p. 255. doi: 10.2307/3212829.

Roy, M., Sorokina, O., Skene, N., *et al.* (2018) 'Proteomic analysis of postsynaptic proteins in regions of the human neocortex', *Nature Neuroscience*. Springer US, 21(1), pp. 130–141. doi: 10.1038/s41593-017-0025-9.

Roy, M., Sorokina, O., McLean, C., *et al.* (2018) 'Regional Diversity in the Postsynaptic Proteome of the Mouse Brain', *Proteomes*, 6(3), p. 31. doi: 10.3390/proteomes6030031.

Ryan, T. J. *et al.* (2015) 'Engram cells retain memory under retrograde amnesia', *Science*, 348(6238), pp. 1007–1013. doi: 10.1126/science.aaa5542.

Ryan, T. J. and Grant, S. G. N. (2009) 'The origin and evolution of synapses', *Nature Reviews Neuroscience*, 10(11), pp. 701–712. doi: 10.1038/nrn2748.

Sans, N. *et al.* (2000) 'A developmental change in NMDA receptor-associated proteins at hippocampal synapses.', *The Journal of neuroscience : the official journal of the Society for Neuroscience*, 20(3), pp. 1260–1271. doi: 10.1016/j.nlm.2011.01.004.Bidirectional.

Sanz-Clemente, A., Nicoll, R. A. and Roche, K. W. (2013) 'Diversity in NMDA receptor composition: Many regulators, many consequences', *Neuroscientist*, 19(1), pp. 62–75. doi: 10.1177/1073858411435129.

Schindelin, J. *et al.* (2012) 'Fiji: An open-source platform for biological-image analysis', *Nature Methods*, 9(7), pp. 676–682. doi: 10.1038/nmeth.2019.

Schirra, R. T. and Zhang, P. (2014) 'Correlative fluorescence and electron microscopy', *Current Protocols in Cytometry*, 2014, p. 12.36.1-12.36.10. doi: 10.1002/0471142956.cy1236s70.

Schluter, O. M., Xu, W. and Malenka, R. C. (2006) 'Alternative N-terminal domains of PSD-95 and SAP97 govern activity-dependent regulation of synaptic AMPA receptor function.', *Neuron*. United States, 51(1), pp. 99–111. doi: 10.1016/j.neuron.2006.05.016.

Schüz, A. and Palm, G. (1989) 'Density of neurons and synapses in the cerebral cortex of the mouse', *Journal of Comparative Neurology*, 286(4), pp. 442–455. doi: 10.1002/cne.902860404.

Sheng, M. and Hoogenraad, C. C. (2007) 'The Postsynaptic Architecture of Excitatory Synapses: A More Quantitative View', *Annual Review of Biochemistry*, 76(1), pp. 823–847. doi: 10.1146/annurev.biochem.76.060805.160029.

Shinohara, Y. *et al.* (2008) 'Left-right asymmetry of the hippocampal synapses with differential subunit allocation of glutamate receptors', *Proceedings of the National Academy of Sciences*. United States, 105(49), pp. 19498–19503. doi: 10.1073/pnas.0807461105.

Shinohara, Y. (2009) 'Size and receptor density of glutamatergic synapses: a viewpoint from left-right asymmetry of CA3-CA1 connections', *Frontiers in Neuroanatomy*, 3(July), pp. 1–6. doi: 10.3389/neuro.05.010.2009.

Simhal, A. K. *et al.* (2017) 'Probabilistic fluorescence-based synapse detection', *PLoS Computational Biology*, 13(4), pp. 1–24. doi: 10.1371/journal.pcbi.1005493.

Spiess, A. N. and Neumeyer, N. (2010) 'An evaluation of R2as an inadequate measure for nonlinear models in pharmacological and biochemical research: A Monte Carlo approach', *BMC Pharmacology*, 10, pp. 1–11. doi: 10.1186/1471-2210-10-6.

Strange, B. A. *et al.* (2014) 'Functional organization of the hippocampal longitudinal axis', *Nature Reviews Neuroscience*. Nature Publishing Group, 15(10), pp. 655–669. doi: 10.1038/nrn3785.

Sytnyk, V. *et al.* (2006) 'NCAM promotes assembly and activity-dependent

remodeling of the postsynaptic signaling complex', *Journal of Cell Biology*, 174(7), pp. 1071–1085. doi: 10.1083/jcb.200604145.

Tao-Cheng, J. H. *et al.* (2014) 'Homer is concentrated at the postsynaptic density and does not redistribute after acute synaptic stimulation', *Neuroscience*, 266(301), pp. 80–90. doi: 10.1016/j.neuroscience.2014.01.066.

Tarpey, P. *et al.* (2004) 'Mutations in the DLG3 gene cause nonsyndromic X-linked mental retardation.', *American journal of human genetics*. United States, 75(2), pp. 318–324. doi: 10.1086/422703.

Thompson, C. L. *et al.* (2008) 'Genomic Anatomy of the Hippocampus', *Neuron*. Elsevier Ltd, 60(6), pp. 1010–1021. doi: 10.1016/j.neuron.2008.12.008.

Tinevez, J. Y. *et al.* (2017) 'TrackMate: An open and extensible platform for single-particle tracking', *Methods*. The Author(s), 115, pp. 80–90. doi: 10.1016/j.ymeth.2016.09.016.

Tonegawa, S. *et al.* (2015) 'Memory engram storage and retrieval', *Current Opinion in Neurobiology*, 35, pp. 101–109. doi: 10.1016/j.conb.2015.07.009.

Torquato, S., Lu, B. and Rubinstein, J. (1990) 'Nearest-neighbor distribution functions in many-body systems', *Physical Review A*. American Physical Society, 41(4), pp. 2059–2075. doi: 10.1103/PhysRevA.41.2059.

Tovar, K. R. and Westbrook, G. L. (2002) 'Mobile NMDA receptors at hippocampal synapses', *Neuron*, 34(2), pp. 255–264. doi: 10.1016/S0896-6273(02)00658-X.

Traynelis, S. *et al.* (2010) 'Glutamate Receptor Ion Channels : Structure , Regulation , and Function', *Pharmacological Reviews*. Edited by D. Sibley, 62(3), p. 405 LP-496. doi: 10.1124/pr.109.002451.405.

Valtschanoff, J. G. and Weinberg, R. J. (2001) 'Laminar organization of the NMDA receptor complex within the postsynaptic density.', *The Journal of neuroscience : the official journal of the Society for Neuroscience*, 21(4), pp. 1211–7. doi: 21/4/1211 [pii].

Vazdarjanova, A. (2004) 'Differences in Hippocampal Neuronal Population Responses to Modifications of an Environmental Context: Evidence for Distinct, Yet Complementary, Functions of CA3 and CA1 Ensembles', *Journal of Neuroscience*, 24(29), pp. 6489–6496. doi: 10.1523/JNEUROSCI.0350-04.2004.

Wang, P. Y. *et al.* (2011) 'Functional NMDA Receptors at Axonal Growth Cones of

Young Hippocampal Neurons', *Journal of Neuroscience*, 31(25), pp. 9289–9297. doi: 10.1523/JNEUROSCI.5639-10.2011.

Washbourne, P. (2004) 'Cycling of NMDA Receptors during Trafficking in Neurons before Synapse Formation', *Journal of Neuroscience*, 24(38), pp. 8253–8264. doi: 10.1523/JNEUROSCI.2555-04.2004.

Weingarten, J. *et al.* (2014) 'The proteome of the presynaptic active zone from mouse brain', *Molecular and Cellular Neuroscience*. Elsevier Inc., 59, pp. 106–118. doi: 10.1016/j.mcn.2014.02.003.

Wiegand, T. and Moloney, K. A. (2004) 'Rings, circles, and null-models for point pattern analysis in ecology', *Oikos*, pp. 209–229. doi: 10.1111/j.0030-1299.2004.12497.x.

Won, S. *et al.* (2017) 'MAGUKs: multifaceted synaptic organizers', *Current Opinion in Neurobiology*. Elsevier Ltd, 43, pp. 94–101. doi: 10.1016/j.conb.2017.01.006.

Wurm, C. A. *et al.* (2010) 'Sample Preparation for STED Microscopy BT - Live Cell Imaging: Methods and Protocols', in Papkovsky, D. B. (ed.). Totowa, NJ: Humana Press, pp. 185–199. doi: 10.1007/978-1-60761-404-3_11.

Yassa, M. A. and Stark, C. E. L. (2011) 'Pattern separation in the hippocampus', *Trends in Neurosciences*. Elsevier Ltd, 34(10), pp. 515–525. doi: 10.1016/j.tins.2011.06.006.

Zhang, B. *et al.* (2008) 'Statistical colocalization in biological imaging with false discovery control', *2008 5th IEEE International Symposium on Biomedical Imaging: From Nano to Macro, Proceedings, ISBI*, pp. 1327–1330. doi: 10.1109/ISBI.2008.4541249.

Zhang, B. and Chenouard, N. (2008) 'STATISTICAL COLOCALIZATION IN BIOLOGICAL IMAGING WITH FALSE DISCOVERY CONTROL Unit ´ e Analyse d ' Images Quantitative Institut Pasteur 75015 Paris France', pp. 1327–1330.

Zheng, C. Y. *et al.* (2010) 'SAP102 Is a Highly Mobile MAGUK in Spines', *Journal of Neuroscience*, 30(13), pp. 4757–4766. doi: 10.1523/JNEUROSCI.6108-09.2010.

Zheng, C. Y. *et al.* (2011) 'MAGUKs, synaptic development, and synaptic plasticity', *Neuroscientist*, 17(5), pp. 493–512. doi: 10.1177/1073858410386384.

Zhu, F. *et al.* (2018) 'Architecture of the Mouse Brain Synaptome', *Neuron*, 99(4), p. 781–799.e10. doi: 10.1016/j.neuron.2018.07.007.

Zhu, J., Shang, Y. and Zhang, M. (2016) ‘Mechanistic basis of MAGUK-organized complexes in synaptic development and signalling’, *Nature Reviews Neuroscience*. Nature Publishing Group, 17(4), pp. 209–223. doi: 10.1038/nrn.2016.18.

Appendices

Electronic appendix

This thesis has an electronic appendix containing all tools used for image analysis (as referenced throughout the Methods section) and relevant instructions.

The electronic appendix also contains a ‘Sample Images’ folder. Downsampled whole-hippocampus stitched montages and full resolution fluorescence microscopy images of GluN1, PSD95 and SAP102 in the CA1rad, CA3rad, DGmo and DGpo are provided.

Under ‘Sample Images’, the sample images used to train the TrackMate puncta detector, as well as associated Cell Counter (Fiji plugin) files with the coordinates of manually counted puncta are also included.

Developmental trajectories of synaptic protein puncta

Table with total numbers of distinct synaptic protein puncta (including double and triple assemblies) analysed in each region across all ages and all mice.

Region	Total Distinct Synaptic Protein Puncta Analysed (Millions)
DGmo	12.56
CA1ori	6.43
CA1rad	11.29
CA1slm	4.00
CA2ori	0.69
CA2rad	0.76
CA2slm	0.44
CA3ori	3.03
CA3rad	2.91
CA3slm	0.64
CA3slu	0.95
DGpo	0.90
SUB	4.15
TH	6.27
CTX	6.50

All figures in this section are standardised. For a given region, the 6-panel figures (A-F) show the developmental trajectories of individual proteins (PSD95, SAP102 and GluN1) and the 10-panel figures (A-J) show a comprehensive overview of the developmental trajectories of all 7 punctum subtypes. The following figure legends apply to all figures in this section:

6-panel figure legend:

Developmental trajectories of PSD95, SAP102 and GluN1. A and B. Average PSD95-containing synaptic punctum densities (A) and proportions (B). **C and D.** Average SAP102-containing synaptic punctum densities (C) and proportions (D). **E and F.** Average GluN1-containing synaptic punctum densities (E) and proportions (F).

10-panel figure legend:

Developmental trajectories of 7 synaptic punctum subtypes. A and B. Average subtype densities (A) and proportions of all puncta (B). **C to I.** Developmental trajectories of individual subtype densities (circles – subtype density measurements in individual mice; black lines – average values). Y-axis scales vary. For each subtype, asterisks indicate p-values of the Mann-Whitney test comparing its density at one age with that at the preceding age (* $p<0.05$, ** $p<0.01$). **J.** Total number of synaptic puncta (density x region surface area) analysed at every age (circles – total puncta numbers in individual mice; black line – average).

DGmo

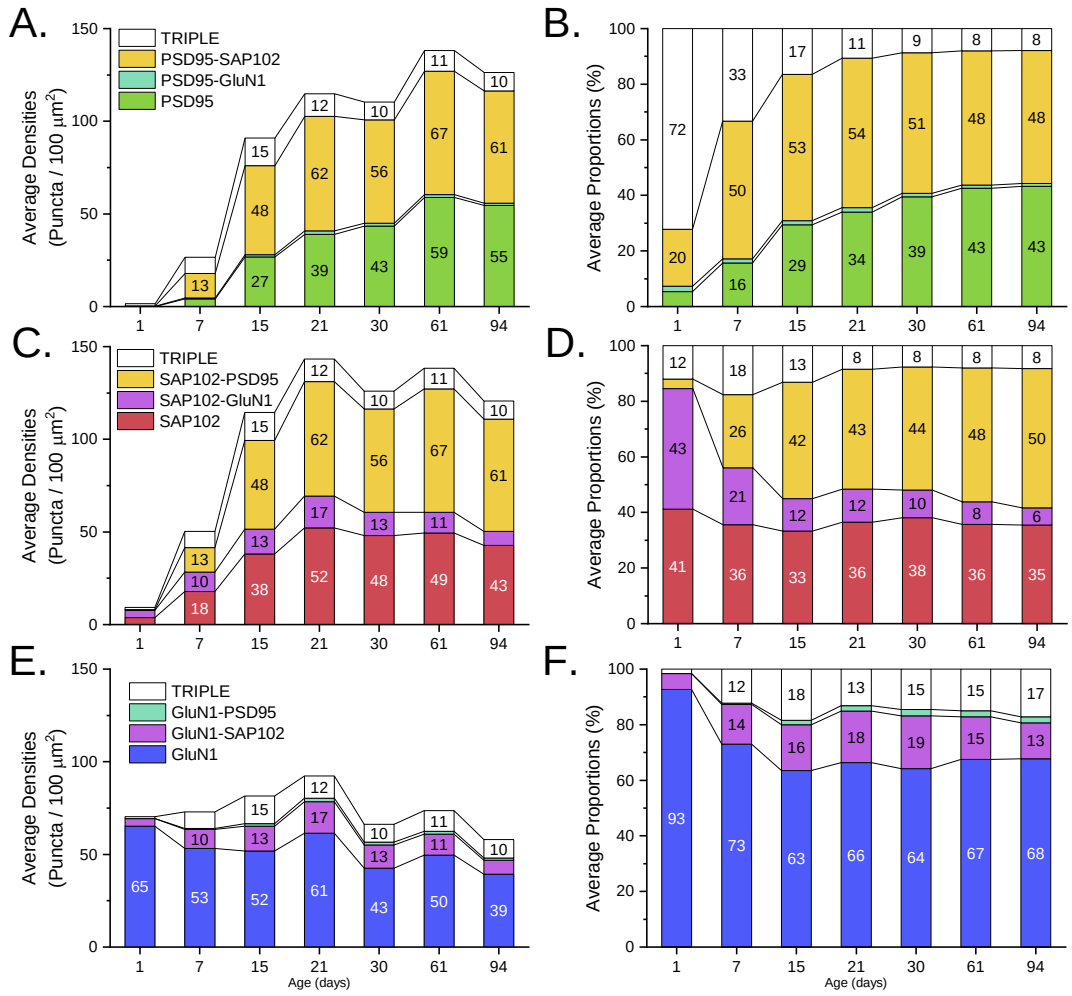
A.
TRIPLE
PSD95-SAP102
PSD95-GluN1
PSD95
Average Densities (Puncta / 100 µm²)
B.
Average Proportions (%)
C.
TRIPLE
SAP102-PSD95
SAP102-GluN1
SAP102
Average Densities (Puncta / 100 µm²)
D.
Average Proportions (%)
E.
TRIPLE
GluN1-PSD95
GluN1-SAP102
GluN1
Average Densities (Puncta / 100 µm²)
Age (days)
F.
Average Proportions (%)
Age (days)

DGmo

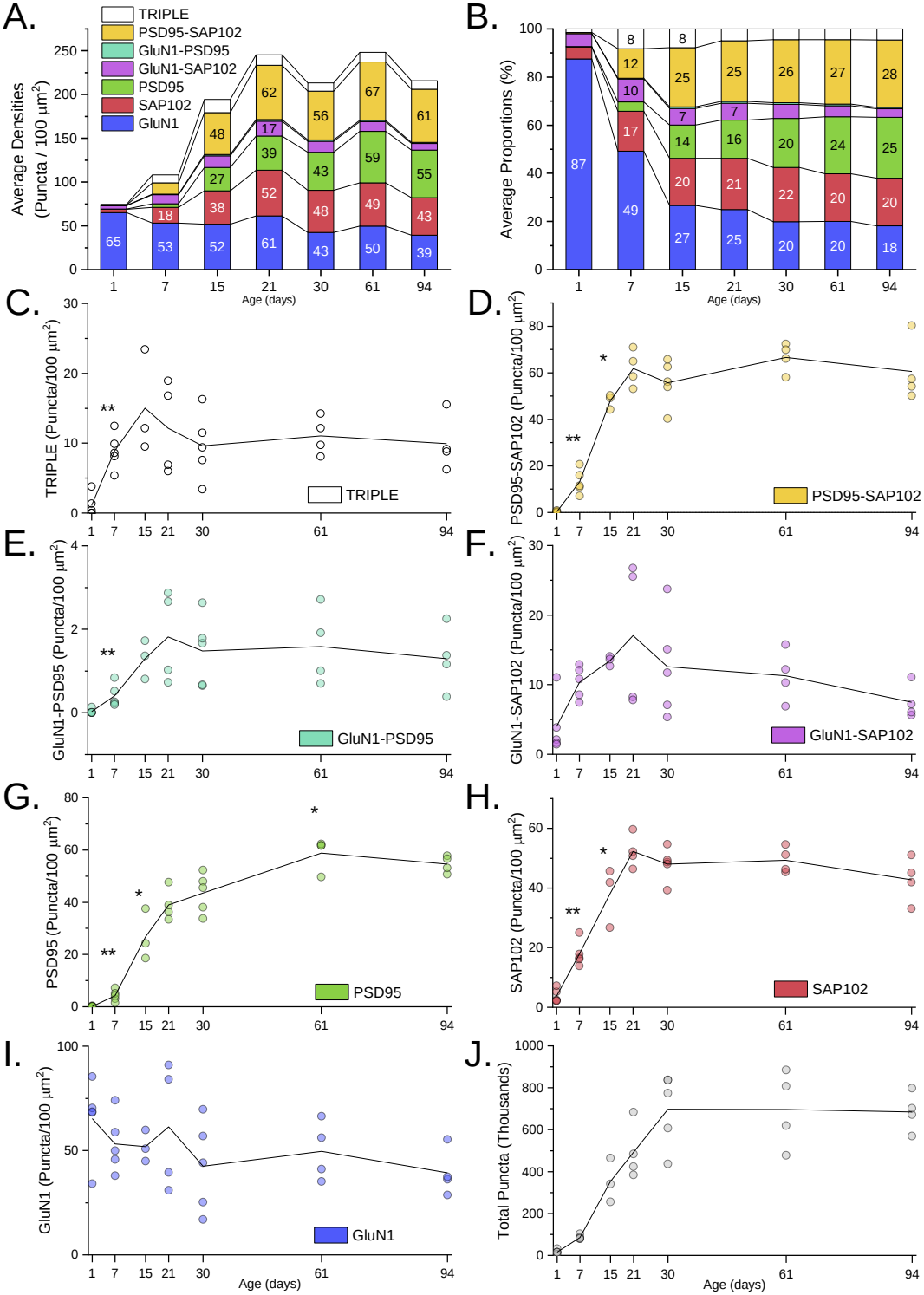
A.
TRIPLE
PSD95-SAP102
GluN1-PSD95
GluN1-SAP102
PSD95
SAP102
GluN1
Average Densities (Puncta / 100 µm²)
Age (days)
B.
Average Proportions (%)
Age (days)
C.
TRIPLE (Puncta/100 µm²)
TRIPLE
D.
PSD95-SAP102 (Puncta/100 µm²)
PSD95-SAP102
E.
GluN1-PSD95 (Puncta/100 µm²)
GluN1-PSD95
F.
GluN1-SAP102 (Puncta/100 µm²)
GluN1-SAP102
G.
PSD95 (Puncta/100 µm²)
PSD95
H.
SAP102 (Puncta/100 µm²)
SAP102
I.
GluN1 (Puncta/100 µm²)
GluN1
Age (days)
J.
Total Puncta (Thousands)
Age (days)

CA1ori

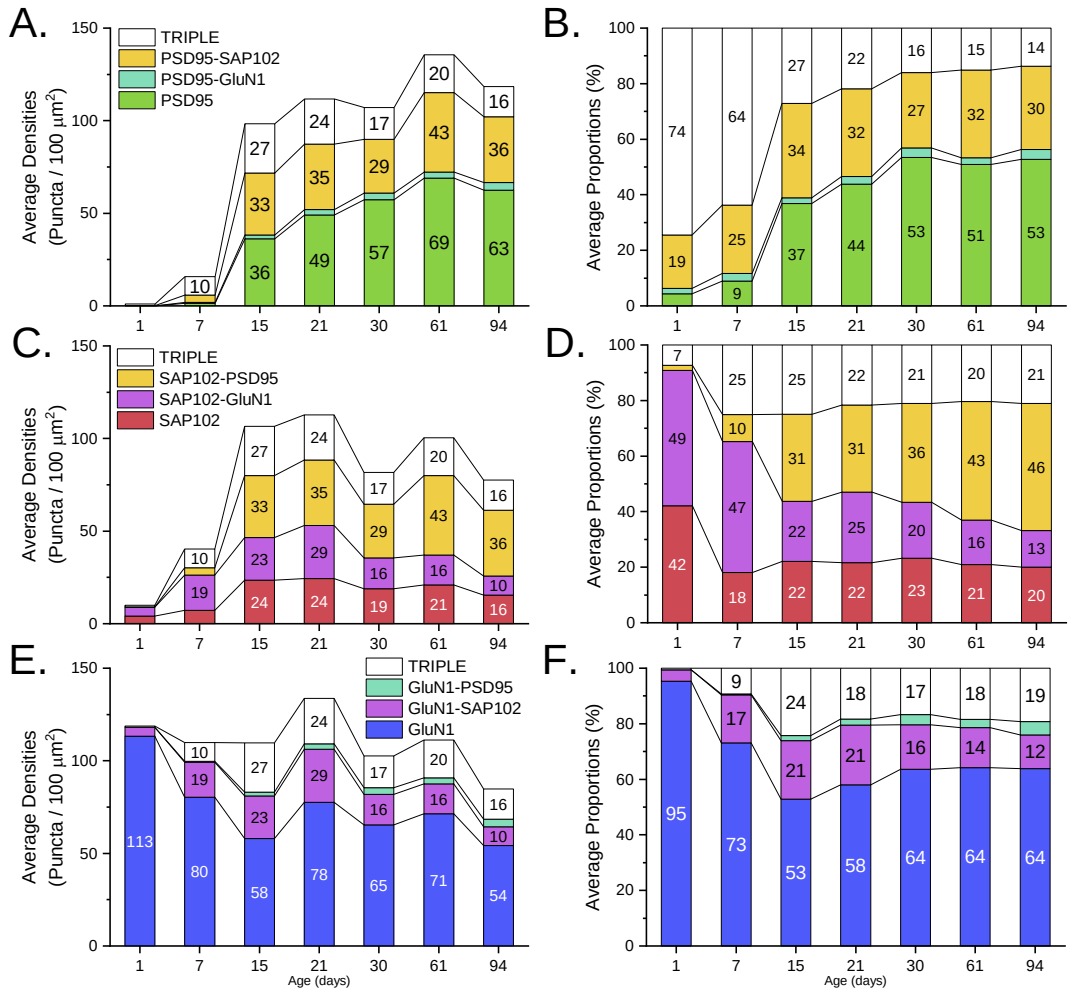
A.
TRIPLE
PSD95-SAP102
PSD95-GluN1
PSD95
Average Densities (Puncta / 100 µm²)
B.
Average Proportions (%)
C.
TRIPLE
SAP102-PSD95
SAP102-GluN1
SAP102
Average Densities (Puncta / 100 µm²)
D.
Average Proportions (%)
E.
TRIPLE
GluN1-PSD95
GluN1-SAP102
GluN1
Average Densities (Puncta / 100 µm²)
Age (days)
F.
Average Proportions (%)
Age (days)

CA1ori

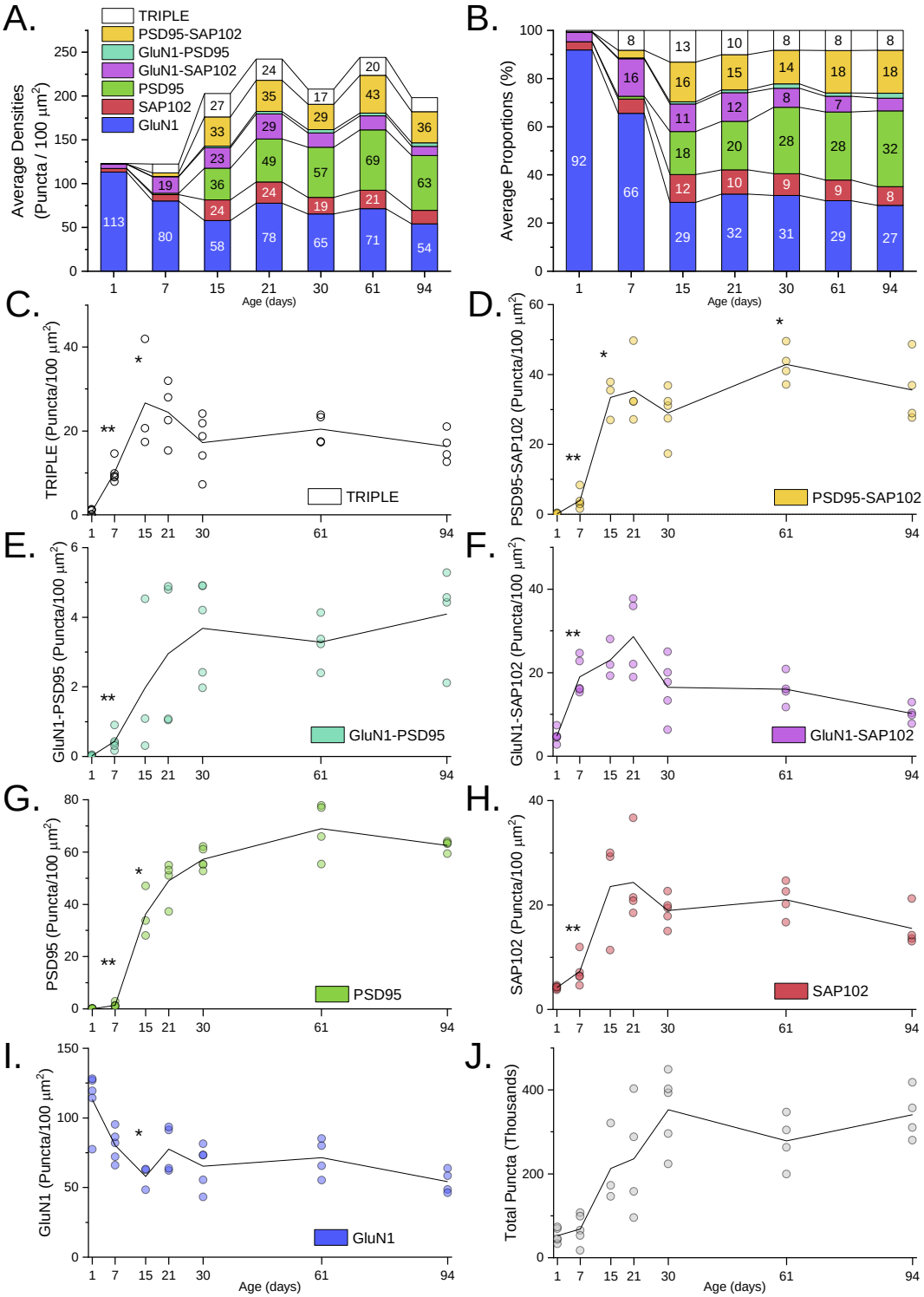
A.
TRIPLE
PSD95-SAP102
GluN1-PSD95
GluN1-SAP102
PSD95
SAP102
GluN1
Average Densities (Puncta / 100 µm²)
Age (days)
B.
Average Proportions (%)
Age (days)
C.
TRIPLE (Puncta/100 µm²)
TRIPLE
D.
PSD95-SAP102 (Puncta/100 µm²)
PSD95-SAP102
E.
GluN1-PSD95 (Puncta/100 µm²)
GluN1-PSD95
F.
GluN1-SAP102 (Puncta/100 µm²)
GluN1-SAP102
G.
PSD95 (Puncta/100 µm²)
PSD95
H.
SAP102 (Puncta/100 µm²)
SAP102
I.
GluN1 (Puncta/100 µm²)
GluN1
Age (days)
J.
Total Puncta (Thousands)
Age (days)

CA1rad

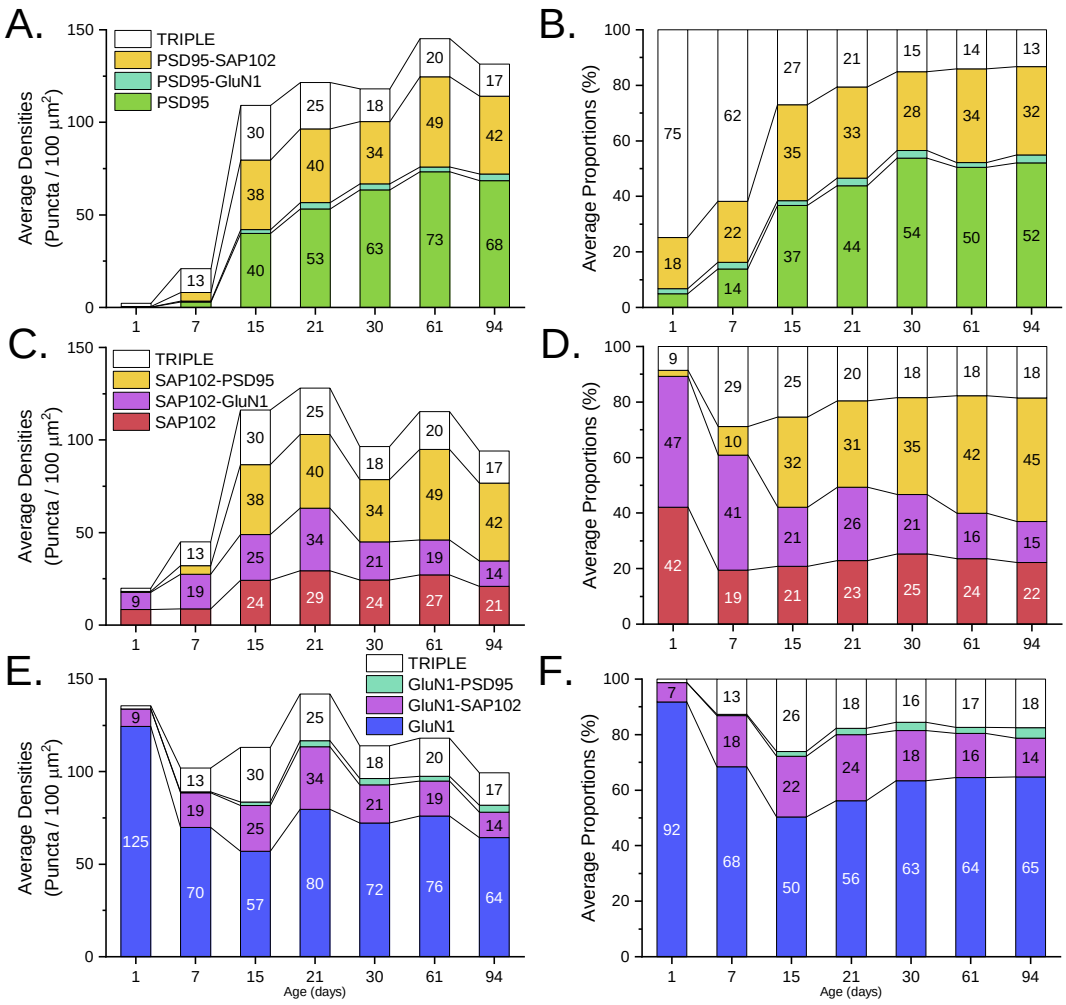
A.
B.
C.
D.
E.
F.
TRIPLE
PSD95-SAP102
PSD95-GluN1
PSD95
SAP102-PSD95
SAP102-GluN1
SAP102
GluN1-PSD95
GluN1-SAP102
GluN1
Average Densities (Puncta / 100 µm²)
Average Proportions (%)
Age (days)

CA1rad

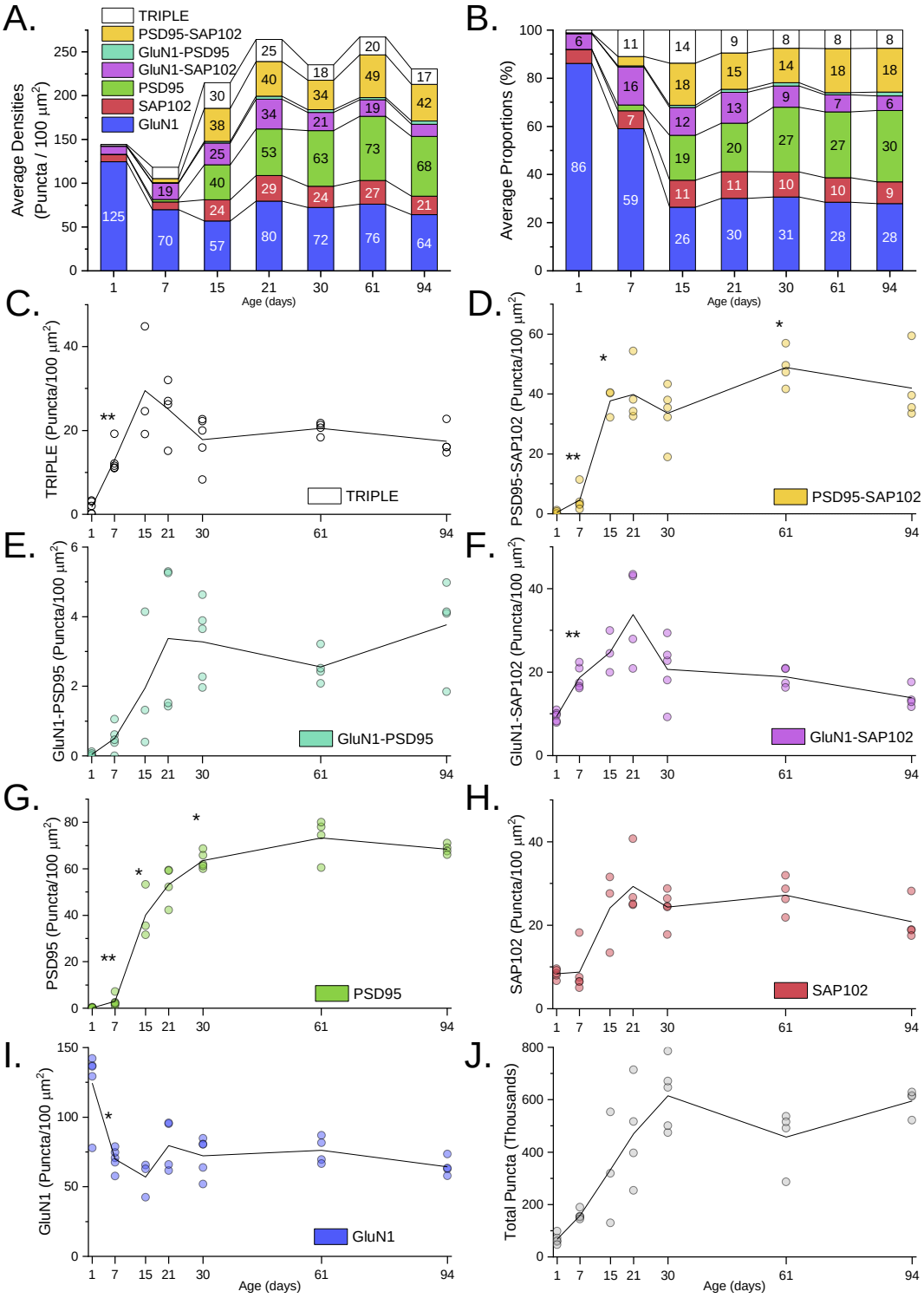
A.
TRIPLE
PSD95-SAP102
GluN1-PSD95
GluN1-SAP102
PSD95
SAP102
GluN1
Average Densities (Puncta / 100 µm²)
Age (days)
B.
Average Proportions (%)
Age (days)
C.
TRIPLE (Puncta/100 µm²)
TRIPLE
D.
PSD95-SAP102 (Puncta/100 µm²)
PSD95-SAP102
E.
GluN1-PSD95 (Puncta/100 µm²)
GluN1-PSD95
F.
GluN1-SAP102 (Puncta/100 µm²)
GluN1-SAP102
G.
PSD95 (Puncta/100 µm²)
PSD95
H.
SAP102 (Puncta/100 µm²)
SAP102
I.
GluN1 (Puncta/100 µm²)
GluN1
Age (days)
J.
Total Puncta (Thousands)
Age (days)

CA1slm

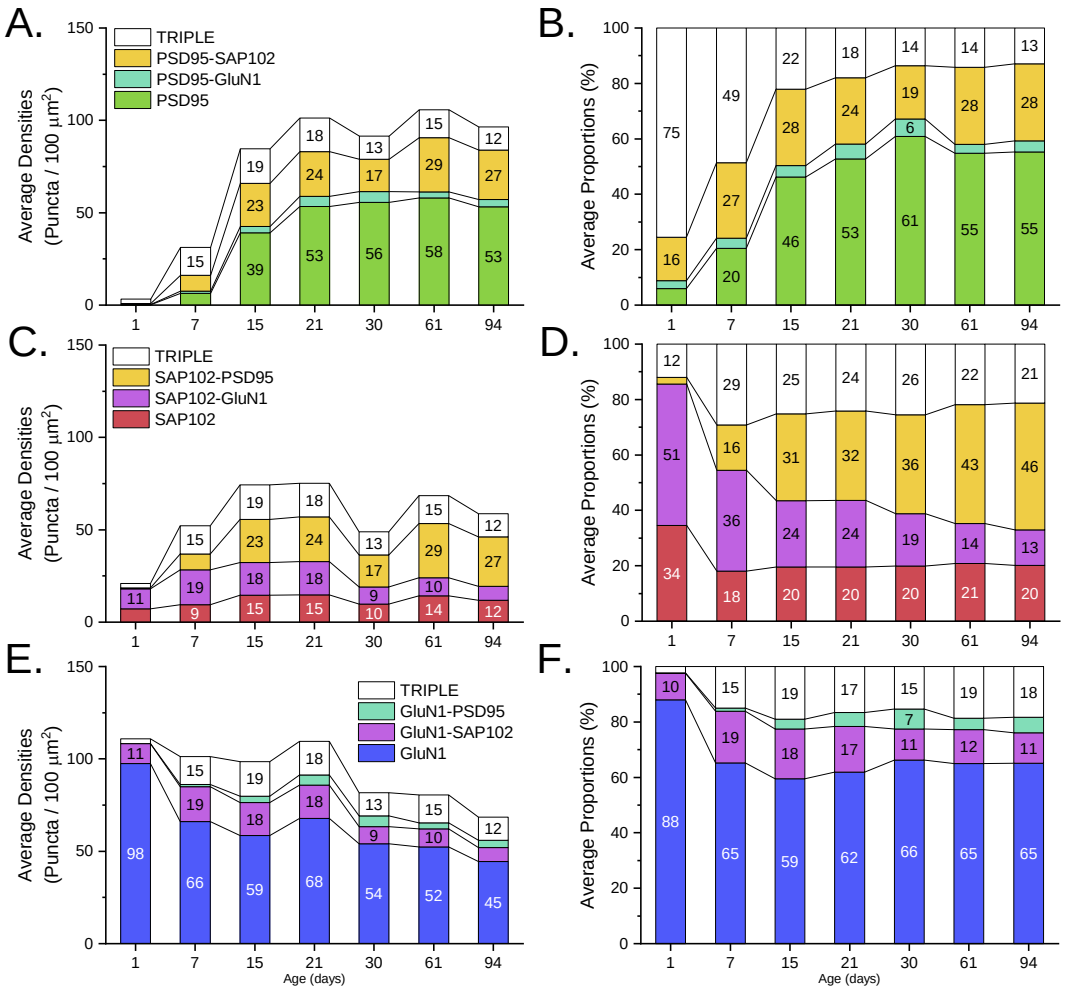
A.
B.
C.
D.
E.
F.
TRIPLE
PSD95-SAP102
PSD95-GluN1
PSD95
SAP102-PSD95
SAP102-GluN1
SAP102
GluN1-PSD95
GluN1-SAP102
GluN1
Average Densities (Puncta / 100 µm²)
Average Proportions (%)
Age (days)

CA1slm

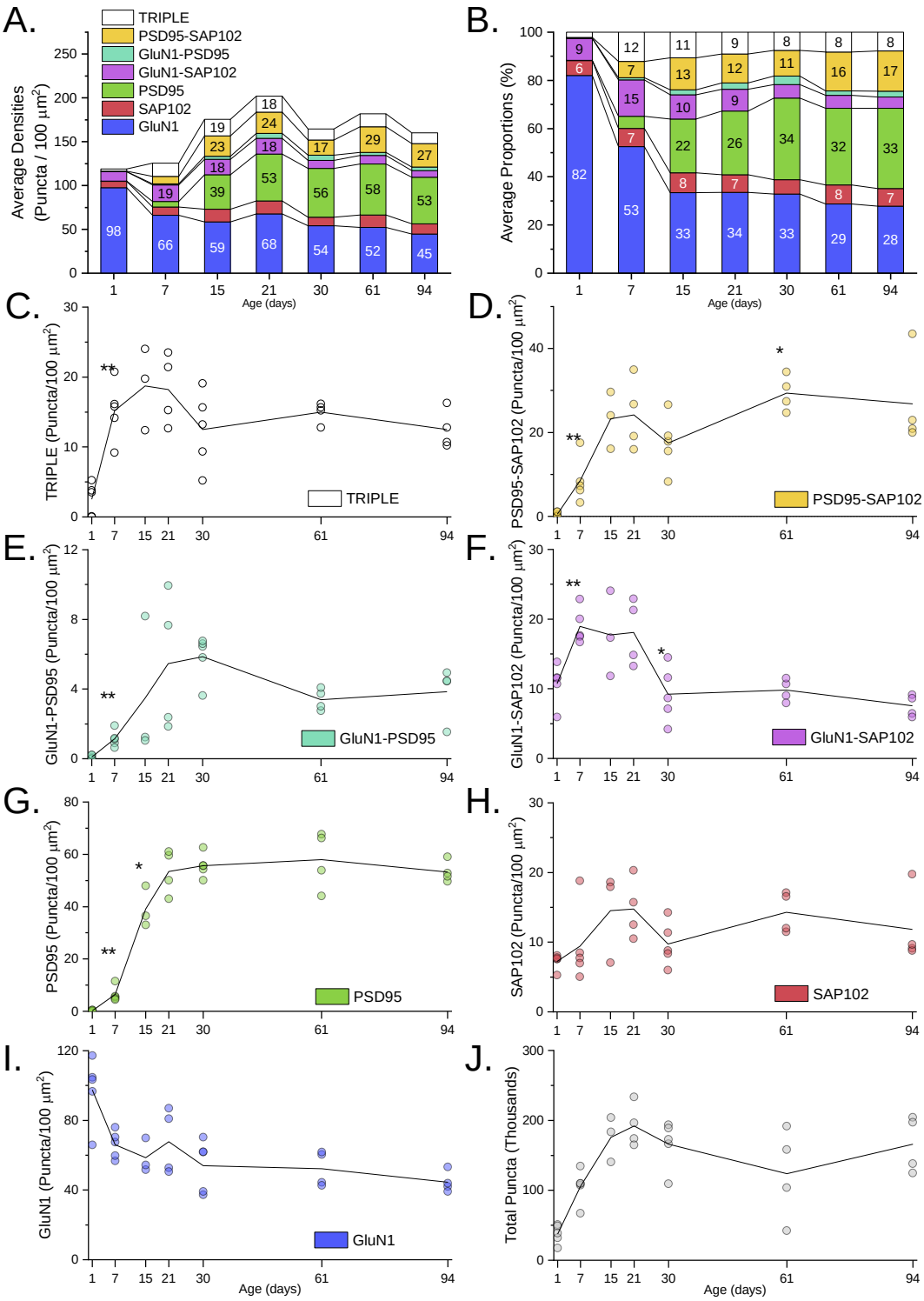
A.
TRIPLE
PSD95-SAP102
GluN1-PSD95
GluN1-SAP102
PSD95
SAP102
GluN1
Average Densities (Puncta / 100 µm²)
Age (days)
B.
Average Proportions (%)
Age (days)
C.
TRIPLE (Puncta/100 µm²)
TRIPLE
D.
PSD95-SAP102 (Puncta/100 µm²)
PSD95-SAP102
E.
GluN1-PSD95 (Puncta/100 µm²)
GluN1-PSD95
F.
GluN1-SAP102 (Puncta/100 µm²)
GluN1-SAP102
G.
PSD95 (Puncta/100 µm²)
PSD95
H.
SAP102 (Puncta/100 µm²)
SAP102
I.
GluN1 (Puncta/100 µm²)
GluN1
Age (days)
J.
Total Puncta (Thousands)
Age (days)

CA2ori

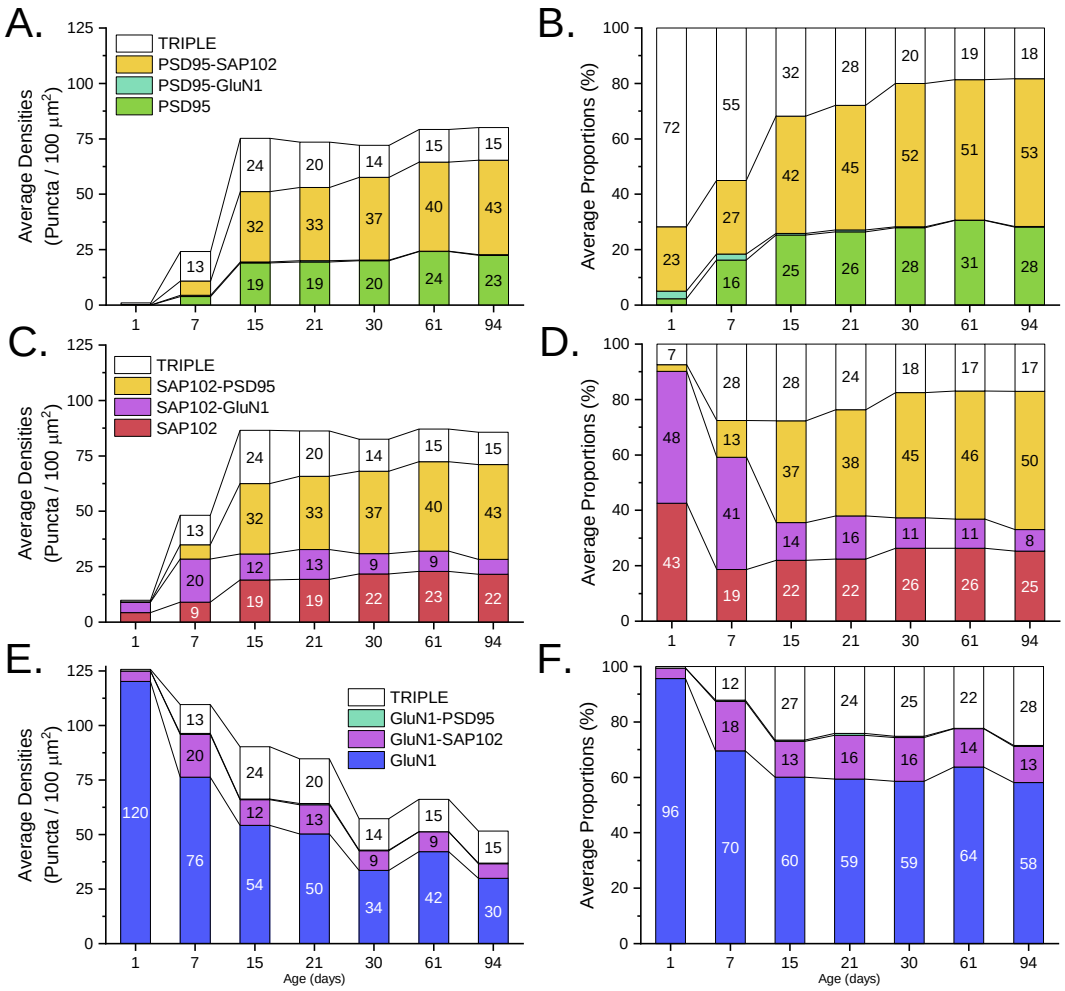
A.
B.
C.
D.
E.
F.
TRIPLE
PSD95-SAP102
PSD95-GluN1
PSD95
SAP102-PSD95
SAP102-GluN1
SAP102
GluN1-PSD95
GluN1-SAP102
GluN1
Average Densities (Puncta / 100 µm²)
Average Proportions (%)
Age (days)

CA2ori

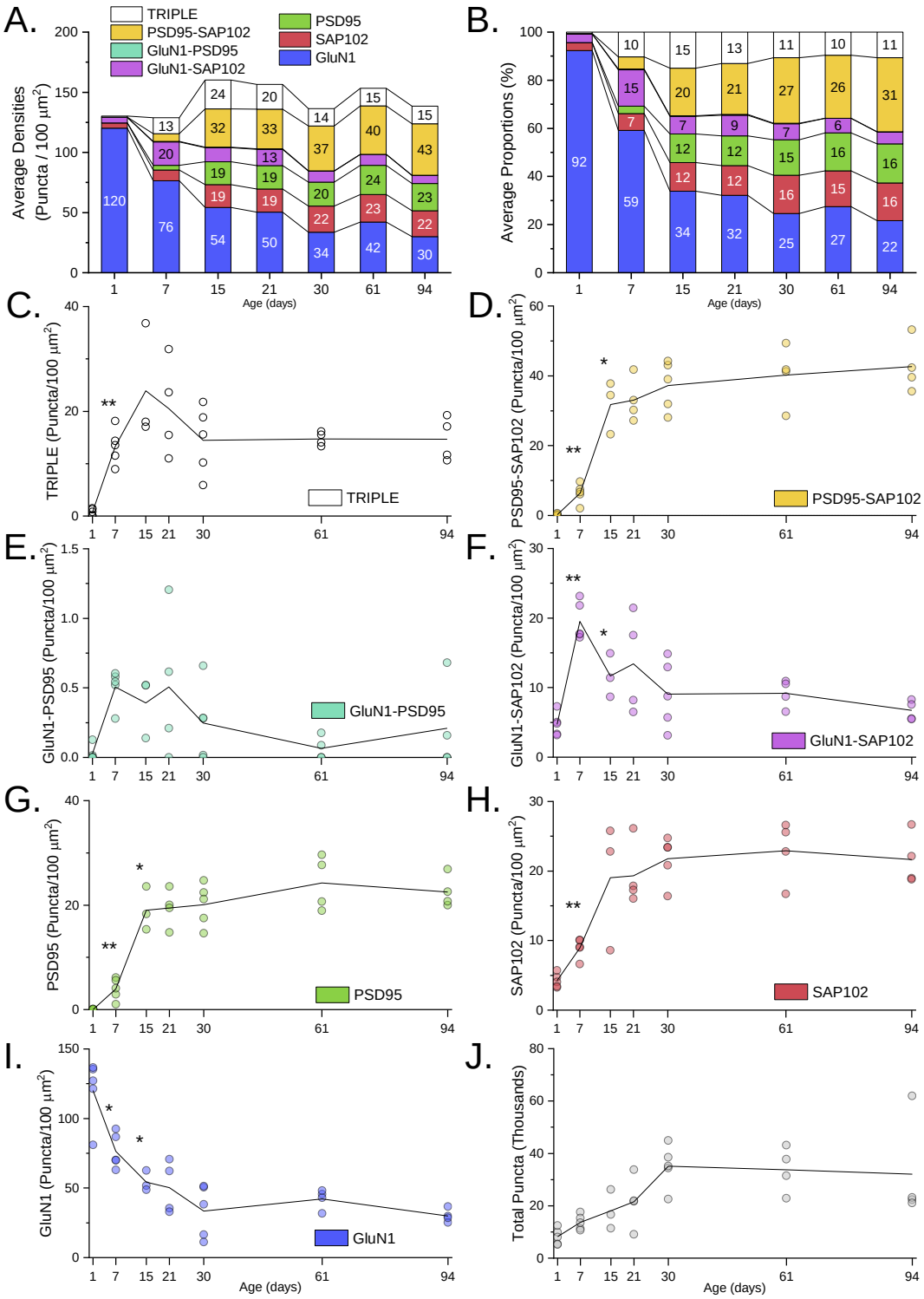
A.
TRIPLE
PSD95-SAP102
GluN1-PSD95
GluN1-SAP102
PSD95
SAP102
GluN1
Average Densities (Puncta / 100 µm²)
Age (days)
B.
Average Proportions (%)
Age (days)
C.
TRIPLE (Puncta/100 µm²)
TRIPLE
D.
PSD95-SAP102 (Puncta/100 µm²)
PSD95-SAP102
E.
GluN1-PSD95 (Puncta/100 µm²)
GluN1-PSD95
F.
GluN1-SAP102 (Puncta/100 µm²)
GluN1-SAP102
G.
PSD95 (Puncta/100 µm²)
PSD95
H.
SAP102 (Puncta/100 µm²)
SAP102
I.
GluN1 (Puncta/100 µm²)
GluN1
Age (days)
J.
Total Puncta (Thousands)
Age (days)

CA2rad

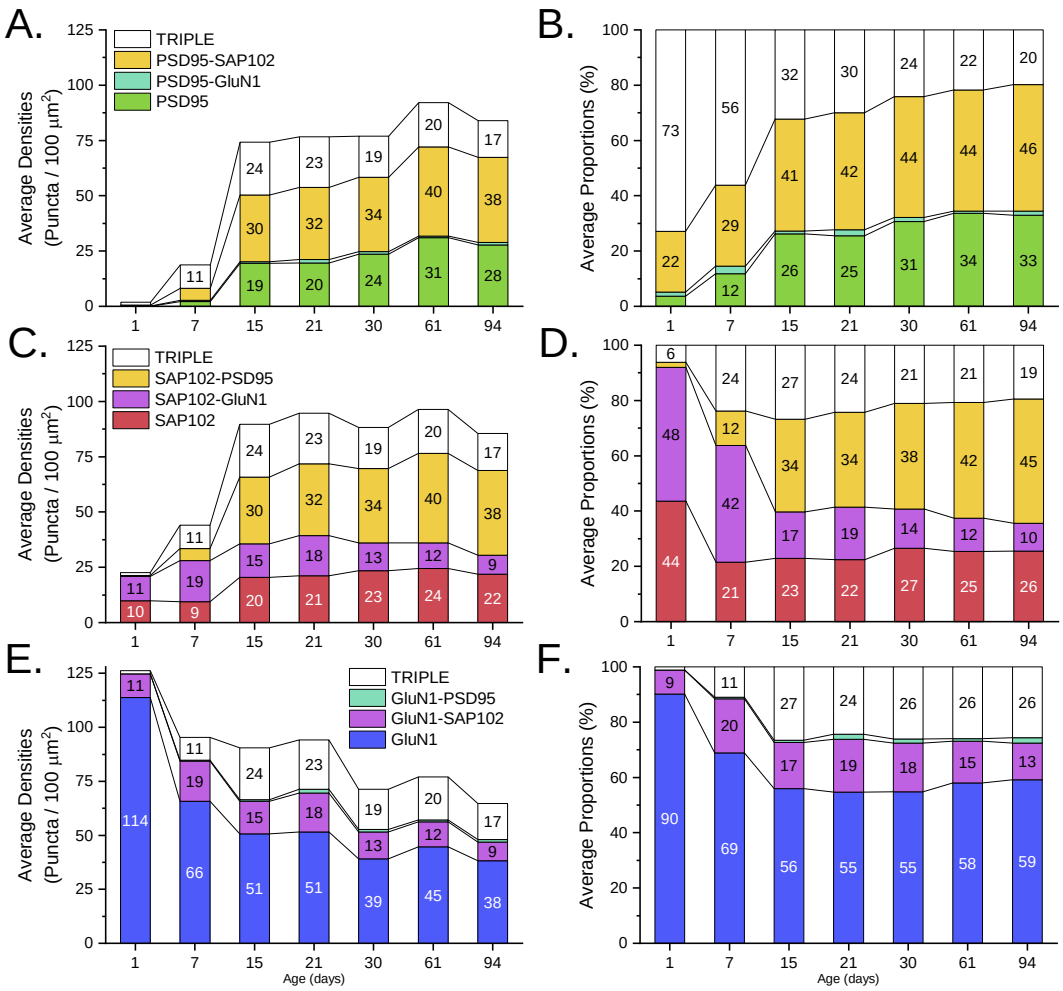
A.
TRIPLE
PSD95-SAP102
PSD95-GluN1
PSD95
Average Densities (Puncta / 100 µm²)
B.
Average Proportions (%)
C.
TRIPLE
SAP102-PSD95
SAP102-GluN1
SAP102
Average Densities (Puncta / 100 µm²)
D.
Average Proportions (%)
E.
TRIPLE
GluN1-PSD95
GluN1-SAP102
GluN1
Average Densities (Puncta / 100 µm²)
Age (days)
F.
Average Proportions (%)
Age (days)

CA2rad

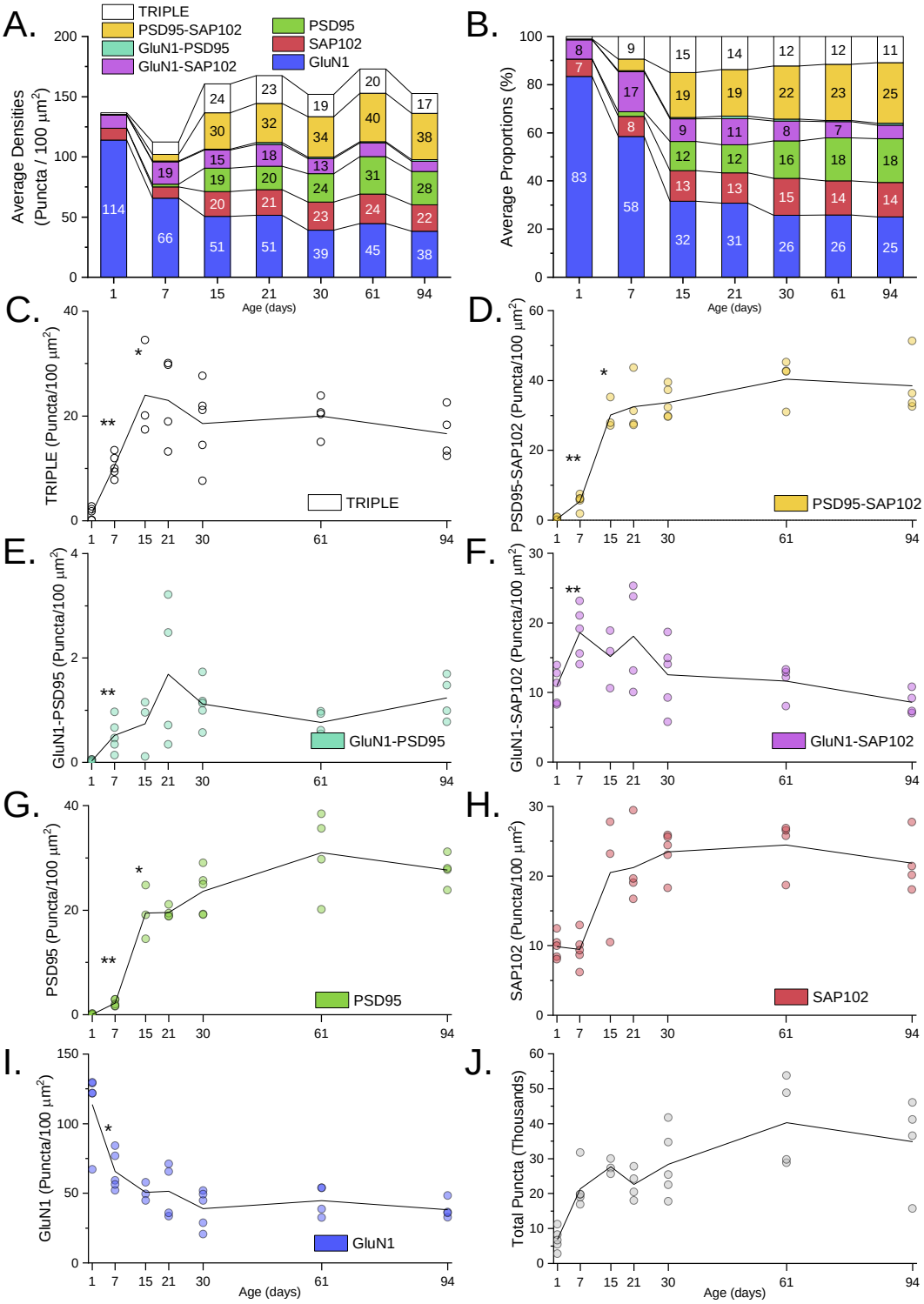
A.
TRIPLE
PSD95-SAP102
GluN1-PSD95
GluN1-SAP102
PSD95
SAP102
GluN1
Average Densities (Puncta / 100 µm²)
Age (days)
B.
Average Proportions (%)
Age (days)
C.
TRIPLE (Puncta/100 µm²)
TRIPLE
D.
PSD95-SAP102 (Puncta/100 µm²)
PSD95-SAP102
E.
GluN1-PSD95 (Puncta/100 µm²)
GluN1-PSD95
F.
GluN1-SAP102 (Puncta/100 µm²)
GluN1-SAP102
G.
PSD95 (Puncta/100 µm²)
PSD95
H.
SAP102 (Puncta/100 µm²)
SAP102
I.
GluN1 (Puncta/100 µm²)
GluN1
Age (days)
J.
Total Puncta (Thousands)
Age (days)

CA2slm

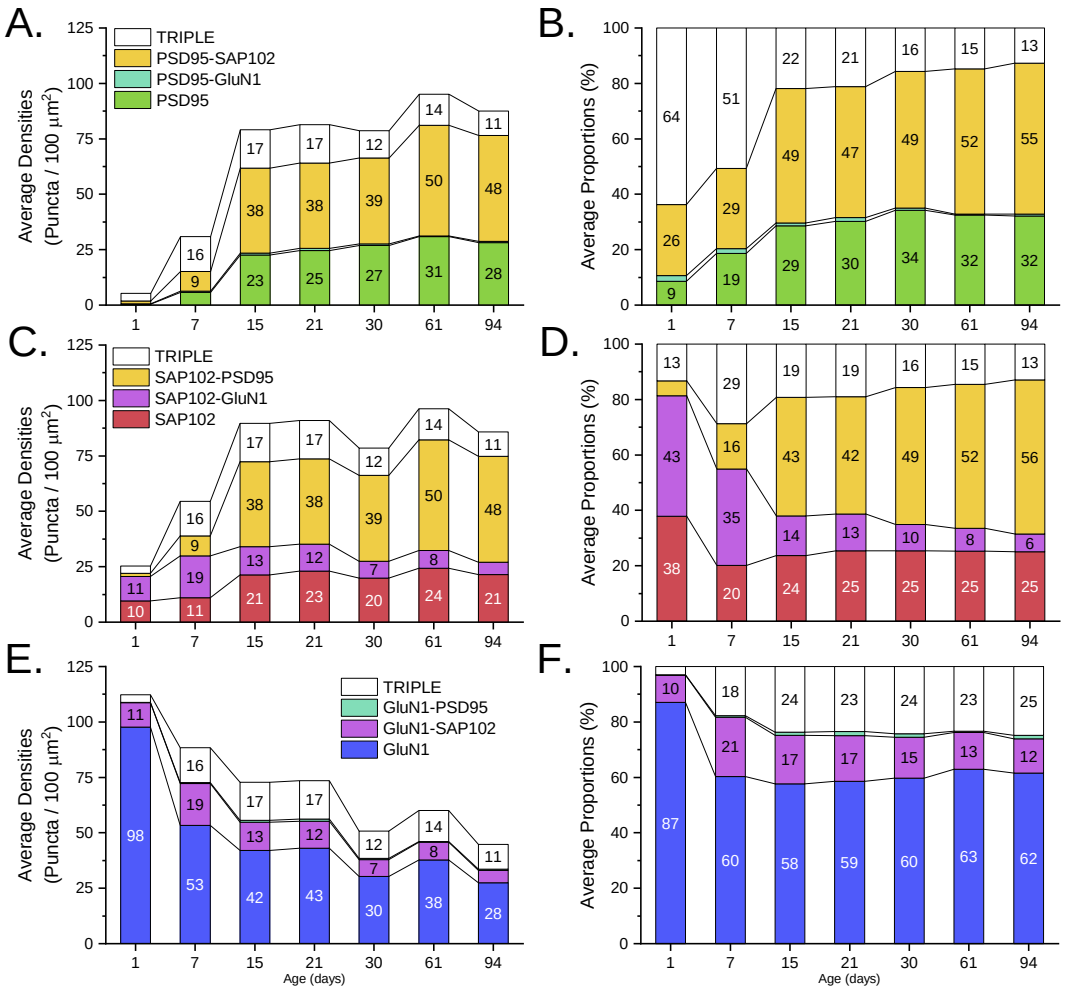
A.
B.
C.
D.
E.
F.
TRIPLE
PSD95-SAP102
PSD95-GluN1
PSD95
SAP102-PSD95
SAP102-GluN1
SAP102
GluN1-PSD95
GluN1-SAP102
GluN1
Average Densities (Puncta / 100 µm²)
Average Proportions (%)
Age (days)

CA2slm

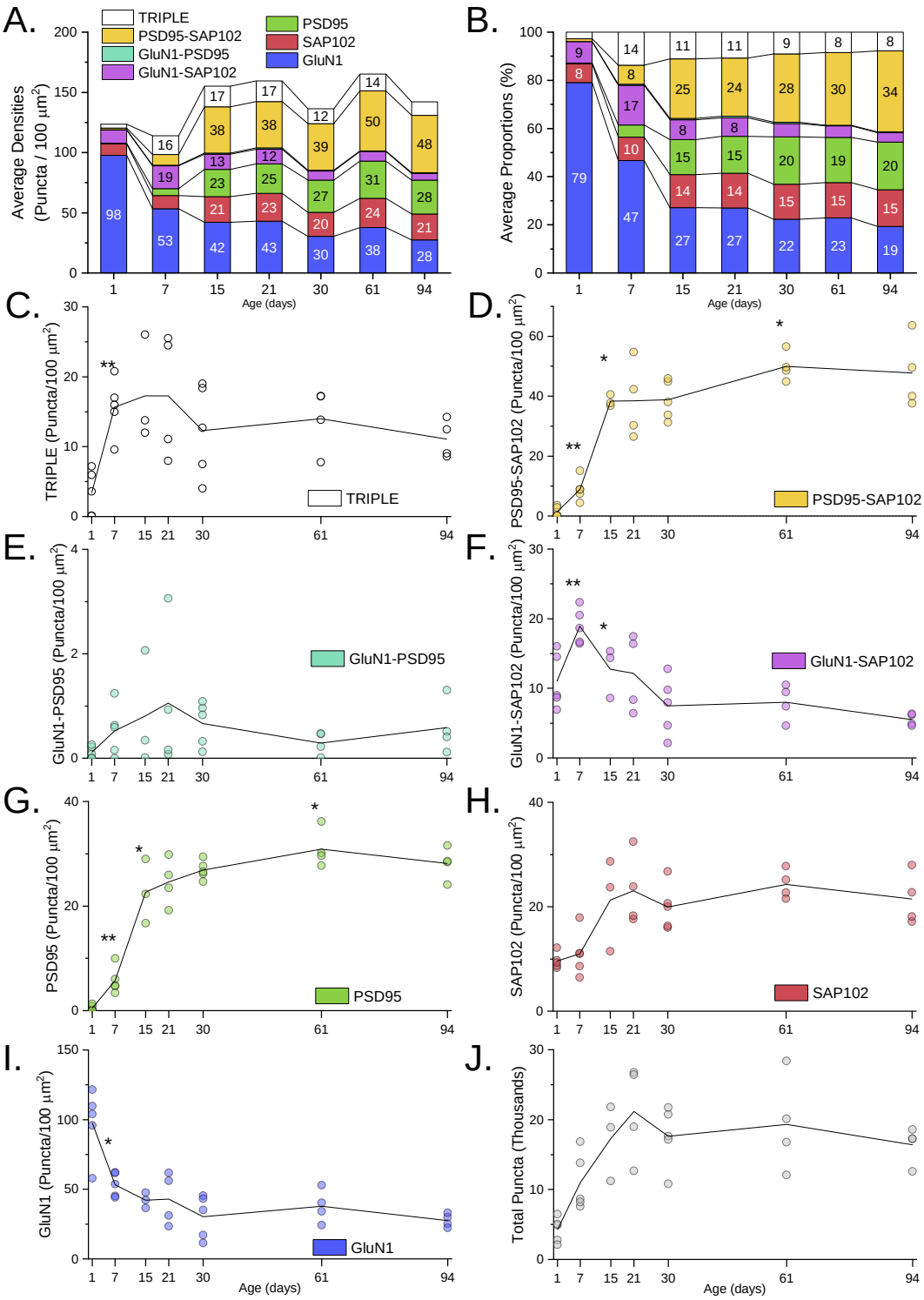
A.
TRIPLE
PSD95-SAP102
GluN1-PSD95
GluN1-SAP102
PSD95
SAP102
GluN1
Average Densities (Puncta / 100 µm²)
B.
Average Proportions (%)
Age (days)
C.
TRIPLE (Puncta/100 µm²)
D.
PSD95-SAP102 (Puncta/100 µm²)
E.
GluN1-PSD95 (Puncta/100 µm²)
F.
GluN1-SAP102 (Puncta/100 µm²)
G.
PSD95 (Puncta/100 µm²)
H.
SAP102 (Puncta/100 µm²)
I.
GluN1 (Puncta/100 µm²)
J.
Total Puncta (Thousands)

CA3ori

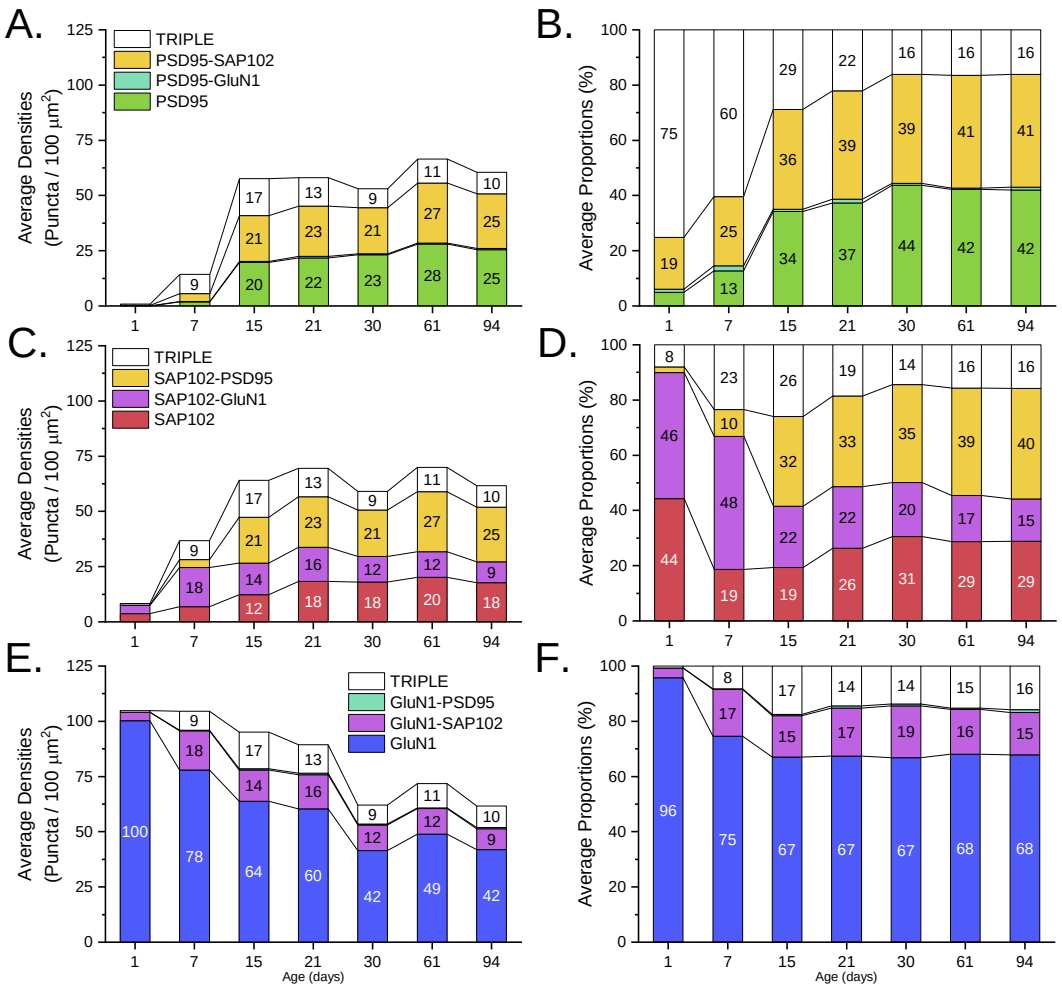
A.
B.
C.
D.
E.
F.
TRIPLE
PSD95-SAP102
PSD95-GluN1
PSD95
SAP102-PSD95
SAP102-GluN1
SAP102
GluN1-PSD95
GluN1-SAP102
GluN1
Average Densities (Puncta / 100 µm²)
Average Proportions (%)
Age (days)

CA3ori

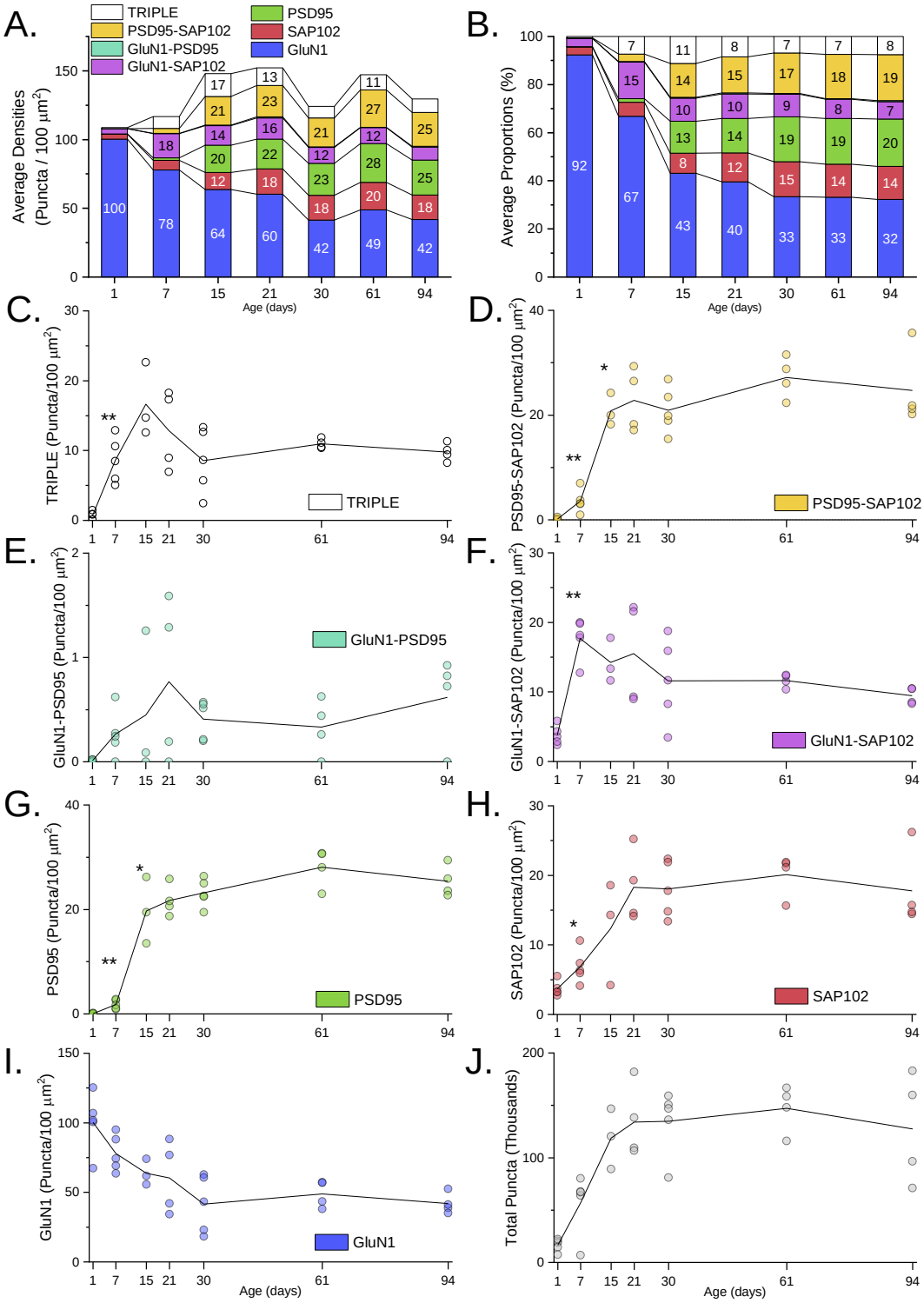
A.
TRIPLE
PSD95-SAP102
GluN1-PSD95
GluN1-SAP102
PSD95
SAP102
GluN1
Average Densities (Puncta / 100 µm²)
B.
Average Proportions (%)
Age (days)
C.
TRIPLE (Puncta/100 µm²)
D.
PSD95-SAP102 (Puncta/100 µm²)
E.
GluN1-PSD95 (Puncta/100 µm²)
F.
GluN1-SAP102 (Puncta/100 µm²)
G.
PSD95 (Puncta/100 µm²)
H.
SAP102 (Puncta/100 µm²)
I.
GluN1 (Puncta/100 µm²)
J.
Total Puncta (Thousands)

CA3rad

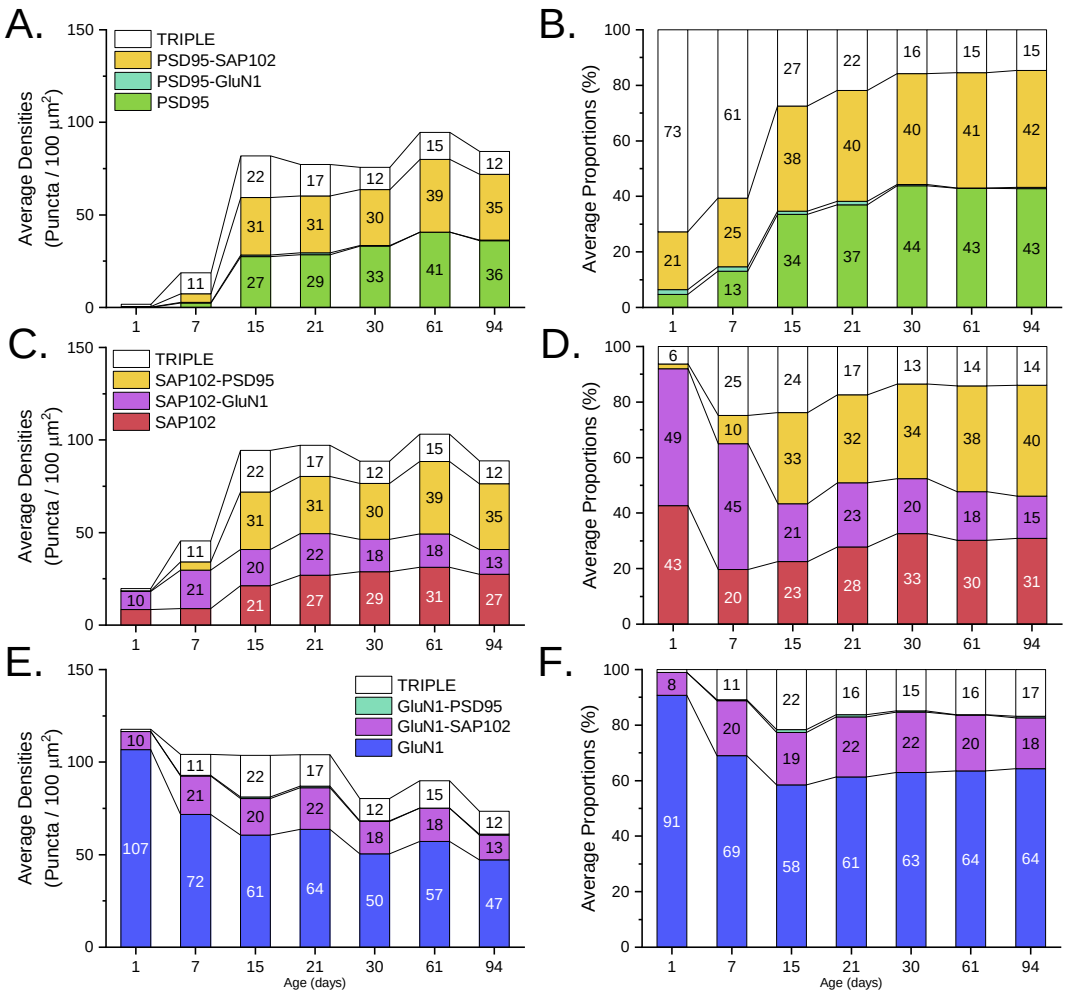
A.
TRIPLE
PSD95-SAP102
PSD95-GluN1
PSD95
Average Densities (Puncta / 100 µm²)
B.
Average Proportions (%)
C.
TRIPLE
SAP102-PSD95
SAP102-GluN1
SAP102
Average Densities (Puncta / 100 µm²)
D.
Average Proportions (%)
E.
TRIPLE
GluN1-PSD95
GluN1-SAP102
GluN1
Average Densities (Puncta / 100 µm²)
Age (days)
F.
Average Proportions (%)
Age (days)

CA3rad

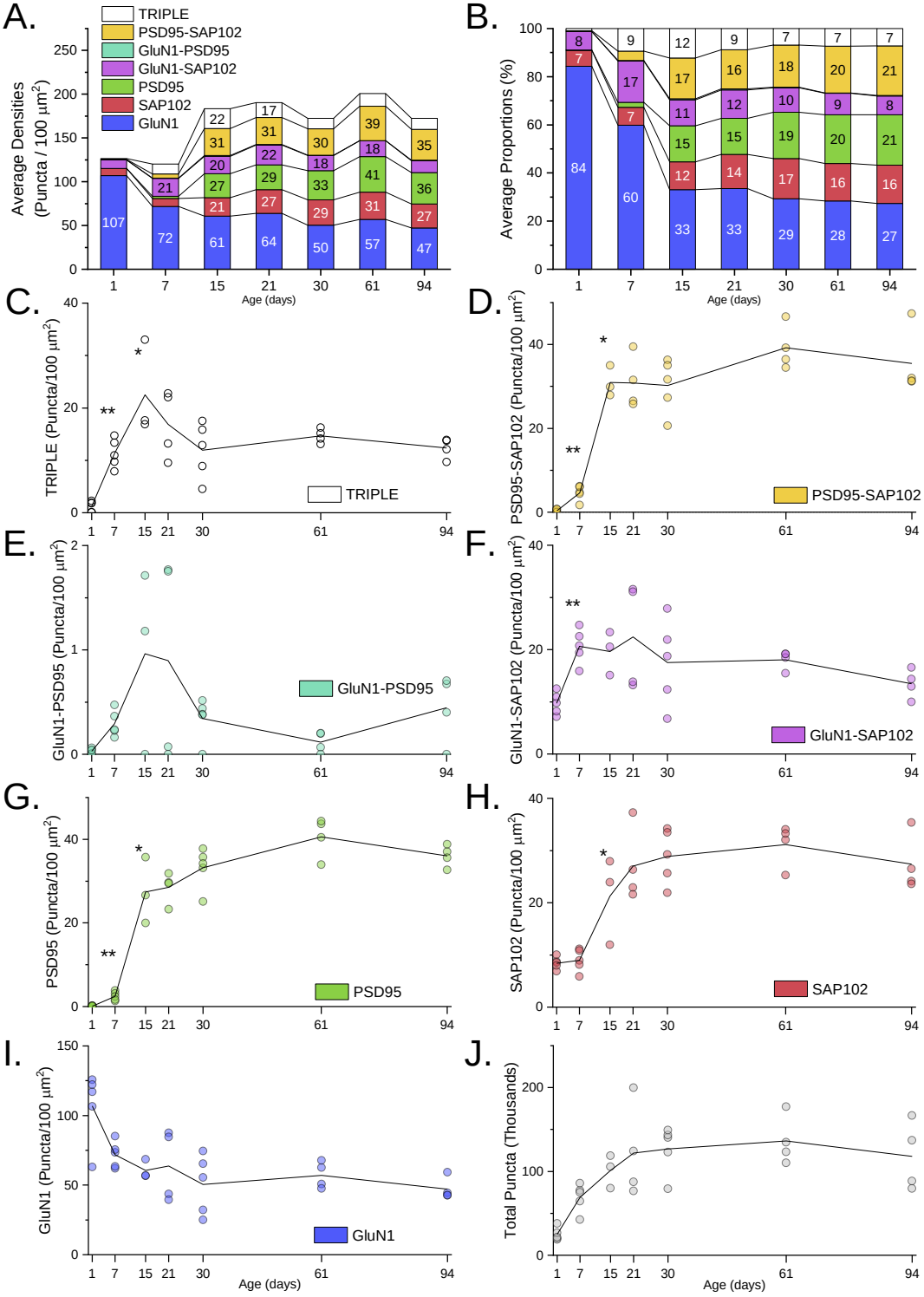
A.
TRIPLE
PSD95-SAP102
GluN1-PSD95
GluN1-SAP102
PSD95
SAP102
GluN1
Average Densities (Puncta / 100 µm²)
Age (days)
B.
Average Proportions (%)
Age (days)
C.
TRIPLE (Puncta/100 µm²)
TRIPLE
D.
PSD95-SAP102 (Puncta/100 µm²)
PSD95-SAP102
E.
GluN1-PSD95 (Puncta/100 µm²)
GluN1-PSD95
F.
GluN1-SAP102 (Puncta/100 µm²)
GluN1-SAP102
G.
PSD95 (Puncta/100 µm²)
PSD95
H.
SAP102 (Puncta/100 µm²)
SAP102
I.
GluN1 (Puncta/100 µm²)
GluN1
Age (days)
J.
Total Puncta (Thousands)
Age (days)

CA3slm

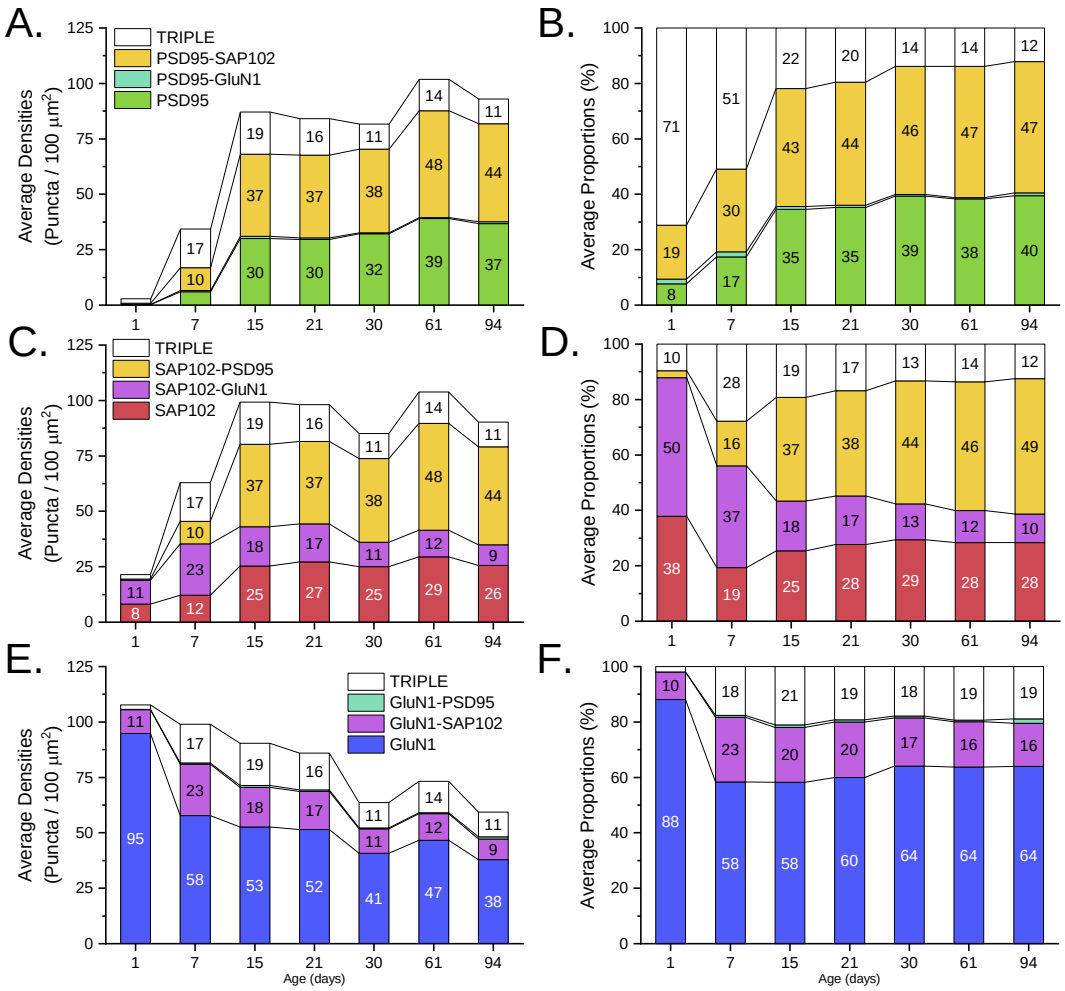
A.
B.
C.
D.
E.
F.
TRIPLE
PSD95-SAP102
PSD95-GluN1
PSD95
SAP102-PSD95
SAP102-GluN1
SAP102
GluN1-PSD95
GluN1-SAP102
GluN1
Average Densities (Puncta / 100 µm²)
Average Proportions (%)
Age (days)

CA3slm

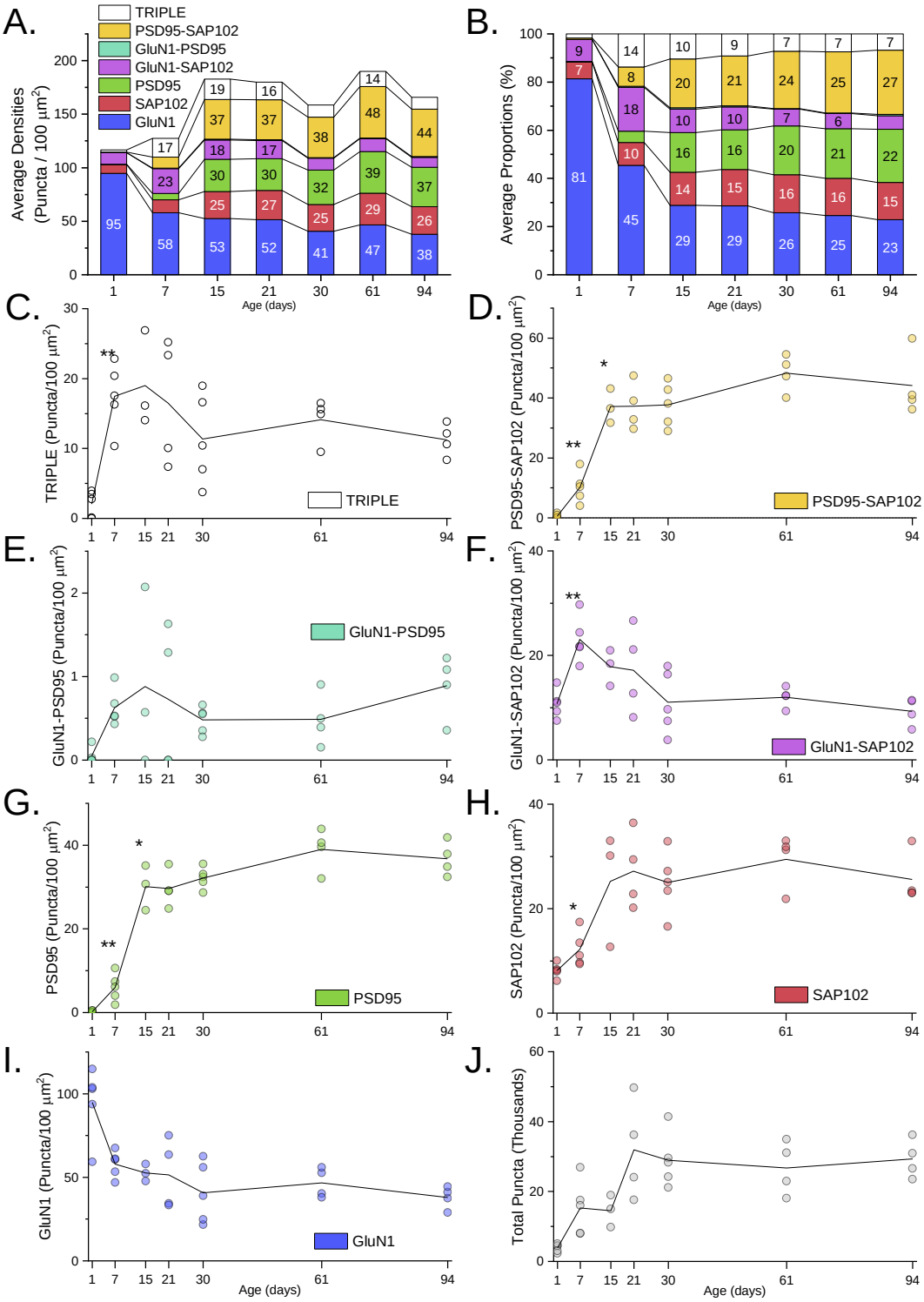
A.
TRIPLE
PSD95-SAP102
GluN1-PSD95
GluN1-SAP102
PSD95
SAP102
GluN1
Average Densities (Puncta / 100 µm²)
Age (days)
B.
Average Proportions (%)
Age (days)
C.
TRIPLE (Puncta/100 µm²)
TRIPLE
D.
PSD95-SAP102 (Puncta/100 µm²)
PSD95-SAP102
E.
GluN1-PSD95 (Puncta/100 µm²)
GluN1-PSD95
F.
GluN1-SAP102 (Puncta/100 µm²)
GluN1-SAP102
G.
PSD95 (Puncta/100 µm²)
PSD95
H.
SAP102 (Puncta/100 µm²)
SAP102
I.
GluN1 (Puncta/100 µm²)
GluN1
Age (days)
J.
Total Puncta (Thousands)
Age (days)

CA3slu

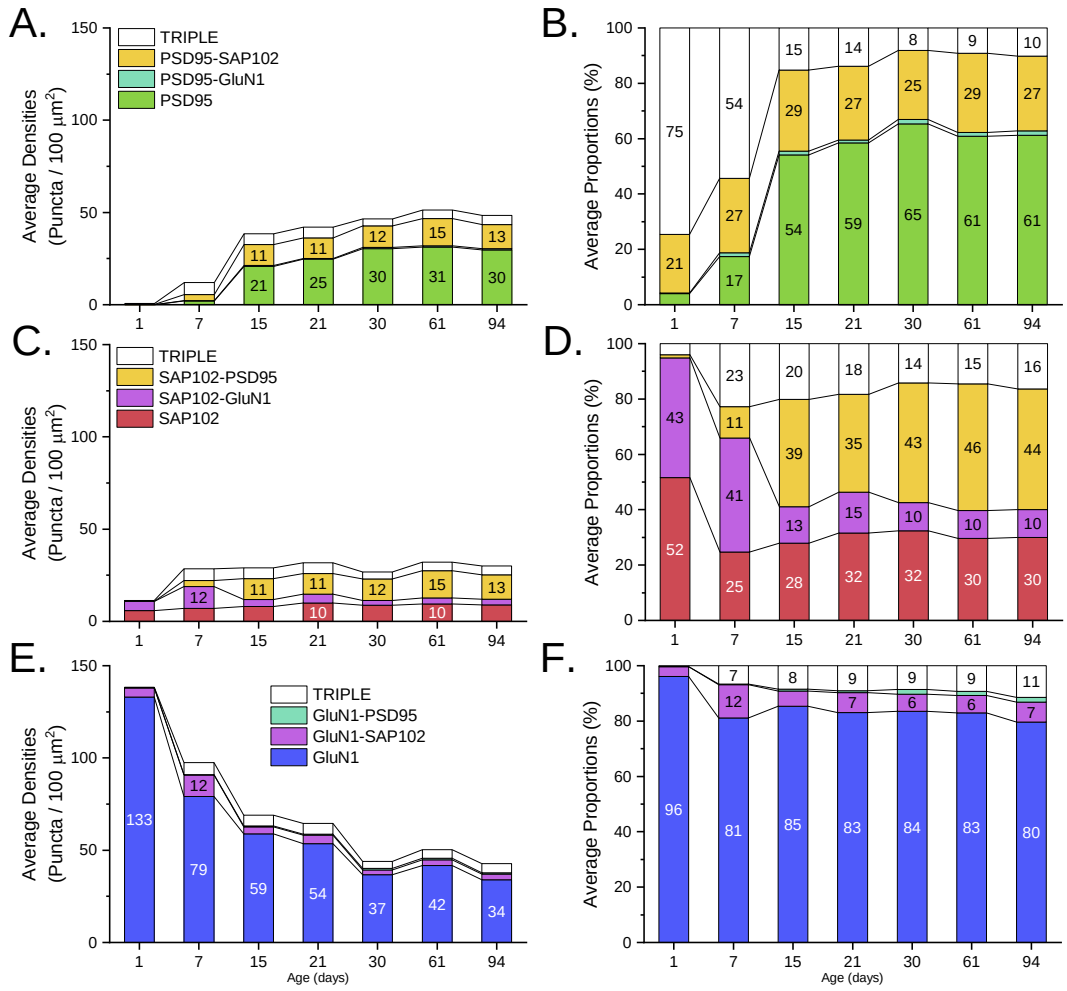
A.
TRIPLE
PSD95-SAP102
PSD95-GluN1
PSD95
Average Densities (Puncta / 100 µm²)
B.
Average Proportions (%)
C.
TRIPLE
SAP102-PSD95
SAP102-GluN1
SAP102
Average Densities (Puncta / 100 µm²)
D.
Average Proportions (%)
E.
TRIPLE
GluN1-PSD95
GluN1-SAP102
GluN1
Average Densities (Puncta / 100 µm²)
Age (days)
F.
Average Proportions (%)
Age (days)

CA3slu

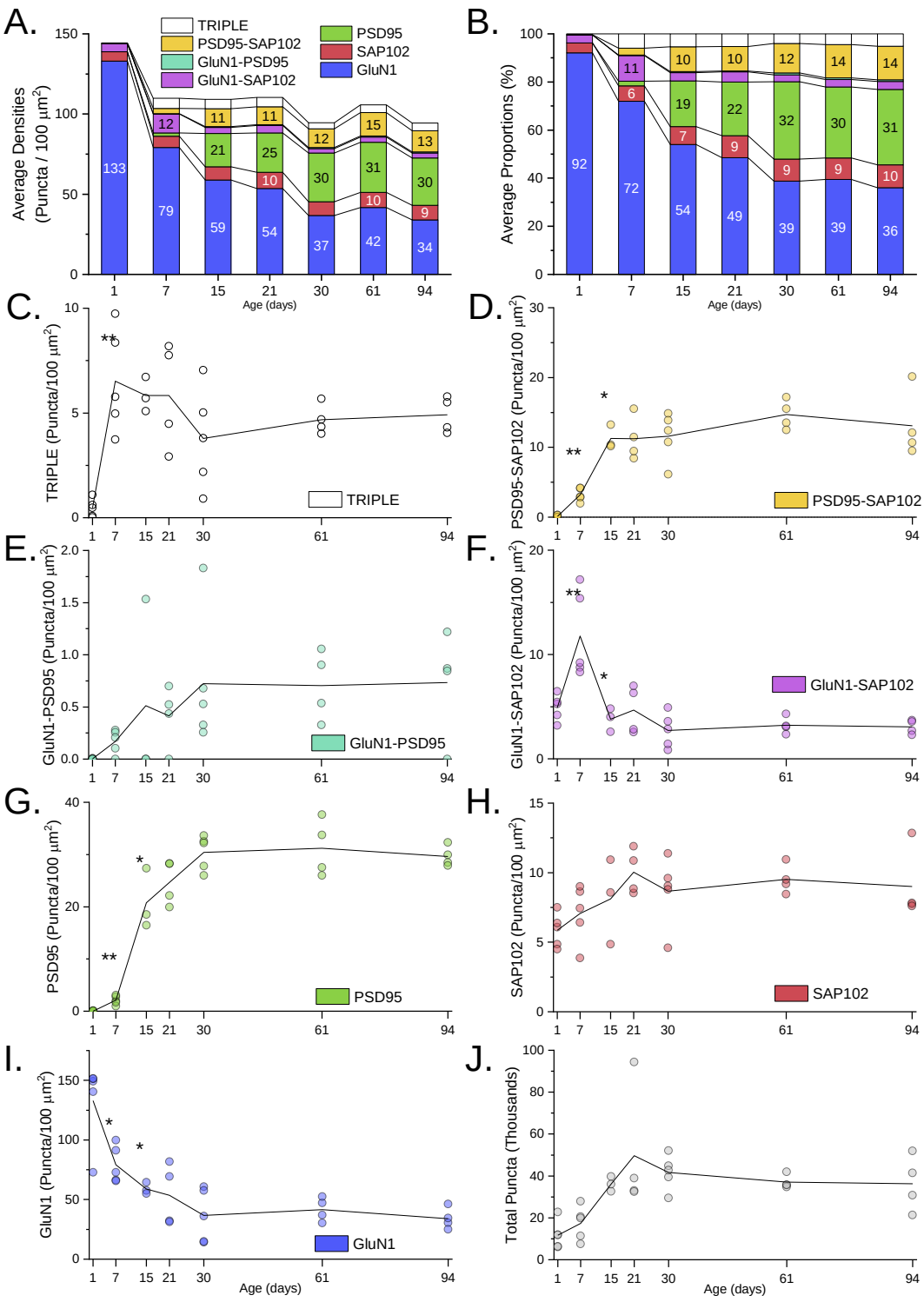
A.
TRIPLE
PSD95-SAP102
GluN1-PSD95
GluN1-SAP102
PSD95
SAP102
GluN1
Average Densities (Puncta / 100 µm²)
B.
Average Proportions (%)
Age (days)
C.
TRIPLE (Puncta/100 µm²)
D.
PSD95-SAP102 (Puncta/100 µm²)
E.
GluN1-PSD95 (Puncta/100 µm²)
F.
GluN1-SAP102 (Puncta/100 µm²)
G.
PSD95 (Puncta/100 µm²)
H.
SAP102 (Puncta/100 µm²)
I.
GluN1 (Puncta/100 µm²)
J.
Total Puncta (Thousands)

DGpo

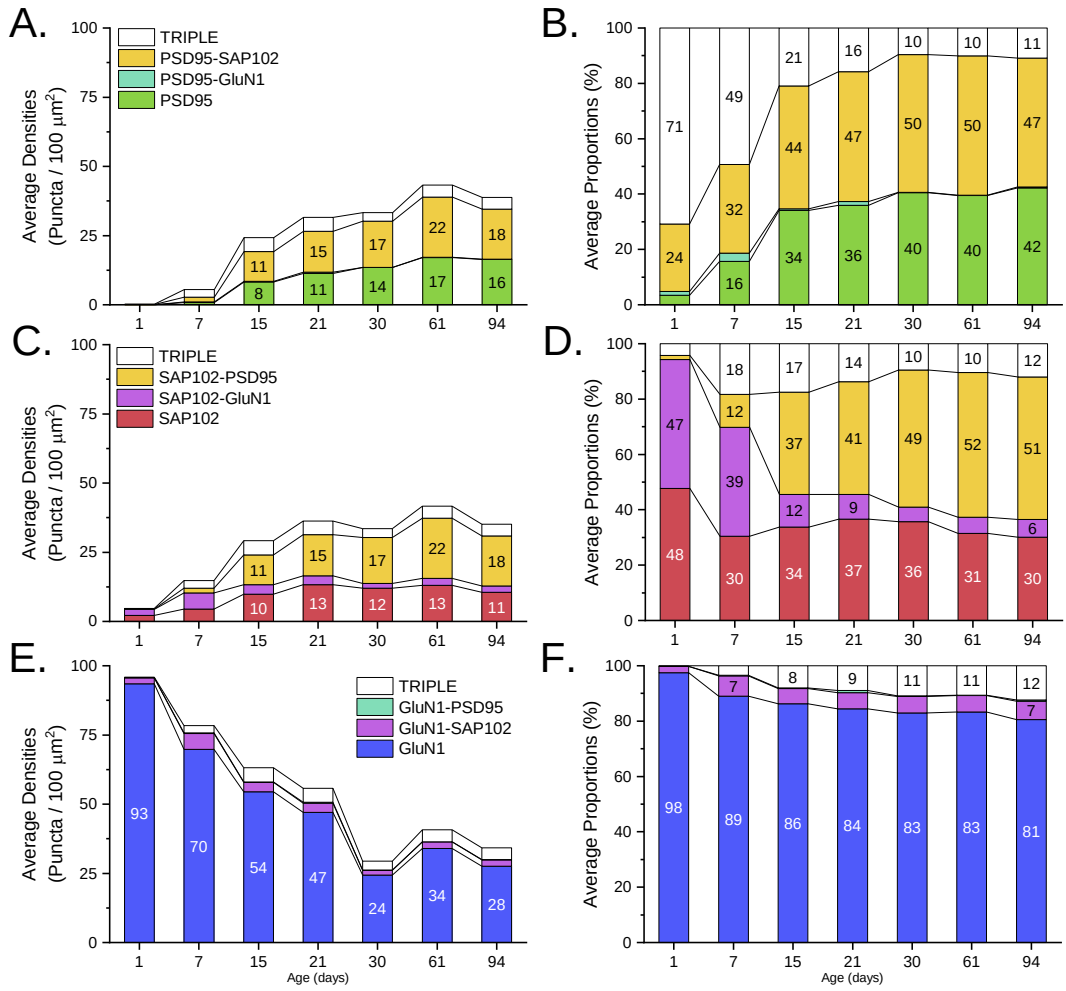
A.
TRIPLE
PSD95-SAP102
PSD95-GluN1
PSD95
Average Densities (Puncta / 100 µm²)
B.
Average Proportions (%)
C.
TRIPLE
SAP102-PSD95
SAP102-GluN1
SAP102
Average Densities (Puncta / 100 µm²)
D.
Average Proportions (%)
E.
TRIPLE
GluN1-PSD95
GluN1-SAP102
GluN1
Average Densities (Puncta / 100 µm²)
Age (days)
F.
Average Proportions (%)
Age (days)

DGpo

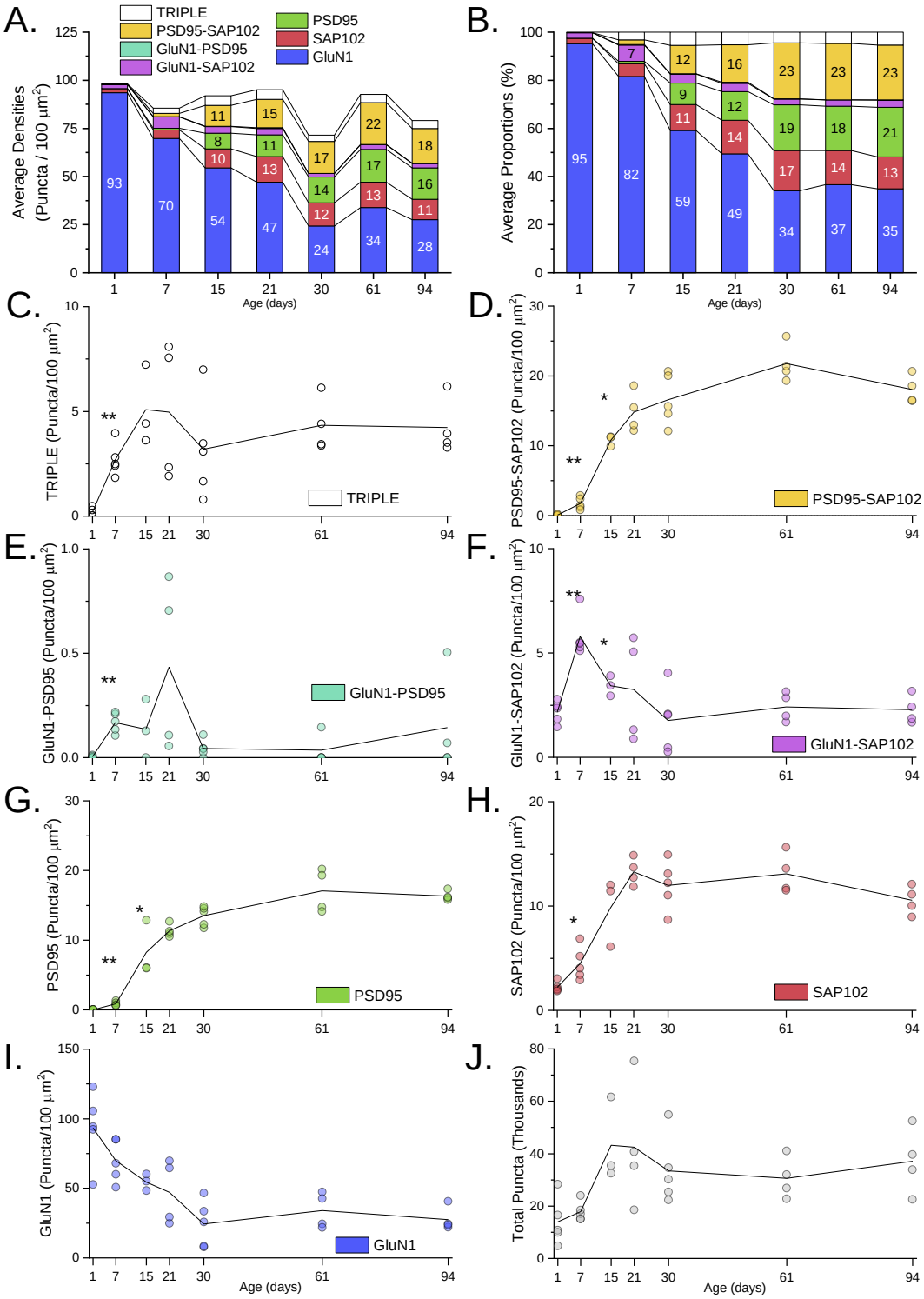
A.
TRIPLE
PSD95-SAP102
GluN1-PSD95
GluN1-SAP102
PSD95
SAP102
GluN1
Average Densities (Puncta / 100 µm²)
Age (days)
B.
Average Proportions (%)
Age (days)
C.
TRIPLE (Puncta/100 µm²)
TRIPLE
D.
PSD95-SAP102 (Puncta/100 µm²)
PSD95-SAP102
E.
GluN1-PSD95 (Puncta/100 µm²)
GluN1-PSD95
F.
GluN1-SAP102 (Puncta/100 µm²)
GluN1-SAP102
G.
PSD95 (Puncta/100 µm²)
PSD95
H.
SAP102 (Puncta/100 µm²)
SAP102
I.
GluN1 (Puncta/100 µm²)
GluN1
Age (days)
J.
Total Puncta (Thousands)
Age (days)

SUB

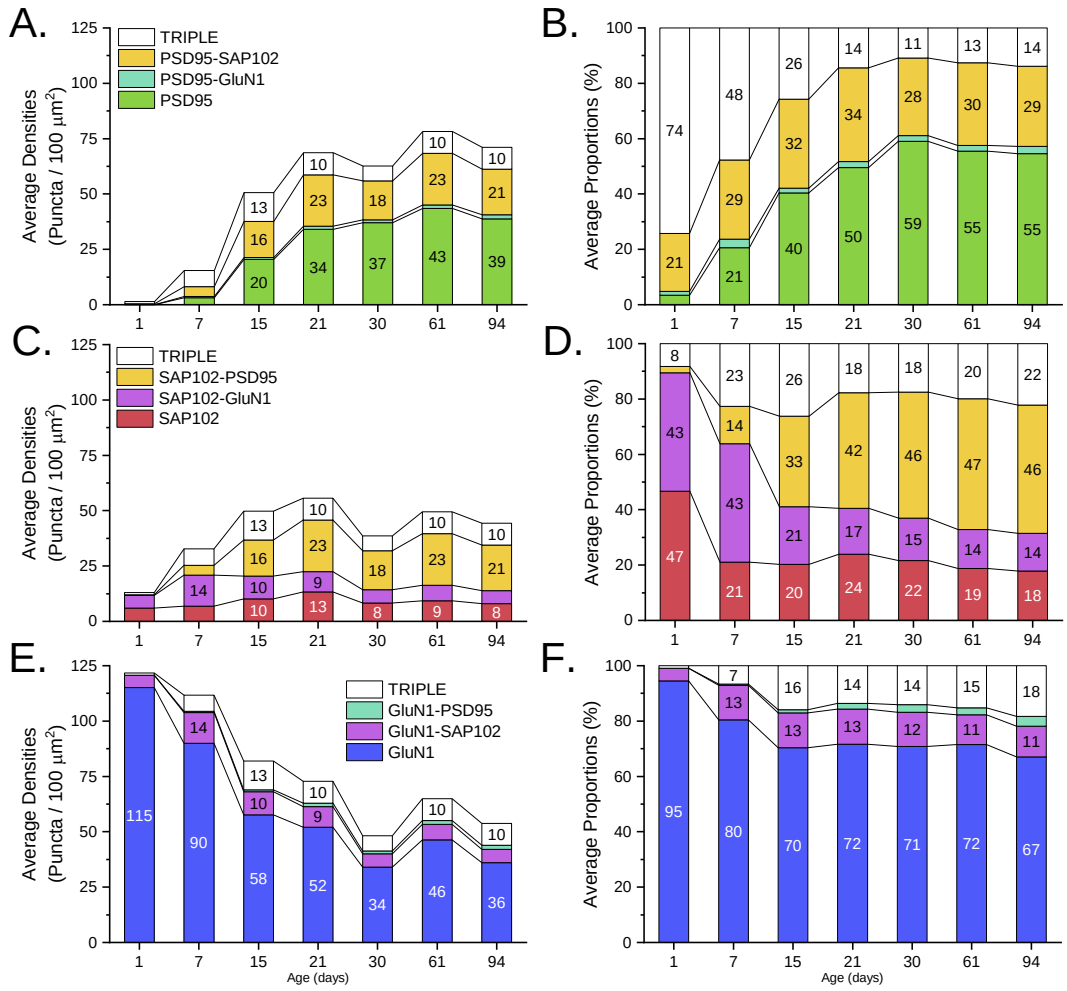
A.
B.
C.
D.
E.
F.
TRIPLE
PSD95-SAP102
PSD95-GluN1
PSD95
SAP102-PSD95
SAP102-GluN1
SAP102
GluN1-PSD95
GluN1-SAP102
GluN1
Average Densities (Puncta / 100 µm²)
Average Proportions (%)
Age (days)

SUB

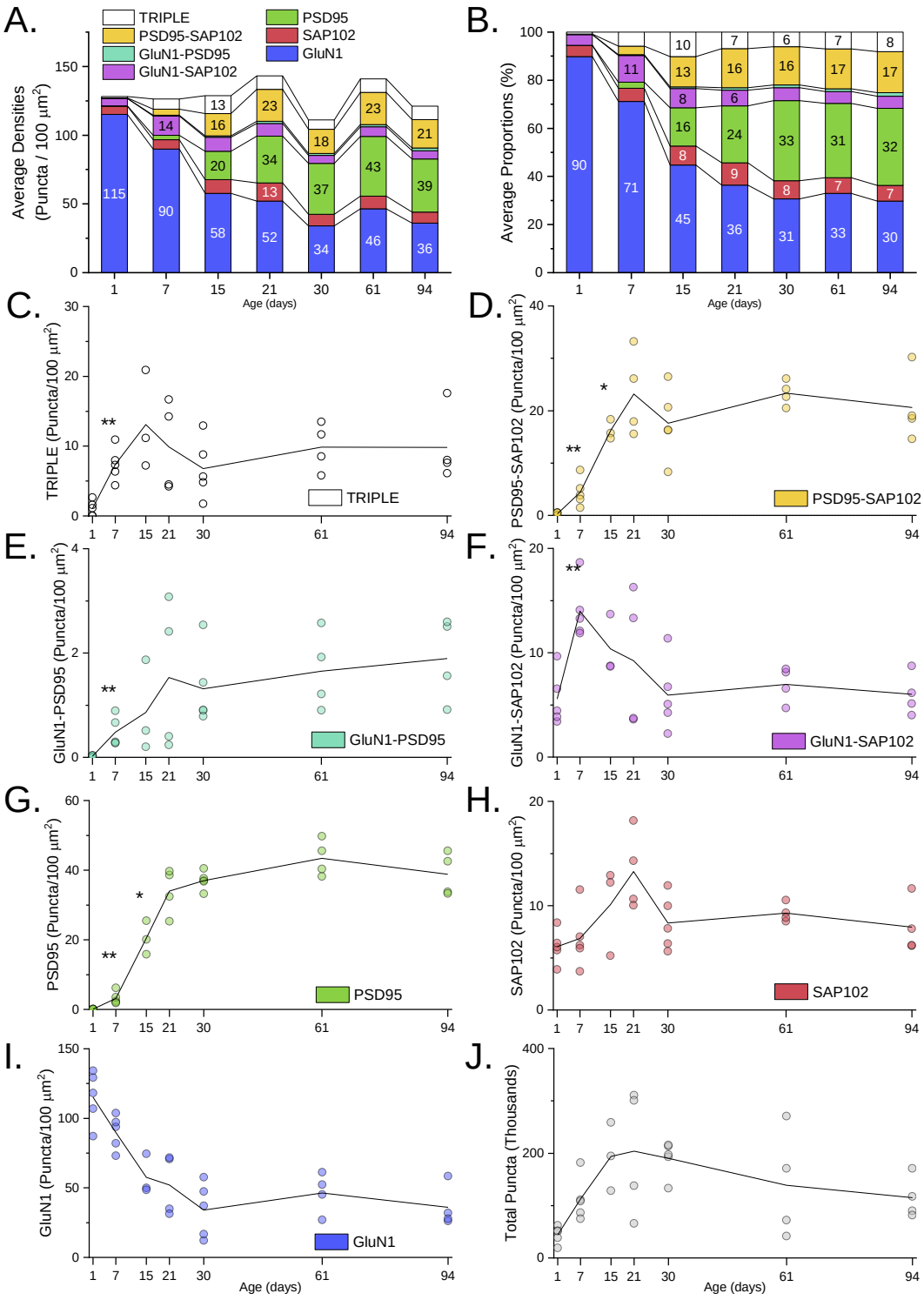
A.
TRIPLE
PSD95-SAP102
GluN1-PSD95
GluN1-SAP102
PSD95
SAP102
GluN1
Average Densities (Puncta / 100 µm²)
Age (days)
B.
Average Proportions (%)
Age (days)
C.
TRIPLE (Puncta/100 µm²)
TRIPLE
D.
PSD95-SAP102 (Puncta/100 µm²)
PSD95-SAP102
E.
GluN1-PSD95 (Puncta/100 µm²)
GluN1-PSD95
F.
GluN1-SAP102 (Puncta/100 µm²)
GluN1-SAP102
G.
PSD95 (Puncta/100 µm²)
PSD95
H.
SAP102 (Puncta/100 µm²)
SAP102
I.
GluN1 (Puncta/100 µm²)
GluN1
Age (days)
J.
Total Puncta (Thousands)
Age (days)

TH

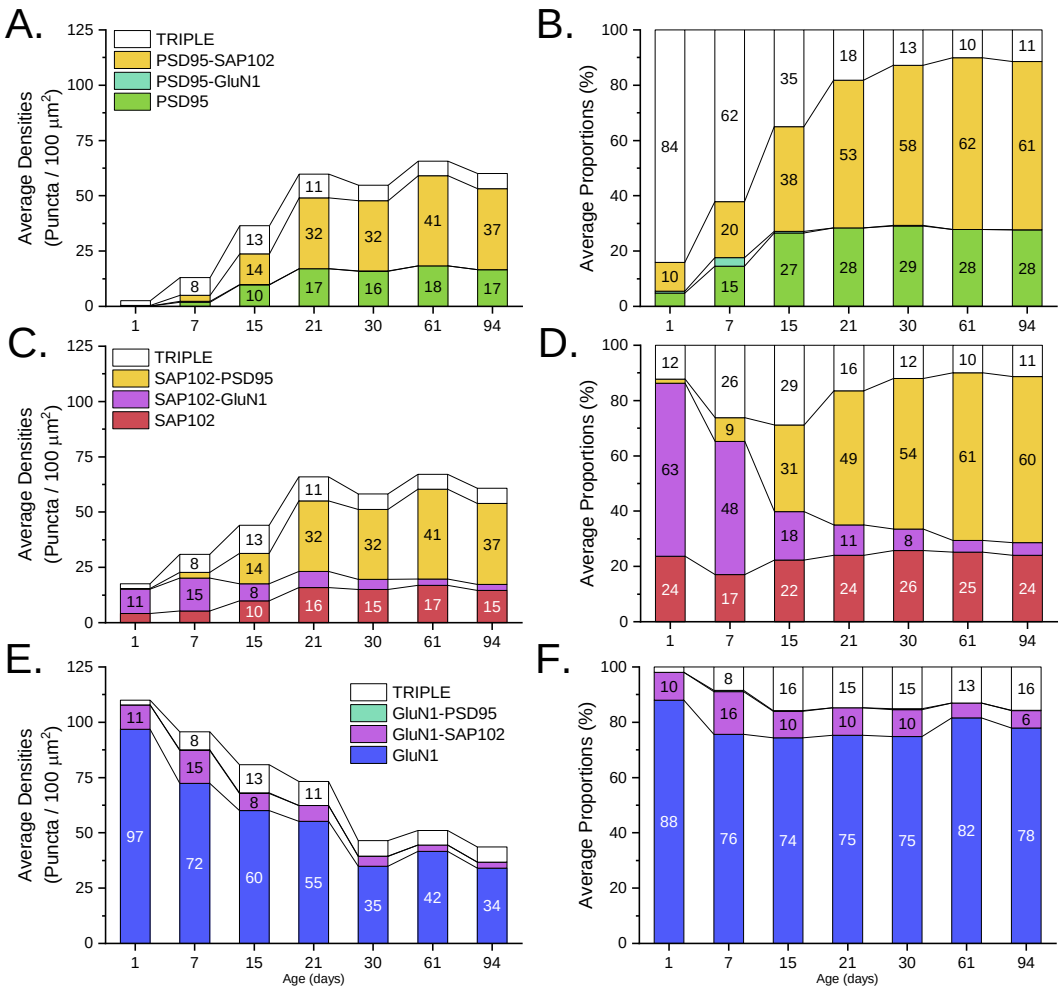
A.
TRIPLE
PSD95-SAP102
PSD95-GluN1
PSD95
Average Densities (Puncta / 100 µm²)
B.
Average Proportions (%)
C.
TRIPLE
SAP102-PSD95
SAP102-GluN1
SAP102
Average Densities (Puncta / 100 µm²)
D.
Average Proportions (%)
E.
TRIPLE
GluN1-PSD95
GluN1-SAP102
GluN1
Average Densities (Puncta / 100 µm²)
Age (days)
F.
Average Proportions (%)
Age (days)

TH

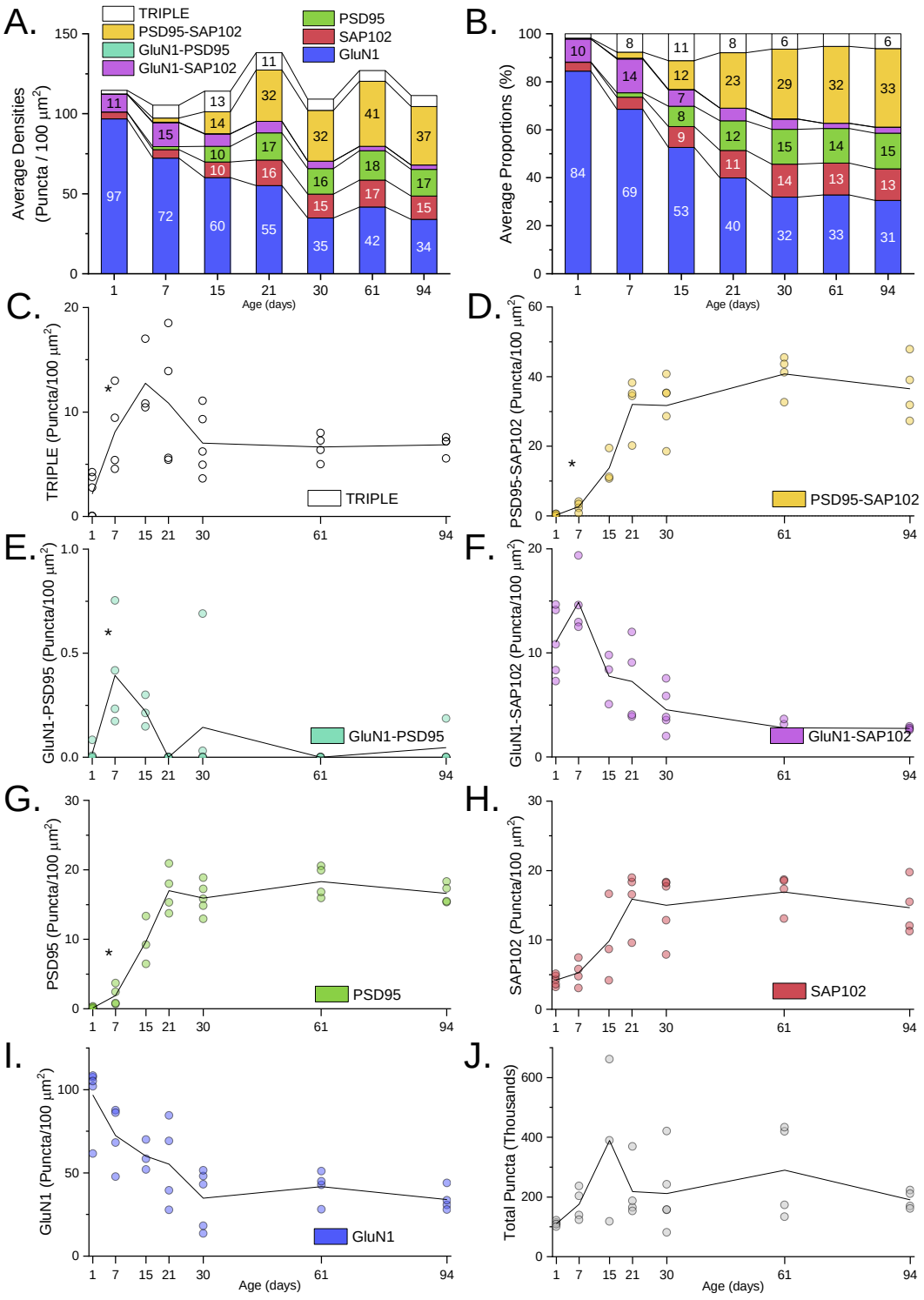
A.
TRIPLE
PSD95-SAP102
GluN1-PSD95
GluN1-SAP102
PSD95
SAP102
GluN1
Average Densities (Puncta / 100 µm²)
Age (days)
B.
Average Proportions (%)
Age (days)
C.
TRIPLE (Puncta/100 µm²)
TRIPLE
D.
PSD95-SAP102 (Puncta/100 µm²)
PSD95-SAP102
E.
GluN1-PSD95 (Puncta/100 µm²)
GluN1-PSD95
F.
GluN1-SAP102 (Puncta/100 µm²)
GluN1-SAP102
G.
PSD95 (Puncta/100 µm²)
PSD95
H.
SAP102 (Puncta/100 µm²)
SAP102
I.
GluN1 (Puncta/100 µm²)
GluN1
Age (days)
J.
Total Puncta (Thousands)
Age (days)

CTX

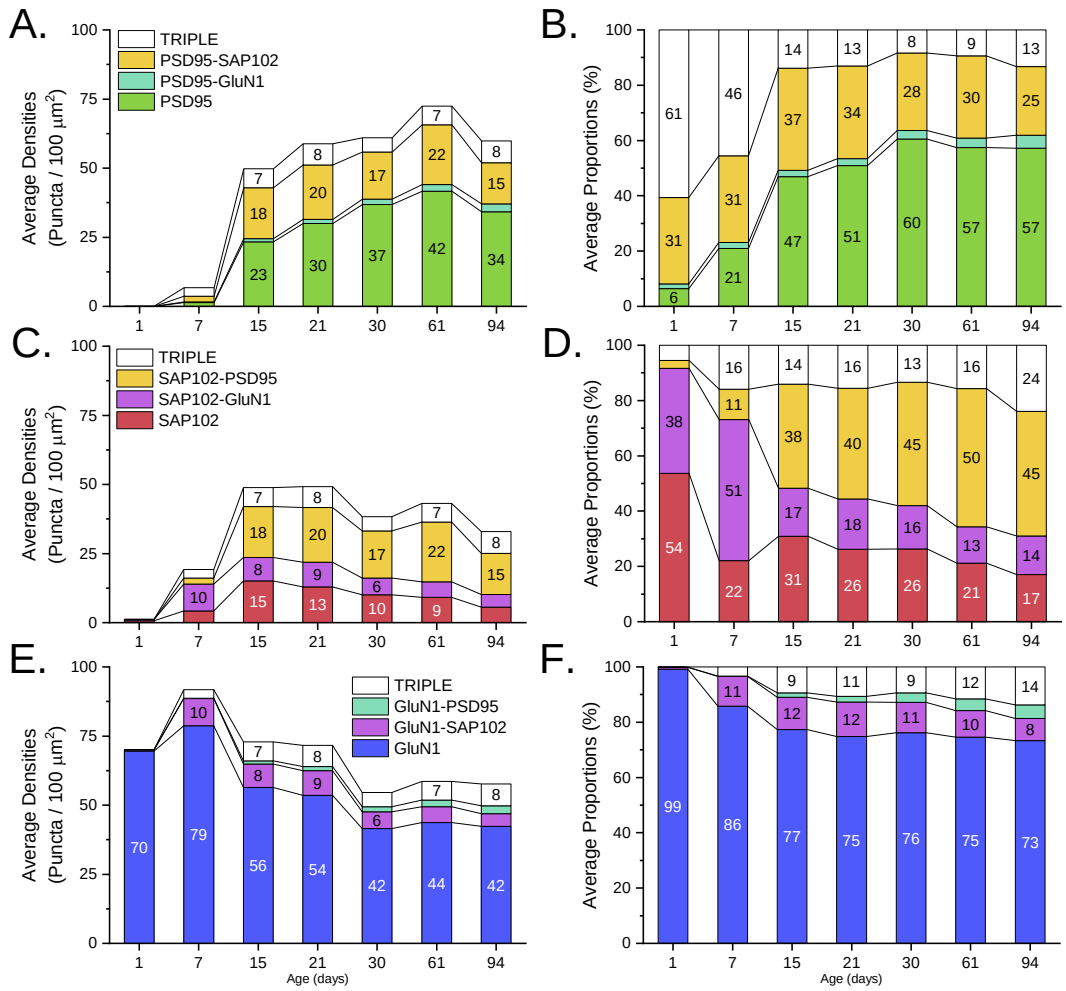
A.
B.
C.
D.
E.
F.
TRIPLE
PSD95-SAP102
PSD95-GluN1
PSD95
SAP102-PSD95
SAP102-GluN1
SAP102
GluN1-PSD95
GluN1-SAP102
GluN1
Average Densities (Puncta / 100 µm²)
Average Proportions (%)
Age (days)

CTX

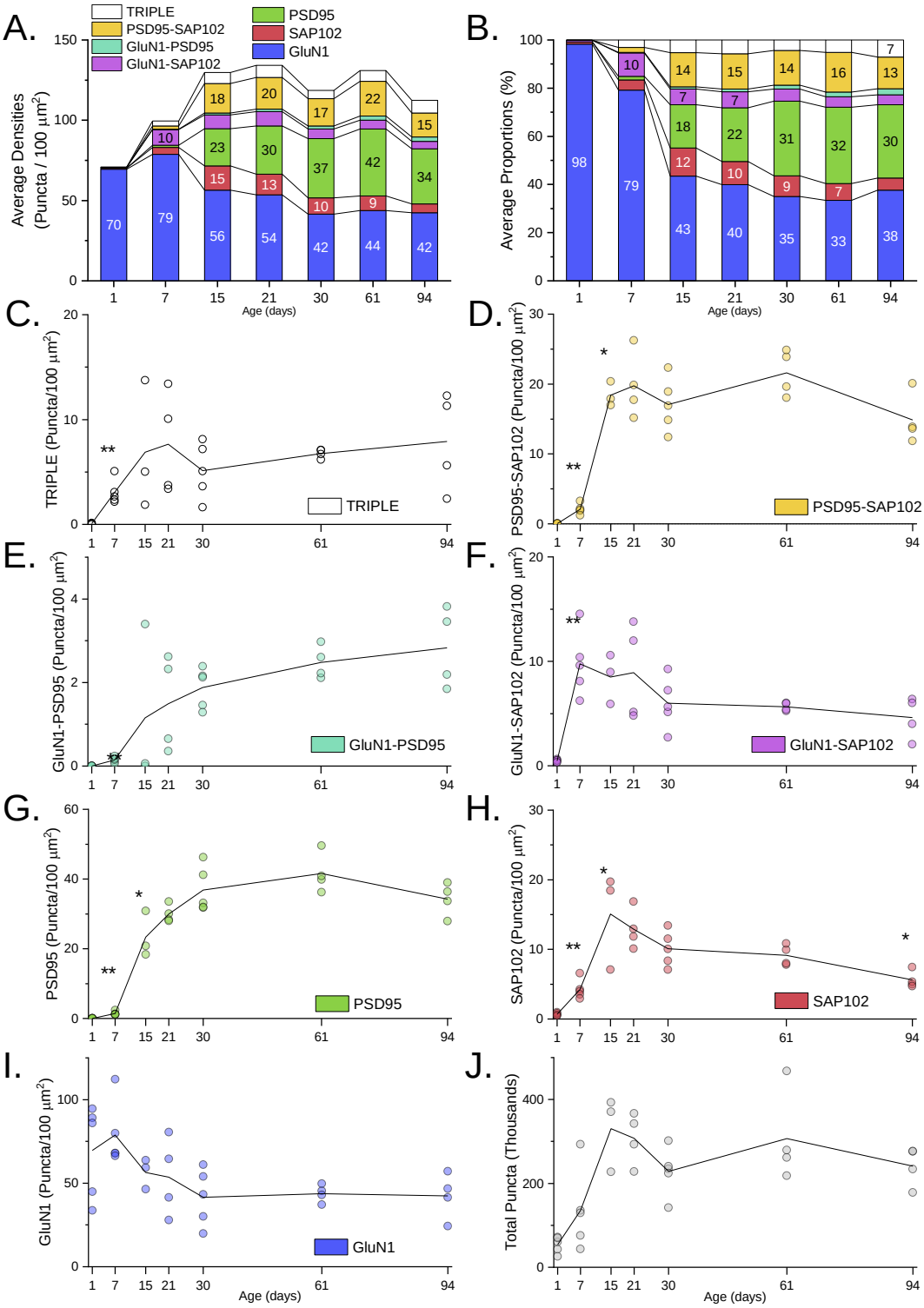
A.
TRIPLE
PSD95-SAP102
GluN1-PSD95
GluN1-SAP102
PSD95
SAP102
GluN1
Average Densities (Puncta / 100 µm²)
Age (days)
B.
Average Proportions (%)
Age (days)
C.
TRIPLE (Puncta/100 µm²)
TRIPLE
D.
PSD95-SAP102 (Puncta/100 µm²)
PSD95-SAP102
E.
GluN1-PSD95 (Puncta/100 µm²)
GluN1-PSD95
F.
GluN1-SAP102 (Puncta/100 µm²)
GluN1-SAP102
G.
PSD95 (Puncta/100 µm²)
PSD95
H.
SAP102 (Puncta/100 µm²)
SAP102
I.
GluN1 (Puncta/100 µm²)
GluN1
Age (days)
J.
Total Puncta (Thousands)
Age (days)

CA1rad tangential gradients in coronal and sagittal plane

Figures are the same type as before. X-axis denotes segments along the tangential axis of the CA1rad instead of age groups.

CA1rad tangential gradient CORONAL PLANE (P94)

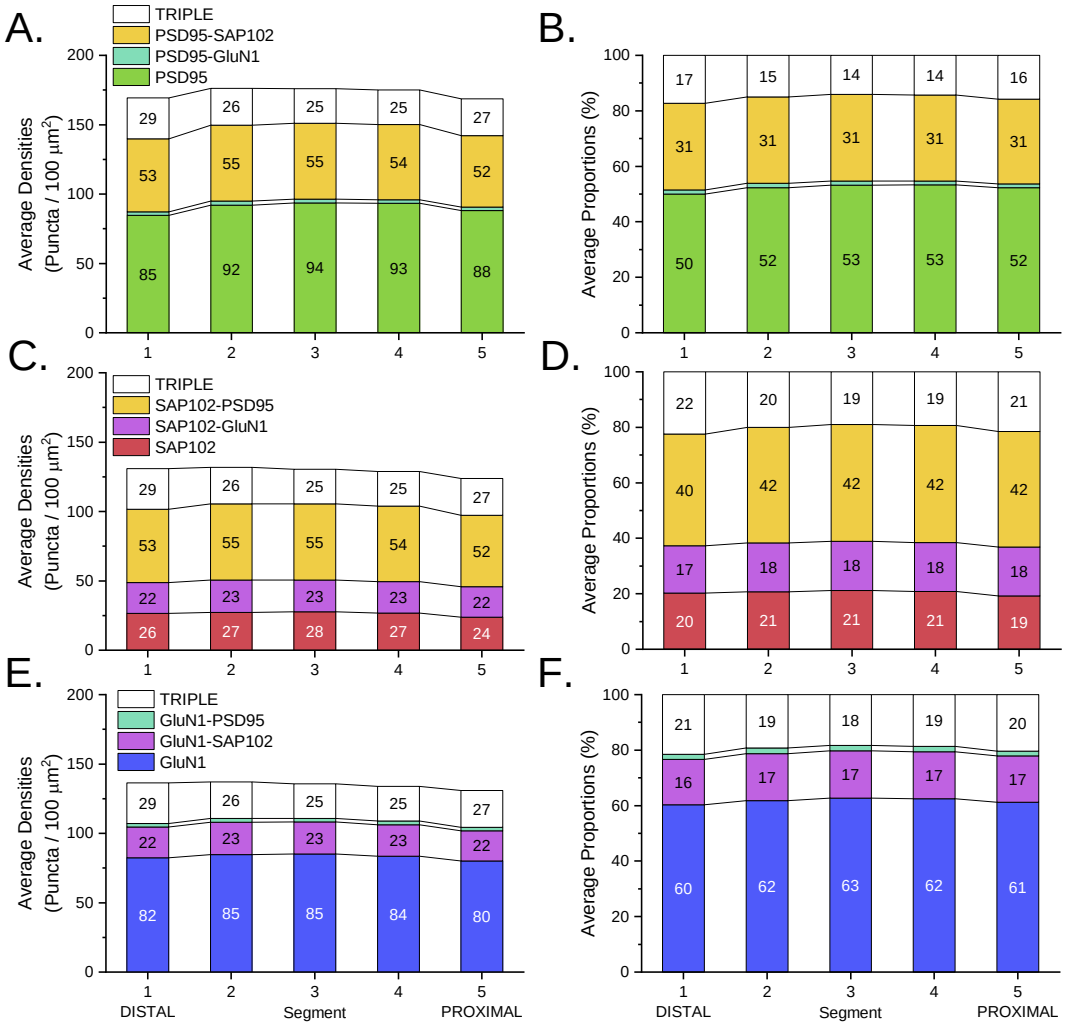

CA1rad tangential gradient CORONAL PLANE (P94)

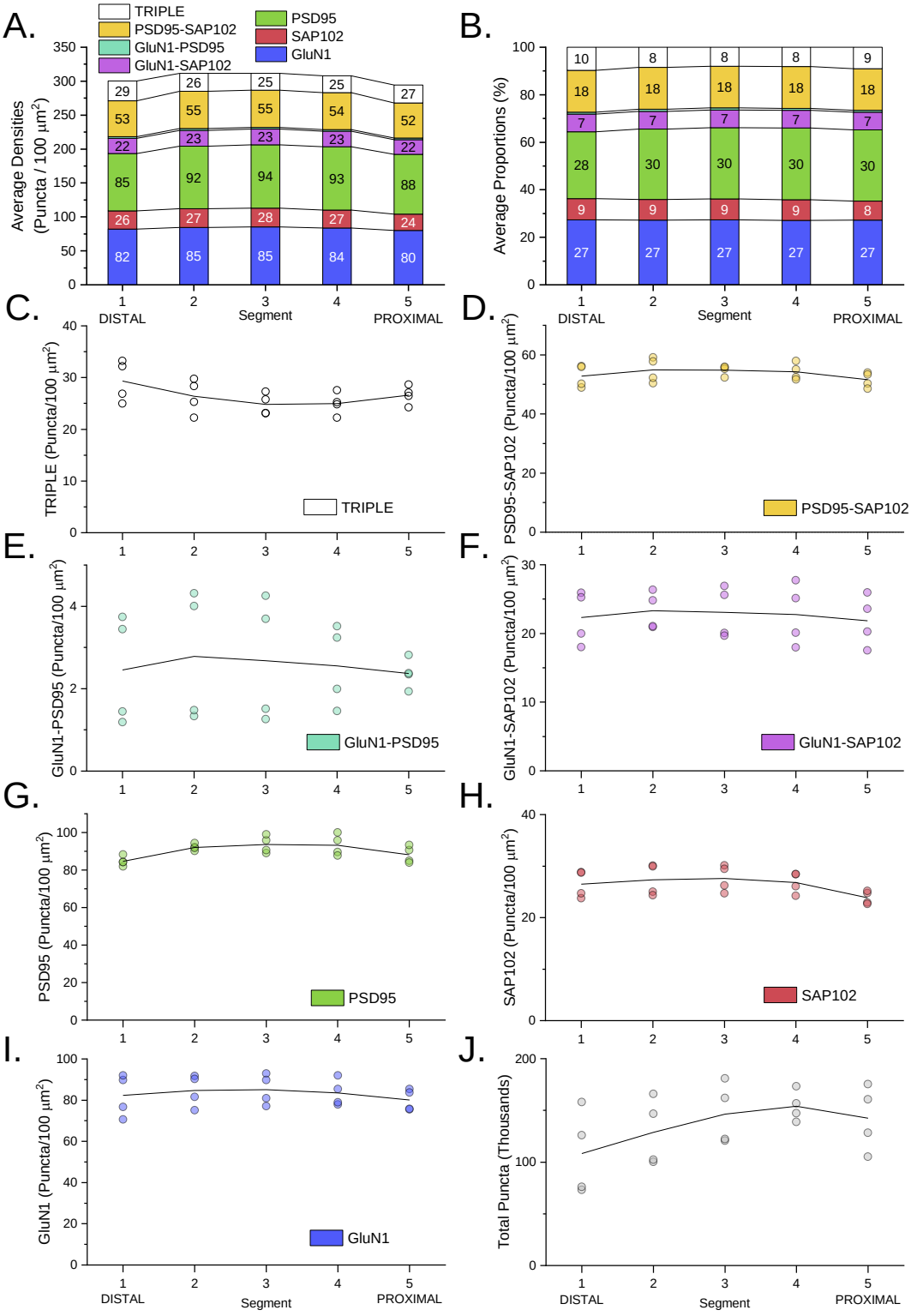

CA1rad tangential gradient SAGITTAL PLANE (P94)

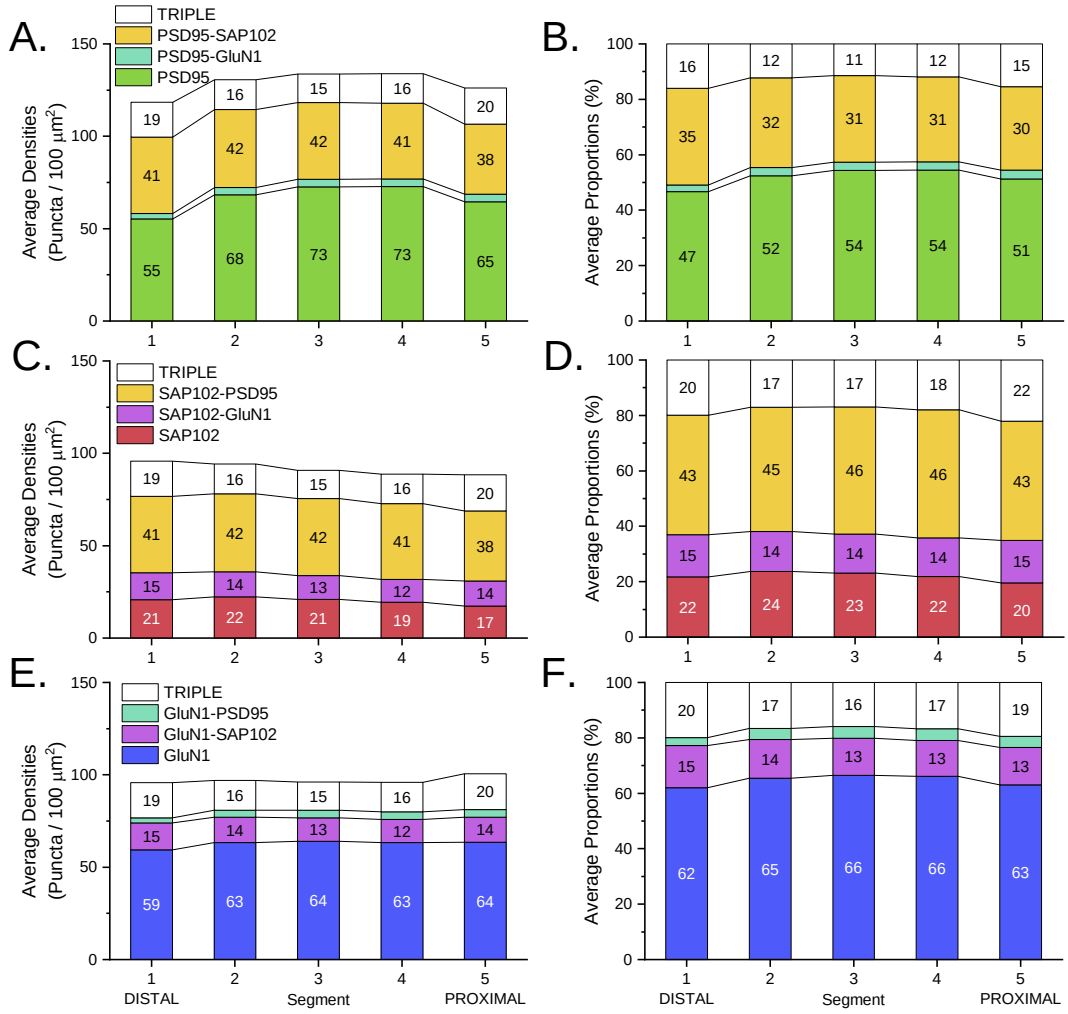

CA1rad tangential gradient SAGITTAL PLANE (P94)